Dissertation zur Erlangung des akademischen Grades *Doktor der Naturwissenschaften*
der Fakultät für Physik der Ludwig-Maximilians-Universität München

On the role of cosmic rays in clusters of galaxies

vorgelegt von Christoph Pfrommer aus Ulm/Donau

München, 31. Aug. 2005

Dissertation der Fakultät für Physik der
Ludwig-Maximilians-Universität München

Christoph Pfrommer:
On the role of cosmic rays in clusters of galaxies
Dissertation der Fakultät für Physik der Ludwig-Maximilians Universität München
ausgeführt am Max-Planck-Institut für Astrophysik

Stufen

Wie jede Blüte welkt und jede Jugend
Dem Alter weicht, blüht jede Lebensstufe,
Blüht jede Weisheit auch und jede Tugend
Zu ihrer Zeit und darf nicht ewig dauern.
Es muß das Herz bei jedem Lebensrufe
Bereit zum Abschied sein und Neubeginne,
Um sich in Tapferkeit und ohne Trauern
In andre, neue Bindungen zu geben.
Und jedem Anfang wohnt ein Zauber inne,
Der uns beschützt und der uns hilft, zu leben.

Wir sollen heiter Raum um Raum durchschreiten,
An keinem wie an einer Heimat hängen,
Der Weltgeist will nicht fesseln uns und engen,
Er will uns Stuf' um Stufe heben, weiten.
Kaum sind wir heimisch einem Lebenskreise
Und traulich eingewohnt, so droht Erschlaffen,
Nur wer bereit zu Aufbruch ist und Reise,
Mag lähmender Gewöhnung sich entraffen.
Es wird vielleicht auch noch die Todesstunde
Uns neuen Räumen jung entgegensenden,
Des Lebens Ruf an uns wird niemals enden ...
Wohlan denn, Herz, nimm Abschied und gesunde!

aus Hermann Hesse: Das Glasperlenspiel

Contents

1. Abstract

On the role of cosmic rays in clusters of galaxies

We take a multi-faceted approach to study the relativistic cosmic ray (CR) proton population in galaxy clusters. CR protons may be accelerated by structure formation shock waves, injected from radio galaxies into the intra-cluster medium, or result from supernova driven galactic winds. This thesis addresses the following questions: do CR protons exist in galaxy clusters? What is the dynamic and cosmological impact of CRs? How can we observe them? How can we describe CRs and their interactions? The first major part of this thesis investigates the question of the dynamic influence of CRs on the intra-cluster medium and searches for unbiased tracers of their existence using multi-frequency observational results. To this end, I develop an analytical framework to describe the hadronic interactions of CR protons with the ambient thermal plasma. In the second part, a description of CR gas for cosmological applications is presented that is especially suited for hydrodynamical simulations. During the course of this work, I focus on developing a formalism for instantaneously identifying and estimating the strength of structure formation shocks during cosmological simulations to accelerate CRs through diffusive shock acceleration.

Since the energetically dominant CR population is trapped by cluster magnetic fields, it can only be observed indirectly through non-thermal radiative processes. CR protons interact hadronically with the ambient plasma and produce mainly neutral and charged pions that successively decay into γ-rays, secondary electrons, and neutrinos. I develop an analytic formalism which describes the induced radio synchrotron, inverse Compton, and γ-ray emission. Comparing the expected γ-ray flux to the upper limits obtained by the γ-ray observatory EGRET, I am able to constrain the CR proton energy density in nearby cooling core clusters to $< 20\%$ relative to the thermal energy density. In this context, I study the hypothesis that the diffuse radio synchrotron emission of galaxy clusters is produced by hadronically originating relativistic electrons and I develop a non-parametric criterion to obtain the minimum energy state for an observed radio synchrotron emission: the excellent agreement between the observed and theoretically expected radio surface brightness profile of the Perseus mini-halo and the small amount of energy density in CR protons needed to account for the observed radio emission makes this hadronic model an attractive explanation of radio mini-halos found in cooling core clusters. To explain the giant radio halo of Coma within the hadronic model of secondary electrons, the CR proton-to-thermal energy density profile has to increase radially up to moderate CR energy densities. Cosmological simulations that self-consistently follow CR acceleration at shock waves predict such an energy density profile: strong shock waves, that occur predominantly in low density regions, are able to efficiently accelerate high-energetic CRs, whereas weak central flow shocks inject only a low-energetic CR population which is strongly diminished by Coulomb interactions. This implies that the dynamic importance of the shock-injected CR energy density is largest in the low-density halo infall regions, but is less important for the weaker shocks occurring in central high-density cluster regions.

As an extension of this work, I propose a new method in order to elucidate the content of the radio plasma bubbles located at cool cores of galaxy clusters. Using the Sunyaev-Zel'dovich (SZ) effect, the *Atacama Large Millimeter Array* and the *Green Bank Telescope* should be able to infer the dynamically dominant CR component of the plasma bubbles in suitable galaxy clusters within short observation times. Future high-sensitivity multi-frequency SZ observations will be able to infer the energy spectrum of the dynamically dominant electron population. This knowledge can yield indirect indications for an underlying composition of relativistic outflows of radio galaxies because plasma bubbles represent the relic fluid of jets.

In the second major part of my thesis, I address the problem of constructing an accurate and self-consistent model for the description of CRs that aims at studying the dynamic influence of CRs on structure formation and galaxy evolution. This will not only allow the production of realistic non-thermal emission signatures of galaxies and clusters of galaxies, but also allow in-vivo studies of dynamic effects driven by relativistic particles and the star formation history. The developed model self-consistently traces relativistic protons originating from various kinds of sources, such as structure formation shock waves and supernovae driven galactic winds, and also accounts for

dissipative processes in the relativistic gas component. To this end, I develop a formalism for the identification and accurate estimation of the strength of structure formation shocks *during* cosmological smoothed particle hydrodynamics simulations. Shocks not only play a decisive role for the thermalization of gas in virializing structures but also for the acceleration of CRs through diffusive shock acceleration. The formalism is applicable both to ordinary non-relativistic thermal gas and to plasmas composed of CRs and thermal gas. I apply these methods to studying the properties of structure formation shocks in high-resolution hydrodynamic simulations of the ΛCDM model and find that most of the energy is dissipated in weak internal shocks which are predominantly central flow shocks or merger shock waves traversing halo centers. Collapsed cosmological structures are surrounded by external shocks with a much higher Mach number, but they play only a minor role in the energy balance of thermalization. I show that after the epoch of cosmic reionization, the Mach number distribution is significantly modified by an efficient suppression of strong external shock waves due to the associated increase of the sound speed of the diffuse gas.

Kosmische Strahlung in Galaxienhaufen

Für die Untersuchung der relativistischen Protonenpopulation (*engl.: cosmic rays, CRs*) in Galaxienhaufen haben wir einen vielschichtigen Ansatz gewählt. CR-Protonen können an Stoßwellen während der kosmischen Strukturentstehung beschleunigt werden, sie können von Radiogalaxien in das Gas des Galaxienhaufens injiziert werden oder aus galaktischen Winden entstehen, die von Supernova-Explosionen angetrieben werden. Diese Doktorarbeit hat sich mit folgenden Fragen befaßt: Existieren CR-Protonen in Galaxienhaufen? Welchen dynamischen und kosmologischen Einfluß haben CRs? Wie können wir diese beobachten? Wie können wir CRs und ihre Wechselwirkungen beschreiben? Der erste Teil dieser Arbeit untersucht, ob CRs einen dynamischen Einfluß auf das Gas in Galaxienhaufens haben und sucht nach Indikatoren für die Existenz von CRs unter der Verwendung von Daten aus Multifrequenz-Beobachtungen. Zu diesem Zweck entwickle ich einen analytischen Formalismus, um die hadronische Wechselwirkung von CR-Protonen mit dem umgebenden thermischen Gas zu beschreiben. Im zweiten Teil stelle ich eine Beschreibung für CR-Gas in kosmologischen Anwendungen vor, das für hydrodynamische Simulationen besonders geeignet ist. Im weiteren Verlauf dieser Arbeit konzentriere ich mich auf die Entwicklung eines Formalismus, der die Stärke von Strukturentstehungs-Stoßwellen unmittelbar während kosmologischer Simulationen genau bestimmt, um die CRs mit diffusiver Stoßwellenbeschleunigung zu generieren.

Da die energetisch dominierende CR-Population durch Magnetfelder des Galaxienhaufens gebunden ist, kann sie nur indirekt durch nicht-thermische Strahlungsprozesse nachgewiesen werden. CR-Protonen wechselwirken hadronisch mit dem sie umgebenden Plasma und produzieren hauptsächlich neutrale und geladene Pionen, die sukzessive in γ-Strahlung, sekundäre Elektronen und Neutrinos zerfallen. Ich entwickle einen analytischen Formalismus, der die induzierte Radio-Synchrotronstrahlung, inverse Compton-Emission und γ-Strahlung beschreibt. Durch Vergleich des erwarteten γ-Strahlenflusses mit den mit Hilfe des EGRET-Satelliten gewonnenen oberen Grenzen an die emittierte γ-Strahlung ist es mir möglich, die Energiedichte der CR-Protonen in nahen Galaxienhaufen mit kalten Zentren auf $< 20\%$ relativ zur thermischen Energiedichte zu beschränken. In diesem Zusammenhang untersuche ich die Hypothese, daß die diffuse Radio-Synchrotronstrahlung von Galaxienhaufen durch hadronisch generierte relativistische Elektronen produziert wurde. Dazu entwickle ich ein nicht-parametrisches Kriterium, um den energetisch begünstigten Zustand für die beobachtete Radio-Synchrotronemission zu erhalten. Die ausgezeichnete Übereinstimmung des beobachteten mit dem theoretisch erwarteten Radiohelligkeitsprofil des Radiominihalos im Perseus-Haufen sowie die kleine Energiedichte der CR-Protonen, die zur Erklärung der beobachteten Radioemission benötigt wird, macht dieses hadronische Modell zu einer attraktiven Erklärung für Radiominihalos in Galaxienhaufen mit kalten Zentren. Um den riesigen Radiohalo im Coma-Haufen mit dem hadronischen Modell zu erklären, muß das Profil der CR-Protonen-Energiedichte relativ zur thermischen Energiedichte mit größeren Radien zu moderaten CR-Energiedichten ansteigen. Kosmologische Simulationen, die der CR-Beschleunigung an Stoßwellen selbstkonsistent folgen, sagen solch ein Energiedichteprofil voraus: Starke Stoßwellen, die sich vor allem in unterdichten Regionen bilden, können hochenergetische CRs sehr effizient beschleunigen. Im Gegensatz dazu injizieren schwache Strömungsstoßwellen nur eine niederenergetische CR-Protonenpopulation, die durch Coulomb-Wechselwirkungen stark verringert wird. Daraus kann man schließen, daß der dynamische Einfluß der CRs aus Stoßwellen am größten in unterdichten Akkretionsregionen und kleiner in den schwächeren Strömungsstoßwellen ist, die in den zentralen dichten Haufenregionen vorkommen.

Als Erweiterung dieser Arbeit schlage ich eine neue Methode vor, um den Inhalt von Radioplasmablasen in den kalten Zentren von Galaxienhaufen aufzuklären. Unter Zuhilfenahme des Sunyaev-Zel'dovich (SZ)-Effektes sollten das *Atacama Large Millimeter Array* und das *Green Bank Teleskop* den dynamisch dominierenden CR-Bestandteil in geeigneten Galaxienhaufen innerhalb kurzer Beobachtungszeiten identifizieren können. Zukünftige hochsensitive Multifrequenz-SZ-Beobachtungen werden das Energiespektrum der dynamisch dominierenden Elektronenpopulation messen können. Dieses Wissen kann indirekte Hinweise auf die zugrundeliegende Zusammensetzung relativistischer Jets in Radiogalaxien liefern, da die Plasmablasen das Relikt der Jets darstellen.

Im zweiten großen Teil meiner Doktorarbeit beschäftige ich mich mit der Konstruktion eines genauen und selbstkonsistenten Modells für die Beschreibung der CRs. Dieses zielt darauf ab, den dynamischen Einfluß der CRs auf die Strukturentstehung und die Galaxienentwicklung zu studieren. Das Modell wird nicht nur realistische, nicht-thermische Emissionssignaturen von Galaxien und Galaxienhaufen erzeugen können, sondern auch *in vivo*-Studien dynamischer, von CRs verursachter Effekte in Verbindung mit Sternentstehung erlauben. Das entwickelte Modell folgt selbstkonsistent den relativistischen Protonen, die aus verschiedenen Quellen wie Stoßwellen der Strukturentstehung und von Supernovae verursachten galaktischen Winden entstehen. Außerdem werden auch dissipative Prozesse der CRs berücksichtigt. Zu diesem Zweck entwickle ich einen Formalismus für das Auffinden von

Stoßwellen, der ihre Stärke im Verlauf kosmologischer SPH (*engl.: smoothed particle hydrodynamics*)-Simulationen genau abschätzen kann. Stoßwellen sind nicht nur für die Thermalisierung des Gases in virialisierten Strukturen verantwortlich, sondern auch für die Beschleunigung von CRs durch diffusive Stoßwellenbeschleunigung. Man kann den Formalismus sowohl auf gewöhnliches, nicht-relativistisches thermisches Gas anwenden, als auch auf Plasmen, die aus einer Mischung von CRs und thermischen Gases bestehen. Eine Anwendung dieser Methoden auf Stoßwellen der kosmologischen Strukturentstehung in hochaufgelösten hydrodynamischen Simulationen im ΛCDM-Modell zeigt, daß die meiste Energie in schwachen internen Stoßwellen dissipiert wird, die vor allem zentrale Strömungs-Stoßwellen oder von Haufenkollisionen induzierten Stoßwellen darstellen, welche die Halozentren durchlaufen. Kollabierte kosmologische Strukturen sind von externen Stoßwellen mit viel größeren Machzahlen umgeben, die aber in der Energiebilanz der Thermalisierung nur eine untergeordnete Rolle spielen. Ich zeige, daß nach der Epoche der kosmischen Reionisation die Machzahlverteilung signifikant durch eine effiziente Unterdrückung der starken externen Stoßwellen aufgrund des damit verbundenen Anwachsens der Schallgeschwindigkeit des diffusen Gases modifiziert wird.

4

2. Introduction and motivation

2.1. Motivation

An astonishingly complete picture of cosmology and structure formation emerged over the past decades to the standard model of *concordance cosmology*: according to this model, the geometry of the observable Universe is indistinguishable from a flat geometry on spatial hypersurfaces of constant time, implying that the total energy density is similar to the critical density needed to close the Universe. The two dominant components of the Universe seem to be a non-baryonic form of dark matter whose gravity is responsible for structure formation, and a yet unknown form of dark energy, whose negative pressure is currently causing the Universe to accelerate. The mean density of baryonic matter is approximately 15% of the total matter density, and baryonic matter is only visible because the gravitational attraction of non-baryonic dark matter has drawn baryonic matter into deep potential wells where a small fraction of it condensed to form stars and galaxies. The cosmological model is supported by many observations ranging from big bang nucleosynthesis, cosmic microwave background radiation, measurements of the Lyman-α forest and cluster abundances, to the accelerated expansion of the Universe as observed by highly redshifted type Ia supernovae. This wealth of concurring observations is complemented by numerical simulations of cosmological structure formation. They are an inevitable tool for studying the non-linear evolution of structure formation, baryonic physics in clusters of galaxies, and galaxy evolution.

However, some inconsistencies with the standard model on galactic scales cast a doubt on this successful picture, two of which shall be mentioned in the following: numerical simulations predict too much substructure in galactic halos which is not observed, the so-called *substructure problem*. While it is yet unclear what exactly causes these low mass substructures (if they exist) to be devoid of stars, the solution might consist in finding a consistent physical mechanism keeping those environments from forming stars. Secondly, it shall be pointed out that hydrodynamical simulations still fail in successfully simulating the formation of galactic discs from first principles. The resulting simulated disks and their angular momentum are too small, giving rise to the *angular momentum problem*. These problems indicate that an essential ingredient in the physical description of cosmic structure formation processes may have been neglected. This thesis investigates one prime candidate for such a missing link, namely cosmic rays.

Galactic non-equilibrium processes like shock waves and turbulence have generated magnetic fields and *cosmic rays* (CRs) in the interstellar medium. Cosmic rays are relativistic particles, mainly protons and α-particles that play a decisive role within our Galaxy: their pressure, along with that of the thermal gas, balances gravity, they trace past energetic events such as supernovae, and they reveal the underlying structure of the baryonic matter distribution through their interactions. Numerical simulations and semi-analytic descriptions of galaxy and cluster formation have neglected these non-thermal components so far for simplicity despite their importance. Relativistic protons are expected to impact on the star formation rate owing to their additional pressure and their significantly enlarged cooling time compared to the thermal gas. This could lead to an efficient and halo mass dependent feedback mechanism which naturally explains why low mass dark matter halos, seen numerously in numerical structure formation simulations, apparently do not exhibit high star formation rates. Secondly, the energy density of the relativistic proton component might prevent the thermal gas from vigorously cooling at the early stages of the assembly of the galactic disk leading to suppression of angular momentum transfer from thermal gas to dark matter. Thus, the CR population might resolve naturally the substructure and the angular momentum problems.

On larger scales, clusters of galaxies provide useful laboratories for investigating non-equilibrium processes including turbulence and resulting non-thermal components. Apart from the underlying dark matter component, the main constituent of the intra-cluster medium is a thermal gas with temperatures kT of a few keV that makes galaxy clusters powerful X-ray emitters. This X-ray emission probes the morphology of the cluster's baryonic component and traces radiative processes such as radiative cooling, feedback and metal enrichment which provide important indications as to the dynamical state of the cluster apart from carrying cosmological information. Evidence for the existence of relativistic electrons and cluster-wide magnetic fields is provided by Mpc-sized diffuse structures

of radio synchrotron emission (the so called 'cluster radio halos' and 'cluster radio relics') and Faraday rotation measures of radio lobes. To date, it is unclear which processes are responsible for the acceleration of these relativistic electrons which cause the huge extended radio emission of clusters, leading to the so-called *cluster radio halo problem*. Clusters of galaxies are also expected to contain significant populations of relativistic protons originating from structure formation shocks, radio galaxies, and supernova driven galactic winds. The interplay of relativistic protons, magnetic fields, and turbulence in connection with the central active galactic nucleus might provide an efficient feedback mechanism that is able to prevent cluster cooling cores from catastrophic cooling which is not observed in X-rays, the *cluster cooling flow problem*. The individual morphology and the statistics of non-thermal emission mechanisms induced by relativistic particles are tracers of the cluster evolution which first need to be understood before using clusters as precision cosmological probes.

These considerations motivate the study of galactic and cosmological non-equilibrium processes in order to gain insight into fundamental problems of cluster evolution and galaxy formation. This thesis seeks to put forward first steps towards an understanding of the cosmological role of CR protons and opens up a new direction towards cosmological research of structure formation while incorporating ideas and theories from cosmic ray and plasma physics. The quantitative investigation of non-thermal components requires new analytical and numerical tools which are developed in the course of this thesis to provide the foundation for answering the presented cosmological problems. There are other candidates than CRs that may solve the presented cosmological riddles, but there is still no consensus on the relative importance of these mechanisms. Thus, the first major part of this thesis is dedicated to the study of CR protons in clusters of galaxies and their hadronic interactions with the ambient thermal plasma using multi-frequency observational results. Developing an analytical framework for these interactions and applying it to clusters of galaxies, we investigate the question of the dynamical influence of CRs on the intra-cluster medium. The answer is subtle because on the one hand CRs do not seem to dominate the energy density of the central cluster regions while they may be responsible for the huge diffuse radio synchrotron emission as observed in numerous clusters. On the other hand, there are theoretical reasons to believe that CRs can dominate the outskirts of clusters since strong structure formation shock waves are efficient in accelerating CRs and infalling spiral galaxies into the cluster's potential experience stripping of their CR rich interstellar medium there. In the second part, a description of CR gas for cosmological applications especially suited for hydrodynamical simulations is presented. In the course, I focus on developing a formalism of instantaneously identifying and estimating the strength of structure formation shocks during cosmological simulations to accelerate CRs through diffusive shock acceleration. Both the analytical and the numerical studies provide arguments in favor of a hadronic origin of radio synchrotron emitting CR electrons and suggest a solution to the cluster radio halo problem. This enables valuable insight in the dynamical relevance of CRs on cluster scales while providing the opportunity of interesting future discoveries and solutions to the presented galactic problems.

2.2. Structure

An introduction to fundamental cosmological concepts and the theory of cosmic structure formation as relevant for this PhD thesis is presented in Chapter 3. In this context, the formation and physics of clusters of galaxies is illustrated while relating these to multi-frequency observational signatures. An overview of the theoretical background of galactic cosmic rays is presented in Chapter 4. In the following, the key concepts of non-thermal emission processes such as synchrotron radiation, inverse Compton emission, and pion decay induced γ-ray emission are introduced.

In Chapter 5, I develop a theoretical framework for analytically modeling multi-frequency signatures resulting from hadronic CR proton interactions with the ambient thermal plasma of the intra-cluster medium. These interactions produce charged and neutral pions which successively decay into γ-rays and relativistic electrons or positrons. Self-consistent analytical formulae describing the γ-ray source function resulting from decaying neutral pions and the stationary spectrum of hadronically originating secondary electrons are derived. The latter allow the calculation of accompanying synchrotron and inverse Compton emission and yield thus complementary information on the non-thermal energetic content of clusters.

The formalism of the previous chapter is then applied in Chapter 6 to nearby clusters of galaxies using multi-frequency observations. Using EGRET upper limits on the γ-ray emission of clusters, I constrain the CR proton population in galaxy clusters and study the hypothesis that the diffuse radio synchrotron emission of galaxy clusters is produced by hadronically originating relativistic electrons. This model can be tested with future sensitive γ-ray

observations of the accompanying neutral pion decays. The TeV γ-ray detection by the HEGRA collaboration of the giant elliptical galaxy M 87 might be the first detection of hadronically originating γ-rays from a galaxy cluster since both, the expected radial γ-ray profile and the required amount of CR protons, support this scenario.

In Chapter 7, I estimate magnetic field strengths and CR energy densities of radio emitting galaxy clusters by minimizing the total non-thermal energy density contained in CR electrons, protons, and magnetic fields. The *classical* minimum energy estimate can be constructed independently of the origin of the radio synchrotron emitting CR electrons yielding thus an absolute minimum of the non-thermal energy density. Provided the observed synchrotron emission is generated by a CR electron population originating from hadronic CR proton interactions, I introduce the *hadronic* minimum energy criterion which is a non-parametric approach yielding an absolute minimum energy state and providing a solid foundation to scrutinize the hadronic model on the basis of radio synchrotron emission alone.

The *Chandra* X-ray Observatory is finding a large number of cavities in the X-ray emitting intra-cluster medium which often coincide with the lobes of the central radio galaxy. Therefore, it can be assumed that these cavities are partly or completely inflated by CR gas of unknown composition (electron/proton or electron/positron gas). In Chapter 8, I propose high-resolution Sunyaev-Zel'dovich (SZ) observations to unveil the yet unknown dynamically dominant component of the radio plasma bubbles. The thermal and relativistic SZ emission of different compositions of these plasma bubbles are calculated while simultaneously allowing for the cluster's kinetic SZ effect. Future high-sensitivity multi-frequency SZ observations will be able to infer the energy spectrum of the dynamically dominant electron population in order to measure its temperature or spectral characteristics. This knowledge can yield indirect indications for an underlying radio jet model.

In Chapter 9, an approximative framework for treating the dynamical and radiative effects of CRs for cosmological applications such as numerical simulations or semi-analytical methods is developed. Particle number, momentum and energy conservation principles are used to derive evolution equations for the basic CR variables due to adiabatic and non-adiabatic processes. These are compression, rarefaction, CR injection via shocks of supernova remnants and structure formation shock waves, in-situ re-acceleration of CRs, CR spatial diffusion, CR energy losses due to Coulomb interactions, Bremsstrahlung, and hadronic interactions with the background gas, including the associated γ-ray and radio emission due to subsequent pion decay.

The properties of cosmological structure formation shock waves in high-resolution hydrodynamic simulations of a ΛCDM universe are studied in Chapter 10. I quantify their decisive role in the evolution of the thermalization of the cosmic plasma as well as in accelerating relativistic CRs through diffusive shock acceleration. I develop a formalism for instantaneously identifying and accurately estimating the strength of structure formation shocks during cosmological smoothed particle hydrodynamics simulations for both, non-relativistic thermal gas and plasma composed of CRs and thermal gas. Performing cosmological simulations, the influence of cosmic reionization on the Mach number distribution as well as the spatial characteristics of the shock-injected CR energy is studied in detail which allows conclusions on the dynamical relevance of CRs on cluster scales.

In Chapter 11, I present the most important findings and conclusions while putting them into a cosmological context and pointing out the future perspective.

3. Cosmology and cosmic structure formation

Abstract

This chapter presents an introduction to the theory of cosmic structure formation as well as fundamental cosmological concepts which are relevant for the scope of this PhD thesis. After introducing the family of Friedmann-Lemaître cosmological models together with some basic definitions in Sect. 3.1, the theory of the cosmological structure formation ranging from the linear into the non-linear regimes is presented in Sect. 3.2. Finally, in Sect. 3.3 the interplay of different physical processes in clusters of galaxies is highlighted while relating these to multi-frequency observational signatures.

3.1. Friedmann-Lemaître cosmological models

The cosmological background model is described by the highly-symmetric Robertson-Walker metric which is characterized by two free parameters: hypersurfaces of constant cosmic time are homogeneous and isotropic three-spaces which are either flat, hyperbolically or spherically curved, and change with time according to a cosmic scale factor. The homogeneous dynamics of the Universe is governed by this cosmic scale factor which obeys Friedmann's equations being derived from Einstein's field equations assuming the symmetry of the metric.

3.1.1. Geometry of space-time

3.1.1.1. Cosmological principles

The standard cosmological model is based upon two fundamental postulates:

- When averaged over sufficiently large scales, there exists a mean motion of radiation and matter in the Universe. From a reference system comoving with that mean motion, all averaged observables are isotropic.

- The position of any observer following this mean motion is not preferred over others, i.e. they experience the same history of the Universe and measure the same averaged observable properties (the so-called cosmological Copernican principle).

The first postulate is supported by observations of galaxy populations in the observed Universe today, which is perceived to be isotropic on the largest scales ($\gg 10\,h^{-1}\mathrm{Mpc} \sim$ scale of a galaxy cluster). Another strong argument in favor of isotropy is the perfect rotational invariance of the cosmic microwave background (CMB) temperature in the comoving frame. Observers at rest in a frame comoving with the expanding Universe are called *fundamental observers*. The smoothness of the CMB, $\delta T/T_0 \sim 10^{-5}$ on all angular scales measured, is an indication of an isotropic and homogeneous distribution of matter and radiation at early times. Accepting the isotropy on the spatial hyper-surface around a fundamental observer and applying the cosmological principle in space leads to isotropy around any point on a spatial hyper-surface. Assuming further that the metric is an analytic function of the coordinates immediately implies homogeneity.

3.1.1.2. Robertson-Walker metric

Taking the symmetry assumptions of isotropy and homogeneity motivated by observations, the metric can be written in the form (for derivation see Misner, Thorne & Wheeler (1973) or d'Inverno (1992))

$$\mathrm{d}s^2 = g_{\mu\nu}x^\mu x^\nu = c^2\mathrm{d}t^2 - a(t)^2 \left[\mathrm{d}w^2 + f_K^2(w)\left(\mathrm{d}\theta^2 + \sin^2\theta\mathrm{d}\phi^2\right)\right], \tag{3.1}$$

which is called the *Robertson-Walker metric*. Here, Einstein's sum convention was used and $\mu, \nu \in \{0, \ldots, 3\}$. If one considers space-time as being filled with a fluid, then the coordinates (w, θ, ϕ) are the coordinates of a comoving fluid element where w is the radial distance from the origin and (θ, ϕ) are the two angles characterizing a point on the unit sphere around the origin. The coordinate t is the proper time of a clock comoving with such an element with constant w, θ, ϕ. Specifically,

$$f_K(w) = \begin{cases} \frac{1}{\sqrt{K}} \sin(\sqrt{K}w) & (K > 0) \\ w & (K = 0) \\ \frac{1}{\sqrt{-K}} \sinh[\sqrt{-K}w] & (K < 0) \end{cases}. \tag{3.2}$$

Due to its high symmetry, the Robertson-Walker metric allows only two free parameters: K, which is related to the curvature of three-dimensional spatial hyper-surfaces, $R^{(3)} = 6Ka^{-2}(t)$. One distinguishes between three different geometries of an open ($K < 0$), a flat ($K = 0$) and a closed ($K > 0$) Universe according to the sign of the curvature. It is important to notice that $f_K(w)$ and therefore $|K|^{-1/2}$ both have the dimension of length. The other parameter $a(t)$ describes the conformal mapping between hyper-surfaces separated by time-like vectors and is a function of cosmic time t only. In the dynamical context, this parameter describes the evolution of the Universe and is therefore called the *cosmic scale factor* $a(t)$. Conventionally, it is normalized such that its value is unity at the present epoch t_0. If the radius r of the two-spheres is defined by $r \equiv f_K(w)$, then the metric takes the following form:

$$ds^2 = c^2 dt^2 - a(t)^2 \left[\frac{dr^2}{1 - Kr^2} + r^2 \left(d\theta^2 + \sin^2 \theta d\phi^2 \right) \right]. \tag{3.3}$$

This metric shows that hyper-surfaces of constant cosmic time t form a maximally symmetric space, i.e. a space with constant curvature. However the curvature of the overall space-time can change with time. The time dependence of the cosmic scale factor and the dependence of K on the matter content of the Universe uniquely determine space-time.

3.1.1.3. Cosmological redshift

Owing to the expansion of the Universe, photons are redshifted during their propagation from the source to the observer. Consider a comoving source emitting light with a wavelength λ_s at t_s which reaches the observer with wavelength λ_o at t_o. Photons travel on radial null geodesics of zero proper time, $ds^2 = c^2 d\tau^2 = c^2 dt^2 - a(t)^2 dw^2 = 0$. Because the comoving coordinate distance w from the source to the observer is constant and time independent by definition, it follows

$$w = \int_o^s dw = \int_{t_s}^{t_o} \frac{c \, dt}{a(t)} = \text{const.} \quad \rightarrow \quad \frac{\delta t_o}{\delta t_s} = \frac{a(t_o)}{a(t_s)}. \tag{3.4}$$

The redshift is defined as the relative change in wavelength $1 + z = \lambda_o / \lambda_s$. Relating the inverse of the emitted and observed time intervals to the frequencies of the light, $\delta t_s = \nu_s^{-1}$ and $\delta t_o = \nu_o^{-1}$ yields the important relation

$$1 + z = \frac{a(t_o)}{a(t_s)} \equiv \frac{1}{a(t_s)} \qquad \text{for} \qquad a(t_o) = 1. \tag{3.5}$$

3.1.2. Homogeneous dynamics of the Universe

3.1.2.1. Einstein's equations and Friedmann world models

According to General Relativity, space-time is a four-dimensional manifold, whose metric tensor $g_{\mu\nu}$ is a dynamical field. The dynamics of this field is governed by Einstein's field equations (1915)

$$G_{\mu\nu} \equiv R_{\mu\nu} - \frac{R}{2} g_{\mu\nu} = \frac{8\pi G}{c^4} T_{\mu\nu} + \Lambda g_{\mu\nu}, \tag{3.6}$$

where both the energy-momentum tensor $T_{\mu\nu}$ of matter and radiation and the cosmological constant Λ act as sources of gravity which itself couples to the right-hand side of the equation. These considerations show the inherent non-linearity of the field equations. Here, $R_{\mu\nu} = R^\alpha_{\mu\alpha\nu}$ denotes the Ricci tensor and $R = R_{\mu\nu} g^{\mu\nu}$ the Ricci scalar.[1]

---

[1] The sign conventions for the formulae of General Relativity are chosen in agreement with the textbook of Landau & Lifshitz (1975) implying the particular choice of signature $(+ - - -)$, where the zeroth component refers to the time. The sign convention for the Riemann tensor is $R^\alpha_{\mu\beta\nu} \equiv \Gamma^\alpha_{\mu\nu,\beta} - \Gamma^\alpha_{\mu\beta,\nu} + \Gamma^\rho_{\mu\nu}\Gamma^\alpha_{\rho\beta} - \Gamma^\rho_{\mu\beta}\Gamma^\alpha_{\rho\nu}$.

Friedmann's solution of an expanding Universe solves Einstein's equations (3.6) assuming the energy-momentum tensor of a perfect fluid, which is completely determined by the energy density ρ, the pressure p and the four-velocity u_μ of the fluid,

$$T_{\mu\nu} = \left(\rho + \frac{p}{c^2}\right) u_\mu u_\nu - p g_{\mu\nu}. \tag{3.7}$$

With this energy-momentum tensor of Eqn. (3.7) and the metric of Eqn. (3.1), the general set of Einstein's field equations (3.6) is reduced to two independent ordinary differential equations for the three unknown functions of time, $a(t)$, $\rho(t)$ and $p(t)$:

$$\left(\frac{\dot{a}}{a}\right)^2 = \frac{8\pi G}{3}\rho - \frac{Kc^2}{a^2} + \frac{\Lambda c^2}{3} \quad \text{and} \quad \frac{\ddot{a}}{a} = -\frac{4}{3}\pi G\left(\rho + \frac{3p}{c^2}\right) + \frac{\Lambda c^2}{3}, \tag{3.8}$$

where the dot denotes the derivative with respect to the coordinate time t. The two equations (3.8) can be combined to yield the *adiabatic equation*,

$$\frac{\mathrm{d}}{\mathrm{d}t}\left[a^3(t)\rho(t)c^2\right] + p(t)\frac{\mathrm{d}}{\mathrm{d}t}\left[a^3(t)\right] = 0. \tag{3.9}$$

This can also be independently obtained by virtue of the conservation equations of Einstein's field equations, $T^{\mu\nu}_{;\nu} = 0$, which itself is a necessary requirement for the contracted Bianchi identities $G^{\mu\nu}_{;\nu} = 0$ to hold identically. The semicolon denotes the covariant derivative. The first term of the adiabatic equation is proportional to the change of energy contained in a fixed comoving volume, which has the meaning of an "internal" energy, whereas the second term is proportional to the change of the proper volume. So Eqn. (3.9) states the first law of thermodynamics in a cosmological context and conserves the entropy per comoving volume in thermal equilibrium, $S = (\rho c^2 + p)V/T = \text{const}$. The first of Friedmann's equations (3.8) defines the *Hubble function $H(t)$* which is a measure for the expansion rate of the Universe[2],

$$H(t) \equiv \frac{\mathrm{d}}{\mathrm{d}t}\ln(a) = \frac{\dot{a}}{a} \quad \rightarrow \quad H^2(t) = H_0^2\left[\frac{\Omega_\mathrm{r}}{a^4(t)} + \frac{\Omega_\mathrm{m}}{a^3(t)} - \frac{\Omega_\mathrm{c}}{a^2(t)} + \Omega_\Lambda\right]. \tag{3.10}$$

The value of the Hubble function at the present epoch is the *Hubble constant $H(t_0) \equiv H_0$*, whose uncertainty is commonly expressed as $H_0 = 100\,h\,\mathrm{km\,s^{-1}\,Mpc^{-1}}$. Measurements of the CMB anisotropies (Spergel et al. 2003) and from Cepheid variable stars in distant galaxies (Freedman et al. 2001) converge on a value of $h = 0.71 \pm 0.04$. The *critical density* of the Universe is given by

$$\rho_\mathrm{cr} \equiv \frac{3H_0^2}{8\pi G} \simeq 1.9 \cdot 10^{-29}\,h^2\,\mathrm{g\,cm^{-3}}. \tag{3.11}$$

If the sum of all cosmological fluid densities equals ρ_cr, spatial hypersurfaces are flat and the curvature K vanishes. The energy density of cosmological fluids (radiation $3p/c^2$, matter ρ, curvature K, and the cosmological constant Λ) can be expressed in units of the critical density yielding

$$\Omega_\mathrm{r} = \frac{3p}{\rho_\mathrm{cr}c^2}, \quad \Omega_\mathrm{m} = \frac{\rho}{\rho_\mathrm{cr}}, \quad \Omega_\mathrm{c} = \frac{Kc^2}{H_0^2}, \quad \text{and} \quad \Omega_\Lambda = \frac{\Lambda c^2}{3H_0^2}. \tag{3.12}$$

Taking the Hubble function of Eqn. (3.10) at the present time where the scale factor is normalized to unity and recalling the previous definitions leads to an expression for the curvature

$$\Omega_\mathrm{c} = \Omega_\mathrm{m} + \Omega_\mathrm{r} + \Omega_\Lambda - 1 \equiv \Omega_\mathrm{tot} - 1, \tag{3.13}$$

which defines the total density Ω_tot.

3.1.2.2. Different Epochs of the Universe

The under-determined set of Friedmann's equations (3.8) is completed by the equation of state, $p = p(\rho, S)$. The equation of state of all cosmologically relevant fluids (denoted by f) can be parameterized by $p = \omega_\mathrm{f}\rho c^2$, where ω_f

---

[2]The scaling of the density parameters Ω_r and Ω_m with the scale factor will be derived in Sect. 3.1.2.2.

is assumed to be independent of time and temperature in the simplest cases. Inserting this expression into Eqn. (3.9) yields the following solution

$$\rho_{\rm f}(t) = \rho_{\rm f,0} \, a^{-3(1+\omega_{\rm f})}. \tag{3.14}$$

In the course of its evolution, the Universe passed three epochs, in which its dynamics was mainly determined by one of the components, radiation, matter and vacuum energy, respectively.

- The *radiation dominated* era is characterized by $\omega_{\rm r} = \frac{1}{3}$, which is valid for a non-degenerate ultra-relativistic gas in thermal equilibrium and leads to $\rho_{\rm r} \propto a^{-4}$. In addition to a volume factor of a^3 for the dilution effect as the Universe expands, there is an additional factor of a for the redshift of photon momentum.

- The *matter dominated* era is described by a pressure-less fluid, $\omega_{\rm m} = 0$, which is a good approximation for a non-relativistic gas or fluid with the property $p \ll \rho c^2$. Thus, the density evolution reads $\rho_{\rm m} \propto a^{-3}$. The matter density gets diluted at the same rate as the proper volume increases, which is the conservation law of the total amount of energy in the comoving frame. Since the slope of the radiation energy density $\rho_{\rm r}$ as a function of the scale factor is steeper than that of the matter density $\rho_{\rm m}$, it follows that the early Universe was radiation dominated. After a transition period, the so-called *matter-radiation equality* at $a_{\rm eq}$ with equal densities of the two fluids, the matter dominated regime took over. The energy density of ordinary and relativistic matter were equal when the scale factor $a(t)$ was

$$a_{\rm eq} = \left(\frac{\rho_{\rm r}}{\rho_{\rm m}}\right)_{\rm today} \simeq 3.2 \times 10^{-5}\Omega_{\rm m}^{-1}h^{-2} \quad \rightarrow \quad z_{\rm eq} \simeq 4200\,, \tag{3.15}$$

  using current most favored density values as given below.

  The period of *recombination* occurred during the matter dominated era and represents the epoch when the Universe became transparent for photons. Before the time of recombination, the Universe was completely ionized. In this state of hot primeval plasma, the photons where tightly coupled to the baryons by Compton interactions between photons and electrons, and Coulomb interactions between electrons and protons. Because the mean free path of the photons was much shorter than the horizon scale $cH(a)^{-1}$, the photons were in thermal equilibrium at this time. During the evolution of the Universe, its temperature decreased due to cosmic expansion up to some point where thermal energy was no longer high enough to keep the proton-electron plasma ionized. At this time, protons and electrons combined to form neutral hydrogen atoms and the Universe became transparent for electromagnetic radiation, i.e. the photons decoupled from matter. These photons reaching fundamental observers appear to originate from a spherical surface called the *surface of last scattering* with its radius being the distance a photon has traveled since the time of decoupling at $z_{\rm rec} = 1089$.

- Finally, the possible era of the *domination of a cosmological constant* is described by a fluid with negative pressure, $\omega_\Lambda = -1$. This can be obtained from the definition of the energy-momentum tensor of the cosmological constant Λ, which is treated in this context as a perfect fluid component of the Universe, $8\pi G c^{-4} T_\Lambda^{\mu\nu} \equiv \Lambda g^{\mu\nu}$. After taking the trace of this equation and using the definitions in Eqn. (3.12), the desired equation of state follows. This gives rise to a constant energy density, $\rho_\Lambda \propto {\rm const}$. The transition from the matter dominated epoch into the Λ-dominated epoch occurred at

$$a_{\rm eq,\Lambda} = \sqrt[3]{\frac{\rho_{\rm m}}{\rho_\Lambda}} \simeq 0.7 \quad \rightarrow \quad z_{\rm eq,\Lambda} \simeq 0.4\,, \tag{3.16}$$

  using density values for $\rho_{\rm m}$ and ρ_Λ at the present epoch.

The cosmological constant represents a cosmological fluid which is constant in space and time, the physical origin of which can not be successfully explained. Generalizing this behavior while allowing for variations in space and time, a new field referred to as quintessence with the density $\Omega_{\rm Q}$ has been invented (Wetterich 1988, Ratra & Peebles 1988, Wetterich 1995). To date, the most sensitive measurements of the density parameters have been carried out by the WMAP satellite (Spergel et al. 2003). They obtained the following values for the matter density $\Omega_{\rm m} = 0.27 \pm 0.04$, baryonic density $\Omega_{\rm b} = 0.044 \pm 0.004$, curvature $\Omega_{\rm c} = 0.02 \pm 0.02$, and the cosmological constant $\Omega_\Lambda = 0.73 \pm 0.04$. Previous considerations showed that the radiation density $\Omega_{\rm r} \simeq 3.2 \times 10^{-5}h^{-2}$ is dynamically negligible at the present epoch.

3.1.2.3. Distances in cosmology

In an arbitrary curved space-time, such as that underlying General Relativity, the term "distance" no longer has a unique meaning. Due to the high symmetry of Euclidean space, "distance" combines different properties which are no longer equivalent in General Relativity, so that each desired property needs its own distance definition in curved space-time. For the purpose of this thesis, four different distance scales are important, the proper distance, the comoving distance, the angular diameter distance, and the luminosity distance. Distances between different time-like geodesic lines are measured by light signals, which are emitted at time t_s from the source and observed at time t_o. Assuming the scale factor $a(t)$ to be a monotonic function, which is at least true piecewise, the coordinate time t can be related in a unique way to the cosmic scale factor a, which occurs in the Friedmann equation.

Proper distance   The *proper distance* $D_{\text{prop}}(z_o, z_s)$ is the elapsed coordinate time a light signal needs to propagate from the source at $z_s = z(t_s)$ to the observer at $z_o = z(t_o)$ and is defined by $dD_{\text{prop}} \equiv -c\,dt = -c\,da\,\dot{a}^{-1} = -c\,da\,(aH)^{-1}$. The last step uses the definition of the Hubble parameter in Eqn. (3.10) and the minus sign arises because of the choice of the coordinate origin at the observer and the requirement of an increasing distance the further back one goes in time. This yields

$$D_{\text{prop}}(z_o, z_s) = \frac{c}{H_0} \int_{a(z_s)}^{a(z_o)} \frac{da}{\sqrt{\Omega_m a^{-1} + (1 - \Omega_m - \Omega_\Lambda) + \Omega_\Lambda a^2}}. \tag{3.17}$$

Comoving distance   The *comoving distance* $D_{\text{com}}(z_o, z_s)$ is the distance on the spatial hyper-surface $t = t_0$ between the world-lines of a source and an observer locked into the Hubble flow. In other words it is the radial distance on this hyper-surface with the scale factor, i.e. the cosmic expansion, divided out. Its definition $dD_{\text{com}} \equiv dw$ can be rewritten using the fact that photons travel on null-geodesics yielding $dD_{\text{com}} = -c\,a^{-1}\,dt = -c\,da(a\dot{a})^{-1} = -c\,da(a^2 H)^{-1}$. Hence,

$$D_{\text{com}}(z_o, z_s) = \frac{c}{H_0} \int_{a(z_s)}^{a(z_o)} \frac{da}{\sqrt{\Omega_m a + (1 - \Omega_m - \Omega_\Lambda)a^2 + \Omega_\Lambda a^4}} = w(z_o, z_s). \tag{3.18}$$

Angular diameter distance   The *angular diameter distance* $D_{\text{ang}}(z_o, z_s)$ is defined such that the relation in Euclidean space between the physical size of the cross-section δA of an object and the solid angle $\delta\Omega$ that it subtends also holds in curved space, $\delta\Omega\, D_{\text{ang}}^2 = \delta A$. Using the expression for the physical surface area of a 2-sphere centered at the observer

$$A_2 = \int_\Omega d\Omega \sqrt{-g^{(3)}} = 4\pi a(z_s)^2 f_K^2[w(z_o, z_s)] \quad \text{and} \quad \frac{\delta\Omega}{4\pi} = \frac{\delta A}{4\pi a(z_s)^2 f_K^2[w(z_o, z_s)]}, \tag{3.19}$$

one obtains the formula for the angular diameter distance

$$D_{\text{ang}}(z_o, z_s) \equiv \left(\frac{\delta A}{\delta\Omega}\right)^{1/2} = a(z_s)f_K[w(z_o, z_s)] = a(z_s)f_K[D_{\text{com}}(z_o, z_s)]. \tag{3.20}$$

Luminosity distance   Finally, the *luminosity distance* $D_{\text{lum}}(z_o, z_s)$ relates the luminosity of a source at z_s to the flux received by an observer at z_o,

$$D_{\text{lum}}(z_o, z_s) \equiv \left[\frac{a(z_o)}{a(z_s)}\right]^2 D_{\text{ang}}(z_o, z_s) = \frac{a(z_o)^2}{a(z_s)} f_K[D_{\text{com}}(z_o, z_s)]. \tag{3.21}$$

The luminosity distance is proportional to the angular diameter distance which relates the physical size of the source to its apparent angular size on the observer's sky. The energy flux is furthermore diminished because the photons are redshifted by $a(z_o)a(z_s)^{-1}$, and their arrival times are delayed by another factor of $a(z_o)a(z_s)^{-1}$ yielding the final formula.

The integral representation of both the proper and comoving distances leads to the nice property of their being additive functions, i.e. two adjacent distances can be computed using the starting point of the first one and the ending point of the second one, $D_{\text{com}}(z_1, z_2) + D_{\text{com}}(z_2, z_3) = D_{\text{com}}(z_1, z_3)$. The angular diameter distance and the luminosity distance do not have the additive property in general.
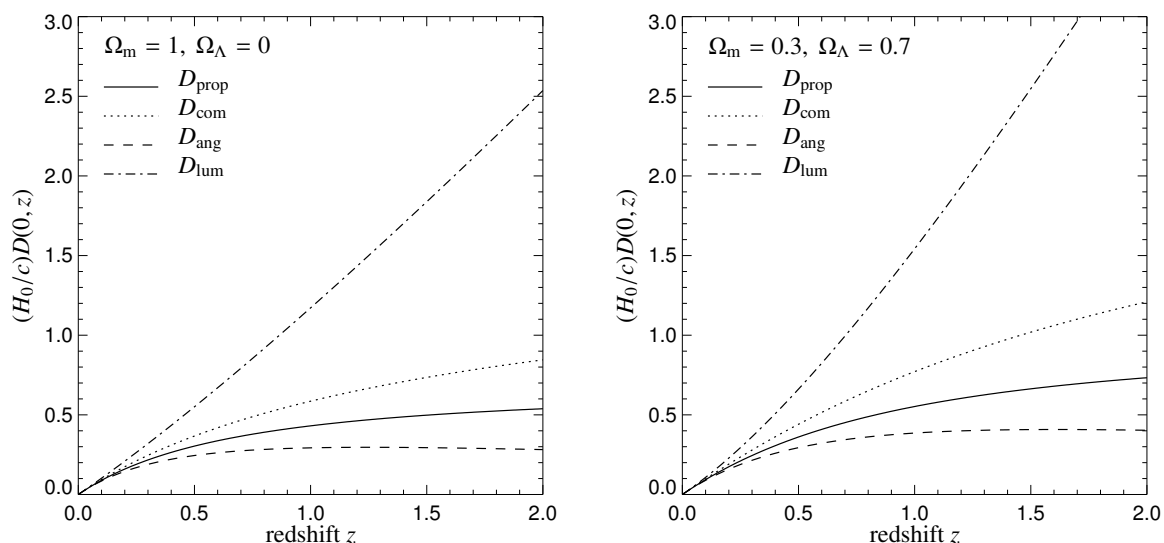
Figure 3.1.: Four distance definitions are plotted as a function of source redshift z with the observer being at redshift zero. These are the proper distance D_{prop} (solid line), the comoving distance D_{com} (dotted line), the angular diameter distance D_{ang} (dashed line), and the luminosity distance D_{lum} (dashed-dotted line). On the left-hand side an Einstein-de Sitter cosmology is shown in comparison with the currently preferred ΛCDM cosmology on the right-hand side.

3.2. Structure formation

Theories of structure formation hypothesize that structure grows via gravitational instability from initial density fluctuations within a very homogeneous and isotropic background distribution. The theory how these structures formed includes the following three main aspects: (i) The properties of the initial conditions of the density fluctuations generated by some physical mechanism which is not contained in the standard model of structure formation. Among many theories, an inflationary period in the very early Universe would be the most promising idea relating quantum fluctuations to macroscopic density perturbations and predicting the statistics of these seed fluctuations to be Gaussian (Guth 1981, Albrecht & Steinhardt 1982). (ii) The nature of gravitationally interacting particle species in the Universe and their interactions leading to the growth of structures, and (iii) the time evolution of the amplitudes of the density perturbations in an expanding Universe by gravitational instability are the other two pillars. As long as the density contrast is smaller than unity, it is sufficient to describe the evolution of the perturbations by linear perturbation theory until late times. In order to study the growth of structure in the non-linear regime governing the formation of galaxies or clusters of galaxies, numerical N-body simulations have been a very successful tool.

3.2.1. Properties of dark matter

The dominant interaction governing the evolution and dynamics of galaxies, clusters and large scale structure is gravitation due to the long range of its interaction and the fact that gravity can not be shielded like the electromagnetic force. The importance of gravitation for cosmology is supported by the growing evidence for *dark matter* constituting the major fraction of matter in our Universe today. Since dark matter does not couple to photons, it has to be detected by means of its gravitational or weak interactions. The most stringent arguments in favor of this matter to be *dark*, i.e. not interacting electromagnetically are the following: the time elapsed since the decoupling of pure baryonic density perturbations from the primordial photon-baryon plasma was not long enough to produce all the structure observed today with the size of density perturbations inferred from the anisotropies of the cosmic microwave background. Furthermore, indirect evidence of dark matter can be inferred by the gravitational effect on visible matter or radiation such as flat rotation curves in spiral galaxies, by the analysis of peculiar velocity fields of

galaxies averaged over very large scales, and by discrepancies of mass estimates for galaxy clusters by the gravitational lensing effect on background galaxies or the virial theorem on the one hand and the combined baryonic mass in stars and hot plasma on the other hand (Allen et al. 2002, David et al. 1995).

Dark matter is thought to be composed of yet undiscovered elementary particles which primarily interact by gravity and carry neither an electromagnetic nor a strong charge in most scenarios while they can possibly interact through the weak nuclear force. In order to account for a significant fraction of the critical density ρ_{cr}, they must have the property of being stable particles with very weak self-interaction rates such that the annihilation ceased in the very early Universe before their number density had decreased too much. Another line of arguments in favor of a very small self-interaction cross-section is its impact on the central structure of dark matter halos (Yoshida et al. 2000). Dark matter might be detected by its annihilation signal from individual dark matter halos (Stoehr et al. 2003) while this process could be responsible for the excess of the cosmological γ-ray background around 10 GeV (Elsässer & Mannheim 2005, Strong et al. 2004). If the dark matter particle is non-relativistic, trans-relativistic, or relativistic at the time of decoupling from weak interactions it is named *cold*, *warm*, or *hot*, respectively. The neutrino as a representative of *warm dark matter* seems to be ruled out of accounting for the bulk of dark matter, since it predicts structure formation from the top down, starting with superclusters and subsequently separating into clusters and galaxies (White, Frenk & Davis 1983). This would contradict observational evidence that structure formed bottom up leading to the *hierarchical model* of structure formation. This scenario is corroborated by *cold dark matter models* (CDM), with its most promising candidate the lightest super symmetric particle, presumably the neutralino (see Jungman, Kamionkowski & Griest 1996, for a review).

3.2.2. Linear growth of density perturbations

The dark matter perturbations are characterized by the *density contrast* $\delta(\boldsymbol{x}, a)$ at the comoving position $\boldsymbol{x}$,

$$\delta(\boldsymbol{x}, a) = \frac{\rho(\boldsymbol{x}, a) - \langle\rho(a)\rangle}{\langle\rho(a)\rangle}, \tag{3.22}$$

where $\langle\rho(a)\rangle = \Omega_{m}\rho_{cr}a^{-3}$ is the volume averaged cosmological matter density. Provided the density contrast $\delta(\boldsymbol{x}, a)$ is smaller than unity, the solution for matter under the influence of its own self-gravity can be found expanding the linearized equations of motions in the Newtonian framework, because small perturbations imply weak gravitational fields and space is locally flat. However, if the wavelength of the perturbations are of the order of the horizon scale, general relativistic effects need to be considered due to the fact that the horizon is comparable to the curvature radius of space-time. Nevertheless, both the Newtonian and the relativistic approach yield for an adiabatic change of volume elements in the linear regime $\delta \ll 1$ the solution

$$\delta(a) \propto a^{3\omega_r+1} = \begin{cases} a^2 & \text{before } a_{eq}, \quad \text{radiation dominated era:} \quad \omega_r = \frac{1}{3} \\ a & \text{after } a_{eq}, \quad \text{matter dominated era:} \quad \omega_m = 0 \end{cases}, \tag{3.23}$$

as long as the Einstein-de Sitter limit holds, i.e. $\Omega_m(a) \simeq 1$. At late times, when this limit no longer applies in the case of a non-zero cosmological constant ($\Omega_m \neq 1$, $\Omega_\Lambda \neq 0$), the amplitude of the growing perturbation mode is given by

$$\frac{\delta(a)}{\delta_0} = a\frac{\tilde{g}(a)}{\tilde{g}(1)} \equiv D_+(a), \tag{3.24}$$

where δ_0 is the density contrast linearly extrapolated to the present and the density dependent growth function $\tilde{g}(a, \Omega_m, \Omega_\Lambda)$ is approximated by Carroll, Press & Turner (1992)

$$\tilde{g}(a, \Omega_m, \Omega_\Lambda) = \frac{5}{2}\Omega_m(a)\left[\Omega_m^{4/7}(a) - \Omega_\Lambda(a) + \left(1 + \frac{\Omega_m(a)}{2}\right)\left(1 + \frac{\Omega_\Lambda(a)}{70}\right)\right]^{-1}. \tag{3.25}$$

3.2.3. Statistical description and initial conditions

3.2.3.1. Linear growth of perturbation modes

In linear perturbation theory, the density field grows homogeneously implying that individual Fourier modes evolve independently, $\hat{\delta}(\boldsymbol{k}, a) = D_+(a)\hat{\delta}(\boldsymbol{k})$. Here, the density field has been conveniently decomposed into Fourier modes

using the convention $\hat{\delta}(\boldsymbol{k}, a) \equiv \int \mathrm{d}^3 x\, \delta(\boldsymbol{x}, a) e^{i\boldsymbol{kx}}$. This approach is strictly only valid in flat space. Because observations seem to agree on space being flat at the present epoch (Spergel et al. 2003), the dynamics of Friedmann's equations guarantees that space is even flatter at earlier times and at late times, the interesting scales λ are much smaller than the curvature radius of the Universe, $cH^{-1}(a)$.

A perturbation mode of a certain comoving wavelength λ enters the comoving horizon $d_H(a) = c/[aH(a)]$ if their scales become comparable to each other and therefore causally connected. If $\lambda < d_H(a_{\mathrm{eq}})$, the density perturbation enters the horizon during the radiation dominated epoch at $a_{\mathrm{enter}} < a_{\mathrm{eq}}$, in which the expansion time-scale $t_{\mathrm{exp}} = H^{-1}$ is given by the radiation density ρ_{r}, which is shorter than the collapse time-scale of dark matter, t_{col}:

$$t_{\mathrm{exp}} \sim \frac{1}{\sqrt{G\rho_{\mathrm{r}}}} < \frac{1}{\sqrt{G\rho_{\mathrm{dm}}}} \sim t_{\mathrm{col}} \tag{3.26}$$

This comparison shows that the radiation driven expansion prevents the collapse of dark matter perturbations within the horizon, while perturbations on larger scales are not affected by this suppression and continue to grow according to Eqn. (3.23). It follows that the suppression factor for perturbations with $\lambda < d_H(a_{\mathrm{eq}})$ can be written as

$$f_{\mathrm{sup}} = \left(\frac{a_{\mathrm{enter}}}{a_{\mathrm{eq}}}\right)^2 . \tag{3.27}$$

The condition for the comoving wavelength λ entering the horizon at the time of matter-radiation-equality is given by $\lambda = d_H(a_{\mathrm{enter}}) = c/[a_{\mathrm{enter}}H(a_{\mathrm{enter}})]$. Recalling the definition of a_{eq} in Eqn. (3.15), $a_{\mathrm{eq}} = \Omega_{\mathrm{r}}/\Omega_{\mathrm{m}}$, the Hubble function in the Einstein-de Sitter regime can be approximated by

$$H(a) = H_0\sqrt{\Omega_{\mathrm{r}}a^{-4} + \Omega_{\mathrm{m}}a^{-3}} = H_0\, \Omega_{\mathrm{m}}^{1/2}a^{-3/2}\sqrt{1 + \frac{a_{\mathrm{eq}}}{a}} . \tag{3.28}$$

Hence, inserting this equation into the expression for the comoving horizon yields a relation between the scale factor at the time of entering and the perturbation mode of comoving wavelength λ,

$$\lambda \propto \begin{cases} a_{\mathrm{enter}} & \text{for} & a_{\mathrm{enter}} \ll a_{\mathrm{eq}} \\ a_{\mathrm{enter}}^{1/2} & \text{for} & a_{\mathrm{eq}} \ll a_{\mathrm{enter}} \ll 1 \end{cases} . \tag{3.29}$$

Thus, the suppression factor in Eqn. (3.27) can be written using the expression for the wave number of the perturbation $k = \lambda^{-1}$ and the horizon size at the time of matter-radiation equality, $k_0 = d_H^{-1}(a_{\mathrm{eq}})$,

$$f_{\mathrm{sup}} = \left(\frac{k_0}{k}\right)^2 . \tag{3.30}$$

There is another process modifying the growth of structure if there are relativistic dark matter particles, so-called hot dark matter (HDM). The free streaming of these particles exponentially damps density perturbations, which are smaller than a certain minimum size necessary to keep them gravitationally bound.

3.2.3.2. Density power spectrum and transfer function

Assuming statistically isotropic and homogeneous Gaussian density fluctuations $\delta(\boldsymbol{x})$, they can be completely characterized by the power spectrum which is defined by

$$\left\langle\hat{\delta}(\boldsymbol{k}, a)\hat{\delta}^*(\boldsymbol{k}, a)\right\rangle = (2\pi)^3\delta_{\mathrm{D}}(\boldsymbol{k} - \boldsymbol{k}')P_\delta(k, a) \quad\text{and} \tag{3.31}$$

$$P_\delta(k, a) = A(a)T^2(k, a)P_{\mathrm{i}}(k, a_{\mathrm{i}}). \tag{3.32}$$

Here the asterisk denotes complex conjugation, $A(a)$ is the normalization of the power spectrum (see Sect. 3.2.3.3), and $P_{\mathrm{i}}(k, a_{\mathrm{i}}) = \langle|\delta_{\mathrm{i}}(k)|^2\rangle$ is the primordial power spectrum at some very early time before any scale of interest has entered the horizon. We introduced the concept of the *linear transfer function* $T(k, a)$ in order to relate the linear perturbations of the mode $\boldsymbol{k}$ at a given scale factor a after matter-radiation equality a_{eq} to the initial perturbation

mode $\boldsymbol{k}_i$. Thus, the transfer function joins the unaffected growth of fluctuations on the largest scales to the suppressed growth on small scales and is defined for adiabatic perturbations as

$$T^2(k,a) = \left[\frac{a}{D_+(a)}\right]^2 \frac{\left\langle \hat{\delta}^2(\boldsymbol{k},a)\right\rangle}{\left\langle \hat{\delta}_i^2(\boldsymbol{k}_i,a_i)\right\rangle},$$

(3.33)

where $D_+(a)$ is the linear growth factor between scale factor a and the present (Eqn. (3.24)) and the normalization scale factor is arbitrary, as long as it refers to a time before any scale of interest has entered the horizon. $T(k,a)$ depends only on the matter content of the Universe, e.g. the properties of CDM particles and on the specific cosmology, because the growth factor depends on the density parameters Ω_m and Ω_Λ. However, it does not depend on the initial amplitudes of the perturbations. Bardeen et al. (1986) provide an accurate fitting function of $T(k,a)$ for CDM models.

The growth of the density contrast, $\delta \propto a^{3\omega_f+1}$ (Eqn. (3.23)), makes the spectral change as $P_\delta \propto a^{2(3\omega_f+1)}$. At $a_{\text{enter}} \ll a_{\text{eq}}$, the power spectrum has thus changed to

$$P_{\text{enter}}(k) \propto a_{\text{enter}}^{2(3\omega_f+1)} \propto k^{-4}P_i(k),$$

(3.34)

using Eqn. (3.29) for perturbation modes with wave numbers $k \gg k_0$, i.e. $\lambda \ll d_{\text{H}}(a_{\text{eq}})$. The most common variants of inflationary models predict the total power of density perturbations at a_{enter} to be almost scale invariant. This implies $k^3 P_{\text{enter}} = \text{const.}$, or $P_{\text{enter}}(k) \propto k^{-3}$. Consequently, the primordial spectrum has to scale with k as $P_i(k) \propto k$. This *scale invariant* spectrum is called the *Harrison-Zel'dovich* power spectrum. The initial power spectrum is commonly parameterized as

$$P_i(k) \propto k^{n_s},$$

(3.35)

which defines the spectral tilt n_s of (scalar) density perturbations. Summarizing the presented arguments, the linear power spectrum has the following asymptotic behavior at $a \gg a_{\text{eq}}$ while assuming $n_s \approx 1$,

$$P_\delta(k) \propto \begin{cases} k & \text{for} \quad k \ll k_0 \\ k^{-3} & \text{for} \quad k \gg k_0 \end{cases}.$$

(3.36)

3.2.3.3. Normalization

Having discussed the shape of the power spectrum, its normalization will be considered in the following. There are primarily three different methods, normalizing the power spectrum at different scales and unfortunately also leading different answers. This representation follows the review by Bartelmann & Schneider (2001).

1. At the largest scales, normalization is done by the cosmic microwave background anisotropies which have been measured over the full sky by the DMR experiment onboard the COBE (COsmic Background Explorer) satellite at an angular scale of $\phi \sim 7°$ (Banday et al. 1997). The WMAP satellite (Spergel et al. 2003) supported the measured normalization. CMB temperature fluctuations can be related to density perturbations and after adopting a specific cosmology, this yields a characteristic shape of the density power spectrum. The power spectrum can be normalized at the comoving wave number k and related to the measured angular multipole scale $\ell = f_K(w)k$. Both scalar and tensor perturbations give rise to CMB temperature fluctuations while density perturbations are *only* determined by scalar perturbations. This could lead to a possible overestimate of the normalization constant of the density power spectrum.

2. At intermediate scales of about $10h^{-1}$ Mpc, the power spectrum is normalized by the local abundance of galaxy clusters (White et al. 1993). Since galaxy clusters formed by gravitational instability from dark matter density perturbations in the hierarchical model, the spatial number density of clusters is a measure for the amplitude of dark matter fluctuations. Requiring the power spectrum to reproduce the observed local spatial number density of clusters determines its normalization.

3. Finally, the power spectrum can be normalized by the local variance of galaxy counts, as suggested by Davis & Peebles (1983), assuming galaxies to be biased tracers of the underlying dark matter perturbations. Measuring the variance of galaxy numbers within spheres of radius $8h^{-1}$ Mpc leads to the result $\sigma_{8,\text{galaxies}} \approx 1$. Assuming
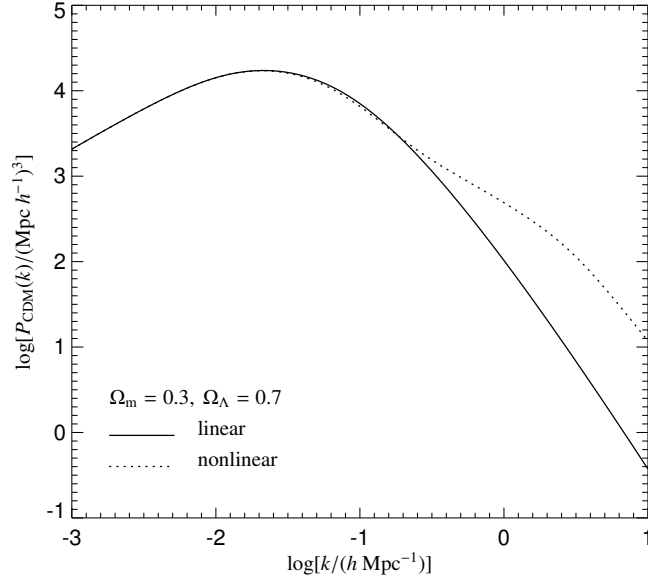
Figure 3.2.: ΛCDM power spectrum of the density contrast, normalized to the local abundance of galaxy clusters using $h = 0.7$. The solid curve shows the linear, the dashed curve the non-linear power spectrum using the formula of Peacock & Dodds (1996).

an expression for the bias, one can relate the variation in the galaxy counts to the dark matter fluctuations and obtains the amplitude $A(t_0)$ of the power spectrum, using (3.32) and

$$\sigma_8 \equiv \sigma(R = 8h^{-1} \text{ Mpc}, t_0) = 4\pi \int \frac{k^2 \mathrm{d}k}{(2\pi)^3} P_\delta(k) W_8^2(k) \stackrel{!}{=} 1 \,. \tag{3.37}$$

The window $W_R(k)$ denotes the three-dimensional Fourier transform of the Heaviside function $H(R - |\boldsymbol{r}|)$,

$$W_R(k) = \frac{3[\sin(kR) - kR\cos(kR)]}{(kR)^3} = \frac{3 j_1(kR)}{kR} \,, \tag{3.38}$$

where $j_1(x)$ is the spherical Bessel function of the first kind.

3.2.4. Non-linear evolution and numerical simulations

3.2.4.1. Properties of non-linear evolution

The final goal of theoretical cosmology is to find self-consistent physical concepts which are powerful enough to predict the evolution of the Universe and the structure formation leading to gravitationally bound objects consistent with astronomical observations. One challenge is that the objects we are able to observe in the Universe are the result of non-linear evolution, because clusters typically have a density contrast $\delta \sim 10^3$ and galaxies even have overdensities of $\delta \sim 10^6$ for which linear perturbation theory is no longer applicable. The process of structure formation proceeds inhomogeneously in the overdense regions causing different Fourier modes to couple. This can be understood by considering linear growth, $\delta(a, \boldsymbol{x}) = D_+(a)\delta_0(\boldsymbol{x})$ which acquires in addition to the time dependence a spatial dependence for non-linear growth, $\delta(a, \boldsymbol{x}) = D_+(a, \boldsymbol{x})\delta_0(\boldsymbol{x})$, such that the spatial multiplication translates to a convolution in Fourier space. By the process of non-linear evolution non-Gaussian features are also introduced into the distribution of density perturbations: the density contrast δ has a lower bound by definition, i.e. $\delta \geq -1$ so that its original Gaussian distribution evolves into an approximately log-normal distribution in the course of structure formation (Jain et al. 2000). Thus, higher order moments are needed for the complete description of the statistical

properties of the fields under consideration while the convergence of the N-point statistics is not guaranteed. Recently, other statistical approaches have been developed such as Minkowski functionals which provide a more robust morphological description of highly non-linear structures (Mecke et al. 1994, Kerscher et al. 1997, Schmalzing et al. 1999, Novikov et al. 2000).

3.2.4.2. Numerical simulations

Fundamental equations   One way of studying the non-linear evolution is numerical integration of the equations of motion with given initial conditions arising from linear theory, which is a reasonable approximation at high redshifts. The continuum limit of non-interacting dark matter is described by the collisionless Boltzmann equation coupled to the Poisson equation in an expanding background Universe:

$$\frac{\mathrm{d}}{\mathrm{d}t}f(\boldsymbol{r},\boldsymbol{v},t) \equiv \dot{f} + (\boldsymbol{v}\nabla)f - \nabla\Phi\nabla_{\boldsymbol{v}}f = 0, \qquad \Delta\Phi(\boldsymbol{r},t) = 4\pi G \int f(\boldsymbol{r},\boldsymbol{v},t)\mathrm{d}\boldsymbol{v}, \qquad (3.39)$$

where $f(\boldsymbol{r},\boldsymbol{v},t)$ denotes the distribution function in phase space and $\dot{f}$ describes the partial derivative of f with respect to the time. *N-body simulations* are particularly suited to solve these equations since phase space density is sampled by a large number N of tracer particles which are integrated along characteristic curves of the collisionless Boltzmann equation. The accuracy of this approach depends on a sufficiently high number of particles. Fitting formulae describing the non-linear behavior of $P_\delta(k)$ have been derived from N-body simulations by Jain et al. (1995) and Peacock & Dodds (1996). While the linear power spectrum declines on small scales $\propto k^{-3}$, the amplitude of the non-linear power spectrum is substantially increased on these small scales at the expense of larger-scale structure (see Fig. 3.2). For the largest scales the non-linear power spectrum remains unaffected.

A simple model of the intergalactic or the interstellar medium can be obtained by modeling it as an ideal inviscid gas which is coupled to dark matter through its gravitational interaction. The hydrodynamics of the gas is governed by the continuity equation, the Euler equation, and the conservation equation for the thermal energy u:

$$\frac{\mathrm{d}\rho}{\mathrm{d}t} + \rho\nabla\boldsymbol{v} = 0, \qquad \frac{\mathrm{d}\boldsymbol{v}}{\mathrm{d}t} = -\frac{\nabla p}{\rho} - \nabla\Phi, \qquad \frac{\mathrm{d}u}{\mathrm{d}t} = -\frac{P}{\rho}\nabla\boldsymbol{v} - \frac{\Lambda(u,\rho)}{\rho}, \qquad (3.40)$$

where $\Lambda(u,\rho)$ describes external sinks or sources of heat for the gas, and we used the Lagrangian time derivative, $\mathrm{d}/\mathrm{d}t \equiv \partial/\partial t + \boldsymbol{v}\nabla$. The equation of state $P = (\gamma - 1)\rho u$ closes the above system of coupled differential equations.

Numerical methods   Gravitational interactions of a collisionless fluid are computed in virtually all cosmological codes by means of the N-body method. There are a diversity of methods for the approximation of the gravitational field. Particle-mesh (PM) methods (Klypin & Shandarin 1983, White et al. 1983) are the fastest algorithms (of complexity $N \log N$ per time step) for computing the *long-range gravitational force* on one particle exerted by the others while they are not suited to obtain high spatial resolution: the discrete mass distribution is smoothed on a three-dimensional mesh and the Newtonian potential is then obtained in Fourier space because of the algebraic property of Poisson's equation there. To increase the spatial resolution, *short–range forces* can be computed by direct summation between all pairs of particles (Hockney & Eastwood 1981, Efstathiou et al. 1985) while putting up with the higher complexity N^2 of the scheme. Within clustered regions, containing approximately 10^5 particles, it is more efficient to refine the original mesh recursively by higher resolution Fourier-meshes (Couchman 1991), although leaving the problem of solving fast-Fourier transforms with non-periodic boundary conditions. Alternatively, the adaptive refinement of the mesh can be obtained with the potential found in real space using relaxation methods (Kravtsov et al. 1997).

A different approach is pursued by hierarchical tree algorithms (Barnes & Hut 1986, Dehnen 2000) which expand the gravitational field into multipoles and have no resolution limit, in principle. This method is however very inefficient compared to Fourier-based methods for regions with low density contrast. TreePM hybrid methods (Xu 1995, Springel 2005) combine these two different approaches: they use the tree methods for computing short-range gravitational forces while exploiting the particle-mesh scheme for long-range scales.

Hydrodynamical solvers of cosmological codes are generally classified into two main categories: (1) Lagrangian methods like smoothed particle hydrodynamics (SPH) and (2) Eulerian codes. SPH methods were first proposed by Gingold & Monaghan (1977) and Lucy (1977) and approximate continuous density fields by discrete distributions of point particles. Subsequently, improved SPH techniques have been developed for cosmological applications (Evrard

1988, Hernquist & Katz 1989, Navarro & White 1993, Springel & Hernquist 2002, Springel 2005). Contrarily, Eulerian methods discretize space and represent continuous fields on a mesh. Originally, codes employed a mesh which is fixed in space (Cen & Ostriker 1993, Yepes et al. 1995) or adaptively moving (Pen 1998) while more recently, adaptive mesh refinement (AMR) algorithms have been developed for cosmological applications (Berger & Colella 1989, Bryan & Norman 1997, Norman & Bryan 1999, Kravtsov et al. 2002).

Grid-based techniques offer superior power for capturing hydrodynamical shocks, in some algorithms even without the aid of artificial viscosity and showing low residual numerical viscosity. However, codes employing static meshes still lack the resolution and flexibility necessary to tackle structure formation in a hierarchically clustering Universe which is characterized by the presence of substructure at all stages of evolution. These techniques are particularly seriously limited when studying the formation of individual galaxies in a cosmological volume because internal galactic structure such as disk and bulge components are not sufficiently resolved. Recently, a new generation of AMR codes finds more application in cosmology (Abel et al. 2002, Kravtsov et al. 2002, Refregier & Teyssier 2002). However, some grid-based problems remain even here because these codes impose symmetries which result in advection errors and the dynamics not being Galilean-invariant. Being interested in dynamical implications of CRs on structure formation and galaxy evolution, one faces not only the problem of the interplay of gravity and hydrodynamics of a plasma composed of CRs and thermal particles but in addition radiative processes such as cooling and supernova feedback. To date, there is no AMR code encompassing these requirements although there are recent efforts towards this goal (Kang & Jones 2005, Jones & Kang 2005).

In contrast, SPH methods appear better suited for these problems due to their Lagrangian nature because they adaptively increase the resolution in dense regions such as galactic halos or centers of galaxy clusters which are the regions of primary interest in this aspect of cosmology. One drawback of SPH is the dependence on the artificial viscosity which has to provide the necessary entropy injection in shocks. Monaghan (1997) modified the parameterization of the artificial viscosity in analogy with the Riemann problem. Although the discontinuities are broadened over the SPH smoothing scale, post-shock quantities are calculated very accurately.

3.3. Clusters of galaxies

The standard model of cosmology envisions structure formation as a hierarchical process in which gravity is continuously drawing matter together to form increasingly larger structures. Clusters of galaxies currently sit atop this hierarchy as the largest objects that have had time to collapse under the influence of their own gravity (Sect. 3.3.1). There are two different approaches to classify these uniquely useful tracers of cosmic evolution: the theoretical approach characterizes them according to their dynamical state in combination with concurrent physical processes (Sect. 3.3.2) while the observational approach connects multifrequency signatures to obtain a complete understanding (Sect. 3.3.3). The presentation in this section has been inspired by reviews of Sarazin (1988) and Voit (2005).

3.3.1. Cluster formation

Structure formation predicts the hierarchical build-up of dark matter halos from small scales to successively larger scales. The gravitational pull of the density perturbations on the smallest scales causes them to deviate from the Hubble flow and slows the expansion of their matter, eventually halting and reversing the expansion because the density perturbations have larger amplitude on smaller mass scales. In the course of evolution, these small structures merge and coalesce to form progressively larger structures as perturbations on larger mass scales reach the non-linear regime. A full understanding of this hierarchical merging process requires numerical simulations, although its basic concepts can be obtained by means of the analytical spherical collapse model (Gunn & Gott 1972, Fillmore & Goldreich 1984, Bertschinger 1985).

However, the accretion process in real clusters is not symmetric. Gravitational forces between infalling matter clumps produce a time-varying collective potential which randomizes the velocities of the infalling particles yielding a Maxwellian velocity distribution characterized by the velocity dispersion of the particles as the most probable state. Since the energy and the angular momentum are not conserved for individual particles, phase mixing occurs which results in damping of bulk motions. This process is known as *violent relaxation* (Lynden-Bell 1967) and leads to a state of virial equilibrium in which the total kinetic energy E_{kin} is related to the total gravitational potential energy E_{grav} through the equation

$$E_{\mathrm{grav}} + 2E_{\mathrm{kin}} = 4\pi P_{\mathrm{inf}} r_{\mathrm{inf}}^3, \tag{3.41}$$

where P_inf is the effective pressure due to infalling matter at the boundary r_inf of a collapsed system: in a steady state, the momentum flux of particles exiting the boundary balances that entering, so the boundary is formally equivalent to a reflecting wall which adds a pressure correction term, offsetting some of the gravitational energy (The & White 1986). Once the collapse of the cluster is completed, violent relaxation is ineffective, and the cluster relaxes through *two-body interactions* (Chandrasekhar 1942, Spitzer & Harm 1958). While these processes are unlikely to be important for small substructures, they can be significant for large halos near the cluster core: Chandrasekhar (1942) showed that a massive object moving through a homogeneous and isotropic Maxwellian distribution of lighter collisionless particles suffers a drag force called *dynamical friction* which is independent on the mass of the lighter particles and leads to a slow-down of the massive object due to collective two-body encounters with the lighter particles.

The final maximum entropy state of a relaxed collisionless system would be a self-gravitating isothermal sphere, in which the velocity dispersion σ_v is constant and isotropic at every point and $\rho_\text{m}(r) = \sigma_v^2/(2\pi G r^2)$ (Lynden-Bell 1967). This model has the unfortunate property of an infinite mass and energy so that it is never realized in nature. Numerical N-body simulations find that the profile of dark matter halos is described by a universal law (Navarro, Frenk & White 1997, (NFW))

$$\frac{\rho(x)}{\rho_\text{cr}} = \frac{\delta_\text{c}}{x(1+x)^2} \quad \text{with} \quad x = \frac{r}{r_\text{s}}, \tag{3.42}$$

and $r_\text{s} = r_\text{vir}/c$. r_vir denotes the virial radius within which the mean matter density is $200\rho_\text{cr}$ and c is the concentration parameter, and

$$\delta_\text{c} = \frac{200}{3}\frac{c^3}{\ln(1+c) - \frac{c}{1+c}}. \tag{3.43}$$

Typical concentration parameters for simulated clusters are in the range $c \sim 4\ldots 10$ with the largest mass systems showing the smallest concentration parameter and a typical scatter in $\ln c$ of $0.2\ldots 0.35$ (Jing 2000). Even with this more sophisticated density profile the mass diverges logarithmically with radius. Thus, the cluster's mass and relations linking that mass to observables depend crucially on the definition of the outer boundary of the cluster. It turns out that there is no simple unique mass definition satisfying the needs of all applications. An example of such a definition is obtained by truncating the isothermal sphere at the virial radius, arriving at a relation between velocity dispersion σ_v and virial mass M_vir, $M_\text{vir} \propto \sigma_v^3$ (Evrard 1989, Eke et al. 1996, Evrard 2004). On the other hand, cluster masses in numerical simulations are frequently defined using the *friends-of-friends* algorithm that links neighboring mass particles (Davis et al. 1985) while clusters defined in such a way often show irregular boundaries which complicates the connection to observations (White 2001).

Since the dynamical time scale of cluster evolution is of the order of 1 Gyr, it is impossible to observe the evolution of individual clusters but rather how the demographics of the entire cluster population changes with redshift. An important statistical concept is the cluster mass function in this context which yields the mass density of clusters with mass larger than M in a comoving volume element (Press & Schechter 1974) and can be expressed as

$$n_\text{PS}(M,z)\text{d}M = \frac{\langle \rho_0 \rangle}{\sqrt{2\pi}D_+(z)M^2}\left(1 + \frac{n}{3}\right)\left(\frac{M}{M_*}\right)^{(n+3)/6}\exp\left[-\frac{1}{2D_+^2(z)}\left(\frac{M}{M_*}\right)^{(n+3)/3}\right]\text{d}M,$$

where M_* and $\langle \rho_0 \rangle$ are the nonlinear mass today and the mean background density at the present epoch, and $D_+(z)$ is the linear growth factor of density perturbations, normalized to unity today. $n \approx -1$ denotes the effective exponent of the dark matter power spectrum at the cluster scale. Bond et al. (1991) and Sheth & Tormen (1999) proposed a significantly improved analytic derivation of the mass function while Jenkins et al. (2001) measured the mass function of dark matter halos in numerical simulations and obtained results consistent with Sheth & Tormen's.

3.3.2. Dynamical state and physical processes

Baryonic plasma follows these transient potential wells provided by dark matter. The luminous content of galaxies results from cooling processes and condensation within an extended dark matter halo (White & Rees 1978). Clusters have been traditionally characterized by accumulations of galaxies ranging from large groups of a few tens of galaxies up to the largest clusters comprising few thousand galaxies. Clusters are the largest gravitationally bound objects in the Universe and reach masses up a few times $10^{15}M_\odot$. In the cores of galaxy clusters, hot plasma has been detected both through its X-ray emission and by Compton up-scattering of photons from the cosmic

microwave background radiation. This plasma shows typical temperatures of $kT \sim (1 \ldots 10)$ keV and is dilute, $n_e \sim (10^{-2} \ldots 10^{-3})$ cm^{-3}.

Clusters are *virtually closed systems* which do neither lose their intra-cluster medium (ICM) nor their member galaxies.[3] Considering their entirety, they gather a very large sample of matter, thus providing a representative sample of the whole Universe. Together with precise BBN baryon density estimates, this can be used to infer the total matter density $\Omega_m = \Omega_{dm} + \Omega_b$ (White et al. 1993). According to ROSAT results (Briel et al. 1992), most of the baryons in clusters reside in the hot, X-ray emitting intra-cluster plasma and are not bound in stars. From a flux limited sample of X-ray emitting clusters, Mohr et al. (1999) have compiled the gas-to-total mass ratio $\langle f_{ICM} \rangle \simeq 0.075 \, h^{-3/2}$. Using the present day value of Hubble's constant, one arrives at the following picture for a galaxy cluster's composition: $\sim 85\%$ of the mass consists of dark matter, $\sim 12\%$ is made out of hot plasma, and the reminder is locked into stars.

Dynamical friction decelerates more massive galaxies near the cluster's core until they spiral towards the center (Lecar 1975). The kinetic energy removed from the massive galaxies is transferred to lighter galaxies or dark matter particles so that their population expands in the cluster's potential. Thus, dynamical friction generates mass segregation in a cluster such that more massive galaxies are found preferably at smaller radii. Massive galaxies spiraling into the cluster center will eventually merge to form a single supergiant elliptical galaxy if they are not tidally disrupted (Ostriker & Tremaine 1975, White 1976). This formation scenario explains naturally the extremely high luminosities of cD galaxies which are sitting nearly at rest at the bottom of the cluster's potential well and are dominating the center.

Clusters of galaxies are constantly growing through mergers. A major merger where comparably massive clusters with a mass ratio $\lesssim 3$ collide occurs on average approximately every Gyr. Mergers induce *collisionless shock waves* which dissipate gravitational energy associated with hierarchical clustering into thermal energy of the IGM apart from the additional contribution due to adiabatic compression caused by the later infalling material which itself is compressed at these shock waves.[4] Observations of such shock waves reveal that the plasma lags behind the dark matter clump which itself is coincident with the effectively collisionless subcluster galaxies (Markevitch et al. 2004). Besides thermalization, the collisionless shock is able to accelerate electrons and ions of the high-energy tail of the Maxwellian through diffusive shock acceleration (for reviews see Drury 1983b, Blandford & Eichler 1987, Malkov & Drury 2001). These energetic ions are reflected at magnetic irregularities through magnetic resonances between the gyro-motion and waves in the magnetized plasma and are able to gain energy in moving back and forth the shock front. Relativistic electrons emit synchrotron radiation in the presence of magnetic fields which has been observed as extended radio relics observed in the cluster outskirts, thus tracing shock waves in the radio band (e.g., Röttgering et al. 1997). Additionally, merging subclumps stir turbulence with the largest eddies injected on the scale of the merging impact parameter. Subsequently, the cluster is relaxing on a timescale which is longer than the crossing time of the cluster,

$$t_{\rm cross} \equiv \frac{r}{\sigma_v} \sim 10^9 \, {\rm yr} \left(\frac{r}{\rm Mpc} \right) \left(\frac{\sigma_v}{10^3 \rm km/s} \right)^{-1} < t_{\rm relax} < t_{\rm Hubble} \sim 10^{10} \, {\rm yr}, \qquad (3.44)$$

where σ_v denotes the velocity dispersion. During this relaxation process, thermal energy is successively radiated away through bremsstrahlung, a process which is most efficient in the densest regions at the cluster center. This process cools the cluster core so that the ICM responds in developing a denser core in order to maintain hydrostatic equilibrium. Theoretically, this process is instable leading to catastrophic cooling of cluster cooling cores which is not observed in X-rays, giving rise to the so-called *cluster cooling flow problem*. The central plasma in relaxed clusters with a short cooling time is observed to develop cool cores with central temperatures $\sim T_0/2$, but very little X-ray line emission is seen from plasma at $\lesssim T_0/3$ (Peterson et al. 2001, 2003). Some sort of physical heating mechanism seems to inhibit condensation below this temperature or balancing the energy losses by a comparable

---

[3]In this context, virtually closed does not imply them to be isolated systems because there is no clean boundary separating the cluster from the rest of the Universe and they accrete constantly mass through any sufficiently remote boundary surface.

[4]A shock wave can be generally defined as a transition layer which propagates through a plasma and changes its state. The thickness of the transition layer (the shock front) is determined by the physical process responsible for the energy conversion from the kinetic energy of the incoming plasma to internal degrees of freedom of the downstream plasma. In an ordinary gas shock the energy is transferred by two-body collisions to the random thermal motion of the gas molecules and the thickness is of the order of a few collisional mean free paths. However, in tenuous plasmas collisions are rare and the energy transfer proceeds through collective electromagnetic effects. Thus the thickness of these collisionless shocks is of the order of the gyro-radius of a thermal ion (or the Debye length if electrostatic effects are important).

amount of energy injection. A couple of candidates have been proposed for resupplying the heat radiated away, four of which shall be presented in the following:

- Dissipation of mechanical energy released by the expansion and buoyant motion of radio bubbles inflated by the central radio galaxies (Churazov et al. 2001, Brüggen & Kaiser 2001, Quilis et al. 2001, Brüggen et al. 2002, Chandran 2004, Hoeft & Brüggen 2004, Dennis & Chandran 2005, Ensslin & Vogt 2005). The centers of many clusters with low-entropy plasma whose cooling time is less than the Hubble time also contain active galactic nuclei that are ejecting jets of relativistic plasma into the ICM (Burns 1990) which supports this model. This scenario is theoretically compelling because the energy balancing mechanism provides a stable self-adjusting feedback mechanism: If the radio galaxy activity is triggered by cold ambient plasma from the core condensing onto the central supermassive black hole, the galaxy activity increases until it disrupts further accretion.

- Thermal conductivity would allow the inward transport of heat from the hotter ambient ICM towards the central core and thus offsetting the cooling (Malyshkin 2001, Narayan & Medvedev 2001, Voigt et al. 2002, Ruszkowski & Begelman 2002, Cho et al. 2003, Jubelgas et al. 2004, Chandran & Maron 2004). This scenario faces severe problems to explain the absence of cooling: (i) thermal conductivity needs to be close to Spitzer's estimate, and therefore not suppressed by magnetic fields. (ii) The required energy injection needs to be fine-tuned because too strong conduction would erase the cool core, but too weak conduction cannot prevent the cooling catastrophe, thus leading to an unstable solution for the conductively heated cool core. Furthermore, it is unable to explain the existence of cold gas clouds which need sufficient insulation from the keV plasma (Soker 2003, Nipoti & Binney 2004).

- A significant relativistic component, in the form of cosmic rays (CRs), present in the intracluster medium and significantly frozen to the thermal plasma, can provide a temperature floor regardless of the nature of the heating process. Such an addition qualitatively alters the conventional isobaric thermal instability criterion, such that a fluid parcel becomes thermally stable when its thermal pressure drops below a threshold fraction of its CR pressure (Chandran 2004, Cen 2005). The drawback of this model is, that an overall heating process is still required to balance the radiative cooling losses while the energy density of CRs seems to be only a small fraction of the thermal energy density within cool cores (Pfrommer & Enßlin 2004a).

- Supernovae driven galactic winds are another candidate for supplying the feedback that suppresses condensation, but is is questionable if this process can provide enough energy to offset cooling. The amount of energy input needed to balance the radiative energy losses while avoiding overcooling is ~ 1 keV per gas particle in the ICM (Voit et al. 2002, Tornatore et al. 2003). However, almost the entire supernova energy has to be transfered to thermal energy of the ICM with implausible high efficiencies and virtually no radiative loses (Kravtsov & Yepes 2000) which is unlikely given the high central plasma densities.

To date, there is still no consensus on the relative importance of these mechanisms. The final solution might require an interplay of different scenarios depending on still unknown boundary conditions. Overall, clusters of galaxies provide useful laboratories for investigating the non-linear phase of structure formation, the interaction of dark matter with baryonic physics, and studying the interplay active galaxies with the ICM with the additional potential of yielding valuable insight into plasma physics.

3.3.3. Multi-frequency observations of clusters

The most important observational findings leading to the emergence of the previous physical interpretations will be presented in this section. It provides the background for many implicit assumptions of the following chapters.

3.3.3.1. Optical properties of clusters

Observables in the optical band include the total luminosity of the cluster galaxies, that scales with the cluster mass, the velocity dispersion of cluster member galaxies, responding to the depth of the cluster's potential, and the amount of gravitational lensing which background galaxies experience by the cluster's potential. The first concentrations of luminous objects in the constellations Virgo and Coma Berenices were already recognized by the end of the eighteenth century by Messier (1784) and Herschel (1785). George Abell and collaborators performed pioneering

work in compiling a nearly complete catalogue of nearby clusters according to well defined optical criteria (Abell 1958, Abell et al. 1989). Today, optical cluster identification techniques extend and refine Abell's basic approach (e.g. Dalton et al. 1997), sometimes augmenting it with information on galaxy colors to enhance the cluster contrast against the background galaxy counts (e.g. Bahcall et al. 2003).

Generally, cluster galaxies follow a luminosity function proposed by Schechter (1976) when neglecting cD galaxies, with the number of galaxies per unit luminosity and per unit volume distributed according to

$$\varphi_L(x)\mathrm{d}x = \varphi^* x^{-\alpha} \exp(-x)\mathrm{d}x \quad \text{with} \quad x = \frac{L}{L^*}, \tag{3.45}$$

with a characteristic luminosity L^* corresponding to a characteristic magnitude $M_B^* = -20.6$, the normalization $\varphi^* = 0.04\,h^3/\mathrm{Mpc}^3$, and the faint end slope $\alpha = 5/4$. Because the shape of the luminosity distribution function of cluster galaxies is nearly universal, observing the high end tip of that distribution allows one to normalize the overall cluster luminosity function, yielding estimates for both the cluster's total optical luminosity and, less accurately, its mass. The faint end slope of the luminosity function of $\alpha = 5/4$ is smaller compared to that of the mass function of $\alpha = 5/3$: there needs to be a halo mass dependent physical mechanism which prevents these systems from forming stars (White & Frenk 1991, Benson et al. 2003). Although there have been some scenarios proposed, including energy injection through photoionization during the reionization epoch (Benson et al. 2002) or tidal interactions with neighboring galaxies and with the hierarchically growing cluster halo (Gnedin 2003), it is to date unknown what causes these low-mass systems to be so faint.

Optical observations offer two complementary methods to infer the cluster's morphology and the true mass concentrations, through the orbital velocities of the member galaxies and the degree to which the background galaxy images are distorted by the cluster's gravitational potential. Because the velocity distribution of galaxies within a relaxed cluster is expected to be Gaussian in velocity space, one is able to fit the velocity distribution $\exp[-(v_r - \langle v \rangle)^2/(2\sigma_{1D}^2)]$ to these galaxies to obtain the one-dimensional velocity dispersion σ_{1D} for the cluster. Using the approximation of galaxies as test particles in the cluster's potential, one can apply the virial theorem of Eqn. (3.41) with $E_{\mathrm{kin}} = 3M\sigma_{1D}^2/2$ to infer a mass estimate. Since clusters are dynamical systems that have not finished forming and equilibrating, these estimates are generally uncertain.

Gravitational lensing of background galaxies has originally been proposed by Zwicky (1937) to infer the cluster mass. Lensing is sensitive to the cluster's morphology and mass distribution within a given projected radius $r_\perp$, because the mass within this radius deflects photons towards our line-of-sight through the cluster center. When the deflection angle is small compared to the angular impact parameter of the galaxy to the cluster center, the galaxy images are tangentially stretched to $r_\perp$. This phenomenon is called "weak lensing", and one can only determine statistical properties of the lensing system by averaging over the field of view: due to intrinsic ellipticities of the individual galaxies, statistical techniques using apertures with angular size of the order $1'$ are needed in order to infer properties of the local gravitational field of the lens. Conventionally, this method is applied to faint distant galaxy populations, whose shapes and sizes are weakly distorted by the gravitational tidal field of the deflecting object. However, one has to assume, that the intrinsic ellipticities of galaxies are uncorrelated (for an excellent review of this field, see Bartelmann & Schneider 2001).

3.3.3.2. X-ray emission of thermal plasma

Observables in the X-ray band include the overall X-ray luminosity of a cluster, emitted by the hot plasma trapped in the cluster's gravitational potential, the cluster's temperature inferred from the X-ray spectrum of that plasma, and the abundances of various elements inferred from the emission lines in this spectrum. Extended X-ray emission from galaxy clusters was first observed in the early 1970's (Gursky et al. 1971, Forman et al. 1972). For typical cluster temperatures ($kT \gtrsim 2\,\mathrm{keV}$) the emissivity of thermal bremsstrahlung dominates over the line emission while the situation reverses below that temperature given heavy metal abundances relative to hydrogen of ~ 0.3 times those found in the Sun. Clusters can radiate bolometric X-ray luminosities up to $L_X = 10^{45}$ erg/s. The rate at which the intra-cluster medium (ICM) radiates can be expressed in a cooling function of the plasma which is proportional to $n_e n_{\mathrm{ion}} \Lambda_X(T)$, where $\Lambda_X(T) \propto \sqrt{kT}$ in the regime of thermal bremsstrahlung. This X-ray emissivity is extremely sensitive to any substructure due to its dependence on the square of the density.

Assuming spherical symmetry, the equation of hydrostatic equilibrium can be written

$$\frac{\mathrm{d}\ln\rho_\mathrm{p}}{\mathrm{d}\ln r} + \frac{\mathrm{d}\ln T_\mathrm{p}}{\mathrm{d}\ln r} = -2\frac{T(r)}{T_\mathrm{p}}, \tag{3.46}$$

where ρ_p is the plasma density, T_p the plasma temperature, and $kT(r) = GM(r)\mu/(2r)$ which can be identified with the characteristic temperature of a singular isothermal sphere in the case of a density distribution $\rho = \sigma_\mathrm{1D}/(2\pi Gr^2)$.[5] Assuming furthermore, that the plasma is isothermal yields the classical beta model for the X-ray surface brightness of clusters (Cavaliere & Fusco-Femiano 1976). If the velocity dispersion of dark matter particles is also isothermal with a constant velocity dispersion σ_1D, then Poisson's equation implies

$$\frac{\mathrm{d}\ln\rho_\mathrm{p}}{\mathrm{d}\ln r} = -\frac{\mu}{kT_\mathrm{p}}\frac{\mathrm{d}\Phi}{\mathrm{d}r} = \beta\frac{\mathrm{d}\ln\rho}{\mathrm{d}\ln r}, \tag{3.47}$$

where $\beta \equiv \mu\sigma_\mathrm{1D}^2/(kT_\mathrm{p})$. Taking the same assumptions (i.e. spherical symmetry, isotropy of velocities, a self-gravitating system in a stationary state), King (1966) has developed a self-consistent truncated density distribution for clusters. For the phase space density he assumes

$$f(\boldsymbol{r},\boldsymbol{v})\mathrm{d}^3r\,\mathrm{d}^3v \propto \exp\left(\frac{\Phi(0)}{\sigma_\infty^2}\right)\left[\exp\left(-\frac{v^2/2 + \Phi(r)}{\sigma_\infty^2}\right) - 1\right]\mathrm{d}^3r\,\mathrm{d}^3v, \tag{3.48}$$

where σ_∞ is the radial velocity dispersion in an untruncated cluster. The velocity distribution is thus truncated at the escape velocity v_e: $f(\boldsymbol{r},|\boldsymbol{v}| > v_\mathrm{e}) = 0$ where $v_\mathrm{e}^2 = -2\Phi(r)$, and the potential vanishes at infinity, $\Phi(\infty) = 0$. Integrating this phase space density over all velocities yields $\rho(r)$ as a function of $\Phi(r)$ which has to be solved for self-consistently by inserting into Poisson's equation. Since there is no simple analytic solution for $\rho(r)$ to this potential, King (1962) provides the approximate solution $\rho(r) \propto [1 + (r/r_\mathrm{c})^2]^{-3/2}$, where r_c denotes the core radius that prevents the profile from becoming singular at the origin, and the plasma density becomes

$$\rho_\mathrm{p}(r) = \rho_\mathrm{p}(0)\left[1 + \left(\frac{r}{r_\mathrm{c}}\right)^2\right]^{-3\beta/2}, \tag{3.49}$$

where Eqn. (3.47) has been used. The expected X-ray surface brightness for an isothermal plasma with $T_\mathrm{p} = T_\mathrm{e}$ is then obtained by projection

$$S_\mathrm{X}(r_\perp) = 2\int_{r_\perp}^\infty \mathrm{d}r\,\frac{r\,n_\mathrm{e}^2(r)\,\Lambda_\mathrm{X}[T_\mathrm{e}(r)]}{\sqrt{r^2 - r_\perp^2}} = S_0\left[1 + \left(\frac{r_\perp}{r_\mathrm{c}}\right)^2\right]^{-3\beta+1/2}, \tag{3.50}$$

where S_0 is the central X-ray surface brightness. The observed X-ray surface brightness can be inverted using the Abel integral equation to obtain the radial density profile (see Appendix A). Beta models generally describe the observed surface brightness well up to $\sim 3r_\mathrm{c}$, with typical values of $\beta \sim 2/3$ and $r_\mathrm{c} \sim 0.1r_\mathrm{vir}$ for rich clusters (Jones & Forman 1984). Because dark matter profiles are rather of NFW type (Eqn. (3.42)) than following the cored profile proposed by King, only the success of describing X-ray surface brightness profiles by beta profiles for the ICM justifies their use. The real ICM is sometimes far from hydrostatic equilibrium especially during a merger event and shows a wealth of structure such as cold fronts, X-ray cavities, and additional substructure. Thus, these equations might yield misleading answers and need to be cross-correlated with additional information of other wavebands. Indeed, a Fourier analysis of spatially-resolved plasma pressure maps of the Coma galaxy cluster reveals the presence of a scale-invariant pressure fluctuation spectrum in the range between 40 and 90 kpc and is found to be well described by a projected Kolmogorov/Oboukhov-type turbulence spectrum. This indicates that at least $\sim 10\%$ of the total ICM pressure is in turbulent form (Schuecker et al. 2004).

Using the emission line fluxes, abundances of elements like iron, oxygen, and silicon are straightforwardly to measure in the ICM. Collisional de-excitation is negligible because the ICM is so dilute. Thus, every collisional excitation produces a photon that leaves the cluster. The observed spectrum can therefore be fitted by a optically-thin spectrum of a collisionally-ionized, single temperature plasma, while adjusting the abundances in the model to produce the best fit. Because the most abundant elements are nearly completely ionized in the hottest clusters, these abundance determinations depend on the strength of the K-shell emission lines of iron, one of the rare lines which can be measured in these environments. The total amount of iron obtained from these measurements exceeds the total amount of iron contained within all the stars in the cluster galaxies (Renzini 1997) and is comparable to

---

[5]Here, $\mu = 4m_\mathrm{p}/(3 + 5X_\mathrm{H})$ is the mean particle weight assuming full ionization and $X_\mathrm{H} = 0.76$ is the primordial hydrogen mass fraction.

the amount of iron produced by all the supernovae that are believed to have exploded during the cluster's history (David et al. 1991). Supernovae are believed to drive strong galactic winds that enrich the ICM with heavy elements (Heckman et al. 1990). However, hydrodynamical simulation fail in producing these winds, because much of the energy released by core collapse supernovae is transfered to the cool gas rather than driving a powerful gaseous outflow (Mac Low & Ferrara 1999). Strong galactic winds might be driven by relativistic protons through Parker instabilities of spiral disks solving the *enrichment problem* of high iron abundances of the ICM as the study of the isolated Parker instability suggests (Hanasz & Lesch 2003).

3.3.3.3. Sunyaev-Zel'dovich effect

Hot plasma in galaxy clusters can also be observed through its effect on the cosmic microwave background (CMB). Photons of the CMB experience inverse Compton collisions with thermal electrons of the hot dilute intra-cluster plasma, an effect predicted by Sunyaev & Zel'dovich (1972) (for a comprehensive review, see Birkinshaw 1999). At the angular position of galaxy clusters, the CMB spectrum is modulated as photons are redistributed from the low-frequency part of the spectrum below a characteristic crossover frequency to higher frequencies implying a net energy transfer from the thermal intra-cluster plasma to CMB photons, known as the thermal Sunyaev-Zel'dovich (SZ) effect. To lowest order, the distorted spectrum can be separated into an universal frequency-dependent function that is independent of cluster parameters and the amplitude of the frequency modulation. This so-called Compton-y parameter is proportional to the product of the probability that a photon passing through the cluster will Compton scatter and the typical energy gain of a scattered photon:

$$y = \int \frac{kT_e}{m_e c^2} n_e \sigma_T \mathrm{d}l. \tag{3.51}$$

The line-of-sight integration extends from the observer to the last scattering surface of the CMB at redshift $z \simeq 1100$. Here, σ_T denotes the Thompson cross section, m_e the electron rest mass, T_e and n_e are electron temperature and thermal electron number density, respectively. The peculiar motion of a cluster with respect to the rest frame of the CMB produces an additional spectral distortion due to the Doppler effect, called kinetic SZ effect. A detailed introduction including the relativistic SZ effect will be given in Sect. 8.2.

The SZ effect is independent of distances and represents thus an invaluable tool for detecting galaxy clusters out to very high redshifts which are otherwise not detectable in optical or X-ray surveys. Because not all clusters will be well resolved, the observables of SZ surveys are the line-of-sight Comptonization integrated over the solid angle subtended by the cluster or the beam, whichever shows the small angular extent, $Y = \int y \mathrm{d}A \propto \int n_e kT_e \mathrm{d}V$. Thus, the Y parameter is a measure of the total thermal energy within a cluster. Additionally, the study of the cluster's outskirts greatly benefits from the fact that the thermal SZ effect depends on the thermal pressure rather than the density squared in the case of X-ray emissivity. Combining maps of the SZ effect, the X-ray surface brightness, and from gravitational lensing, it might be possible to reconstruct the three-dimensional appearance of the cluster (Zaroubi et al. 2001). So far, the SZ effect has only been exploited for cosmological purposes while we propose to use high-resolution SZ observations to unveil the still unknown dynamically dominant component of the radio plasma bubbles within cool cluster cores in Chapter 8.

3.3.3.4. Non-thermal emission processes

In the previous three sections, techniques for inferring the dark matter, baryonic, and turbulent content of clusters were presented while non-thermal radiation provides completely complementary information to these components. CR electrons within the ICM have two preferred emission mechanisms: (i) their gyro motion around magnetic field lines generates diffuse radio synchrotron radiation and (ii) through inverse Compton collisions with photons of the ambient starlight and the CMB, CR electrons are able to up-scatter these photons into the wave band ranging from extreme ultra-violet (EUV) to the hard X-ray band. Observables in the radio band include the radio surface brightness of a cluster, revealing a combination of the energy density of CR electrons and the magnetic field, and the spectral index inferred from multi-frequency radio observations that traces the underlying CR electron population. In contrast, inverse Compton emission reveals a cleaner signature of the CR electron population which is not confused by magnetic fields. Combining these two emission processes unveils the energy density of the intra-cluster magnetic field. An upper limit on the inverse Compton emission in combination with observed synchrotron emission translates into a lower limit of the magnetic field strength.

Diffuse extended radio synchrotron emission that cannot be attributed to individual galaxies in a galaxy cluster is termed radio halo and shows a similar morphology compared to the thermal X-ray emission (e.g., Kim et al. 1989, Giovannini et al. 1993, Deiss et al. 1997, Giovannini et al. 1999, Liang et al. 2000) while there are smaller counterparts named radio mini-halos (e.g., Pedlar et al. 1990). In addition, there have been extended radio relics observed in the cluster periphery (e.g., Röttgering et al. 1997) which may well coincide with merger shock waves running into the shallower gravitational potential in the cluster outskirts as proposed by Enßlin et al. (1998) and successfully reproduced in a simulation of this process by Roettiger et al. (1999). A taxonomy of particle accelera-tion processes leading to these radio appearances will be given in Sect. 6.1. It has been recognized that radio halos in galaxy clusters are preferentially associated with massive ($L_X > 0.5 \times 10^{45}$ erg s^{-1}) clusters that are experiencing violent mergers and have a seriously disrupted cluster core, as indicated by substructure in the X-ray images and temperature maps (see Feretti 1999, and references therein). The association of radio halos with clusters currently experiencing the largest departures from a virialized state may account for both the vital role of mergers in accel-erating the relativistic particles responsible for the radio emission as well as the rare occurrence of radio halos in cluster samples (Buote 2001). Based on these observations, Enßlin & Röttgering (2002) developed a redshift de-pendent radio halo luminosity function and predicted large numbers of radio halos to be detected with future radio telescopes.

Some clusters have also been reported to exhibit an excess EUV/hard X-ray emission compared to the expected thermal bremsstrahlung of the hot ICM (Lieu et al. 1996, Fusco-Femiano et al. 1999, Sanders et al. 2005). This emission is most probably produced by inverse Compton up-scattering of CMB photons by relativistic electrons according to the formula $\nu_{IC} = \nu_{init}\gamma^2_{CRe}4/3$ (Hwang 1997, Enßlin & Biermann 1998, Enßlin et al. 1999). Here, ν_{init} denotes the initial frequency of the photon which gets up-scattered to the final frequency ν_{IC} by a CR electron of Lorentz factor γ_{CRe}. 'Mildly' relativistic CR electrons ($\gamma_e \simeq 100 - 300$) are injected over cosmological timescales into the ICM and have a comparably long lifetimes of a few times 10^9 years (see Sarazin 2002, and references therein) that predestines them to be responsible for the excess EUV emission. Less energetic CR electrons suffer from efficient Coulomb losses while more energetic CR electrons loose their energy on much shorter timescales due to inverse Compton/synchrotron losses. It has been proposed that a fraction of the diffuse cosmological γ-ray background radiation originates from the same inverse Compton processes of higher energetic electrons which are freshly accelerated at shock waves (Loeb & Waxman 2000, Miniati 2002, Reimer et al. 2003, Berrington & Dermer 2003, Kuo et al. 2005).

A different piece of evidence for magnetic fields comes from Faraday rotation which arises owing to the bire-fringence of magnetized plasma causing the plane of polarization to rotate for a nonzero magnetic field component along the propagation direction of the photons (Clarke et al. 2001). Although this methods yields reliable magnetic field strength, it is only applicable within finite windows given by the extent of the sources emitting polarized radia-tion. To date, the most sophisticated methods use a maximum likelihood estimator for the derivation of the magnetic power spectra (Vogt & Enßlin 2005) which is based on the theory of turbulent Faraday screens (Enßlin & Vogt 2003, Vogt & Enßlin 2003) yielding self-consistently the magnetic field strength and the magnetic autocorrelation length.

Coma cluster   Perseus cluster
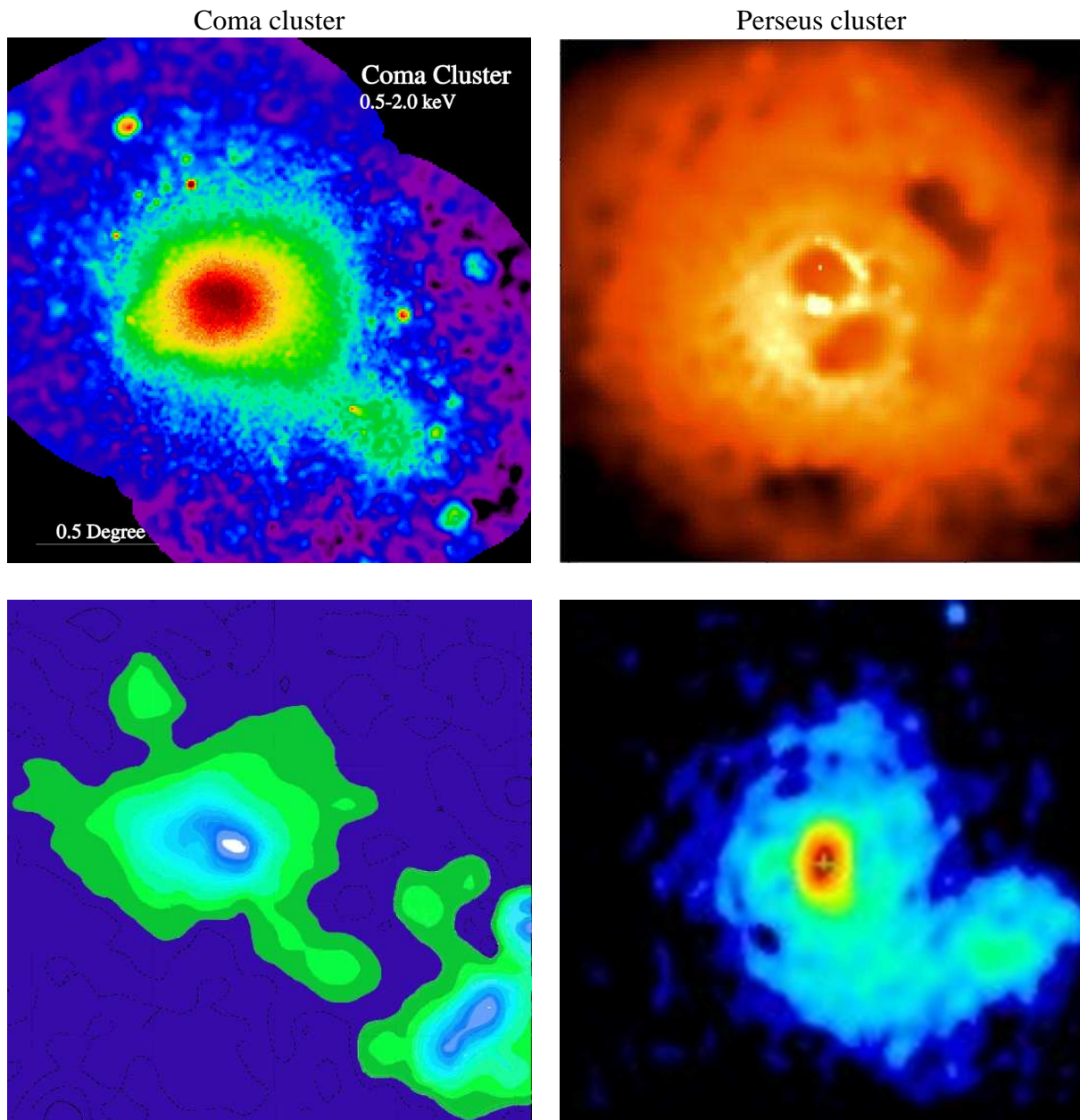
Figure 3.3.: Comparison of thermal X-ray emission and radio synchrotron emission of two prominent galaxy clusters, the Coma cluster (*left panels*) and the Perseus cluster (*right panels*). The *upper panels* show the X-ray emission and the *lower panels* show the radio synchrotron emission. The Coma cluster is characterized by the merging of the larger, brighter central cluster and the fainter group of galaxies to the lower right (the field is $\sim 2.5° \times 2.5°$ in both cases). The image of the Perseus cluster shows the cluster core region (6×6 arcmin^2 for the X-ray map, 9×9 arcmin^2 for the radio map). The bright yellow spot in the center of the X-ray map is due to accreting plasma onto a giant black hole in the nucleus of the central galaxy. The twin dark cavities are thought to be buoyant magnetized bubbles of relativistic particles produced by energy released from the vicinity of the black hole (for the origin of the radio synchrotron emission, refer to Chapter 6). (Credit: Coma/X-ray: ROSAT/MPE/Snowden, Perseus/X-ray: NASA/IoA/Fabian et al., Coma/radio: Deiss/Effelsberg, Perseus/radio: Pedlar/VLA).

4. Cosmic ray physics

Abstract

This thesis exclusively studies extragalactic cosmic rays whose proton and nuclear component is little known. Galactic cosmic rays are much better studied, however, numerous fundamental questions are still open, almost 100 years after their discovery by Hess. This chapter presents an overview of the physics of cosmic rays. After introducing basic physical concepts of cosmic rays, observational properties and theories about the origin of galactic cosmic rays are discussed in Sect. 4.1. In the following, non-thermal emission processes are introduced in Sect. 4.2 including synchrotron radiation and inverse Compton emission. Finally, the hadronic physics of inelastic cosmic ray collisions leading to pion decay induced γ-ray emission is presented in Sect. 4.3.

4.1. Galactic cosmic rays

Cosmic rays (CRs) were discovered by Hess (1912) and realized to originate outside the Earth. The Earth's magnetic field acts on energetic particles according to their charge and affects them differently coming from east or west, thus proving that the majority of CRs are charged particles. The energy spectrum of highly energetic CRs from 10^{10} eV (where the magnetic field of the Sun is no longer a concern) up to 10^{20} eV is well represented by a piecewise power-law indicating that CR particles are produced in non-thermal processes. In contrast, on extragalactic scales in the inter-galactic medium, there is hardly anything known about these non-thermal components because the energetically dominant CRs below 10^{16} eV are trapped by cluster magnetic fields and can only be observed indirectly through non-thermal radiative processes. This section is intended to give a short overview of the most important observational findings and physical concepts which are the guiding lines for the further course of the thesis (for an excellent introduction in this field, see Schlickeiser (2002) or Lemoine & Sigl (2001)).

4.1.1. Physical concepts

4.1.1.1. Transport of cosmic rays

Consider a spatial random coordinate $x(t)$ of a CR particle diffusing in a fluid of bulk velocity v. For simplicity, we restrict ourselves to the one-dimensional case. During a time interval which is much shorter compared to the diffusion time, the particle's position varies by $\Delta x = v\Delta t + \delta x$. The first contribution is due to the bulk motion of the scattering medium and the second term is due to the random walk diffusion with vanishing mean and the variance $\langle \delta x^2 \rangle = 2D(x, p)\Delta t$, where $D(x, p)$ denotes the diffusion coefficient. The distribution of galactic CRs is governed by a competition between injection, escape, energy gain (acceleration), and energy loss (catastrophic and continuous) processes. The transport equation which describes the balance of these processes is a Fokker-Planck type equation that includes the description of fluid motions, radiative losses, and phase space diffusion. It can be obtained by considering the collisionless Boltzmann equation and working out the magneto-hydrodynamic forces acting on a CR particle including the Lorentz force as well as pitch angle scattering on hydro-magnetic waves (Skilling 1975). The transport equation governs the evolution of the isotropic part $f(x, p)$ of the CR distribution function in phase space, assuming weak anisotropy of the CR momentum distribution function:

$$\frac{\partial}{\partial t}f + \frac{\partial}{\partial x}v(x, p)f = -\frac{1}{p^2}\frac{\partial}{\partial p}p^2 A(x, p)f + \frac{1}{p^2}\frac{\partial}{\partial p}p^2 \Gamma(x, p)\frac{\partial}{\partial p}f + \frac{\partial}{\partial x}D(x, p)\frac{\partial}{\partial x}f + s(x, p). \tag{4.1}$$

The distribution is normalized such that the number density of CRs $n_{\mathrm{CR}} = \int f 4\pi p^2 \mathrm{d}p$. The 'friction' term A describes not only various kinds of energy losses but also the energy gain by first order processes in $\beta \equiv v/c$ (adopting relativistic particles), the second contribution on the right-hand side describes the energy gain through

the second order Fermi process, the third term on the right-hand side describes spatial diffusion, and the last term accounts for sources such as freshly injected CR particles at shocks whose origin can be understood by means of plasma physical calculations. The physical meaning of these processes will be sketched in the following:

- **Synchrotron and inverse Compton losses.** A relativistic charged particle of a Lorentz factor $\gamma = (1-\beta^2)^{-1/2}$ experiences Compton scattering with either real or virtual photons (which represent the magnetic field in the case of synchrotron radiation). This causes the particle to emit photons in the forward direction into a narrow cone of half-angle γ^{-1} with respect to its momentum leading to an energy loss which can effectively be described by a friction force in opposite direction to its momentum:

$$A_{\mathrm{rad}} \equiv \left.\frac{\langle \Delta p \rangle}{\Delta t}\right|_{\mathrm{rad}} = -\frac{4}{3}\sigma_{\mathrm{T}}\left(\frac{m_{\mathrm{e}}}{m}\right)^2 (\varepsilon_B + \varepsilon_{\mathrm{ph}})\gamma^2, \tag{4.2}$$

where σ_{T} denotes the Thompson cross section, $\varepsilon_B = B^2/(8\pi)$ and $\varepsilon_{\mathrm{ph}}$ are the energy densities of the magnetic field (responsible for synchrotron losses) and the low energy photon field (causing the Compton effect in the Thompson regime). The radiative losses of baryons are suppressed by $(m_{\mathrm{e}}/m)^2$ such that they can be neglected unless they are ultra-high energetic CRs with energies $\gtrsim 10^{18}$ eV.

- **First order Fermi process.** The contribution of the first order Fermi process can be described by a non inertial entrainment due to the deceleration of the scattering medium: a compressed flow ($\nabla \cdot \boldsymbol{v} < 0$) produces first order acceleration of charged particles. In this situation, the inertial force is $F_j = -p_i(\partial v_j/\partial x_i)$ that gives rise to an accelerating power

$$P_{\mathrm{acc}} = -\langle v_j p_i \rangle \frac{\partial v_j}{\partial x_i} = -\frac{pv}{3}\nabla \cdot \boldsymbol{v} \quad \rightarrow \quad A_{\mathrm{acc}} = -\frac{p}{3}\frac{\partial v}{\partial x}. \tag{4.3}$$

- **Second order Fermi process.** Charged particles gyrate around, and travel slowly along magnetic field lines. Occasionally, they get scattered on magnetic irregularities and plasma waves (mostly Alfvén waves). This scattering process can be described by a random walk of the particle's pitch angle with the magnetic field direction, θ, yielding the characteristic variance $\langle \delta \mu^2 \rangle \propto \nu_{\mathrm{s}}\Delta t$ where ν_{s} denotes the average scattering frequency and $\mu = \cos\theta$. Because the particle scatters off moving targets, the particle systematically gains energy through random variations of the CR momentum $\delta p = \pm\beta_{\mathrm{A}} p\delta\mu$ where $\beta_{\mathrm{A}} = v_{\mathrm{A}}/c$ is the dimensionless Alfvén velocity in the case of scattering Alfvén waves. The second order Fermi process is thus described by a diffusion process in momentum space with the momentum diffusion coefficient

$$\Gamma \equiv \frac{\langle \delta p^2 \rangle}{2\Delta t} \sim \beta_{\mathrm{A}}^2 \nu_{\mathrm{s}} p^2. \tag{4.4}$$

- **Diffusive losses from the disk.** CRs experience momentum dependent diffusion in a turbulent magnetic field with a Kolmogorov-type spectrum on small scales. This process leads to a loss time scale which is proportional to $p^{-1/3}$. In an equilibrium situation, this results in a steepening of the observed spectrum within the disc by $p^{-1/3}$ relative to the injected spectrum.

- **Radioactive decay.** The observed isotope ratios resulting from radioactive decay provide a clock for cosmic ray transport and yields the time scale of diffusive losses from the disk. For any given isotope, radioactive decay can be a loss or a gain process in the equation of balance.

- **Coulomb and ionization losses** are strongest for protons or heavier nuclei, but also relevant for electrons. The ionization process limits the lower energy of the proton spectrum to approximately 50 MeV after traversing a path length through most of the interstellar medium (Nath & Biermann 1994). Energetic CRs experience energy losses even within an ionized medium through Coulomb interactions. Coulomb losses efficiently remove the low-energetic part of the injected CR spectrum on a short timescale and redistribute these particles and their energy into the thermal pool.

- **Catastrophic losses.** Another loss process is the inelastic reaction of CR nuclei with atoms and molecules of the interstellar medium. The CR protons interact hadronically with the ambient thermal gas and produce mainly neutral and charged pions, provided their momentum exceeds the kinematic threshold of 0.78 GeV for the reaction. The neutral pions successively decay into γ-rays while the charged pions decay into secondary electrons and neutrinos.

- **Spallation.** Spallation describes the destruction of atomic nuclei in a collision with a CR particle that is in most cases a proton or an alpha particle. In this destruction process, many pieces of debris are formed where commonly a single nucleon gets stripped and a distribution of lighter nuclei is obtained. Since the abundances of the elements Lithium, Beryllium, and Boron are much larger in CRs than in the interstellar medium, spallation processes are assumed to account for the origin of these elements. For any specific isotope, spallation can again occur as a loss or a gain process in the equation of balance.

4.1.1.2. Cosmic ray acceleration

The CR spectrum obeys a piecewise power-law which is referred to as their non-thermal property. The most successful theory in explaining this behavior describes the acceleration of energetic particles at shock waves traversing magnetized plasma. The original idea dates back to Fermi (1949) and was modified in the context of astrophysical shocks in the late seventies by several authors (Krimsky 1977, Bell 1978b, Blandford & Ostriker 1978).

Fermi's original theory Fermi realized that CRs gain energy when scattering off magnetized clouds of gas moving through the interstellar medium at velocity v. Entering the cloud, a CR ion scatters off magnetic irregularities in the magnetic field which is tied to the partly ionized gas. Magnetic irregularities are ubiquitous in a plasma that gets stirred by stellar winds, ionization fronts, supernova explosions, or by energetic particles moving through. In the rest frame of the cloud: (i) the particle's energy is conserved because of elastic collisions between the CR and the cloud as a whole being more massive than the CR; (ii) the direction of the CR is randomized by the scattering processes and leaves the cloud in a random direction. Performing a Lorentz transformation into the frame of the cloud and out of it again after taking in account previous considerations yields an energy gain $\Delta E/E \propto \beta^2 \equiv (v/c)^2$ that is second order in β and because $\beta \ll 1$, the average gain is small.

Diffusive shock acceleration Fermi's original theory was modified to describe the more efficient acceleration taking place in converging flows such as shock waves. A collisionless shock wave is able to accelerate ions from the high-energy tail of the Maxwellian through a process called *diffusive shock acceleration* (for reviews see Drury 1983b, Blandford & Eichler 1987, Malkov & Drury 2001). These energetic ions are reflected at magnetic irregularities through magnetic resonances between the gyro-motion and waves in the magnetized plasma and are able to gain energy in moving back and forth the shock front.

A shock is a transition layer where the mean plasma velocity changes rapidly over a width determined by plasma physical processes, and in dissipational shocks, most of the incident kinetic energy flux is converted into thermal energy. It is convenient to describe a shock with respect to its rest frame which we assume to be non-relativistic. The shock transition layer separates two regions: the velocity field decays from its upstream supersonic value $v_1 > c_{s1}$ to a subsonic one $v_2 < c_{s2}$, where the indices 1 and 2 refer to the *upstream regime* (pre-shock regime) in front of the shock and the *downstream regime* (post-shock regime) in the wake of the shock wave, and c_s is the sound speed. The strength of the shock is measured by the Mach number $\mathcal{M} = v_1/c_{s1}$. The Rankine-Hugoniot jump relations for the density, velocity and pressure can be derived considering the conservation laws of mass, momentum, and energy:

$$\rho_1 v_1 = \rho_2 v_2, \tag{4.5}$$

$$P_1 + \rho_1 v_1^2 = P_2 + \rho_2 v_2^2, \tag{4.6}$$

$$(\varepsilon_1 + P_1)\rho_1^{-1} + \frac{v_1^2}{2} = (\varepsilon_2 + P_2)\rho_2^{-1} + \frac{v_2^2}{2}. \tag{4.7}$$

where ρ, P_i, and ε_i denote the density, the pressure, and internal energy density, respectively. The compression ratio is defined as $r \equiv \rho_2/\rho_1$ and can be written for polytropic fluids solely as a function of the Mach number using the Rankine-Hugoniot jump relations:

$$r = \frac{\gamma + 1}{\gamma - 1 + 2/\mathcal{M}^2}. \tag{4.8}$$

In a strong shock ($\mathcal{M} \gg 1$), if the shocked plasma is non-relativistic, the adiabatic index $\gamma = 5/3$ and the compression ratio approaches 4 while a plasma with relativistic pressure has $\gamma = 4/3$ and $r = 7$. In the case of a strong cooling shock wave, the compression ratio can go to infinity. Considering diffusion of the CR pressure or an oblique magnetic field, the simple jump condition is modified and can develop a precursor.

An energetic particle that has a higher individual velocity than the plasma flow in the shock frame may be able to travel against the stream and gets trapped at the shock for a while and thereby experiences this system as a permanently compressing flow. Thus, particles gain energy in going back and forth the shock front. In one cycle coming from upstream, scattering downstream, and coming back upstream, particles gain typically an additional fraction of v_{sh}/c in momentum (assuming relativistic particles). However, due to convection of the flow, the CR population loses a fraction v_{sh}/c of its members that escape from this process downstream. Compared to Fermi's original theory, this is a more efficient acceleration mechanism (1st order in β) owing to the symmetry breaking shock front. In the linear regime, this process naturally leads to a CR power-law distribution in particle momentum, $p^{-\alpha}$, which joins in a smooth manner into the shock-heated thermal distribution. The general expression for the spectral index of such a CR population is $\alpha = 3r/(r-1)$ in three-dimensional phase space. For relativistic particles the resulting energy distribution is then given by $E^{2-\alpha}$, a result which will be used frequently in the course of this thesis.

There is a very esthetical way of deriving the distribution function resulting from diffusive shock acceleration that uses the cosmic ray transport equation (Blandford & Ostriker 1978), which will be presented in the following. We neglect the second order Fermi process and the radiative losses in the CR transport equation, and assume a sharp shock transition which means that the shock width is much smaller than the diffusion length of CRs, $D(x,p)/v$. Again, we consider a spatial random coordinate $x(t)$ of a CR particle diffusing in a fluid of bulk velocity v. The fluid velocity is described by $v(x) = v_1 + (v_2 - v_1)\theta(x)$ and $\partial v/\partial x = (v_2 - v_1)\delta_D(x)$. Assuming this kinematic structure of the shock implicitly accounts for shock heating through dissipation and acts therefore as a thermodynamical background model. The stationary solution of the CR distribution function obeys the following transport equation:

$$v\frac{\partial}{\partial x}f - \frac{1}{3}\frac{\partial v}{\partial x}p\frac{\partial}{\partial p}f = \frac{\partial}{\partial x}D(x,p)\frac{\partial}{\partial x}f + v_1 g(p)\delta_D(x). \tag{4.9}$$

The last term is a special form of the source term $s(x,p)$ that accounts for injection of a CR population at shocks. This equation describes only the transport of the relativistic particle population over the shock wave while the distribution of particles in thermal equilibrium constituting the Maxwellian is not explicitly followed and only taken into consideration through their impact on the background velocity solution which we assume for the moment. The injected CR distribution function $g(p)$ is normalized such that $n_{CR,inj} = \eta_{CR}n_{th1} = \int g(p)4\pi p^2 dp$, where η denotes the efficiency of CR injection relative to the thermal Maxwellian in the upstream regime. This equation can be integrated on both sides of the shock front. Convection opposes diffusion ahead of the shock while it is not possible to balance convection against diffusion behind the shock when neglecting loss processes and accounting for particle acceleration through diffusive shock acceleration at the shock front. The only possible solution in this regime is a spatially constant distribution function:

$$f(x,p) = \begin{cases} f_1(p) + [f_2(p) - f_1(p)]\exp\left[-\int_x^0 \frac{v_1\,dx}{D(x,p)}\right], & x < 0 \\ f_2(p), & x > 0 \end{cases}, \tag{4.10}$$

with $f_1(p) = f(-\infty, p)$ and $f_2(p) = f(\infty, p) = f(0, p)$. The distribution function exponentially decreases from the shock front into the upstream regime over a diffusion length D_1/v_1. In particular, the relativistic pressure exponentially decreases into the upstream regime and generates a precursor. The flux of particles at a given momentum must be continuous. The continuity condition is obtained by rewriting the transport equation (4.9), yielding

$$\frac{\partial}{\partial x}\left[D(x,p)\frac{\partial f}{\partial x} + \frac{v}{3}\frac{\partial f}{\partial \ln p}\right] = v\frac{\partial}{\partial x}\frac{\partial(fp^3)}{\partial p^3} + v_1 g(p)\delta_D(x) \quad \rightarrow \quad \left[D(x,p)\frac{\partial f}{\partial x} + \frac{v}{3}\frac{\partial f}{\partial \ln p}\right]_{0_-}^{0_+} = v_1 g(p) \tag{4.11}$$

The continuity condition follows from integrating the transport equation and requiring the continuity of f. Therefore, the quantity in square brackets, which is the flux at a given momentum, must be continuous at the shock front. Joining the solution left- and rightwards of the shock (Eqn. (4.10)) and using the continuity condition of Eqn. (4.11), we obtain a differential equation for the transmitted distribution function $f_2(p)$,

$$\frac{\partial f_2}{\partial \ln p} = \frac{3r}{r-1}[f_1(p) + g(p) - f_2(p)] \quad \rightarrow \quad f_2(p) = \alpha p^{-\alpha}\int_{p_{min}}^p dp'\,[f_1(p') + g(p')]\,p'^{\alpha-1}, \tag{4.12}$$

with the characteristic spectral index $\alpha \equiv 3r/(r-1)$. The distribution function of the accelerated CR population is independent of the functional form of $D(x,p)$ as long as it is positive. The CR power-law is governed only by the kine-

matic structure of the shock front, i.e. the compression ratio r at the shock, and does not depend on the incident kinetic energy flux. However, the transmitted distribution function f_2 depends on the functional form of the initial CR distribution function f_1 in the upstream regime and the injected CR population $g(p)$. As simple example, consider no pre-existing CR distribution and a narrow injection in momentum space, $g(p) = \eta_{CR} n_{th1} \delta_D(p - p_{inj})/(4\pi p_{inj}^2)$. The resulting CR population obeys a power-law in momentum:

$$f_2(p) = \frac{\alpha \, \eta_{CR} n_{th1}}{4\pi p_{inj}^3} \left(\frac{p}{p_{inj}} \right)^{-\alpha} \theta(p - p_{inj}). \tag{4.13}$$

The presented model mimics the necessary requirements for diffusive shock acceleration of energetic particles: the particle's effective velocity component parallel to the shock normal has to be larger than the velocity of the shock wave and its energy has to be large enough to escape the "trapping" process by Alfvén waves being generated in the downstream turbulence (Malkov & Völk 1995, Malkov & Völk 1998). Thus, only particles of the high-energy tail of the Maxwellian are able to return to the upstream shock regime in order to become accelerated. The complicated detailed physical processes of the specific underlying acceleration mechanism are conveniently compressed into a few parameters (Jones & Kang 1993, Berezhko et al. 1994, Kang & Jones 1995), one of which defines the momentum threshold for the particles of the thermal distribution to be accelerated, $p_{inj} = x_{inj} p_{th} = x_{inj} [2 \, k T_2/(m_p c^2)]^{1/2}$. Theoretical studies of shock acceleration at galactic supernova remnants suggest $x_{inj} \sim 3.5$ implying an particle injection efficiency of $\eta_{CR} \sim 10^{-4}$ (Drury et al. 1989, Jones & Kang 1993, Berezhko et al. 1994, Kang & Jones 1995, Malkov & Völk 1995).

4.1.2. Observational properties of galactic cosmic rays

4.1.2.1. Our Galaxy and the interstellar medium

Our Galaxy is a spiral galaxy which is characterized by a disc of stars and gas, mixed with interstellar dust, and embedded into a spheroidal halo of old stars. The age of the system is about 13 billion years and the extent of the disc is about 30 kpc across. The very center hosts a supermassive black hole with a mass of $3.7 \times 10^6 M_\odot$ (Schödel et al. 2002). In the outer parts, the mass of the Galaxy is dominated by dark matter while the innermost part is dominated by baryonic matter. The mass ratio of dark matter to stars to interstellar matter in our Galaxy is about 100:10:1.

The gas in between the stars is composed of hot plasma ($\sim$ 0.3 keV), various stages of cooler gas including molecular clouds, dust, CRs, and magnetic fields (Snowden et al. 1997, Valinia & Marshall 1998, Pietz et al. 1998). All three components, gas, magnetic fields, and CR protons are in equipartition with an energy density of about 1 eV per cm^3, which is similar to the energy density of the CMB, $\varepsilon_{CMB} \simeq 0.1$ eV per cm^3. The average density of neutral hydrogen gas with temperatures of a few 10^3 K is about 1 particle per cm^3 which is distributed in a disc of scale height $\sim$ 100 pc. In contrast, the hotter gas extends further from the symmetry plane, about 2 kpc on either side. From the ratio of radioactive isotopes resulting from spallation to stable isotopes, the transport time of CRs at 1 GeV can be deduced to be 3×10^7 years.

The magnetic field in our Galaxy has a total strength of 6 μG in the solar neighborhood, slightly increasing towards the center. Less than half of the total magnetic field strength is arranged in a regular component showing a circular ring-like pattern. Other spiral galaxies show that the underlying symmetry follows the structure of the spiral arms. On smaller scales, there are occasional field reversals which are still parallel to the circle around the center. Finally, at scales smaller than the scale height of the hot disk, the magnetic field can be described by a Kolmogorov turbulence spectrum (Goldstein et al. 1995). The magnetic field is regenerated at a time scale less or equal to the rotational timescale, with circumstantial evidence suggesting that is happens at a few times 10^7 years. This again coincides with the time scale at which CRs diffuse out of the disc. It is yet unclear which processes drive this galactic system towards equipartition.

4.1.2.2. Energy spectrum of cosmic rays

The solar wind prevents low energetic charged particles from reaching the inner solar system due to interactions with the magnetic field in the solar wind which acts effectively as a mirror. The solar wind is a steady stream of magnetized plasma which the Sun emits into all directions and which is responsible for our being unable to observe directly interstellar energetic particles of energies $\lesssim$ 300 MeV. For protons above 10 GeV – or other nuclei of the
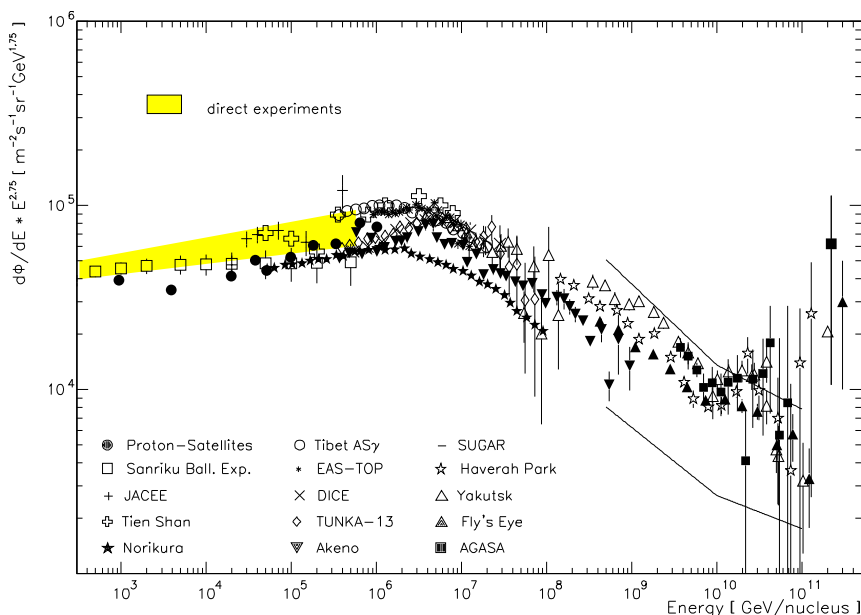
Figure 4.1.: The CR all-particle spectrum observed by different experiments above 10^{11} eV (from Wiebel-Sooth & Biermann 1998). The differential flux was multiplied with $E^{2.75}$ to project out the steeply falling character. The "knee" can be seen at 4×10^{15} eV, the "second knee" at 3×10^{17} eV, and the "ankle" at 5×10^{18} eV.

same energy to charge ratio – the effect of the solar wind becomes negligible. Charged energetic particles gyrate around the magnetic field of our Galaxy with the radius of gyration, called Larmor radius which is proportional to the momentum of the particle perpendicular to the magnetic field direction, $p_\perp$:

$$ r_{\text{L}} \equiv \frac{p_\perp c}{ZeB} \simeq 2 Z^{-1} \left(\frac{E}{10 \,\text{GeV}} \right) \left(\frac{B}{\mu\text{G}} \right)^{-1} \text{AU}, \qquad (4.14) $$

where Z denotes the charge number of the nuclei and B the strength of the magnetic field. This shows that a charged particle of 10 GeV within a μG magnetic field has a Larmor radius which is twice the Earth's orbit around the Sun and proves the negligible effect of the solar wind on these particles. Highly relativistic particles above 3×10^{18} eV per unit Z cannot gyrate in the disk of the Galaxy, their Larmor radius is larger than the thickness of the disk. These particles must originate outside the Galaxy, and indeed at that energy there is evidence for a change both in chemical composition and in the slope of the spectrum.

The energies of directly observable CRs range from a few hundred MeV to 3×10^{20} eV and the integral flux ranges from 0.1 particle per m^2, per s, per steradian, at 1 TeV per unit Z up to 1 particle per km^2, per steradian, and per century around 10^{20} eV, a decrease by a factor of 3×10^{-15} in integral flux. The spectrum corresponds to the differential flux and is defined as the number of particles at a certain energy E within an infinitesimal energy interval dE. The CR spectrum is shown in Fig. 4.1. CRs have a spectrum near $E^{-2.7}$ up to the knee, at about 4×10^{15} eV, and then about $E^{-3.1}$ beyond, up to the ankle, at about 5×10^{18} eV, beyond which the spectrum becomes hard to quantify, but can be described approximately by $E^{-2.7}$ again. There is no other strong feature in the spectrum, especially no signature of a cutoff at the upper end as predicted by Greisen (1966) and Zatsepin & Kuzmin (1966) (see Sect. 4.1.3.3). There is limited evidence from the newest experiments (AGASA and HiRes) for a *second knee* at 3×10^{17} eV, where the spectrum appears to dip. Both the first and the second knee may be at an energy which is proportional to charge, i.e. at a constant Larmor radius, and therefore may imply a range in energies. The fraction of heavy elements seems to continuously increase towards and beyond the knee to the ankle where the composition appears to become light again, i.e. there is a transition to protons and alpha particles. These measurements support the previous considerations. CR electrons have a spectrum which is similar to that of protons below 10 GeV as inferred from radio synchrotron emission. Relative to the CR protons, CR electrons are however suppressed by a factor of 100. The CR electron spectrum steepens to $E^{-3.3}$ above this energy which can be measured directly.

34

4.1.3. Origin of galactic cosmic rays – theories

4.1.3.1. Injection and acceleration

The problem of the CR origin can be naturally subdivided into two complexes, the injection and the successive acceleration of CRs. There are three different theories explaining the injection of the CR abundances which need to describe both their spatial distribution and the observed peculiar abundances of CRs compared to those of the interstellar medium: Hydrogen and Helium are less abundant in CRs than in the interstellar medium. The abundances of the elements Lithium, Beryllium, and Boron very much larger in CRs compared to the interstellar medium, by several orders of magnitudes. The abundances of the CR sub-Iron elements are also larger than in the interstellar medium relative to Iron as are the abundances of odd-Z elements. The theories for the CR injection are outlined in the following: (i) low mass stars accelerate selectively elements in their coronal activity to supra-thermal energies that are injected into the interstellar medium (Shapiro 1999). (ii) Using the observed similarity of the chemical abundances of dust and CRs, Meyer et al. (1997) and Ramaty et al. (1997) suggest the injection of CRs by ionized dust particles such that the selection effects and the sites of dust formation govern the final CR distribution. (iii) The third model hypothesizes CR injection from stellar winds of heavy stars by analogy with the solar wind and explains selection effects by more efficient injection of doubly-ionized elements.

The idea of using supernova shock waves to accelerate CRs has been proposed long ago by Baade & Zwicky (1934). The standard theory suggests that CR particles were accelerated through diffusive shock acceleration in supernova shock waves which sweep up the powerful magnetized stellar winds of the predecessor stars until they run into the ambient interstellar medium. This theory is able to explain the acceleration of particles up to energies at the ankle at about 3×10^{18} eV. The knee is explained as being due to a decrease of the acceleration efficiency once the Larmor radius of the accelerated particles matches the spatial extent of the shocked shell expanding into the stellar wind. CRs at these energies cannot be sufficiently isotropized and confined in the downstream regime of the shock which leads to an increase of their escape probability into the interstellar medium. The spatial constraint of this acceleration process predicts a maximum energy per charge, or rigidity, which naturally explains the observed transition towards heavier CR element composition at energies beyond the knee. Highly energetic electrons have been directly observed in supernova shocks through their synchrotron and inverse Compton emission up to TeV γ-rays (Aharonian et al. 2004). Although CR protons are by a factor of about 100 more abundant than electrons at 1 GeV, the theory of CR proton acceleration has not been proven directly through observations and has to draw an analogy to the electron acceleration.

4.1.3.2. Transport in the Galaxy

Galactic CRs are injected from their sources with a certain spectrum. In the interstellar medium, these energetic particles are diffusively transported within turbulent magnetic fields with a Kolmogorov-type spectrum on small scales, interacting constantly with matter, magnetic fields and photon fields. On their way to the observer, they have a certain escape probability from the hot galactic disk which increases with momentum. As a consequence their spectrum steepens in an equilibrium situation by $E^{-1/3}$, compared to the injected spectrum. Along this line of argumentation, one deduces from the observed CR spectrum of $E^{-2.7}$ the injection spectrum of $E^{-2.3}$ without taking re-acceleration into account. Synchrotron and inverse Compton losses are the dominant loss processes of the CR electron spectrum above 10 GeV which leads to a steepening by unity. The observed electron spectrum at these energies of $E^{-3.3}$ implies again an injection spectrum of $E^{-2.3}$, thus providing an important consistency check. Radio observations in various locations of our Galaxy and other galaxies show consistency with the expectation that the average spectrum in the energy range above GeV is universal. During their travel inside the Galaxy, the CR protons interact hadronically with the ambient interstellar medium and produce mainly neutral and charged pions. The neutral pions successively decay into γ-rays while the charged pions decay into secondary electrons and neutrinos. Future observations of this γ-ray emission will certainly provide clean signatures on this aspect of CRs.

4.1.3.3. Cosmic rays above the ankle of the spectrum

After the discovery of the CMB, it was realized by Greisen (1966) and Zatsepin & Kuzmin (1966) that a CR proton above the energy of 5×10^{19} eV should suffer strong losses from its interaction with the CMB: in such an interaction, the CMB photon has an energy above the pion's rest mass as seen from the reference frame of the a relativistic proton which leads to the production of a pion. This collision leads to an energy loss of the CR proton of 20% about every

~ 6 Mpc in the observer's frame. Assuming a cosmological distribution of sources for protons at extreme energies, the observed CR spectrum at the Earth is predicted to show a sharp cutoff at 5×10^{19} eV, the GZK-cutoff. On the basis of the limited event statistics, the cutoff is not observed leading to many speculations about the nature and the origin of particles beyond the GZK-energy.

Cosmic rays between the ankle and the expected GZK-cutoff are readily explained by many possible sources, mostly of extragalactic origin. The only exception are galactic pulsars, especially those with very high magnetic fields, called magnetars, which are thought to accelerate charged particles to energies of 10^{21} eV. While this scenario would naturally circumvent the GZK-cutoff, it shows severe problems when accounting for adiabatic losses of the particles' transport from close to the pulsar out to the interstellar medium and it predicts a highly anisotropic distribution on the sky given the strength of the galactic magnetic field. Another scenario are γ-ray bursts at cosmological distances which are able to produce these energetic particles in their relativistic outflows (see Waxman 2000, for a review). Yet another theory proposes the acceleration of highly energetic particles through diffusive shock acceleration at structure formation shock waves which propagate through the cosmic tenuous plasma (Kang et al. 1996). These shock waves dissipate gravitational energy associated with hierarchical clustering into thermal energy of the inter-galactic medium and have scales of many tens of Mpc, and shock velocities of ~ 1000 km/s. However, the maximum energies of the accelerated CRs can hardly reach the energy of the GZK cutoff making a strong contribution to the overall flux unlikely. The most conventional explanation are radio galaxies which drive powerful relativistic outflows that interact strongly with the intergalactic medium in so-called *hot spots*. These hot spots are giant shock waves with sizes up to a few tens of kpc. Integrating over all known radio galaxies explains flux, spectrum as well as the chemical composition of CRs in this energy range (Hillas 1984, Biermann & Strittmatter 1987, Rachen et al. 1993).

4.2. Non-thermal emission processes

The continuum emission processes of non-thermal particle populations extend over wide ranges of the electromagnetic spectrum, from the radio to the high-energy γ-ray region. Overall, the continuum spectrum shows a complex shape, but it can be approximated by a simple power-law form over wide wavelength intervals. In the inter-galactic medium, CRs are only observable through their non-thermal emission processes because the energetically dominant CR component below 10^{16} eV is trapped by cluster magnetic fields. This fact emphasizes the importance of these radiative processes within extra-galactic cosmic ray physics. The discussion of emission processes will be brief in this section, and the emphasis lies on presenting underlying concepts and summarizing important results rather than extensive derivations (for excellent books on this topics, see Jackson 1975, Rybicki & Lightman 1979).

4.2.1. Synchrotron radiation

The motion of a charged particle in a magnetic field $\boldsymbol{B}$ is described in classical electro-dynamics by the Lorentz force

$$\frac{\mathrm{d}}{\mathrm{d}t}(\gamma m \boldsymbol{v}) = \frac{Ze}{c}(\boldsymbol{v} \times \boldsymbol{B}). \tag{4.15}$$

The acceleration $\mathrm{d}\boldsymbol{v}/(\mathrm{d}t)$ is normal to the velocity implying a constant magnitude v of the velocity and thus a constant Lorentz factor γ. Because there is no force acting on the charged particle in the direction of the magnetic field $\boldsymbol{B}$, the component of the velocity parallel to it, $\boldsymbol{v}_{\parallel}$, is constant. It follows that the velocity component normal to the magnetic field $v_{\perp} = (v^2 - v_{\parallel}^2)^{1/2}$ is also constant. Thus, the particle moves in a helix with its axis parallel to the magnetic field. The frequency of the projected orbit on a plane normal to $\boldsymbol{B}$ is called *gyration frequency*:

$$\nu_{\mathrm{g}} = \frac{ZeB}{2\pi\gamma mc}. \tag{4.16}$$

In the following, we only consider electrons because the synchrotron radiation of protons is suppressed by m_{e}^2/m^2. A non-relativistic electron ($\gamma \simeq 1$) emits *cyclotron radiation* at the frequency $\nu_{\mathrm{g}} = eB/(2\pi m_{\mathrm{e}}c)$ in a dipolar spatial pattern with the symmetry axis perpendicular to the acceleration direction. As we increase the electron's velocity in a thought experiment, the higher harmonics of ν_{g} start to contribute to the electron spectrum with a strength that depends on $\beta = v/c$. At relativistic velocities, as γ increases, the gyration frequency decreases according to $\nu_{\mathrm{g}} \propto \gamma^{-1}$. Because of beaming effects of relativistic particles, the emitted radiation is concentrated in the forward direction

into a narrow cone of half-angle γ^{-1} with respect to the electron's momentum. As the electron gyrates around the magnetic field, an observer whose line-of-sight intersects the radiation cone sees a sequence of pulses with a period equal to the Doppler shifted gyration frequency $\nu'_g = \nu_g/(1 - \beta \cos^2 \theta) \simeq \nu_g/\sin^2 \theta$, where θ denotes the pitch angle between the particle's momentum and the magnetic field. The width of the pulse is given by the time taken by the cone to cross the observer's line-of-sight, $\Delta t = 1/(2\pi\gamma^3 \nu_g \sin \theta)$, assuming highly relativistic particles. The observed frequency spectrum consists of a series of peaks at ν'_g and its higher harmonics, with a cutoff at $\sim 1/(2\pi\Delta t)$. For highly relativistic electrons, the harmonics are closely spaced, and in addition, they are broadened when considering an ensemble of CR electrons owing to the distribution of γ and an isotropic pitch angle distribution. The resulting spectrum appears to be continuous and has a maximum at the *critical frequency*

$$\nu_c = \frac{3eB\sin\theta}{4\pi m_e c}\left(\frac{E}{m_e c^2}\right)^2 = 1.6 \times \left(\frac{B_\perp}{1\,\mu\mathrm{G}}\right)\left(\frac{E}{10\,\mathrm{GeV}}\right)^2 \mathrm{GHz}. \tag{4.17}$$

The emitted power, i.e. the energy emitted per unit time and per unit frequency interval as a function of frequency can be obtained from the Fourier transform of the electric field of synchrotron pulses, yielding

$$P_{\mathrm{sync}}(E, \nu) = \frac{\sqrt{3}e^3 B\sin\theta}{m_e c^2} F\left(\frac{\nu}{\nu_c}\right), \quad \text{with} \quad F(x) = x\int_x^\infty K_{5/3}(\xi)\mathrm{d}\xi, \tag{4.18}$$

where $K_{5/3}(\xi)$ is the modified Bessel function of order 5/3. The total power emitted at all frequencies is obtained by integrating $P_{\mathrm{sync}}(E, \nu)$ over ν and over an isotropic distribution function of the pitch angle, $f(\theta)\,\mathrm{d}\theta = \mathrm{d}\Omega(\theta)/(4\pi) = \sin\theta\,\mathrm{d}\theta/2$:

$$P_{\mathrm{sync}} = \frac{4}{3}\sigma_T c\beta^2\gamma^2\varepsilon_B. \tag{4.19}$$

Consider an ensemble of CR electrons with energy in the range (E_1, E_2) and assuming their number density to be distributed according to a power-law as motivated by diffusive shock acceleration:

$$n(E)\mathrm{d}E = CE^{-\alpha_e}\mathrm{d}E. \tag{4.20}$$

The power emitted by electrons as a function of frequency of the emitted radiation peaks at the critical frequency given by Eqn. (4.17) and reads

$$P_{\mathrm{sync}}(\nu) = \int_{E_1}^{E_2} P(E, \nu)n(E)\mathrm{d}E = \frac{\sqrt{3}e^3}{2m_e c^2}\left(\frac{3e}{4\pi m_e^3 c^5}\right)^{\alpha_\nu} C(B\sin\theta)^{\alpha_\nu+1}\nu^{-\alpha_\nu} G\left(\frac{\nu}{\nu_1}, \frac{\nu}{\nu_2}, p\right), \tag{4.21}$$

where $\alpha_\nu = (\alpha_e - 1)/2$, ν_1 and ν_2 are the critical frequencies corresponding to the energies E_1 and E_2, respectively. In general, the function $G(x_1, x_2, p)$ depends on frequency while this dependency can be relaxed in the case of $\nu_1 \ll \nu \ll \nu_2$:

$$G(x_1, x_2, p) = \int_{x_2}^{x_1} x^{(\alpha_e-3)/2}F(x)\mathrm{d}x \quad \rightarrow \quad G(0, \infty, p) = \frac{2^{(\alpha_e-3)/2}}{3}\left(\frac{3\alpha_e+7}{\alpha_e+1}\right)\Gamma\left(\frac{3\alpha_e-1}{12}\right)\Gamma\left(\frac{3\alpha_e+7}{12}\right), \tag{4.22}$$

where $F(x)$ is defined by Eqn. (4.18) and Γ is the usual gamma function. Thus, in this case the emitted spectrum has a very simple power-law form, $P_{\mathrm{sync}}(\nu) \propto \nu^{-\alpha_\nu}$, while the energy spectrum has to depart from this pure power-law behavior at the endpoints.

For an isotropic distribution of particles and orientations of magnetic fields, the averaged emitted power into all spatial directions is obtained by integration, using the isotropic distribution function of the pitch angle:

$$\frac{1}{\sqrt{\pi}}\int_0^\pi (\sin\theta)^k \sin\theta\mathrm{d}\theta = \Gamma\left(\frac{k+2}{2}\right)\Gamma\left(\frac{k+3}{2}\right)^{-1}. \tag{4.23}$$

This results in a replacement of the factor $(\sin\theta)^{\alpha_\nu+1}$ in Eqn. (4.21) by

$$\frac{\sqrt{\pi}}{2}\Gamma\left(\frac{\alpha_e+5}{4}\right)\Gamma\left(\frac{\alpha_e+7}{4}\right)^{-1}. \tag{4.24}$$

4.2.2. Inverse Compton emission

The interaction of an electron with electromagnetic radiation can be seen as the scattering of photons by electrons where energy and momentum are exchanged between the interacting particles. An electron at rest that scatters a photon gains energy in this process by acquiring the recoil velocity to satisfy momentum conservation. Accordingly, the photon loses this energy as its wavelength is increased, giving rise to the *Compton effect*. Using the conservation of relativistic four-momentum, one obtains

$$E_1 = \frac{E}{1 + \frac{E}{m_e c^2}(1 - \cos\theta)}, \tag{4.25}$$

where E and E_1 indicate the energies of the incident and the scattered photon respectively, and θ is the angle between the incident and the scattered directions. The differential cross-section for Compton scattering of unpolarized radiation, obtained by using quantum electrodynamics, is given by the Klein-Nishina formula

$$\frac{d\sigma_{KN}}{d\Omega} = \frac{r_0^2}{2}\left(\frac{E_1}{E}\right)^2\left(\frac{E}{E_1} + \frac{E_1}{E} - \sin^2\theta\right), \tag{4.26}$$

where $r_0 = e^2/(m_e c^2)$ denotes the classical electron radius. When the scattering electron is already moving, energy can pass either from the electron to the photon or vice versa, depending upon the kinematical details of the collision. The process is called *inverse Compton scattering* when a photons gains energy. Generally, the expression for the change in photon energy is very complex (Felten & Morrison 1966) while useful approximations can be obtained considering Lorentz transformations.

Consider a Compton collision between a photon of energy E and an electron with a Lorentz factor γ in the observer's frame Σ. We perform now a Lorentz transformation into the electron's rest frame Σ'. Energy transforms as the time component of the energy-momentum four-vector, so that the photon energy E' in the frame Σ' before scattering is given by $E' = \gamma E(1 - \beta\cos\theta)$, where θ is the angle between the incident electron and the photon direction in the observer's frame Σ. Thus, in the electron's rest frame Σ', the photon scatters with an energy $E' \simeq \gamma E$ for all but very small angles. If the photon has negligible energy in Σ', i.e. $E' \ll m_e c^2$, the interaction can be treated in the *Thompson limit* which is characterized by elastic scattering of the photon: $E_1' \simeq E'$. After transforming back into the observer's frame, using $E_1 = \gamma E_1'(1 + \beta\cos\theta_1')$, the energy of the scattered photon in Σ is given by $E_1 \simeq \gamma^2 E$. The energy of the inverse Compton scattered photon is therefore increased by a factor γ^2, which can be very large for highly relativistic electrons. However, this approximation is only valid if the fraction of energy lost by the electron in a single collision $\gamma^2 E/(\gamma m_e c^2) \ll 1$.

The emitted power of Compton scattering generated by a single electron in an optically thin medium, such that photons undergo a single scattering event before they are escaping from the source, is given by

$$P_{Comp} = \frac{4}{3}\sigma_T c\beta^2\gamma^2\varepsilon_{ph}. \tag{4.27}$$

The total number of incident photons per unit time is $c\sigma_T n_{ph}$, where $n_{ph} = \varepsilon_{ph}/\langle E\rangle$ and $\langle E\rangle$ is the average incident photon energy. The average energy of the scattered photons for $\beta \simeq 1$ is therefore $\langle E_1\rangle = 4/3 \cdot \gamma^2 E$. One realizes the similarity of the synchrotron power in Eqn. (4.19) to the power of Compton scattering in Eqn. (4.27): $P_{Comp}/P_{sync} = \varepsilon_{ph}/\varepsilon_B$. This is due to the symmetry of electromagnetism such that synchrotron emission can be considered to represent the scattering by an electron off virtual photons of the magnetic field. Thus, in the presence of radiation and magnetic fields, electrons can loose their energy either through synchrotron emission or through inverse Compton scattering of the ambient electromagnetic radiation.

When a photon of energy E is scattered by an electron with Lorentz factor γ, the energy of the emitted photon depends on the incident and scattering angles through the differential Klein-Nishina cross-section which yield the scattering probability in a specific direction. Consider the scattering of photons with energy in the range $(E, E + dE)$ by an electron with energy $\gamma m_e c^2$. Assuming $\gamma E \ll m_e c^2$ and isotropic incident radiation, the number of photons of energy E_1 produced per unit energy interval in E_1 and per unit time is given by

$$\frac{dN(E_1, E, \gamma)\,dE}{dt\,dE_1} = \frac{3\sigma_T c}{4\gamma^2 E} f\left(\frac{E_1}{4E\gamma^2}\right)n(E)dE \quad \text{where} \quad f(x) = 2x\ln x + x + 1 - 2x^2, \tag{4.28}$$

and $n(E)$ is the number density of photons. $f(x)$ decreases monotonically from $f(0) = 1$ to $f(1) = 0$, with $x = 1$ corresponding to the maximum photon energy produced in the scattering. The Compton spectrum of the entire electromagnetic field can be obtained by integrating the above expression for scattering from one single electron over the electron energy distribution. Using the power-law distribution of Eqn. (4.20), the integration extends over the range from

$$\gamma_{\min} = \max\left[\frac{1}{2}\left(\frac{E_1}{E}\right)^{1/2}, \gamma_1\right] \quad \text{to} \quad \gamma_{\max} = \min\left[\gamma_2, \frac{1}{2}\left(\frac{E_1}{E}\right)^{1/2}\right], \tag{4.29}$$

where $\gamma_1 = E_1/(m_e c^2)$ and $\gamma_2 = E_2/(m_e c^2)$ are the cutoffs of the electron distribution. Assuming $\gamma_1 \ll \frac{1}{2}(E_1/E)^{1/2} \ll \gamma_2$, the energy spectrum of scattered photons is given by

$$P_{\text{Comp}}(E_1) = \frac{3\sigma_T c C}{8}\left[\frac{2^{\alpha_e+3}(\alpha_e^2 + 4\alpha_e + 11)}{(\alpha_e + 3)^2(\alpha_e + 1)(\alpha_e + 5)}\right] E_1^{-\alpha_\nu} \int_0^\infty E^{(\alpha_e-1)/2} n(E)\mathrm{d}E, \tag{4.30}$$

which is a power-law with the same spectral index compared to the synchrotron case, $\alpha_\nu = (\alpha_e - 1)/2$, because in both cases the produced energy of the photon is proportional to γ^2. If the incident photon spectrum is a black body distribution, then

$$\int E^{(\alpha_e-1)/2} n(E)\mathrm{d}E = \frac{(kT)^{(\alpha_e+5)/2}}{\pi^2(\hbar c)^3}\Gamma\left(\frac{\alpha_e + 5}{2}\right)\zeta\left(\frac{\alpha_e + 5}{2}\right) \tag{4.31}$$

where Γ and ζ are the gamma function and the Riemann ζ function, respectively.

4.3. Inelastic cosmic ray collisions

As previously mentioned, CR protons interact hadronically with the ambient plasma and produce mainly neutral and charged pions. The neutral pions successively decay into γ-rays while the charged pions decay into secondary electrons, positrons, and neutrinos:

$$
\begin{aligned}
\pi^\pm &\rightarrow \mu^\pm + \nu_\mu/\bar{\nu}_\mu \rightarrow e^\pm + \nu_e/\bar{\nu}_e + \nu_\mu + \bar{\nu}_\mu, \\
\pi^0 &\rightarrow 2\gamma.
\end{aligned}
$$

Synchrotron and inverse Compton emission of secondary CR electrons provide a biased tracer of the underlying CR proton population due to the presence of possibly different CR electron populations and the degeneracy of the synchrotron emissivity with the magnetic energy density. In contrast, the γ-ray emission of the π^0-decay provides a cleaner signature of the underlying CR proton population. After deriving kinematical details of the π^0-decay, the pion production spectra resulting from the hadronic CR proton reaction with thermal protons are developed while critically reviewing and comparing reaction models in the literature. Thus, this section shall serve as an introduction to the next chapter where we develop the theoretical framework for hadronic CR proton reactions.

4.3.1. Relativistic kinematics

4.3.1.1. Threshold energy

Consider the inelastic CRp-p collision leading to the creation of a pion in the laboratory system, $p + p \rightarrow p + p + \pi$. To produce a new pion in this reaction, the minimum energy of the incoming protons has to be just enough in the center-of-momentum system (CMS[1]) to produce the rest mass of all outgoing particles. From the invariance of the four-momentum exactly at the threshold of pion production, we obtain

$$
\begin{aligned}
2\gamma_p' m_p &= 2m_p + m_\pi, \tag{4.32} \\
\beta_p' \gamma_p' m_p - \beta_p' \gamma_p' m_p &= 0. \tag{4.33}
\end{aligned}
$$

The threshold CMS energy of each of the protons is $\gamma_p' m_p c^2 = m_p c^2[1 + m_\pi/(2m_p)]$. We perform a Lorentz transformation such that one proton rests in the laboratory frame, $\gamma_p' = \gamma_{\text{LT}}$,

$$\begin{pmatrix} \gamma_p \\ \beta_p\gamma_p \end{pmatrix} = \begin{pmatrix} \gamma_p' & \pm\beta_p'\gamma_p' \\ \pm\beta_p'\gamma_p' & \gamma_p' \end{pmatrix}\begin{pmatrix} \gamma_p' \\ \beta_p'\gamma_p' \end{pmatrix} = \begin{pmatrix} \gamma_p'^2 \pm \beta_p'^2\gamma_p'^2 \\ \pm\beta_p'\gamma_p'^2 + \beta_p'\gamma_p'^2 \end{pmatrix}. \tag{4.34}$$

---

[1]In this section, CMS quantities are denoted with a prime.

Here, the '+' sign accounts for the relativistic proton and the '−' sign for the resting proton in the laboratory frame. Thus, the threshold Lorentz factor of the relativistic proton for pion production is given by $\gamma_{\text{th}} = \gamma_{\text{p}}'^2(1 + \beta_{\text{p}}'^2) = 2\gamma_{\text{p}}'^2 - 1 = 2[1 + m_\pi/(2m_{\text{p}})]^2 - 1 = 1.22 \, \text{GeV}/(m_{\text{p}}c^2)$.

4.3.1.2. Relativistic decay kinematics

Consider the decay of a massive particle of mass M into two daughter particles of masses m_{a} and m_{b} in the CMS. Employing the conservation of the total CMS energy $E' = E_{\text{a}}' + E_{\text{b}}'$ and momentum conservation, $p_{\text{a}}' = -p_{\text{b}}'$, we can express the energy of one daughter particle solely by the masses of the involved particles:

$$E_{\text{a,b}}' = \frac{M^2 + m_{\text{a,b}}^2 - m_{\text{b,a}}^2}{2M} c^2. \tag{4.35}$$

We perform now a Lorentz transformation to the laboratory system where the original mass M had an energy $E_M = \gamma M c^2$, transforming only the projection of p' onto the boost axis,

$$\begin{pmatrix} E_{\text{a,b}} \\ p_{\text{a,b}} c \end{pmatrix} = \begin{pmatrix} \gamma & \beta\gamma \\ \beta\gamma & \gamma \end{pmatrix} \begin{pmatrix} E_{\text{a,b}}' \\ p'c \cos\theta' \end{pmatrix}. \tag{4.36}$$

Using the equality $\beta^2 = (\gamma^2 - 1)/\gamma^2 = (E^2 - M^2 c^4)/E^2$, we arrive at the energy of the decaying particle in the laboratory frame,

$$E_{\text{a,b}} = \frac{E_M}{M} \left[\frac{M^2 + m_{\text{a,b}}^2 - m_{\text{b,a}}^2}{2M} + \sqrt{1 - \frac{M^2 c^4}{E_M^2}} \, p'(M, m_{\text{a}}, m_{\text{b}})c^{-1} \cos\theta' \right], \tag{4.37}$$

where $p'(M, m_{\text{a}}, m_{\text{b}})$ is implicitly given by energy conservation, $(p'^2 c^{-2} + m_{\text{a}}^2)^{1/2} + (p'^2 c^{-2} + m_{\text{b}}^2)^{1/2} = M$. If M decays isotropically, i.e. the emission probability is equally distributed in the CMS frame, the normalized angular distribution function reads $f(\theta')d\theta' = d\Omega(\theta')/(4\pi) = \frac{1}{2}\sin\theta' d\theta'$. Substituting the dimensionless ratio of the CMS energy of the daughter particle to the mass of the parent particle, $\eta \equiv (M^2 + m_{\text{a,b}}^2 - m_{\text{b,a}}^2)/(2M^2)$, and $\kappa \equiv p'/(Mc)$, we obtain the following form of Eqn. (4.37),

$$E(\theta') = E_M(\eta + \beta\kappa \cos\theta'). \tag{4.38}$$

The infinitesimal amount of energy emitted into the azimuthal angle θ' is given by $dE(\theta') = -\beta E_M \kappa \sin\theta' d\theta'$. Thus, the energy distribution of the produced particle is a constant function ranging from $E_{\text{min}} = (\eta - \beta\kappa)E_M$ to $E_{\text{max}} = (\eta + \beta\kappa)E_M$:

$$f(E)dE = f(\theta') \left| \frac{d\theta'}{dE} \right| dE = \frac{1}{2\beta\kappa E_M} dE. \tag{4.39}$$

4.3.2. Pion decay induced γ-ray emission

Equation (4.37) simplifies significantly when both decay particles have zero mass ($\pi^0 \to 2\gamma$):

$$E_\gamma(\theta') = \frac{1}{2}\gamma_\pi m_\pi c^2(1 + \beta_\pi \cos\theta'). \tag{4.40}$$

This equation limits the γ-ray energy, because $-1 \leq \cos\theta' \leq 1$. In particular, for ultra-relativistic pions, i.e. $m_\pi^2 c^4/E_\pi^2 \ll 1$, we obtain $E_\gamma(\theta') = E_\pi \cos^2(\theta'/2)$. The γ-ray energy distribution can be derived using Eqn. (4.39) to obtain the Green's function for the π^0-decay,

$$f(E_\gamma|E_\pi) = \begin{cases} \dfrac{1}{\sqrt{E_\pi^2 - m_\pi^2 c^4}}, & \text{for } \frac{1}{2}E_\pi(1 - \beta_\pi) \leq E_\gamma \leq \frac{1}{2}E_\pi(1 + \beta_\pi), \\ 0, & \text{otherwise.} \end{cases} \tag{4.41}$$

Given the pion source function, the γ-ray source spectrum is given by

$$q_\gamma(\boldsymbol{r}, E_\gamma) = \int_{E_{\pi,\text{min}}}^{E_{\pi,\text{max}}} dE_\pi \frac{q_\pi(\boldsymbol{r}, E_\pi)}{\sqrt{E_\pi^2 - m_\pi^2 c^4}} \xi_{\pi^0 \to 2\gamma} R_{\pi^0 \to 2\gamma}, \tag{4.42}$$

where $R_{\pi^0 \to 2\gamma} \simeq 1$ denotes the branching ratio and $\xi_{\pi^0 \to 2\gamma} = 2$ the multiplicity of the pion decay induced γ-ray emission. The integration limits $E_{\pi,\mathrm{min}}$ and $E_{\pi,\mathrm{max}}$ can be found from the following considerations: $E_{\pi,\mathrm{max}}$ is the maximum pion energy that is able to produce a γ-ray of energy E_γ,

$$E_{\pi,\mathrm{max}} = \frac{E_\gamma}{\left[\cos^2(\theta'/2)\right]_{\mathrm{min}}} \to \infty, \quad \text{since } \left[\cos^2(\theta'/2)\right]_{\mathrm{min}} = 0 \tag{4.43}$$

From conservation of energy, we note that $E_\pi = E_{\gamma,\mathrm{a}} + E_{\gamma,\mathrm{b}}$. In the extreme case where the γ-rays are emitted in the direction of motion,

$$E_{\gamma,\mathrm{min}} = \frac{1}{2}E_\pi(1 - \beta_\pi), \quad \text{and} \quad E_{\gamma,\mathrm{max}} = \frac{1}{2}E_\pi(1 + \beta_\pi). \tag{4.44}$$

Using this equation and rewriting the invariant square of the pion's rest mass, we can express $E_{\gamma,\mathrm{min}}$ in terms of $E_{\gamma,\mathrm{max}}$:

$$(E_{\gamma,\mathrm{min}})(E_{\gamma,\mathrm{max}}) = \frac{1}{4}E_\pi^2(1 - \beta_\pi^2) = \frac{1}{4}m_\pi^2 c^4 \quad \to \quad E_\pi = E_{\gamma,\mathrm{min}} + E_{\gamma,\mathrm{max}} = E_{\gamma,\mathrm{max}} + \frac{m_\pi^2 c^4}{4E_{\gamma,\mathrm{max}}}. \tag{4.45}$$

This criterion can be reversed to put a lower limit on the pion energy integration. Thus, assuming the decay products are distributed isotropically in their rest frame, the π^0-decay induced omnidirectional (i.e. integrated over 4π solid angle) differential γ-ray source function is given by

$$q_\gamma(\boldsymbol{r}, E_\gamma) = 2 \int_{E_\gamma + \frac{m_\pi^2 c^4}{4E_\gamma}}^{\infty} \mathrm{d}E_\pi \frac{q_\pi(\boldsymbol{r}, E_\pi)}{\sqrt{E_\pi^2 - m_\pi^2 c^4}}. \tag{4.46}$$

4.3.3. Pion source function

There are two analytical models in the literature that describe the hadronic CR proton reaction with protons of the ambient thermal plasma while assuming isospin symmetry, $\xi_{\pi^0} = \xi_{\pi^\pm}/2$. Fermi (1950) proposed the *fireball model* which assumes a state of hot quark-gluon plasma in thermal equilibrium after the hadronic interaction that subsequently ablates pions with energy dependent multiplicities. This model is only valid in the high-energy limit for CR protons ($E_\mathrm{p} \gg m_\mathrm{p}c^2$) and produces γ-rays with a power-law distribution that is characterized by the spectral index $\alpha_\gamma = \frac{4}{3}(\alpha_\mathrm{p} - \frac{1}{2})$, as we will see later on in Chapter 5.

In order to make detailed predictions for the π^0-decay induced γ-ray spectrum, more realistic effects near the π^0-production threshold have to be included following *Dermer's model*. At low proton energies, it assumes the CRp-p interaction to be mediated by the excitation of the $\Delta_{3/2}$-resonance which subsequently decays into two protons and a π^0-meson (Stecker 1970). The production spectrum of secondary π^0-mesons is given by a convolution of the normalized $\Delta_{3/2}$-isobar mass spectrum represented by a Breit-Wigner distribution with the energy distribution function. The scaling model used at high energies (Stephens & Badhwar 1981) uses Lorentz invariant cross sections for charged and neutral pion production in p-p interactions inferred from accelerator data. The spectral index of the resulting γ-ray power-law emission resembles that of the parent CR proton population, $\alpha_\gamma = \alpha_\mathrm{p}$, and shows a different asymptotic behavior compared to the simpler fireball model. This has important implications for predictions of future TeV γ-ray observations using Čerenkov telescopes.

The pion production spectrum can be derived from general considerations including branching ratios and multiplicities of the hadronic reaction (Stecker 1971). The pion production spectrum describes the produced number of pions per unit time, volume and energy intervals, $\mathrm{d}N/(\mathrm{d}t\,\mathrm{d}V\,\mathrm{d}E_\pi\,\mathrm{d}E_\mathrm{p})$, and reads in this context

$$q_\pi(E_\pi, E_\mathrm{p}) = c n_\mathrm{N} \xi(E_\mathrm{p}) \sigma_{\mathrm{pp}}^\pi(E_\mathrm{p}) \delta_\mathrm{D}(E_\pi - \langle E_\pi \rangle) \theta(E_\mathrm{p} - E_{\mathrm{th}}), \tag{4.47}$$

where n_N is the target nucleon density in the plasma, σ_{pp}^π the inelastic p-p cross section, $\langle E_\pi \rangle$ the average energy of a single produced pion, and $E_{\mathrm{th}} = 1.22\,\mathrm{GeV}$ denotes the threshold energy for pion production. For a differential CR proton distribution, the pion source function can be marginalized over the proton energy, yielding

$$q_{\pi^\pm}(E_\pi) = \frac{2}{3}q_\pi(E_\pi) = \frac{2}{3} \int_{-\infty}^{\infty} \mathrm{d}E_\mathrm{p} f_\mathrm{p}^{(1)}(E_\mathrm{p}) q_\pi(E_\pi, E_\mathrm{p}). \tag{4.48}$$

Note, that we use an effective one-dimensional CR distribution function $f^{(1)}(p) \equiv 4\pi p^2 f^{(3)}(p)$ which can often be described by a power-law in momentum that is motivated by diffusive shock acceleration:

$$f_p^{(1)}(E_p) = \frac{\tilde{n}_{CR}}{GeV}\left(\frac{pc}{GeV}\right)^{-\alpha_p} \simeq \frac{\tilde{n}_{CR}}{GeV}\left(\frac{E_p}{GeV}\right)^{-\alpha_p}, \tag{4.49}$$

where the last step is strictly only valid in the high energy limit for CR protons ($E_p \gg m_p c^2$).

Fireball model   Following the representation by Mannheim & Schlickeiser (1994), pions are emitted from the thermal fireball in the CMS with multiplicities

$$\xi = \xi_{\pi^0} + \xi_{\pi^\pm} = 3\left(\frac{E_p - E_{th}}{GeV}\right)^{1/4} \simeq 3\left(\frac{T_p}{GeV}\right)^{1/4}, \tag{4.50}$$

where the kinetic CR proton energy is denoted by $T_p = (p^2c^2 + m_p^2c^4)^{1/2} - m_pc^2 \propto pc$, using the ultra-relativistic approximation. It is well known that Eqn. (4.50) overestimates the number of pions at energies above 10^4 GeV. Below that energy, the energy dependence of the mean pion energy is given by

$$\langle E_\pi \rangle(E_p) = K_p\frac{E_p - m_pc^2}{\xi} \simeq \frac{1}{6}\left(\frac{T_p}{GeV}\right)^{3/4} GeV, \tag{4.51}$$

since the limiting value of the inelasticity K_p is roughly 1/2. Performing the integral of Eqn. (4.48) while approximating $E_p \simeq T_p$ when applying above's definitions, the pion source function in the fireball model reads

$$q_{\pi^\pm}(E_\pi) = 2q_{\pi^0}(E_\pi) \simeq 16cn_N\tilde{n}_{CR}\bar{\sigma}_{pp}^\pi GeV^{-1}\left(\frac{6E_\pi}{GeV}\right)^{-\frac{4}{3}(\alpha_p - \frac{1}{2})}. \tag{4.52}$$

The error introduced by assuming a constant cross section for the inelastic pion production, $\bar{\sigma}_{pp}^\pi = 32$ mbarn, grows logarithmically with pion energy.

Dermer's model   In contrast to the fireball model, the scaling behavior in the high-energy limit of Dermer's model can be described by a constant pion multiplicity $\xi(E_p) \simeq \xi = 2$. This reflects the fact that two leading pion jets are leaving the interaction site in direction of the incident protons diametrically and carrying the high longitudinal momenta owing to Lorentz contraction of the interacting nuclei in the center of mass system and Heisenberg's uncertainty relation (Nachtmann 1990). Thus, the energy dependence of the mean pion energy is given by

$$\langle E_\pi \rangle(E_p) \simeq K_p\frac{T_p}{\xi} \simeq \frac{T_p}{2\xi}. \tag{4.53}$$

Applying these definitions to Eqn. (4.48), the pion source function in Dermer's model evaluates to

$$q_{\pi^\pm}(E_\pi) = 2q_{\pi^0}(E_\pi) = \frac{4}{3}\xi^{2-\alpha_p}cn_N\tilde{n}_{CR}\sigma_{pp}^\pi(\alpha_p)GeV^{-1}\left(\frac{2E_\pi}{GeV}\right)^{-\alpha_p}. \tag{4.54}$$

The weak energy dependences of the pion multiplicity and the inelastic cross section can be absorbed in a semi-analytical parameterization of the cross section, $\sigma_{pp}^\pi(\alpha_p)$ (for details, see Chapter 5).

Electron source function   Finally, the electron source function can be obtained by considering the transformation law of distribution functions,

$$q_e(E_e)dE_e = q_\pi(E_\pi)dE_\pi. \tag{4.55}$$

The mean energy of the produced secondary electrons ($\pi^\pm \to e^\pm + 3\nu$) in the laboratory frame is given by $\langle E_e \rangle = \frac{1}{4}\langle E_{\pi^\pm} \rangle$. Using the mean value of the electron energy allows to approximate the electron source function by

$$q_e(E_e) = q_{\pi^\pm}[E_\pi(E_e)]\frac{dE_\pi}{dE_e} = 4q_{\pi^\pm}(4E_e), \tag{4.56}$$

which is the starting point for the discussion of non-thermal emission by secondary electrons in the next chapter.

5. Hadronic cosmic ray proton interactions in clusters of galaxies

Abstract

This chapter provides a theoretical framework for analytically modeling multi-frequency signatures resulting from hadronic cosmic ray proton (CRp) interactions with the ambient thermal gas of the intra-cluster medium (ICM). These interactions produce charged and neutral pions which successively decay into γ-rays and relativistic electrons or positrons. The γ-ray source function resulting from decaying neutral pions is presented for two popular models of the hadronic interaction of relativistic and non-relativistic protons. It is valid over a broad range of γ-ray energies extending from below MeV up to TeV. Using this γ-ray source function, we derive an analytic relation between the γ-ray and bolometric X-ray fluxes: this relation can find application in compiling a suitable sample of galaxy clusters which are promising candidates for future detection of diffuse γ-rays. The stationary spectrum of hadronically originating secondary electrons is provided furthermore. It allows the calculation of accompanying synchrotron and inverse Compton emission and yields thus additional and complementary information about the non-thermal energetic content of clusters.

5.1. Introduction and definitions

In order to study non-thermal emission from galaxy clusters we model the synchrotron and inverse Compton (IC) radiation of secondary cosmic ray electrons (CRe) produced in inelastic collisions by cosmic ray protons (CRp) scattering off thermal nuclei as well as the γ-ray spectrum produced by decaying pions being produced by these CRp-p collisions. Throughout this thesis, we use the following definitions for the differential source function $q(\boldsymbol{r}, E)$, the emissivity $j(\boldsymbol{r}, E)$ and the volume integrated quantities, respectively:

$$q(\boldsymbol{r}, E) = \frac{\mathrm{d}N}{\mathrm{d}t\,\mathrm{d}V\,\mathrm{d}E}, \qquad\qquad j(\boldsymbol{r}, E) = E\,q(\boldsymbol{r}, E), \qquad (5.1)$$

$$Q(E) = \int \mathrm{d}V\,q(\boldsymbol{r}, E), \qquad\qquad J(E) = E\,Q(E), \qquad (5.2)$$

where N denotes the integrated number of particles. From the source function the integrated number density production rate of particles $\lambda(\boldsymbol{r})$, the number of particles produced per unit time interval within a certain volume, $\mathcal{L}$, and the particle flux $\mathcal{F}$ can be derived. The definitions of the energy weighted quantities are denoted on the right hand side, respectively,

$$\lambda(\boldsymbol{r}) = \int \mathrm{d}E\,q(\boldsymbol{r}, E), \qquad\qquad \Lambda(\boldsymbol{r}) = \int \mathrm{d}E\,E\,q(\boldsymbol{r}, E), \qquad (5.3)$$

$$\mathcal{L} = \int \mathrm{d}V\,\lambda(\boldsymbol{r}), \qquad\qquad L = \int \mathrm{d}V\,\Lambda(\boldsymbol{r}), \qquad (5.4)$$

$$\mathcal{F} = \frac{\mathcal{L}}{4\,\pi\,D^2}, \qquad\qquad F = \frac{L}{4\,\pi\,D^2}. \qquad (5.5)$$

This chapter is structured as follows: after introducing the CRp population (Sect. 5.2), we develop an analytic formalism describing the decay of secondary neutral pions into two high-energy γ-rays (Sect. 5.3). Section 5.3.1

uses the analytical fireball model for inelastic CRp interactions with nuclei of the intergalactic medium in the high-energy regime of CRp ($E_p \gg m_p c^2$), following Mannheim & Schlickeiser (1994). Based on that, we develop in Sect. 5.3.2 an analytic formula describing the γ-ray spectrum by parameterizing important effects near the pion threshold using an approximate description developed by Dermer (1986a,b), which combines isobaric (Stecker 1970) and scaling models (Badhwar et al. 1977, Stephens & Badhwar 1981) of the hadronic reaction. Using this formalism, an analytic $\mathcal{F}_\gamma$–F_X scaling relation is derived in the framework of a simple scenario of spatial distribution of CRp (Sect. 5.4). Finally, Sect. 5.5 deals with radio and X-ray emission of secondary electrons being produced by decaying charged pions.

5.2. Cosmic ray proton population

The differential number density distribution of a CRp population can be described by a power-law in momentum p_p,

$$f_p(\mathbf{r}, p_p)\, \mathrm{d}p_p\, \mathrm{d}V = \tilde{n}_{\mathrm{CRp}}(\mathbf{r}) \left(\frac{p_p\, c}{\mathrm{GeV}} \right)^{-\alpha_p} \left(\frac{c\, \mathrm{d}p_p}{\mathrm{GeV}} \right) \mathrm{d}V, \tag{5.6}$$

where the tilde indicates that $\tilde{n}_{\mathrm{CRp}}$ is not a real CRp number density while it exhibits those dimensions. We choose the normalization $\tilde{n}_{\mathrm{CRp}}(\mathbf{r})$ in such a way that the kinetic CRp energy density $\varepsilon_{\mathrm{CRp}}(\mathbf{r})$ is proportional to the thermal energy density $\varepsilon_{\mathrm{th}}(\mathbf{r})$ of the ICM,

$$\varepsilon_{\mathrm{CRp}}(\mathbf{r}) = X_{\mathrm{CRp}}(\mathbf{r})\, \varepsilon_{\mathrm{th}}(\mathbf{r}) = \int_0^\infty \mathrm{d}p\, f_p(\mathbf{r}, p_p)\, E_{\mathrm{kin}}(p_p) \tag{5.7}$$

$$= \frac{\tilde{n}_{\mathrm{CRp}}(\mathbf{r})\, m_p\, c^2}{2\,(\alpha_p - 1)} \left(\frac{m_p\, c^2}{\mathrm{GeV}} \right)^{1-\alpha_p} \mathcal{B}\left(\frac{\alpha_p - 2}{2}, \frac{3 - \alpha_p}{2} \right). \tag{5.8}$$

The kinetic energy of CRp E_{kin} and the thermal energy density of the ICM $\varepsilon_{\mathrm{th}}$ are given by

$$E_{\mathrm{kin}}(p_p) = \sqrt{p_p^2\, c^2 + m_p^2\, c^4} - m_p\, c^2, \tag{5.9}$$

$$\varepsilon_{\mathrm{th}}(\mathbf{r}) = \frac{3}{2}\, d_e\, n_e(\mathbf{r})\, kT_e(\mathbf{r}), \tag{5.10}$$

$$\text{where} \quad d_e = 1 + \frac{1 - \frac{3}{4} X_{\mathrm{He}}}{1 - \frac{1}{2} X_{\mathrm{He}}} \tag{5.11}$$

counts the number of particles per electron in the ICM using the primordial ^{4}He mass fraction $X_{\mathrm{He}} = 0.24$, and $\mathcal{B}(a,b)$ denotes the beta-function (Abramowitz & Stegun 1965). The functional dependence of the CRp scaling parameter $X_{\mathrm{CRp}}(\mathbf{r})$ is a priori unknown. In order to draw astrophysical conclusions for the CRp population in clusters of galaxies, we adopt three different models for the spatial distribution of CRp later on in Chapter 6.

In contrast to relativistic electrons which loose their energy on relatively short time scales compared to the Hubble time through synchrotron emission in cluster magnetic fields and IC scattering with photons of the microwave background, the dominant energy loss mechanisms of CRp are electronic excitations in the plasma (Enßlin et al. 1997), defining a cooling time (Gould 1972)

$$t_{\mathrm{ee}} = \left[-\frac{1}{\gamma_p} \left(\frac{\mathrm{d}\gamma_p}{\mathrm{d}t} \right)_{\mathrm{ee}} \right]^{-1} = \frac{m_e\, c^3\, m_p\, \beta_p\, \gamma_p}{4\,\pi\, e^4\, n_e} \left[\ln\left(\frac{2\gamma_p m_e c^2 \beta_p^2}{\hbar \omega_{\mathrm{pl}}} \right) - \frac{\beta_p^2}{2} \right]^{-1}, \tag{5.12}$$

where $\beta_p c$ denotes the velocity of the proton, γ_p its relativistic Lorentz factor, and $\omega_{\mathrm{pl}} = (4\pi e^2 n_e/m_e)^{1/2}$ the plasma frequency. Inserting typical values for cooling flows yields a lower cutoff on the CRp momentum

$$p_{\mathrm{min}} = \beta_p \gamma_p\, m_p\, c \simeq 0.2 \left(\frac{t_{\mathrm{age}}}{\mathrm{Gyr}} \right) \left(\frac{n_e}{10^{-2}\, \mathrm{cm}^{-3}} \right) \mathrm{GeV} c^{-1}. \tag{5.13}$$

In general, this gives rise to a spatially dependent cutoff of the CRp momentum which increases with time.

In order not to rely on too many assumptions, we do not impose a specific momentum cutoff which is possible since the spectral index α_p varies in our model in between 2 and 3. Instead, we quantify the influence of a lower
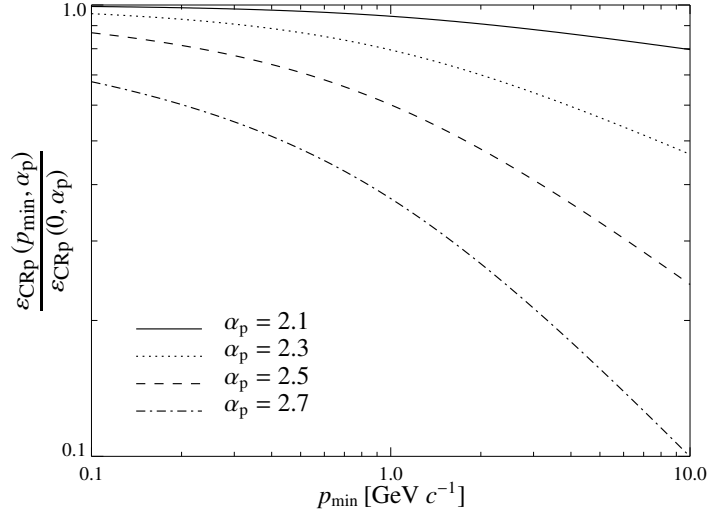
Figure 5.1.: The ratio of CRp energy densities $\varepsilon_{\mathrm{CRp}}(p_{\min}, \alpha_{\mathrm{p}})$ with and without a lower cutoff $p_{\min}$ in the CRp number density distribution function as a function of $p_{\min}$ for different values of the CRp spectral index α_{p} (see Eqn. (5.14)). For CRp the kinematically allowed threshold in order to produce π^0-mesons hadronically is given by $p_{\mathrm{thr}} = 0.78\ \mathrm{GeV}\ c^{-1}$.

cutoff $p_{\min}$ on the population of CRp by taking the ratio of CRp energy densities $\varepsilon_{\mathrm{CRp}}(p_{\min}, \alpha_{\mathrm{p}})$ with and without a lower cutoff. This ratio as shown in Fig. 5.1 can be written using the definition for the normalized lower CRp momentum cutoff $\tilde{p} = \frac{p_{\min}}{m_{\mathrm{p}} c}$,

$$\frac{\varepsilon_{\mathrm{CRp}}(\tilde{p}, \alpha_{\mathrm{p}})}{\varepsilon_{\mathrm{CRp}}(0, \alpha_{\mathrm{p}})} = \frac{\mathcal{B}_x\left(\frac{\alpha_{\mathrm{p}}-2}{2}, \frac{3-\alpha_{\mathrm{p}}}{2}\right) + 2\,\tilde{p}^{1-\alpha_{\mathrm{p}}}\left(\sqrt{1+\tilde{p}^2}-1\right)}{\mathcal{B}\left(\frac{\alpha_{\mathrm{p}}-2}{2}, \frac{3-\alpha_{\mathrm{p}}}{2}\right)}, \tag{5.14}$$

where $\mathcal{B}_x(a, b)$ denotes the incomplete beta-function (Abramowitz & Stegun 1965) with $x = (1 + \tilde{p}^2)^{-1}$. Combining Fig. 5.1 and Eqn. (5.13) demonstrates the small influence of Coulomb cooling to the CRp energy density within cooling flows.

5.3. γ-ray spectrum from hadronic CRp interactions

5.3.1. Fireball model

The CRp interact hadronically with the thermal background gas and produce pions with relative multiplicities $\xi_{\pi^0} = \frac{1}{2}\xi_{\pi^\pm}$ according to isospin symmetry and assuming thermal equilibrium of the pion cloud in the center of mass (Fermi 1950). The charged pions decay into secondary electrons (and neutrinos) and the neutral pions into γ-rays:

$$\begin{aligned} \pi^\pm &\rightarrow \mu^\pm + \nu_\mu/\bar{\nu}_\mu \rightarrow e^\pm + \nu_e/\bar{\nu}_e + \nu_\mu + \bar{\nu}_\mu \\ \pi^0 &\rightarrow 2\gamma\,. \end{aligned}$$
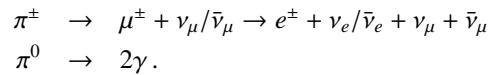
Only CRp above the kinematic threshold $p_{\mathrm{thr}} = 0.78\ \mathrm{GeV}\ c^{-1}$ are able to produce pions hadronically and are therefore visible through their decay products in both the γ-ray and radio bands via radiative processes. Only the CRp population above this threshold is constrained by this work while the lower energy part of this population in general can not be limited by only considering hadronic interactions.

In the high-energy limit for CRp ($E_{\mathrm{p}} \gg m_{\mathrm{p}} c^2$) the pion source function resulting from hadronic CRp-p interactions can be calculated following Mannheim & Schlickeiser (1994) to be

$$q_{\pi^0}(\boldsymbol{r}, E_{\pi^0})\, \mathrm{d}E_{\pi^0}\, \mathrm{d}V \approx 2^3\, \bar{\sigma}_{\mathrm{pp}}\, c\, n_{\mathrm{N}}(\boldsymbol{r})\, \frac{\tilde{n}_{\mathrm{CRp}}(\boldsymbol{r})}{\mathrm{GeV}} \left(\frac{6\,E_{\pi^0}}{\mathrm{GeV}}\right)^{-\alpha_\gamma} \mathrm{d}E_{\pi^0}\, \mathrm{d}V, \tag{5.15}$$

45

where $\alpha_\gamma = 4/3\,(\alpha_p - 1/2)$, $\bar{\sigma}_{pp} = 32$ mbarn is the inelastic p-p cross section, and $n_N(\boldsymbol{r}) = d_{tar}\,n_e(\boldsymbol{r}) = n_e(\boldsymbol{r})/(1 - \frac{1}{2}X_{He})$ is the target nucleon density in the ICM. The π^0-decay induced omnidirectional (i.e. integrated over $4\,\pi$ solid angle) differential γ-ray source function can be calculated in this energy regime assuming the decay products are distributed isotropically in their rest frame, yielding

$$
\begin{aligned}
q_\gamma(\boldsymbol{r}, E_\gamma) &= 2 \int_{E_\gamma + \frac{m_\pi^2 c^4}{4 E_\gamma}}^{\infty} dE_{\pi^0} \, \frac{q_{\pi^0}(\boldsymbol{r}, E_{\pi^0})}{\sqrt{E_{\pi^0}^2 - m_{\pi^0}^2\,c^4}} \\[2mm]
&= 2^3\,\bar{\sigma}_{pp}\,c\,n_N(\boldsymbol{r})\,\frac{\tilde{n}_{CRp}(\boldsymbol{r})}{GeV}\left(\frac{6\,m_{\pi^0}\,c^2}{GeV}\right)^{-\alpha_\gamma}\mathcal{B}_x\left(\frac{\alpha_\gamma}{2}, \frac{1}{2}\right),
\end{aligned}
\tag{5.16}
$$

$$
\text{where} \quad x = \left(\frac{4\,E_\gamma\,m_{\pi^0}\,c^2}{4\,E_\gamma^2 + m_{\pi^0}^2\,c^4}\right)^2.
\tag{5.17}
$$

Owing to Lorentz symmetry, this formula is valid for both limiting energy regimes, $E_\gamma \gg m_{\pi^0}\,c^2/2$ and $E_\gamma \ll m_{\pi^0}\,c^2/2$. Because of an incomplete accounting of physical processes at the threshold of pion production like the velocity distribution of CRp and momentum dependent inelastic CRp-p cross section, Eqn. (5.16) overestimates the number of γ-rays for energies around $E_\gamma \simeq m_{\pi^0}\,c^2/2$.

5.3.2. Dermer's model

In order to make detailed predictions for the π^0-decay induced γ-ray spectrum, more realistic effects near the π^0-production threshold have to be included. This was done by using the code COSMOCR originally designed for cosmic ray studies by Miniati (2001). The underlying $\Delta_{3/2}$-isobaric model was shown to work well at low proton energies (Stecker 1970). It assumes the CRp-p interaction to be mediated by the excitation of the $\Delta_{3/2}$-resonance which subsequently decays into two protons and a π^0-meson. The production spectrum of secondary π^0-mesons is given by a convolution of the normalized $\Delta_{3/2}$-isobar mass spectrum represented by a Breit-Wigner distribution with the energy distribution function. The scaling model used at high energies (Stephens & Badhwar 1981) uses Lorentz invariant cross sections for charged and neutral pion production in p-p interactions inferred from accelerator data. COSMOCR includes also the contribution of the two main kaon decay modes to secondary pion spectra (following Moskalenko & Strong 1998) which are $K^\pm \rightarrow \mu^\pm + \nu_\mu/\bar{\nu}_\mu$ (63.5%) and $K^\pm \rightarrow \pi^0 + \pi^\pm$ (21.2%) where the latter channel also contributes to the γ-ray source function.

In order to derive an analytic formula describing the omnidirectional differential γ-ray source function over the energy range shown in Fig. 5.2, we keep the behavior of the spectrum in the fireball model for $E_\gamma \gg m_{\pi^0}\,c^2/2$ and parameterize the detailed physics at the π^0-threshold by the shape parameter δ_γ which smoothly joins the two power laws to the asymptotic expansion of the $\mathcal{B}$-function of Eqn. (5.16), yielding

$$
q_\gamma(\boldsymbol{r}, E_\gamma)\,dE_\gamma\,dV \simeq \sigma_{pp}\,c\,n_N(\boldsymbol{r})\,\xi^{2-\alpha_\gamma}\,\frac{\tilde{n}_{CRp}(\boldsymbol{r})}{GeV}\,\frac{4}{3\,\alpha_\gamma}\left(\frac{m_{\pi^0}\,c^2}{GeV}\right)^{-\alpha_\gamma}\left[\left(\frac{2\,E_\gamma}{m_{\pi^0}\,c^2}\right)^{\delta_\gamma} + \left(\frac{2\,E_\gamma}{m_{\pi^0}\,c^2}\right)^{-\delta_\gamma}\right]^{-\alpha_\gamma/\delta_\gamma}\,dE_\gamma\,dV. \tag{5.18}
$$

The scaling behavior in the high-energy limit of Dermer's model can be described by a constant pion multiplicity $\xi = 2$ characterizing the two leading pion jets leaving the interaction site in direction of the incident protons diametrically and carrying the high longitudinal momenta owing to Lorentz contraction of the interacting nuclei in the center of mass system and Heisenberg's uncertainty relation (Nachtmann 1990). This assumption of constant pion multiplicity of the scaling model is in contrast to the fireball model (Mannheim & Schlickeiser 1994), which assumes a state of hot quark-gluon plasma in thermal equilibrium after the hadronic interaction subsequently ablating pions with multiplicities $\xi_{\pi^0} \simeq [(E_p - E_{th})/GeV]^{1/4}$, where $E_{th} = 1.22$ GeV denotes the threshold energy for pion production.

The γ-ray source function peaks at the energy of $m_{\pi^0}\,c^2/2 \simeq 67.5$ MeV. It is well known, that the asymptotic slope of the γ-ray spectrum, characterized by its spectral index α_γ, reproduces the spectral index of the population of CRp, $\alpha_\gamma = \alpha_p$ (Dermer 1986b). This is again in contrast to the fireball model which predicts a steeper asymptotic slope in the γ-ray spectrum for $\alpha_p > 2$, amounting to $\alpha_\gamma = 4/3\,(\alpha_p - 1/2)$. In the following we restrict ourselves to Dermer's model because it is better motivated by accelerator data.

By comparing the logarithm of the γ-ray source function of Eqn. (5.18) to numerically calculated spectra using COSMOCR we recognized that the influence of the detailed physics at the threshold together with the kaon contribution can be modeled in our semi-analytic approach in Eqn. (5.18) by self-consistent scaling relations for the shape
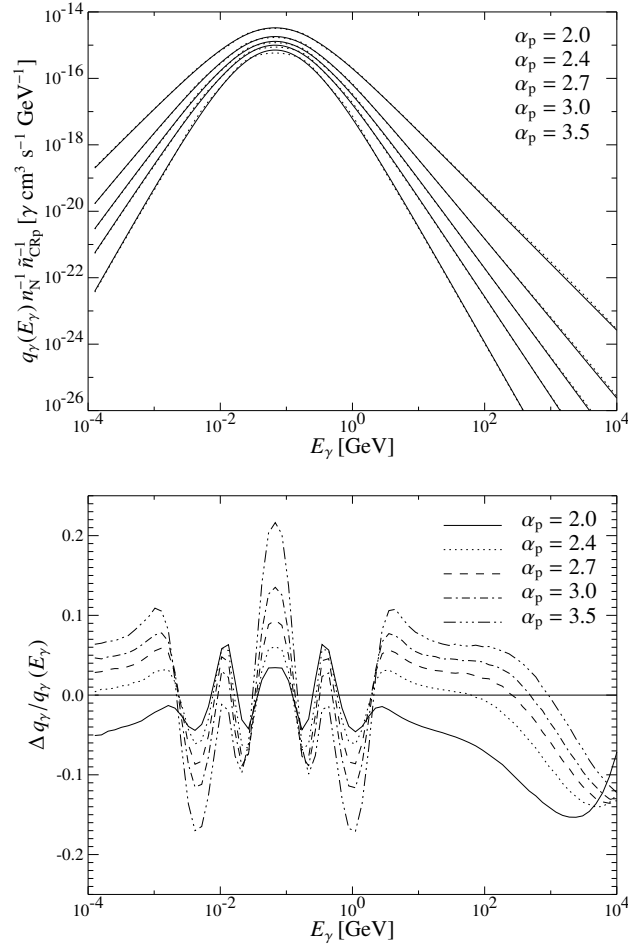
Figure 5.2.: *Upper panel:* The omnidirectional (i.e. integrated over 4π solid angle) differential γ-ray source function $q_\gamma(E_\gamma)$ normalized by the target number density $n_N(\mathbf{r})$ and CRp normalization $\tilde{n}_{\mathrm{CRp}}(\mathbf{r})$ in order to be independent of the spatial dependence of any specific model. The dotted lines show the simulated γ-ray spectra while the solid curves represent our models given by Eqn. (5.18) with the spectral indices from top to bottom, $\alpha_p \in \{2.0, 2.4, 2.7, 3.0, 3.5\}$. *Lower panel:* Relative deviation of our analytic approach to simulated γ-ray spectra.

---

parameter δ_γ and the effective inelastic p-p cross section σ_{pp} including the kaon decay modes. The shape parameter δ_γ scales with the spectral index of the γ-ray spectrum as

$$\delta_\gamma = 0.14\,\alpha_\gamma^{-1.6} + 0.44\,, \tag{5.19}$$

which models the functional behavior of the spectrum (compare Fig. 5.2). The effective cross section σ_{pp} also depends on α_γ which can be modeled by

$$\sigma_{\mathrm{pp}} = 32 \times \left(0.96 + \mathrm{e}^{4.4 - 2.4\,\alpha_\gamma}\right)\ \mathrm{mbarn}\,. \tag{5.20}$$

On the one hand, the enhanced contribution to the normalization of the γ-ray source function $q_\gamma(E_\gamma)$ for flat spectral indices α_γ is due to the larger contribution of the channel $p + p \to K^\pm + X$ relative to $p + p \to \pi^\pm + X$ for larger energies, approaching asymptotically a value of 27 % at energies larger than 1 TeV (Miniati 2001) which we did not account for a priori in our simple model. Secondly, this scaling behavior also includes higher order contributions to the effective pion multiplicity for harder spectra characterized by a lower spectral index α_γ.

The effective description of the spectrum with the smooth peak characterized by the shape parameter δ_γ starts to fail for very steep spectra of $\alpha_\gamma > 3.5$ where relativistic kinematics at the threshold plays a crucial role. Then

the higher number of decaying low energetic π^0-mesons results in a more concentrated peak on top of the boosted broader distribution of decaying highly-energetic pions. The lower panel of Fig. 5.2 shows that the relative deviation of the semi-analytic approach of Eqn. (5.18) to the simulated γ-ray spectra amounts below 0.2 for the spectral range shown in Fig. 5.2, which is sufficient for the purpose of our work.

5.4. Energy band integrated γ-ray luminosity: analytic $\mathcal{F}_\gamma$–F_X scaling relation

In the following, we derive an analytic $\mathcal{F}_\gamma$–F_X scaling relation which should serve as an approximate estimate for a given cluster of galaxies. In our scenario, we parameterize the CRp energy density in terms of the thermal energy density times an arbitrary spatial scaling function, $\varepsilon_{\mathrm{CRp}}(r) = X_{\mathrm{CRp}}(r)\,\varepsilon_{\mathrm{th}}(r)$. The bolometric X-ray emission of the hot thermal intra cluster electrons is given by the cooling function for thermal bremsstrahlung (Rybicki & Lightman 1979),

$$\Lambda_X[n_e(r), T_e(r)] \;=\; \Lambda_0\, n_e(r)^2\,\sqrt{kT_e(r)}\,, \tag{5.21}$$

$$\text{with } \Lambda_0 \;=\; \left(\frac{2\,\pi}{3\,m_e}\right)^{1/2}\frac{2^5\pi\,e^6 d_{\mathrm{tar}}}{3\,h\,m_e\,c^3}\,Z^2\,\bar{g}_B(T_e) \simeq 6.62 \times 10^{-24}\ \mathrm{erg\ s^{-1}\ cm^3\ keV^{-1/2}}, \tag{5.22}$$

where n_e is the electron number density, T_e the temperature, d_{tar} is the nucleon density in the ICM relative to the electrons for primordial element composition, Z the charge number[1] and $\bar{g}_B \simeq 1.2$ is the frequency and velocity averaged Gaunt factor.

In order to obtain the integrated γ-ray source density λ_γ for pion decay induced γ-rays the γ-ray source function $q_\gamma(r, E_\gamma)$ in Eqn. (5.18) can be integrated over an energy interval yielding

$$\lambda_\gamma(r, E_1, E_2) \;=\; \int_{E_1}^{E_2} \mathrm{d}E_\gamma\, q_\gamma(r, E_\gamma) = A_\gamma(\alpha_p)\,N_\gamma(\alpha_p)\,X_{\mathrm{CRp}}(r)\,n_e^2(r)\,kT_e(r)\,, \tag{5.23}$$

$$\text{where } A_\gamma(\alpha_p) \;=\; \frac{\sigma_{\mathrm{pp}}(\alpha_p)\,d_e\,d_{\mathrm{tar}}\,m_{\pi^0}\,c}{\mathrm{GeV}\,m_p}\,, \tag{5.24}$$

$$N_\gamma(\alpha_p) \;=\; \frac{\left(\frac{m_{\pi^0}c^2}{\mathrm{GeV}}\right)^{-\alpha_\gamma}\left[\mathcal{B}_x\left(\frac{\alpha_\gamma+1}{2\,\delta_\gamma}, \frac{\alpha_\gamma-1}{2\,\delta_\gamma}\right)\right]_{x_1}^{x_2}(\alpha_p - 1)}{\left(\frac{m_p c^2}{\mathrm{GeV}}\right)^{1-\alpha_p}\mathcal{B}\left(\frac{\alpha_p-2}{2}, \frac{3-\alpha_p}{2}\right)2^{\alpha_\gamma-2}\,\alpha_\gamma\,\delta_\gamma}\,, \tag{5.25}$$

$$\text{and } x_i \;=\; \left[1 + \left(\frac{m_{\pi^0}c^2}{2\,E_i}\right)^{2\,\delta_\gamma}\right]^{-1} \text{ for } i \in \{1, 2\}\,. \tag{5.26}$$

Here we introduced the abbreviation $[f(x)]_{x_1}^{x_2} = f(x_2) - f(x_1)$. Assuming Dermer's model the γ-ray spectral index scales as $\alpha_\gamma = \alpha_p$ in contrast to the fireball model where $\alpha_\gamma = 4/3\,(\alpha_p - 1/2)$. The shape parameter δ_γ is given by the α_γ–δ_γ scaling relation in Eqn. (5.19) which strictly holds for Dermer's model, but should also be valid for the extended fireball model.

Comparing the integrated γ-ray source density $\lambda_\gamma(E_1, E_2)$ of Eqn. (5.23) to that of thermal bremsstrahlung (Eqn. (5.21)) we obtain an analytic $\mathcal{F}_\gamma$–F_X scaling relation for the ratio of γ-ray fluxes $\mathcal{F}_\gamma$ and bolometric X-ray fluxes F_X,

$$\frac{\mathcal{F}_\gamma(E_1 < E < E_2)}{F_X^{\mathrm{bol}}\,\mathrm{erg}^{-1}} = \frac{A_\gamma(\alpha_p)\,N_\gamma(\alpha_p)}{\Lambda_0\,\mathrm{keV}^{-1/2}\,\mathrm{erg}^{-1}}\left(\frac{\langle kT_e\rangle}{\mathrm{keV}}\right)^{1/2}X_{\mathrm{CRp}}(r)\,, \tag{5.27}$$

where the prefactor is appropriately scaled yielding a dimensionless number which consists of $A_\gamma(\alpha_p)$ (Eqn. (5.24)), $N_\gamma(\alpha_p)$ (Eqn. (5.25)), and Λ_0 (Eqn. (5.22)). The $\mathcal{F}_\gamma$–F_X ratio scales linearly with the scaling function $X_{\mathrm{CRp}}(r)$ given by Eqn. (5.7) and is independent of the underlying cosmology, however not of redshift due to the K-correction. Inferred values for the expected γ-ray flux $\mathcal{F}_\gamma$ are consistent with those obtained by Enßlin et al. (1997) for the spectral index of our Galaxy $\alpha_\gamma = 2.7$. It should be noted, that this scaling relation only applies accurately for isothermal clusters.

---

[1] Setting $Z^2 = 1$ in Eqn. (5.22) is correct for a plasma of primordial element composition which consists of hydrogen and helium only, because $\langle n_N Z^2\rangle = n_N$ in this case. This is a reasonable approximation owing to the small contamination of heavier elements in the ICM.

5.5. Stationary spectrum of hadronically originating secondary electrons

This section is based on a formalism developed in Dolag & Enßlin (2000). The steady-state CRe spectrum is governed by injection of secondaries and cooling processes so that it can be described by the continuity equation

$$\frac{\partial}{\partial E_e}\left(\dot{E}_e(\boldsymbol{r}, E_e) f_e(\boldsymbol{r}, E_e)\right) = q_e(\boldsymbol{r}, E_e). \tag{5.28}$$

For $\dot{E}_e(\boldsymbol{r}, p) < 0$ this equation is solved by

$$f_e(\boldsymbol{r}, E_e) = \frac{1}{|\dot{E}_e(\boldsymbol{r}, E_e)|} \int_{E_e}^{\infty} dE'_e\, q_e(\boldsymbol{r}, E'_e). \tag{5.29}$$

The cooling of the radio emitting CRe is dominated by synchrotron and inverse Compton losses giving

$$-\dot{E}_e(\boldsymbol{r}, E_e) = \frac{4\,\sigma_T\, c}{3\, m_e^2\, c^4}\left(\frac{B^2(\boldsymbol{r})}{8\,\pi} + \frac{B_{\mathrm{CMB}}^2}{8\,\pi}\right) E_e^2, \tag{5.30}$$

where σ_T is the Thomson cross section, $B(\boldsymbol{r})$ is the local magnetic field strength and $B_{\mathrm{CMB}}^2/(8\,\pi)$ is the energy density of the cosmic microwave background expressed by an equivalent field strength $B_{\mathrm{CMB}} = 3.24\,(1 + z)^2\,\mu\mathrm{G}$. The CRe population above a GeV is therefore described by a power-law spectrum

$$f_e(\boldsymbol{r}, E_e) = \frac{\tilde{n}_{\mathrm{CRe}}(\boldsymbol{r})}{\mathrm{GeV}}\left(\frac{E_e}{\mathrm{GeV}}\right)^{-\alpha_e}, \tag{5.31}$$

$$\tilde{n}_{\mathrm{CRe}}(\boldsymbol{r}) = \frac{2^7\,\pi\,16^{-(\alpha_e-1)}\,A_{\mathrm{mod}}}{\alpha_e - 2}\,\frac{\sigma_{\mathrm{pp}}\,m_e^2\,c^4}{\sigma_T\,\mathrm{GeV}}\,\frac{n_N(\boldsymbol{r})\,\tilde{n}_{\mathrm{CRp}}(\boldsymbol{r})}{B^2(\boldsymbol{r}) + B_{\mathrm{CMB}}^2}, \tag{5.32}$$

$$\alpha_e = \begin{cases} \alpha_p + 1 & \text{in Dermer's model}, \\ \frac{4}{3}\alpha_p + \frac{1}{3} & \text{in the fireball model}, \end{cases} \tag{5.33}$$

$$A_{\mathrm{mod}} = \begin{cases} 1 & \text{in Dermer's model}, \\ 3\left(\frac{3}{2}\right)^{-(\alpha_e-1)} & \text{in the fireball model}. \end{cases} \tag{5.34}$$

For the sake of consistency, we use Dermer's model throughout the chapter where the effective cross section σ_{pp} is given by Eqn. (5.20) in contrast to the fireball model where $\sigma_{\mathrm{pp}} = 32$ mbarn. The approach of the scaling relation of Eqn. (5.20) is approximately valid for CRe although the decay channels of charged kaons provide a stronger contribution to the $\pi^\pm$ branching ratio relative to π^0-mesons resulting also in slightly higher injection rates for electrons and positrons. Differences in normalization and radio brightness morphology due to the different models governing the CRp-p interaction are small and irrelevant for our conclusions.

5.5.1. Synchrotron emission of secondary electrons

The synchrotron emissivity j_ν at frequency ν and per steradian of a power law distribution of CRe (Eqn. (5.31)) in an isotropic distribution of magnetic fields and electrons within the halo volume (Eqn. (6.36) in Rybicki & Lightman 1979), is obtained after averaging over an isotropic distribution of electron pitch angles yielding

$$j_\nu(\boldsymbol{r}) = c_2(\alpha_e)\,\tilde{n}_{\mathrm{CRe}}(\boldsymbol{r})\,B(\boldsymbol{r})^{\alpha_\nu+1}\left(\frac{\nu}{c_1}\right)^{-\alpha_\nu} \tag{5.35}$$

with $c_1 = 3\,e\,\mathrm{GeV}^2/(2\,\pi\,m_e^3\,c^5)$,

$$c_2(\alpha_e) = \frac{\sqrt{3\,\pi}}{32\,\pi}\,\frac{e^3}{m_e c^2}\,\frac{\alpha_e + \frac{7}{3}}{\alpha_e + 1}\,\frac{\Gamma\left(\frac{3\alpha_e-1}{12}\right)\Gamma\left(\frac{3\alpha_e+7}{12}\right)\Gamma\left(\frac{\alpha_e+5}{4}\right)}{\Gamma\left(\frac{\alpha_e+7}{4}\right)}, \tag{5.36}$$

where $\Gamma(a)$ denotes the Γ-function (Abramowitz & Stegun 1965) and $\alpha_\nu = (\alpha_e - 1)/2 = \alpha_p/2$ in Dermer's model. In our models the magnetic field $B(r)$ was assumed to be spherically symmetric on cluster core scales and and to follow the electron density $n_e(r)$ (Dolag et al. 1999, 2001):

$$B(r) = B_0 \left[\frac{n_e(r)}{n_e(0)} \right]^{\alpha_B} , \qquad (5.37)$$

where B_0 and α_B are free parameters in our model. Assuming the radio emissivity $j_\nu(r)$ in Eqn. (5.35) to be only a function of radius, then the line of sight integration yields the surface brightness of the radio halo

$$S_\nu(r_\perp) = 2 \int_{r_\perp}^{R} \frac{j_\nu(r) \, r \, \mathrm{d}r}{\sqrt{r^2 - r_\perp^2}} . \qquad (5.38)$$

5.5.2. Inverse Compton emission of secondary electrons

The source function q_{IC} owing to IC scattering of cosmic microwave background (CMB) photons off an isotropic power law distribution of hadronically originating CRe (Eqn. (5.31)) is (derived from Eqn. (7.31) in Rybicki & Lightman 1979, in the case of Thomson scattering),

$$q_{\mathrm{IC}}(\boldsymbol{r}, E_\gamma) = \tilde{q}(\boldsymbol{r}) \, f_{\mathrm{IC}}(\alpha_e) \left(\frac{m_e c^2}{\mathrm{GeV}} \right)^{1-\alpha_e} \left(\frac{E_\gamma}{kT_{\mathrm{CMB}}} \right)^{-(\alpha_\nu+1)} , \qquad (5.39)$$

$$f_{\mathrm{IC}}(\alpha_e) = \frac{2^{\alpha_e+3} \, (\alpha_e^2 + 4\,\alpha_e + 11)}{(\alpha_e + 3)^2 \, (\alpha_e + 5) \, (\alpha_e + 1)} \, \Gamma\left(\frac{\alpha_e + 5}{2} \right) \zeta\left(\frac{\alpha_e + 5}{2} \right) , \qquad (5.40)$$

$$\text{and } \tilde{q}(\boldsymbol{r}) = \frac{8\,\pi^2 \, r_e^2 \, \tilde{n}_{\mathrm{CRe}}(\boldsymbol{r}) \, (kT_{\mathrm{CMB}})^2}{h^3 \, c^2} , \qquad (5.41)$$

where $\alpha_\nu = (\alpha_e - 1)/2$ denotes the spectral index, $r_e = e^2/(m_e c^2)$ the classical electron radius, $\zeta(a)$ the Riemann ζ-function (Abramowitz & Stegun 1965), and $\tilde{n}_{\mathrm{CRe}}(\boldsymbol{r})$ is given by Eqn. (5.32). After integrating over the IC emitting volume in the cluster we obtain the particle flux $\mathcal{F}(E_\gamma)$ (see Eqns. (5.4) and (5.5)). The same CRe population seen in the radio band via synchrotron emission scatter CMB photons into the hard X-ray regime. In the γ-ray spectrum, there is a point of equal contribution of the IC spectrum of the CRe showing a decreasing slope of $-\alpha_\nu - 1 = -\alpha_p/2 - 1$ (assuming Dermer's model) and the pion decay induced γ-ray spectrum being characterized by the rising slope $\alpha_\gamma = \alpha_p$ (see Eqn. (5.18)). In the high energy limit ($E_\gamma \gg m_{\pi^0} c^2/2$), the pion decay induced γ-ray spectrum declines with a slope of $-\alpha_\gamma = -\alpha_p$ which is the same as the IC emission for $\alpha_p = 2$ and slightly steeper for larger values of α_p (for illustration, see Fig. 5.3).
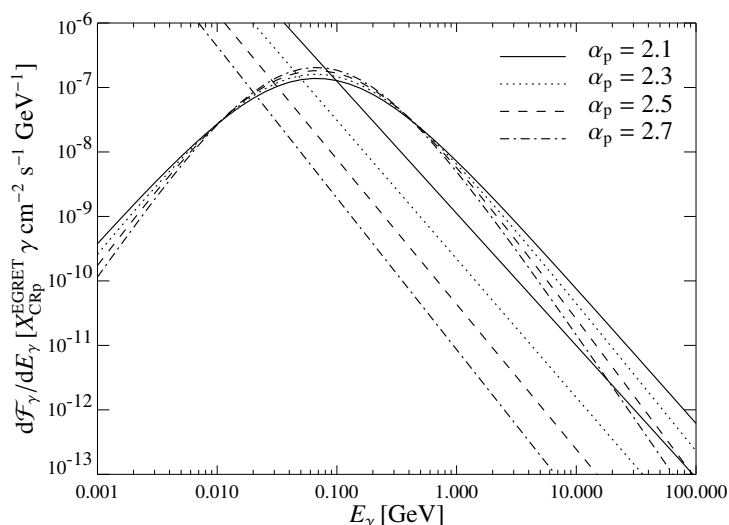
Figure 5.3.: The simulated differential flux of γ-rays from Perseus reaching the Earth. Shown are upper limits of the IC emission of secondary CRe (power-laws, assuming zero magnetic field) as well as pion decay induced γ-ray emission (represented by broad distribution centered on $E_{\mathrm{peak}} \simeq 67.5$ MeV). The normalization of the spectra differing in their values of the CRp spectral index $\alpha_\gamma = \alpha_{\mathrm{p}}$ (Dermer's model) depends on the assumed scaling between CRp and thermal energy density. We fix this scaling parameter X_{CRp} assuming the isobaric model (Sect. 6.2.1 in Chapter 6) by comparing the integrated flux above 100 MeV to EGRET upper limits (see Reimer et al. 2003).

5.6. Summary and outline of astrophysical applications

For the first time we developed an analytic formalism to describe the neutral pion-decay induced γ-ray spectrum self-consistently for a given differential number density distribution of the CRp population being described by a power-law in momentum p_{p} and parametrized by the spectral index α_{p}. We derived an analytic $\mathcal{F}_\gamma$–F_{X} scaling relation for the ratio of γ-ray flux to bolometric X-ray flux. Given the bolometric X-ray luminosity of a particular cluster this formula estimates the expected γ-ray flux $\mathcal{F}_\gamma$ owing to inelastic cosmic ray ion collisions and thus provides observationally promising cluster candidates for constraining the CRp population. We furthermore present formulae describing the synchrotron and inverse Compton emission of hadronically originating secondary electrons assuming an isotropic distribution of magnetic fields following a smooth profile.

In order to obtain reliable flux estimates we are going to introduce in the following three possible spatial distributions of the CRp, whose population is either in fractional pressure equilibrium with the thermal particle population (as assumed for selecting the clusters), experienced adiabatic compression during the formation of the cooling flow cluster or is shaped by diffusion away from a central source of CRp. By modeling the γ-ray emission of these particular clusters and comparing to EGRET upper limits we are going to present bounds on the CRp population. Furthermore, we will derive upper bounds on the CRp population by radio synchrotron emission of hadronically originating CRe and will compare azimuthally averaged radio brightness profiles of the the Perseus radio-mini halo and the radio halo of Coma.

The results of this chapter were worked out in collaboration with T.A. Enßlin. This chapter coincides with the first part of the paper entitled "Constraining the population of cosmic ray protons in cooling flow clusters with γ-ray and radio observations: Are radio mini-halos of hadronic origin?" *and has been published in the journal* Astronomy & Astrophysics *with the reference:* Pfrommer & Enßlin, 2004, A&A, 413, 17.

6. Cosmic rays in nearby clusters of galaxies: signatures and limits

Abstract

This chapter constrains the cosmic-ray proton (CRp) population in galaxy clusters and studies the hypothesis that the diffuse radio synchrotron emission of galaxy clusters is produced by hadronically originating relativistic electrons. Assuming the CRp-to-thermal energy density ratio X_{CRp} and the CRp spectral index to be spatially constant, we use an analytic relation between the γ-ray and bolometric X-ray fluxes to obtain observationally promising cluster candidates for constraining the CRp population. After modeling the spatial distribution of CRp within the intra-cluster medium, we constrain this population by comparing to EGRET upper limits. In nearby cooling flow clusters, we obtain limits on the CRp population of $X_{CRp} < 20\%$. The synchrotron emission from secondary electrons generated in CRp hadronic interactions allows even tighter limits to be placed on the CRp population using radio observations. We obtain excellent agreement between the observed and theoretical radio brightness profiles for Perseus, but not for Coma without a radially increasing CRp-to-thermal energy density profile. Since the CRp and magnetic energy densities necessary to reproduce the observed radio flux are very plausible, we propose synchrotron emission from secondary electrons as an attractive explanation of the radio mini-halos found in cooling flow clusters. This model can be tested with future sensitive γ-ray observations of the accompanying π^0-decays. We identify Perseus, Virgo, Ophiuchus, and Coma as the most promising candidate clusters for such observations.

We furthermore examine the CRp population within the giant elliptical galaxy M 87 using the TeV γ-ray detection of the HEGRA collaboration. In our scenario, the γ-rays are produced by decaying pions which result from hadronic CRp interactions with thermal gas of the interstellar medium of M 87. By comparing the γ-ray emission to upper limits from EGRET, we constrain the spectral index of the CRp population to $\alpha_{GeV}^{TeV} < 2.275$ within our scenario. Both the expected radial γ-ray profile and the required amount of CRp support this hadronic scenario. The accompanying radio mini-halo of hadronically originating cosmic ray electrons is outshone by the synchrotron emission of the relativistic jet of M 87 by one order of magnitude. According to our predictions, the future GLAST mission should allow us to test this hadronic scenario.

6.1. Introduction

6.1.1. Taxonomy of particle acceleration processes

Cooling flows are regions where the influence of non-thermal intra-cluster medium (ICM) components such as magnetic fields and cosmic rays may be strongest within a galaxy cluster owing to strong observed magnetic fields, central active galaxies, and increasing non-thermal-to-thermal energy ratio due to rapid thermal cooling processes. They are also regions where such components are best detectable due to the high gas density which allows for secondary particle production in hadronic interactions of cosmic ray nuclei with the ambient gas. By the term cooling flow we do not rely on specific models but only on observed properties such as declining temperature gradients and enhanced electron density profiles towards the center of the cluster. Occasionally, we refer to the term cooling flow cluster as cool core cluster.

Non-thermal relativistic particle populations such as cosmic ray electrons (CRe) and protons (CRp) can be injected into the ICM mainly by three different processes (following Brunetti 2002) which produce radio signatures that differ morphologically as well as spectrally:

1. **Shock acceleration:** Natural acceleration mechanisms providing relativistic particles are strong structure formation and merger shocks (e.g., Harris et al. 1980, Sarazin 1999). Detailed studies have been undertaken on shocks of cosmological scales (Miniati et al. 2000, Takizawa & Naito 2000). Fermi I acceleration processes of CRe at these shock fronts produce large scale extended peripheral radio relics as proposed by Enßlin et al.

(1998). For instance two prominent relics in Abell 3667 (Röttgering et al. 1997) were successfully reproduced in a simulation of this process by Roettiger et al. (1999).

2. **Reaccelerated electrons:** Secondly, reacceleration processes of mildly relativistic CRe ($\gamma \simeq 100 - 300$) being injected over cosmological timescales into the ICM by sources like radio galaxies, supernova remnants, merger shocks, and galactic winds can provide an efficient supply of highly-energetic CRe. Owing to their long lifetimes of a few times 10^9 years these mildly relativistic CRe can accumulate within the ICM (see Sarazin 2002, and references therein), until they experience continuous in-situ acceleration either via shock acceleration or resonant pitch angle scattering by turbulent Alfvén waves as originally proposed by Jaffe (1977), reconsidered by Schlickeiser et al. (1987), and lately by Ohno et al. (2002). These acceleration processes of CRe possibly yield extended radio halos centered on the cluster (Brunetti et al. 2001) while there are also suggestions that radio mini-halos within a cooling flow cluster originate from these processes (Gitti et al. 2002). There is also evidence that reacceleration processes acting on fossil radio plasma produces small filamentary radio relics at the cluster periphery, so-called revived radio ghosts (Enßlin & Gopal-Krishna 2001, Enßlin & Brüggen 2002) presumably by adiabatic compression in shock waves.

3. **Particles of hadronic origin:** Eventually, CRp can interact hadronically with the thermal ambient gas producing secondary electrons, neutrinos, and γ-rays in inelastic collisions taking place throughout the cluster volume which would generate radio halos through synchrotron emission (first pointed out by Dennison 1980, Vestrand 1982). In the ICM the CRp have lifetimes of the order of the Hubble time (Völk et al. 1996, Enßlin et al. 1997, Berezinsky et al. 1997), long enough to diffuse away from the production site and to maintain a distribution over the cluster volume. This process was reconsidered in more detail by Blasi & Colafrancesco (1999) and by Dolag & Enßlin (2000), the latter authors using numerical hydro-dynamical simulations including magnetic fields. Recently, Miniati et al. (2001) have performed cosmological simulations of cluster formation including injection processes of primary CRp. These authors conclude that under certain conditions extended diffuse radio emission could be due to hadronically produced CRe. However, there are also claims that extended radio halos cannot be generated by secondary electrons due to the morphological steepness of predicted radio brightness profiles in contrast to observations (Brunetti 2002). Besides constraining the population of CRp in the ICM, this work will present arguments for the hadronic origin of radio mini-halos or a substantial contribution of secondary electrons to these mini-halos. We further perform a parameter study which shows that the large cluster radio halos could be also of hadronic origin, provided the CRp-to-thermal energy density profile is radially increasing.

It is very difficult to distinguish between contributions of these three populations of cosmic ray (CR) particles to non-thermal particle populations, especially if all of them account for injection of cosmic rays into the ICM in different strength depending on underlying governing physical processes and parameters. The hadronically produced CRe may be reaccelerated by shocks or cluster turbulence and therefore mix up the different CRe populations.

Radio observations of the radio halo in the Coma cluster find a strong steepening of the synchrotron spectrum with increasing radius (Giovannini et al. 1993). This behavior is expected for a reaccelerated population of CRe (Brunetti et al. 1999, 2001). There is also a report of radial spectral steepening in the case of the radio mini-halo of Perseus according to Sijbring (1993). This, however, could easily be an observational artifact owing to a poor signal-to-noise ratio in the outer core parts of the cluster in combination with the ambiguity of determining the large scale Fourier components owing to the nonuniform coverage of the Fourier plane and missing short-baseline information: the so-called "missing zero spacing"-problem of interferometric radio observations. By comparing the spectral index distribution of the three radio maps (92 cm, 49 cm, and 21 cm), there seems to be likewise a possibility of radial spectral flattening depending on the chosen radial direction. The hadronic electron model does not necessarily produce the radial spectral steepening without fine-tuning.

6.1.2. Assumptions

The purpose of this chapter is to apply our conceptually simple analytic instruments for describing the spectral signatures in radio, X-rays, and γ-rays resulting from inelastic cosmic ray ion collisions (as derived in Chapter 5). It is especially important to constrain the population of CRp within clusters of galaxies in order to understand the governing physical processes of these objects and the important theoretical implications for the non-thermal

content of the ICM, i.e. if non-thermal CR pressure plays an important role in supporting the intra-cluster ionized gas (Enßlin et al. 1997). The assumptions of our models are:

- CRe are taken to originate from hadronic interactions of CRp with thermal ambient protons of the ICM and the CRp population is described by a power-law distribution in momentum. The origin of this population is not specified here, but CRp may be accelerated by shock waves of cluster mergers, accretion shocks (Colafrancesco & Blasi 1998), or injected from radio galaxies into the ICM (Valtaoja 1984, Enßlin et al. 1997, Blasi & Colafrancesco 1999), or result from supernova driven galactic winds (Völk et al. 1996).

- In our isobaric model, the energy density of CRp is assumed to be proportional to the thermal energy density of the ICM. In our scenario of adiabatic compression of CRp during the formation of the cooling flow this proportionality is imposed prior to the transition. This assumption is reasonable if the thermal electron population and the CRp were energized by the same shock wave assuming that there is a constant fraction of energy going into the CRp population by such an acceleration process. As a third model we take a single central point source injecting the CRp which results in a very peaked CRp profile (compare Blasi 1999, Blasi & Colafrancesco 1999).

- The CRp spectral index is assumed to be independent of position and therefore constant over the cluster volume. In some sense this represents an oversimplification which could be abandoned in order to reproduce some specific observational results, which however would be questionable without understanding the underlying physical processes.

- The electron density and temperature profiles of the ICM are assumed to be spherically symmetric and were taken from the literature. This assumption is justified in the case of γ-rays resulting from neutral pion decay because we use cluster volume averaged spectra in order to compare to observation, and is not severe in the case of radio emission, since the profiles are obtained from deprojected X-ray data. The magnetic field configuration is assumed to be spherically symmetric on cluster core scales and follows the electron density with a power-law index as a free parameter within the suggested range (Dolag et al. 2001, 1999).

- No reacceleration or diffusion process of CRe is taken into account in calculating the synchrotron and the inverse Compton (IC) emission. Therefore we provide conservative estimates for the flux.

- The radio spectrum is taken to be quasi-stationary owing to the short electron cooling time which establishes a stationary CRe population on very short timescales. There is a one-to-one correspondence between the CRp power law index and that of the CRe population which is in addition determined by radiative synchrotron losses and IC cooling.

6.1.3. The expected spectral index α_p

The spectral index of the ICM CRp population α_p is not well constrained by observations. However, because galaxy clusters are able to store CRp for cosmological times (Völk et al. 1996, Enßlin et al. 1997, Berezinsky et al. 1997) the spectral index of the global CRp population (allowing for spatial differentiation) is expected to be that of the injection process, if no re-acceleration processes modified the spectrum after injection. We discuss briefly different possible CRp sources in galaxy clusters:

Structure formation shock waves have generated most of the thermal energy content of galaxy clusters. Therefore, it is plausible to assume that they also produced most of the CR energy of clusters. Shock acceleration is able to produce momentum power-law particle distributions characterized by a spectral index, which is in the test-particle picture of non-relativistic shock acceleration

$$\alpha_\mathrm{inj} = \frac{R+2}{R-1}\,, \tag{6.1}$$

where $R \leq 4$ is the shock compression factor. The lowest spectral indices are therefore generated by the strongest shocks, which are preferentially found in peripheral regions of the clusters (Quilis et al. 1998, Miniati et al. 2000). Thus, harder CRp populations ($\alpha_\mathrm{inj} = 2.0...2.5$) are mostly injected into the outskirts of clusters. However, motion of the ICM gas transports them efficiently into the cluster centers (Miniati et al. 2001).

Injection by radio galaxies: Active galactic nuclei (AGN) are able to produce large amounts of relativistic plasma. The composition of this plasma is not known, however, the presence of CRp is assumed in and supported by many

papers. The energetics of AGN is sufficient to inject a significant CRp population into the thermal ICM (Enßlin et al. 1997, 1998, Colafrancesco & Blasi 1998, Blasi 1999, Wu et al. 2000) provided CRp are present in the radio plasma and are able to leave it on cosmological short timescales. If the radio plasma releases all its CRp, a moderately flat injection spectrum can be expected (say $\alpha_{\mathrm{inj}} \approx 2.5$) since radio emission from radio galaxies indicates flat CRe spectra. If, however, only a small fraction of the CRp is able to leave the radio plasma diffusively, an even flatter spectrum (say $\alpha_{\mathrm{inj}} \approx 2.2$) can be expected due to increasing escape probability with momentum (Enßlin 2003).

Supernova Remnants (SNR) are known to be able to produce flat ($\alpha_{\mathrm{inj}} \approx 2.4$) CR populations and they are believed to be the main CRp source of our galaxy (Schlickeiser 2002, and references therein). The reason for the steeper ($\alpha_{\mathrm{p}} \approx 2.7$) galactic CRp spectrum is thought to be the momentum dependent escape probability from our Galaxy. Thus, the spectrum of CRp escaping from galaxies should be flat again ($\alpha_{\mathrm{inj}} \approx 2.4$). The spectrum injected into galaxy clusters could be even flatter, if termination shock waves of the galactic winds are able to re-accelerate them, as proposed by Völk et al. (1996).

The CRp population in galaxy clusters which is able to interact with the thermal gas and thus to produce observable signatures will be a mixture of contributions of the different sources, modified by acceleration and energy loss processes. In order not to rely too much on a specific physical picture, we discuss simplified models, which should be able to capture many typical situations.

6.1.4. Outline of the chapter

This chapter is structured as follows: after modeling the spatial distribution of CRp within cooling flow clusters (Sect. 6.2), we constrain this population by comparing to EGRET upper limits (Sect. 6.3). We furthermore obtain limits on the CRp population by the morphology of radio brightness profiles in the case of Perseus and Coma (Sect. 6.4). We propose the hadronic scenario to explain the detection of TeV γ-rays of the elliptical galaxy M 87 by the HEGRA collaboration in Sect. 6.5. Finally, we investigate the detectability of the hadronically induced diffuse γ-ray emission by future satellite missions and Čerenkov telescopes in Sect. 6.6. Throughout this chapter we assume the standard ΛCDM cosmology with $\Omega_{\mathrm{M}} = 0.3$, $\Omega_{\Lambda} = 0.7$, and $H_0 = 70\,h_{70}$ km s^{-1} Mpc^{-1}, where h_{70} indicates the scaling with H_0.

6.2. Spatial distribution of cosmic ray protons in cooling flow clusters

In the following, we introduce three models for the spatial distribution of CRp within clusters of galaxies. The origin of the CRp population is not specified in the first two models, but the CRp may be accelerated by shock waves of cluster mergers, accretion shocks, or result from supernova driven galactic winds. In contrast to that we explore in the third model the diffusion process of CRp away from a central AGN. Since it is unclear how CRp are distributed spatially in detail, we investigate here three different scenarios which should serve as toy models. We pursue the philosophy of estimating physical parameters from observationally obtained electron density and temperature profiles by using simplified model assumptions for the CRp population. In doing so we try to minimize the dimensionality of parameter space as much as possible in order to track the main physical processes by means of analytically feasible methods and not to rely upon too many assumptions. Therefore the presented CRp profiles which are based on the assumption of spherical symmetry should not be interpreted as a precise estimate of the CRp population but rather as a plausible spherically averaged scenario.

6.2.1. Isobaric model of CRp

In this model we assume that the average kinetic CRp energy density $\varepsilon_{\mathrm{CRp}}(\boldsymbol{r})$ is a constant fraction of the thermal energy density $\varepsilon_{\mathrm{th}}(\boldsymbol{r})$ of the ICM

$$\varepsilon_{\mathrm{CRp}}(\boldsymbol{r}) = X_{\mathrm{CRp}}\, \varepsilon_{\mathrm{th}}(\boldsymbol{r})\,. \tag{6.2}$$

This distribution might be maintained even in the case of a cooling flow cluster by mixing and ongoing turbulent CRp diffusion processes exerted by relativistic plasma bubbles rising in the gravitational potential of the cluster due to buoyant forces (Churazov et al. 2001, and references therein) which possibly leads to fractional pressure equilibrium with the thermal particle population.

6.2.2. Adiabatic compression of CRp

Here we assume the CRp population to be originally isobaric to the thermal population but to become adiabatically compressed during the formation of the cooling flow while it did not relax afterwards. The phase space volume stays constant during this transition and the momenta and volumes scale according to

$$p_p \rightarrow p_p' = \left(\frac{n_e'}{n_e}\right)^{1/3} p_p = C^{1/3} p_p \,, \tag{6.3}$$

$$V_p \rightarrow V_p' = \left(\frac{n_e'}{n_e}\right)^{-1} V_p = C^{-1} V_p \,. \tag{6.4}$$

Here the compression factor $C = C(\boldsymbol{r}) = (n_e'/n_e)(\boldsymbol{r})$ has been introduced, which is larger than unity within cooling flows. Provided that the electrons have been in hydrostatic equilibrium during this transition, this implies $C(\boldsymbol{r}) = T_{\mathrm{cluster}}/T_e'(\boldsymbol{r})$, where T_{cluster} denotes the electron temperature in the outer core region. This transformation implicitly assumes that the ratio of the CRp number densities before and after the adiabatic compression equals that of the electron population. If the differential number density distribution of the CRp population may be described by a power-law in momentum p_p, then after adiabatic compression of CRp the functional shape of their distribution remains unchanged, however shifted according to

$$f'(\boldsymbol{r}', p') = \frac{\tilde{n}_{\mathrm{CRp}}'(\boldsymbol{r}') c}{\mathrm{GeV}} \left(\frac{p' c}{\mathrm{GeV}}\right)^{-\alpha_p} \,, \tag{6.5}$$

$$\tilde{n}_{\mathrm{CRp}}'(\boldsymbol{r}') = \tilde{n}_{\mathrm{CRp}}[\boldsymbol{r}'(\boldsymbol{r})] \, C(\boldsymbol{r}')^{(\alpha_p+2)/3} \,. \tag{6.6}$$

The normalization $\tilde{n}_{\mathrm{CRp}}(\boldsymbol{r})$ is chosen in such a way that the kinetic CRp energy density makes up a constant fraction of the thermal energy density prior to cooling flow formation and is described by a scaling parameter X_{CRp}

$$\varepsilon_{\mathrm{CRp}}(\boldsymbol{r}) = X_{\mathrm{CRp}} \, \varepsilon_{\mathrm{th}}(\boldsymbol{r}) \rightarrow \varepsilon_{\mathrm{CRp}}'(\boldsymbol{r}') = X_{\mathrm{CRp}}'(\boldsymbol{r}') \, \varepsilon_{\mathrm{th}}'(\boldsymbol{r}') \,. \tag{6.7}$$

After adiabatic compression of CRp this scaling parameter has thus changed to

$$X_{\mathrm{CRp}}'(\boldsymbol{r}) = C^{(\alpha_p+2)/3}(\boldsymbol{r}) \, X_{\mathrm{CRp}} \,. \tag{6.8}$$

Since any hadronically induced emissivity scales with X_{CRp}' we obtain the following relation,

$$j^{\,\mathrm{adiabatic}}(\boldsymbol{r}) = C^{(\alpha_p+2)/3}(\boldsymbol{r}) \, j^{\,\mathrm{isobaric}}(\boldsymbol{r}) \,. \tag{6.9}$$

6.2.3. Diffusion of CRp away from a central AGN

Many galaxy clusters – especially those with a cooling flow – harbor a central galaxy, which often exhibits nuclear activity. The relativistic plasma bubbles produced by the AGN may contain relativistic protons, which can partly escape into the thermal ICM. Most of the CRp that have been injected into the cluster center are either diffusively transported into the surrounding ICM (as assumed by Colafrancesco & Blasi 1998, Blasi 1999) or form relativistic bubbles which rise in the gravitational potential of the cluster due to buoyant forces (Churazov et al. 2001, and references therein). An argument in favor of a significant central CRp injection into the ICM is the much more efficient escape of CRp from the magnetic confinement of the radio plasma bubble during the very early stages due to the bubbles higher geometrical compactness and and expected stronger turbulence level (Enßlin 2003). In addition to this, any galactic wind from a central galaxy will also inject CRp into the cluster center. In order to treat these diffusion processes analytically one has to distinguish between clusters containing a cooling flow region or not. In the first case CRp diffusion will shape their emission profiles owing to the peaked cooling flow profiles while the emission strength in non-cooling flow clusters is mainly governed by the effective injection timescale.

Cooling flow clusters: The transport of CRp through the ICM is diffusive, with a diffusion coefficient $\kappa(r, p)$ which in general may depend on momentum and position. For illustration we use

$$\kappa(r, p) = \kappa_0(r) \left(\frac{p\,c}{\mathrm{GeV}}\right)^{\alpha_{\mathrm{diff}}} \,, \tag{6.10}$$

with $\kappa_0 \sim 10^{27\ldots30}\,\mathrm{cm}^2\,\mathrm{s}^{-1}$ being plausible values. By using this ansatz, we ignore likely deviations of the diffusion coefficient from Eqn. (6.10) in the mildly relativistic regime because these CRp are also not constrained by observations of their hadronic interactions. The coefficient α_{diff} describes the momentum dependence of the diffusion and is expected to be $\alpha_{\mathrm{diff}} \approx \frac{1}{3}$ for active CRp diffusion in a Kolmogorov-like small-scale magnetic turbulence spectrum and $\alpha_{\mathrm{diff}} \approx 0$ for passive advective transport in a turbulent flow. In the latter case $\kappa(p) = v_{\mathrm{turb}}\,\lambda_{\mathrm{turb}}/3 \sim 10^{29}\,\mathrm{cm}^2\,\mathrm{s}^{-1}$, where $v_{\mathrm{turb}} \sim 100\,\mathrm{km/s}$ and $\lambda_{\mathrm{turb}} \sim 10\,\mathrm{kpc}$ are the turbulent velocity and coherence length, respectively.

In a stationary situation, which is a valid approximation for timescales longer than the typical CRp diffusion timescale in the case of a stationary or short-term intermittent CRp source, the CRp distribution functions is given by

$$f_{\mathrm{p}}(r, p_{\mathrm{p}}) \;=\; -\frac{Q(p)}{4\,\pi} \int_0^r \frac{\mathrm{d}r'}{\kappa(r', p)\, r'^2} = \frac{Q_{\mathrm{p}}(p)}{4\,\pi\,\kappa(p)\,r}\,, \tag{6.11}$$

$$\text{where} \quad Q_{\mathrm{p}}(p) \;=\; \frac{Q_{\mathrm{p},0}\,c}{\mathrm{GeV}} \left(\frac{p_{\mathrm{p}}\,c}{\mathrm{GeV}}\right)^{-\alpha_{\mathrm{inj}}} \tag{6.12}$$

is the averaged CRp injection rate of the central source. We assume it to be a power-law in momentum with spectral index α_{inj}, which in general is not identical to the spectral index of the CRp population within radio plasma since the escape fraction is expected to depend on momentum (Enßlin 2003). For the last step in Eqn. (6.11) we assume for simplicity the diffusion coefficient to be independent of position. Possible models of spatial distributions for the diffusion coefficient depend strongly on many unknown quantities such as the dominant diffusion mechanism (active diffusion versus passive advective transport), the velocity field, the turbulence scale, and the topology of the magnetic field, only to mention a few. Therefore we are unable to guess a realistic profile for $\kappa_0(r)$ without enlarging the accessible parameter space tremendously. However since we expect the diffusion coefficient not to change dramatically over the cooling flow scale and since the distribution function $f_{\mathrm{p}}(r, p_{\mathrm{p}})$ is sufficiently steep in radius (Eqn. (6.11)) our results should be approximately correct. The total CRp luminosity of the source can be estimated from Eqn. (6.11) to be

$$L_{\mathrm{CRp}} = \frac{m_{\mathrm{p}}\,c^2\,Q_{\mathrm{p},0}}{2(\alpha_{\mathrm{inj}} - 1)} \left(\frac{m_{\mathrm{p}}\,c^2}{\mathrm{GeV}}\right)^{1-\alpha_{\mathrm{inj}}} \mathcal{B}\!\left(\frac{\alpha_{\mathrm{inj}} - 2}{2}, \frac{3 - \alpha_{\mathrm{inj}}}{2}\right). \tag{6.13}$$

Within our model, the CRp distribution function within the thermal ICM can be written as

$$f_{\mathrm{p}}(r, p_{\mathrm{p}}) = \frac{\tilde{n}_{\mathrm{CRp},0}\,c}{\mathrm{GeV}} \left(\frac{r}{h_{70}^{-1}\,\mathrm{kpc}}\right)^{-1} \left(\frac{p_{\mathrm{p}}\,c}{\mathrm{GeV}}\right)^{-\alpha_{\mathrm{p}}}, \tag{6.14}$$

where $\alpha_{\mathrm{p}} = \alpha_{\mathrm{inj}} + \alpha_{\mathrm{diff}}$.[1]

In order to obtain a realistic estimate for the diffusion volume to be considered, the relevant length scale needs to be taken into account. We define the characteristic scale R_{diff} by calculating the second moment of the time-dependent distribution function of the first particles released by the source, yielding

$$R_{\mathrm{diff}} = \sqrt{2\,n_{\mathrm{dim}}\,t_{\mathrm{inj}}\,\kappa(p)} \simeq 80\,h_{70}^{-1/2}\,\mathrm{kpc} \left(\frac{p\,c}{\mathrm{GeV}}\right)^{\alpha_{\mathrm{diff}}/2}, \tag{6.15}$$

where $n_{\mathrm{dim}} = 3$ denotes the number of spatial dimensions. Here we assume a typical lifetime of $t_{\mathrm{inj}} = 3\,h_{70}^{-1}\,\mathrm{Gyr}$ and $\kappa_0 \simeq 10^{29}\,\mathrm{cm}^2\,\mathrm{s}^{-1}$. Beyond this scale R_{diff} there can be a CRp population resulting from diffusion away from the central AGN which is however exponentially suppressed. Because the γ-ray luminosity resulting from hadronic CRp interactions scales as

$$\mathcal{L}_{\gamma} \propto 4\,\pi \int \mathrm{d}r\, r^2 \tilde{n}_{\mathrm{CRp}}(r)\, n_{\mathrm{e}}(r) \propto \int \mathrm{d}r\, r^{1-3\beta}\,, \tag{6.16}$$

---

[1] This seems to be in contradiction to the identity of injection and equilibrium spectral index for a system without escape claimed in Sect. 6.1.3. Formally, we had to include particle escape from the galaxy cluster in order to be able to have a finite steady state solution of the diffusion problem, as given by Eqn. (6.11). In the realistic case of a finite age of the system the stationary solution is only approximately valid in the center of the galaxy cluster. However, only there exists a sufficiently high target density to detect the CRp population. Therefore, although we use a poor description of the CRp profile on large-scales, the estimated γ-ray fluxes should be sufficiently accurate.

we always obtain centrally peaked γ-ray profiles, since the cooling radius is smaller than the diffusion scale, $r_{c_1} < R_{\text{diff}}$, and $\beta > 1/3$ within cooling flow regions (compare Table C.1). Thus, the γ-ray luminosity is only weakly dependent on R_{diff} as long as it reflects the correct order of magnitude.

In this work we constrain $\tilde{n}_{\text{CRp},0}$ with the aid of γ-ray observations of galaxy clusters. From these constraints limits on the averaged CRp luminosity escaping from the radio plasma of the central galaxy can be derived using

$$\frac{L_{\text{CRp}}}{\kappa_0} = \frac{4\pi m_{\text{p}} c^2 \tilde{n}_{\text{CRp},0} h_{70}^{-1} \text{ kpc}}{2(\alpha_{\text{inj}} - 1)} \left(\frac{m_{\text{p}} c^2}{\text{GeV}}\right)^{1-\alpha_{\text{inj}}} \mathcal{B}\left(\frac{\alpha_{\text{inj}} - 2}{2}, \frac{3 - \alpha_{\text{inj}}}{2}\right), \tag{6.17}$$

where we again ignored any possible low-energy spectral cutoff, since it can be included a posteriori with the help of Fig. 5.1. As a rough estimate we find numerically

$$L_{\text{CRp}} = L(\alpha_{\text{inj}}) \, 10^{43} \, h_{70}^{-1/2} \text{ erg s}^{-1} \left(\frac{\kappa_0}{10^{29} \text{ cm}^2 \text{ s}^{-1}}\right) \left(\frac{\tilde{n}_{\text{CRp},0}}{10^{-6} \, h_{70}^{1/2} \text{ cm}^{-3}}\right), \tag{6.18}$$

with $L(\alpha_{\text{inj}}) = 6.1$, 2.2, 1.6, and 1.7 for $\alpha_{\text{inj}} = 2.1$, 2.3, 2.5, and 2.7, respectively. In Sect 6.3.4 we analyze these constraints for our cluster sample in more detail.

Non-cooling flow clusters: In transforming the above considerations on diffusion length scales to the case of non-cooling flow clusters we point out the following differences: in non-cooling flow clusters the core radius is normally larger than the diffusion scale, $r_c > R_{\text{diff}}$, over which the electron density varies only slightly. Thus, a stationary solution to the diffusion equation is not applicable in the case of a flat target profile. It follows that the volume integrated γ-ray spectrum does not depend on the diffusion coefficient but only on the injection time t_{inj} of CRp into the ICM of the cluster core. We therefore adopt a modification to the diffusion model for non-cooling flow clusters. The averaged CRp luminosity of the central galaxy reads in this context

$$L_{\text{CRp}} = \frac{\tilde{N}_{\text{CRp}}}{t_{\text{inj}}} \frac{m_{\text{p}} c^2}{2(\alpha_{\text{inj}} - 1)} \left(\frac{m_{\text{p}} c^2}{\text{GeV}}\right)^{1-\alpha_{\text{inj}}} \mathcal{B}\left(\frac{\alpha_{\text{inj}} - 2}{2}, \frac{3 - \alpha_{\text{inj}}}{2}\right). \tag{6.19}$$

Here $\tilde{N}_{\text{CRp}}$ denotes the integrated number of CRp being injected into the ICM of the cluster and $\alpha_{\text{inj}} = \alpha_{\text{p}}$, because there is no diffusion induced spectral steepening simply due to the fact that the even more energetic CRp which are still significantly contributing to the γ-ray flux in the EGRET energy band are not able to leave the central core region within a reasonable timescale.

6.3. Constraining the population of CRp by the integrated flux of γ-rays in different clusters

6.3.1. Cluster sample

Based on our analytic relation between the γ-ray and bolometric X-ray fluxes (Eqn. (5.27)), we compile a sample of suitable clusters to obtain observationally promising cluster candidates for constraining the CRp population as well as the future detection of diffuse γ-rays resulting from hadronic CRp interactions. As a simple scenario we choose the CRp energy density to be a constant fraction of the thermal energy density, $\varepsilon_{\text{CRp}}(\boldsymbol{r}) = X_{\text{CRp}} \, \varepsilon_{\text{th}}(\boldsymbol{r})$.

Applying the $\mathcal{F}_\gamma$–F_X scaling relation and taking bolometric X-ray fluxes from David et al. (1993) while fixing $X_{\text{CRp}} = 0.01 \, X_{0.01}$ and $\alpha_{\text{p}} = 2.3$ we estimated γ-ray fluxes $\mathcal{F}_{\gamma,\text{est}}(> 100 \text{ MeV})$ for the spectral sensitivity of EGRET in order to choose our cluster sample (see Table C.2). Inferred values for the estimated γ-ray flux $\mathcal{F}_{\gamma,\text{est}}$ by means of the $\mathcal{F}_\gamma$–F_X scaling relation sensitively depend on the bolometric X-ray luminosity of the particular cluster such that values for $\mathcal{F}_{\gamma,\text{est}}$ in Table C.2 represent a rough estimate. A detailed modeling using density and temperature profiles will be described later on in Sect. 6.3.2 in order to obtain upper limits on the CRp population. By comparing γ-ray fluxes $\mathcal{F}_\gamma$ obtained from these two different methods we recognized an inconsistency for the Virgo and Centaurus cluster: this discrepancy is explained by a too small aperture of the X-ray experiments analyzed by David et al. (1993) giving rise to an underestimation of the X-ray flux of these two nearest clusters in our sample ($z_{\text{Virgo}} = 0.0036$ and $z_{\text{Centaurus}} = 0.0114$) and therefore an underestimate of $\mathcal{F}_{\gamma,\text{est}}$ for these two clusters. Moreover, we noticed a systematic discrepancy of the order of 50% between the different methods in cooling flow clusters which is due to an insufficient accounting for the radial temperature variation in Eqn. (5.27).

Parameters of electron density profiles $n_e(r)$ of our cluster sample are given in Table C.1 where the clusters are ordered according to their property of containing a cooling flow (upper part) or not (lower part). Note that the parameters are subject to different formulae (6.20) and (6.21),

$$n_e(r) \;=\; \sum_{i=1}^{2} n_i \left(1 + \frac{r^2}{r_{c_i}^2}\right)^{-3\beta/2}, \tag{6.20}$$

$$n_e(r) \;=\; \left[\frac{\tilde{\Lambda}[T_e(0)]}{\tilde{\Lambda}[T_e(r)]} \times \sum_{i=1}^{2} n_i^2 \left(1 + \frac{r^2}{r_{c_i}^2}\right)^{-3\beta}\right]^{1/2}. \tag{6.21}$$

The last equation (6.21) follows from deprojection of X-ray surface brightness profiles which are represented by double β-models. The derivation of this deprojection is given in Appendix A. For simplicity and consistency with the X-ray surface brightness profiles given in Mohr et al. (1999) we ignored the weak dependency on $T_e(r)$ in Eqn. (6.21). In order to model the temperature profiles $T_e(r)$ for our cooling flow cluster sample we applied the universal temperature profile for relaxed clusters proposed by Allen et al. (2001) to data taken from the literature,

$$T_e(r) = T_0 + (T_1 - T_0) \left[1 + \left(\frac{r}{r_{\text{temp}}}\right)^{-\eta}\right]^{-1}. \tag{6.22}$$

This equation matches the temperature profile well up to radii of $\sim 0.3\, r_{\text{vir}}$, which is sufficient for our purposes since we are especially interested in the core region of clusters. The parameters of the temperature profile for particular cluster are given in Table C.2.

6.3.2. Simulated γ-ray flux normalized by EGRET limits: the case of Perseus cluster

The volume integrated omnidirectional differential γ-ray source function $Q_\gamma(E_\gamma)$ can be obtained by integrating Eqn. (5.18). We integrated the volume out to a radius of $3\, h_{70}^{-1}$ Mpc which corresponds to the characteristic distance where the simple β-model of electron densities breaks down due to accretion shocks in clusters. The integration kernel $q_\gamma(\boldsymbol{r}, E_\gamma)$ scales linearly with $\tilde{n}_{\text{CRp}}(\boldsymbol{r})$ (as shown in Eqn. (5.18)) which is obtained by solving Eqns. (5.7) and (5.10). By comparing the integrated γ-ray flux above 100 MeV, $\mathcal{F}_\gamma(> 100\,\text{MeV})$, to EGRET upper limits (see Reimer et al. 2003), we constrain the CRp scaling parameter X_{CRp}. The inferred value for X_{CRp} in the Perseus cluster normalizes the differential γ-ray flux

$$\frac{d\mathcal{F}_\gamma}{dE_\gamma} \equiv \frac{Q_\gamma(E_\gamma)}{4\pi D^2} \tag{6.23}$$

in Fig. 5.3. The π^0-meson decay induced distinct spectral signature resulting in the peak at a γ-ray energy of $m_{\pi^0} c^2/2 \simeq 67.5$ MeV can be clearly seen.

Figure 5.3 shows also upper limits on the differential γ-ray flux owing to IC emission of hadronically originating CRe represented by power-laws. The IC spectra are computed by means of Eqn. (5.39) for different spectral indices α_p and zero magnetic field. Non-zero magnetic fields can be included since the IC spectra scale according to $B_{\text{CMB}}^2/(B(\boldsymbol{r})^2 + B_{\text{CMB}}^2)$ (see Eqn. (5.32)) which results in a lower normalization.

6.3.3. Results on the scaling parameter X_{CRp} using γ-ray observations in different clusters

By employing the technique described in Sect. 6.3.2 we constrained the CRp scaling parameter X_{CRp} using EGRET upper limits of the γ-ray flux by Reimer et al. (2003). As described in that section, we infer the γ-ray flux of this clusters originating from within a sphere of radius $3\, h_{70}^{-1}$ Mpc. Owing to the vicinity of the Virgo cluster this maximum radius subtends an angle on the sky which is larger than the width of the point spread function of the EGRET instrument ($\theta_{\text{max}} = 5.8° \,[E_\gamma/(100\,\text{MeV})]^{-0.534}$, Reimer et al. (2003)). Thus in the case of Virgo we use this smaller integration volume.

Figure 6.1 shows constraints for X_{CRp} using the isobaric model of CRp described in Sect. 6.2. The adiabatic model yields slightly tighter limits on X_{CRp}. For clusters like Perseus (A 426), Virgo, Ophiuchus, and Coma (A 1656) we can obtain quite tight constraints on the population of CRp. For the sake of completeness, the full table of constraints
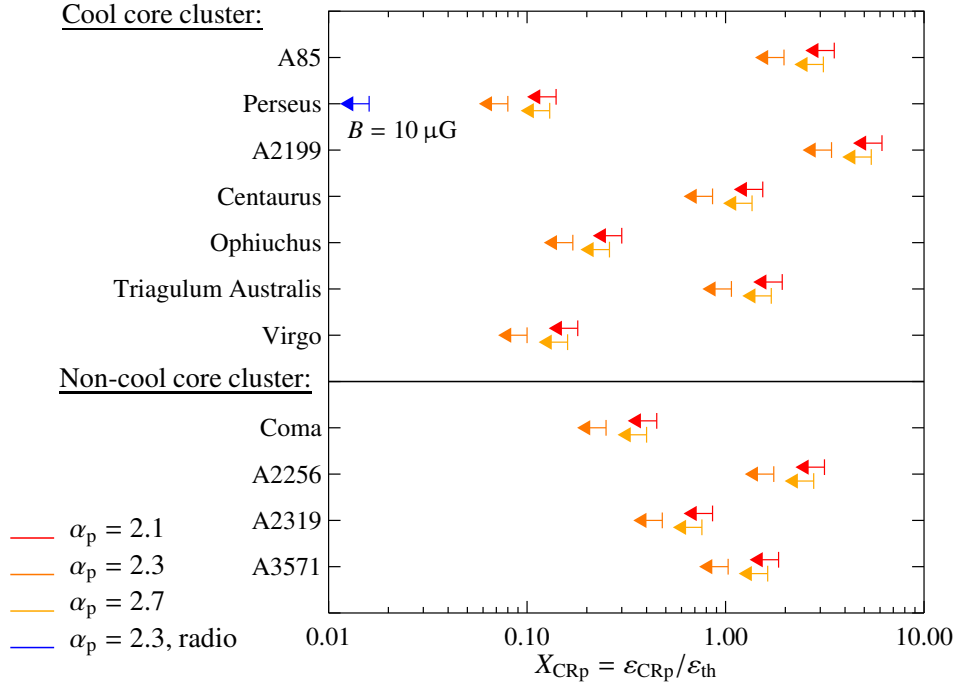
Figure 6.1.: Upper limits on the CRp scaling parameter X_{CRp} by comparing the integrated flux above 100 MeV to EGRET upper limits assuming a γ-ray spectral index in Dermer's model $\alpha_\gamma = \alpha_p$. The spatial distribution of CRp is given by the isobaric model of CRp (see Sect. 6.2.1). The blue arrow refers to the upper limit on X_{CRp} inferred from radio brightness profiles of the radio mini-halo of Perseus cluster for the parameter combination $B_0 = 10\,\mu\text{G}$, $\alpha_B = 0.5$, and $\alpha_p = 2.3$.

for X_{CRp} using the isobaric and the adiabatic model of CRp is shown in Table C.3. Because in the adiabatic model the CRp scaling parameter X_{CRp} is a function of radius, the value $X_{\text{CRp}}^{\text{adiabatic}}$ given in Table C.3 refers to the unprimed quantity in Eqn. (6.8) which reflects the outer core region of the cluster.

6.3.4. Results on L_{CRp} in the AGN-diffusion model

The procedure of inferring constraints on CRp diffusing away from a central source is mostly sensitive to the CRp population of the central cooling flow region rather than the shock region in the outer parts of the cluster. In order to constrain the CRp density parameter $\tilde{n}_{\text{CRp},0}$ and averaged CRp luminosity L_{CRp} of the central active galaxy in our AGN-diffusion model of *cooling flow clusters* we have to calculate the volume integrated omnidirectional differential γ-ray source function $Q_\gamma(E_\gamma)$ (see Eqn. (5.2)). The integration kernel $q_\gamma(E_\gamma)$ is proportional to $\tilde{n}_{\text{CRp}}(r)$ (Eqn. (5.18)) which is obtained by solving Eqns. (5.6) and (6.14). By comparing the integrated γ-ray flux above 100 MeV to EGRET upper limits (see Reimer et al. 2003), we constrain the CRp density parameter $\tilde{n}_{\text{CRp},0}$. In the case of *non-cooling flow clusters* we constrain the averaged CRp luminosity L_{CRp} with the aid of the integrated CRp number parameter $\tilde{N}_{\text{CRp}}$, yielding an indirect measure of a combination of the CRp escape fraction from the radio plasma of the central galaxy and the averaged CRp luminosity of this source.

Upper limits on the CRp density parameter $\tilde{n}_{\text{CRp},0}$, number parameter of CRp $\tilde{N}_{\text{CRp}}$, and averaged CRp luminosity L_{CRp} of the central active galaxy (by means of Eqn. (6.17)) are presented in Table C.4. For the sake of better comparison, Fig. 6.2 additionally illustrates the averaged CRp luminosity L_{CRp} of the central active galaxy. This shows that within this conceptually simple model we are able to put constraints on L_{CRp}. The limits which are strongest in the case of M87 in the Virgo cluster represent conservative bounds since we choose the active CRp diffusion scenario resulting in spectral steepening of the CRp population. We obtain even tighter limits when
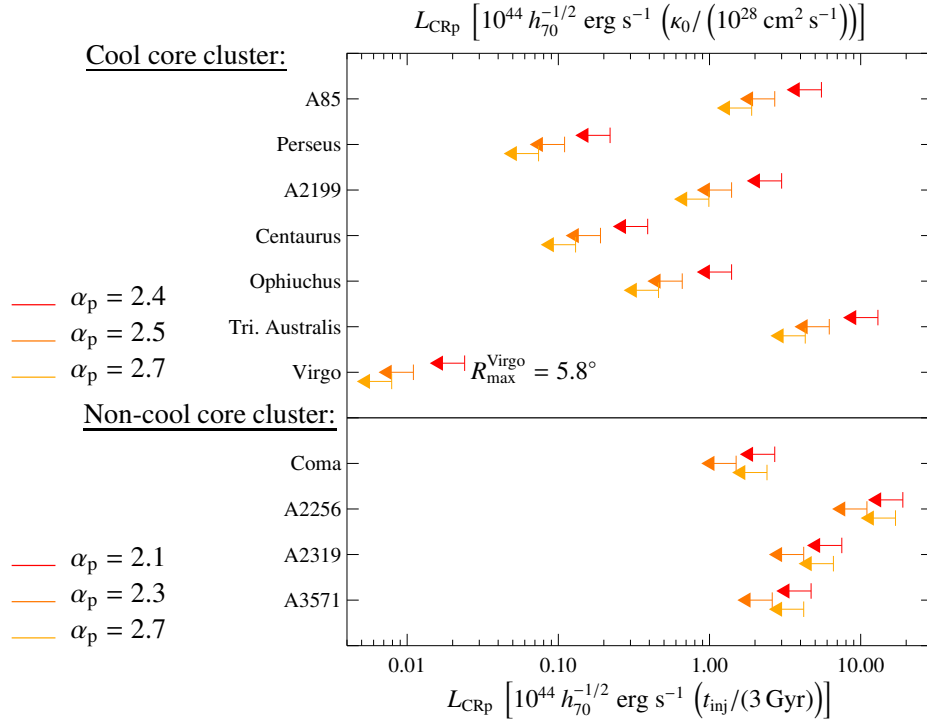
Figure 6.2.: *Cool core clusters:* Upper limits on the average CRp luminosity L_{CRp} of the central active galaxy by comparing the integrated flux above 100 MeV to EGRET upper limits assuming a γ-ray spectral index in Dermer's model $\alpha_\gamma = \alpha_p$. The spatial distribution of CRp is is calculated according to the diffusion model of CRp away from a central AGN assuming $\alpha_p = \alpha_{inj} + \alpha_{diff}$, where $\alpha_{diff} = 1/3$. *Non-cool core clusters:* Upper limits on the average CRp luminosity L_{CRp} without any diffusion induced spectral steepening, i.e. $\alpha_p = \alpha_{inj}$. Note that L_{CRp} scales in the case of cool core clusters with the diffusion coefficient κ_0 while it only depends on the CRp injection time t_{inj} for non-cool core clusters (see Sect. 6.2.3).

---

assuming a passive advective transport of the CRp in a turbulent flow in which case we infer

$$L_{CRp} = L(\alpha_p)\, 10^{42}\, h_{70}^{-1/2}\ \mathrm{erg\ s^{-1}} \left(\frac{\kappa_0}{10^{29}\ \mathrm{cm^2\ s^{-1}}} \right) \tag{6.24}$$

with $L(\alpha_p) = 4.5, 4.8, 7.2$, and 20.9 for $\alpha_p = 2.4, 2.5, 2.7$, and 2.9, respectively. These values are slightly smaller than instantaneous jet power estimates of M87 being of the order of $L_{jet} \simeq 10^{43}$ erg s^{-1} (Bicknell & Begelman 1996, Young et al. 2002). In general, this demonstrates the ability of future high resolution γ-ray observations to constrain the energy fraction of CRp escaping from the radio plasma.

6.4. Radio emissivity of secondary electrons

6.4.1. The radio mini-halo in Perseus

In contrast to γ-rays induced by hadronic CRp interactions whose spectral shape and normalization is only governed by the spectral index α_p as free parameter, the resulting radio emission from secondary electrons also depends on the morphology and strength of the magnetic field $B(r)$. Because only a subsample of cooling flow clusters contain radio mini-halos which are not outshined by the central AGN we decided to concentrate on the Perseus cluster. It has the fortunate property that the radio emission due to the central galaxy NGC 1275 is spatially resolved and can be separated from the diffuse emission due to the radio-mini halo.

Table 6.1.: Upper limits on the CRp scaling parameter X_{CRp} inferred from radio brightness profiles of the radio mini-halo of Perseus cluster for different values of B_0, α_B, and α_{p}.

Model	α_{p}	B_0 [µG]	α_B	$X_{\mathrm{CRp}}^{\mathrm{isobaric}}$	$X_{\mathrm{CRp}}^{\mathrm{adiabatic}}$
1	2.3	10	0.5	0.016	0.006
2	2.1	10	0.5	0.014	0.005
3	2.5	10	0.5	0.033	0.011
4	2.7	10	0.5	0.096	0.031
5	2.3	5	0.5	0.027	0.009
6	2.3	20	0.5	0.012	0.004
7	2.3	10	0.7	0.017	0.006
8	2.3	10	0.9	0.019	0.006

6.4.1.1. Intracluster magnetic fields

Magnetic fields in galaxy clusters seem to be on the level of $\sim$ µG. Indirect estimates of magnetic field strength assuming equipartition of energy density of the fields and that of a radio synchrotron emitting relativistic electron population give low field strengths of ~ 0.1 µG. Also lower limits on the field strength of a comparable level can be derived using the measurements or upper limits on IC scattered CMB photons in the hard X-ray band (Rephaeli et al. 1994, Fusco-Femiano et al. 1999, Enßlin et al. 1999). Conversely, Faraday rotation measurements indicate magnetic fields strengths of several µG in typical galaxy clusters and a few 10 µG in cooling flow regions of clusters (Carilli & Taylor 2002, for a review). Faraday rotation based measurements of the field strength depend on estimating the magnetic autocorrelation length from fluctuations in the Faraday rotation maps. Although the formerly used methods to estimate this length-scale seem to be questionable (Enßlin & Vogt 2003) a refined analysis gives comparable results for the magnetic field strengths (Vogt & Enßlin 2003, in preparation).

6.4.1.2. Comparison of the morphology of radio emissivity from secondary electrons

The radio data was taken from Pedlar et al. (1990) where we neglected the innermost data points because of enhanced contribution to radio brightness of the radio jet of NGC 1275 and the outermost data points due to the limited sensitivity on the larger scales of the specific VLA configuration likely leading to an artificial decline in the radio surface brightness. The values for the azimuthally averaged radio surface brightness were converted assuming a two-dimensional Gaussian beam which leads to a beam area $A_{\mathrm{beam}} = \pi (4 \ln 2)^{-1} \mathrm{FWHM}_x \mathrm{FWHM}_y$. Figure 6.3 shows the radial distribution of radio brightness $S_\nu(r_\perp)$ as a function of impact parameter $r_\perp$ obtained by means of Eqn. (5.38) in comparison to the radio data. The CRp adiabatic and isobaric model being described in Sect. 6.2 are both shown using model parameters of $\alpha_{\mathrm{p}} = 2.3$, $B_0 = 10$ µG, and $\alpha_B = 0.5$, where the latter two parameters refer to Eqn. (5.37). The normalization of the radio brightness depends on the assumed scaling between CRp and thermal energy density. We fix this scaling parameter X_{CRp} by comparing the simulated radio brightness to the measured data at 24.65 h_{70}^{-1} kpc. There is an excellent morphological concordance of the isobaric model of CRp and the radio data for the radio-mini halo of the Perseus cluster. Since the required values of X_{CRp} are plausible (~ 0.01–0.1, see Sect. 6.4.1.3), the hadronic secondary CRe model is a very attractive explanation for the observed radio mini-halos in cooling flow clusters.

6.4.1.3. Results on the scaling parameter X_{CRp} using radio observations in different models

By comparing the simulated radio brightness to the measured radio data at 24.65 h_{70}^{-1} kpc which is the innermost azimuthally averaged data point not being outshined by the radio galaxy cocoon of NGC 1275 we determine the CRp scaling parameter X_{CRp}. Taking this point of reference yields more conservative upper limits for X_{CRp} instead of normalizing by the integrated radio surface brightness especially in the case of poorer morphological matches. The inferred values for X_{CRp} in Table 6.1 are shown for different combinations of B_0, α_B, and α_{p}.

Deduced values of this scaling parameter X_{CRp} which are obtained by considering only pion decay induced sec-
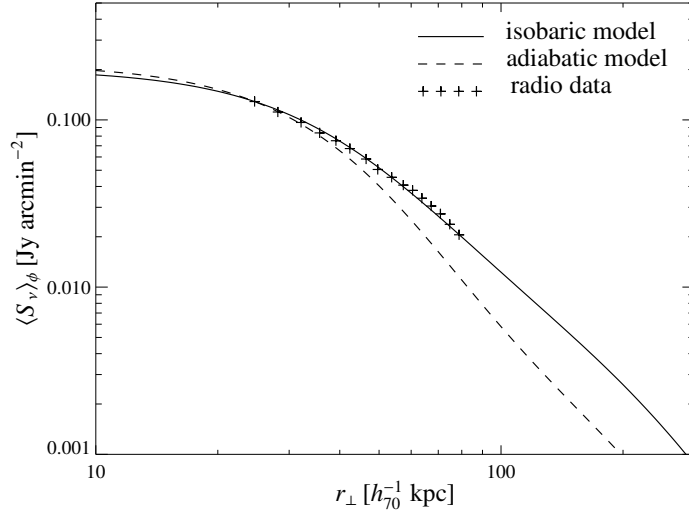
Figure 6.3.: The radial distribution of radio brightness as a function of impact parameter $r_\perp$. Shown are the CRp adiabatic and isobaric model for model parameters $B_0 = 10$ µG, $\alpha_B = 0.5$, and $\alpha_p = 2.3$ (details are described in the text) as well as the azimuthally averaged radio brightness profile of the the Perseus radio-mini halo (data was taken from Pedlar et al. 1990). The normalization of the radio brightness depends on the assumed scaling between CRp and thermal energy density. We fix this scaling parameter X_{CRp} by comparing the simulated radio brightness to the measured data at 24.65 h_{70}^{-1} kpc.

ondary electrons resulting from hadronic CRp interactions in the ICM reflect upper limits because there are also other mechanisms in galaxy clusters leading to relativistic populations of electrons (see Sect. 6.1). By analyzing the variations of our model parameters in Table 6.1 we conclude a weak dependence of X_{CRp} on α_B while the magnetic field strength at the cluster center B_0 and the CRp spectral index α_p show a stronger influence on X_{CRp}. The spectral parameter of the magnetic field α_B impacts mostly on the radial extensions of the radio brightness profiles while the CRp scaling parameter reflects a degeneracy with respect to B_0 and α_p.

Figure 6.4 shows the scaling parameter $X_{CRp}(r)$ as a function of radius r between CRp and thermal energy density in the adiabatic model according to Eqn. (6.8) for models defined in Table 6.1. The enhancement of CRp relative to the thermal energy density owing to adiabatic compression of the CRp population during the formation of the cooling flow can be clearly seen.

6.4.2. Constraints derived from the radio halo of Coma

6.4.2.1. Parameter study of the hadronic scenario

We also applied this formalism of synchrotron radiation emitted by secondary electrons as presented in Sect. 5.5 to the radial distribution of radio brightness in the radio halo of the Coma cluster using radio data at 1.4 GHz by Deiss et al. (1997). Assuming the CRp population to be distributed according to the isobaric model, the spatial radio brightness profile obtained by this secondary electron model declines too fast with increasing impact parameter $r_\perp$ in order to account for the observed extended radio halo of Coma. To check whether this shortfall of the theoretical model represents a serious problem for the hadronic model of radio synchrotron emission we are asking in turn for the necessary radial variation of the CRp scaling parameter $X_{CRp}(r)$ that is able to explain the observed radio halo. Deprojecting the azimuthally averaged observed radio surface brightness profile which is described by a β-model yields (as laid down in Appendix A)

$$j_\nu(r) = \frac{S_0}{2\pi r_c} \frac{6\beta - 1}{\left(1 + r^2/r_c^2\right)^{3\beta}} \mathcal{B}\left(\frac{1}{2}, 3\beta\right), \tag{6.25}$$
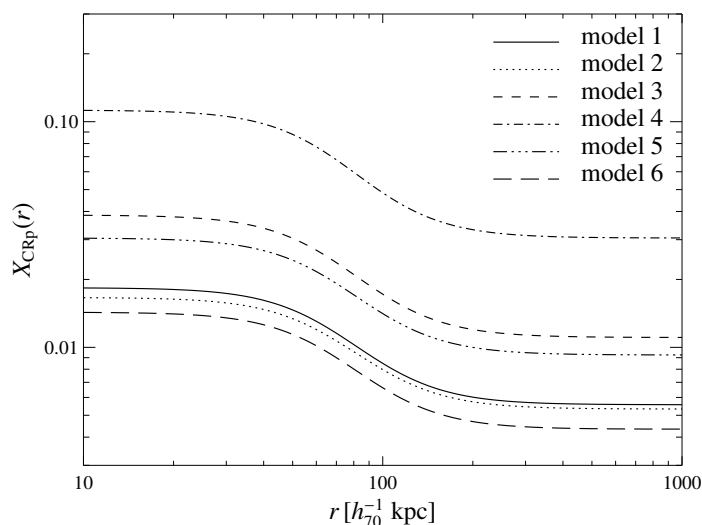
Figure 6.4.: The deprojected scaling parameter $X_{CRp}(r)$ between CRp and thermal energy density in the adiabatic model applied to the mini-radio halo of Perseus and presented for models which are defined in Table 6.1.

where $S_0 = 1.1$ mJy arcmin^{-2}, $r_c = 450\,h_{70}^{-1}$ kpc, and $\beta = 0.78$. By comparing the observed to the theoretically expected radio emissivity at each radius we infer the ratio of CRp-to-thermal energy density $X_{CRp}(r)$. Figure 6.5 shows a comparison of $X_{CRp}(r)$ and the ratio of magnetic-to-thermal energy density $X_B(r) = \varepsilon_B(r)/\varepsilon_{th}(r)$ for particular model parameters α_p, α_B, and B_0. Whereas α_p and B_0 impact mostly on the normalization of both scaling parameters $X_{CRp}(r)$ and $X_B(r)$, the choice of α_B governs the relative curvature of these functions: $X_B(r) \propto n_e(r)^{2\alpha_B-1}$ is curved in a convex fashion for $\alpha_B > 0.5$ and exhibits concave curvature for $\alpha_B < 0.5$ assuming the cluster to be isothermal which is a valid approximation for Coma. While there are combinations of parameters for which $X_{CRp}(r)$ becomes larger than unity and thus question the hadronic scenario (Brunetti 2002), only small variations in parameter space yield plausible values for $X_{CRp}(r)$ (compare Fig. 6.5).

In order to quantify these considerations we perform a parameter study to exclude regions of parameter space spanned by α_p, α_B, and B_0 where the hadronic scenario is challenged to account for the radio halo in Coma. Figure 6.6 shows the resulting contour lines of $X_{CRp}(r \le 1\,h_{70}^{-1}$ Mpc$) = 1$ and $X_{CRp}(r \le 1\,h_{70}^{-1}$ Mpc$) = 0.1$ in this parameter space. The gradient of $X_{CRp}(r \le 1\,h_{70}^{-1}$ Mpc$)$ points towards the lower right corner in Fig. 6.6 and thus leaves the upper left region of parameter space where the hadronic scenario is able to account for the observed radio halo depending on the specific choice of α_B. Since $X_B(r \le 1\,h_{70}^{-1}$ Mpc$) < 0.1$ for the entire region of parameter space investigated here there are no further constraints imposed on the hadronic scenario.

Choosing the energy density of the magnetic field to decline like the thermal energy density, i.e. $\alpha_B = 0.5$, requires $X_{CRp}(r)$ to increase by a factor of less than two orders of magnitude from the center to the outer parts of the cluster in order to reproduce the observed radio halo of Coma. This factor, however, is reduced for smaller values of α_B. It is further reduced due to the non-spherical morphology of Coma, as explained in the following. The X-ray emissivity and the radio emissivity resulting from hadronic CRp interactions differ in their scaling with the electron density according to

$$\Lambda_X(r) \quad \propto \quad n_e(r)^2 \quad \text{and} \tag{6.26}$$

$$j_\nu(r) \quad \propto \quad X_{CRp}(r)\,n_e(r)^{2+\alpha_B(1+\alpha_p/2)} \sim X_{CRp}(r)\,n_e(r)^{3\ldots4} \tag{6.27}$$

within the framework set by our model and depending on the particular choice of α_B and α_p. Thus, any anisotropy like the Coma X-ray and radio bridge yields biased azimuthal averages when comparing observational to theoretical radio surface brightness profiles where the latter uses density profiles obtained by deprojecting X-ray profiles. Remarkably, this discrepancy is largest for large values of α_B and α_p for which we infer the tightest limits on the hadronic scenario (cf. Fig. 6.6) and thus softens these limits. This results in biased profiles of $X_{CRp}(r)$ which increase
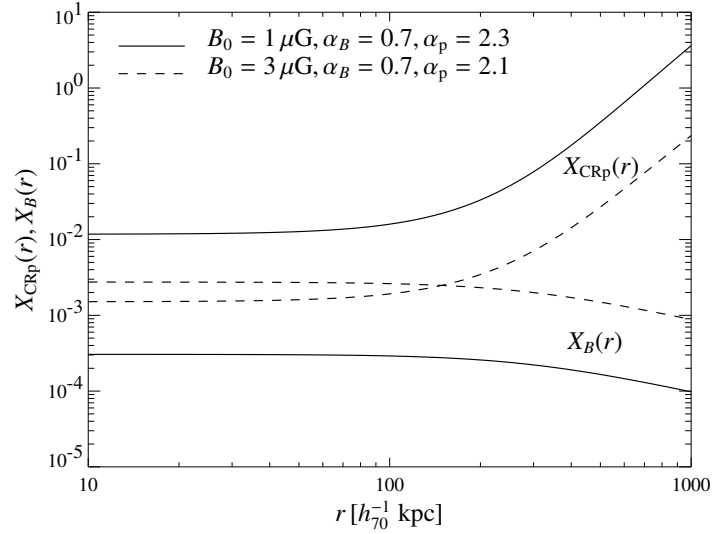
Figure 6.5.: The deprojected CRp scaling parameter $X_{CRp}(r)$ required to account for the observed radio halo in Coma within the framework of the hadronic scenario. The rising curves with increasing radius represent $X_{CRp}(r)$ while the declining curves show $X_B(r)$ for the particular choice of a magnetic field being frozen into the flow and isotropized, i.e. $\alpha_B = 0.7$ (Tribble 1993).

too strongly towards larger radii (cf. also Dolag & Enßlin 2000). Pursuing an approach of averaging only along the line of sight could attenuate the bias (Govoni et al. 2001).

An increase of $X_{CRp}(r)$ towards the cluster's periphery is indeed observed in cosmological structure formation simulations due to adiabatic compression inside the cluster which increases the thermal pressure at a higher rate than the CRp pressure (Miniati et al. 2001). Bearing in mind that the CRp-to-thermal pressure ratio of Miniati et al. (2001) is obtained from volume averages and the energy density stored in magnetic fields declines shallower in comparison to the thermal energy density we conclude that our results arising the parameter study may be well in agreement with these simulations.

6.4.2.2. The spectrum of the Coma radio halo

One might object that the CRp spectral index should be determined better owing to radio observations than the range of $\alpha_p = (2, 3)$ being considered in the previous parameter study (Sect. 6.4.2.1). The following line of argumentation shows, that this, on the contrary, is not the case. First, there is an ambiguity of relating the CRp spectral index α_p to the induced synchrotron spectral index α_ν which is either $\alpha_\nu = \alpha_p/2$ (Dermer's model) or $\alpha_\nu = (2\,\alpha_p - 1)/3$ (fireball model). When comparing multifrequency observations of diffuse radio emission of the ICM which extends to several GHz the Sunyaev-Zel'dovich (SZ) distortion of the spectrum has to be taken care of. At these frequencies of the Rayleigh-Jeans part of the Planck spectrum the SZ effect amounts to a decrement which introduces a cutoff in the radio spectrum as can be seen in Fig. 6.7. Following Enßlin (2002) the SZ luminosity reads for Coma in the Rayleigh-Jeans part

$$F_{SZ}^{Coma} = -4.1 \times 10^{-3} \nu_{GHz}^2 \, h_{70}^{-1/2} \, \text{Jy}, \tag{6.28}$$

where $\nu_{GHz} = \nu/\text{GHz}$.[2] However, the SZ amplitude is uncertain within a factor of 2 which stems mostly from density profiles being inferred from X-ray observations and extrapolated to R_{shock}. Furthermore, the multifrequency dataset as compiled by Thierbach et al. (2003) is inhomogeneous because the solid angle over which the observed radio fluxes have been integrated may vary among these observations. Finally, the quoted uncertainties may underestimate the systematic uncertainties which e.g. result from incomplete accounting for point source subtraction.

---

[2]Here we corrected for a missing factor of 2 in Eqn. (4) in Enßlin (2002) and changed the slope of the β-profile to $\beta = 0.75$ (Briel et al. 1992).
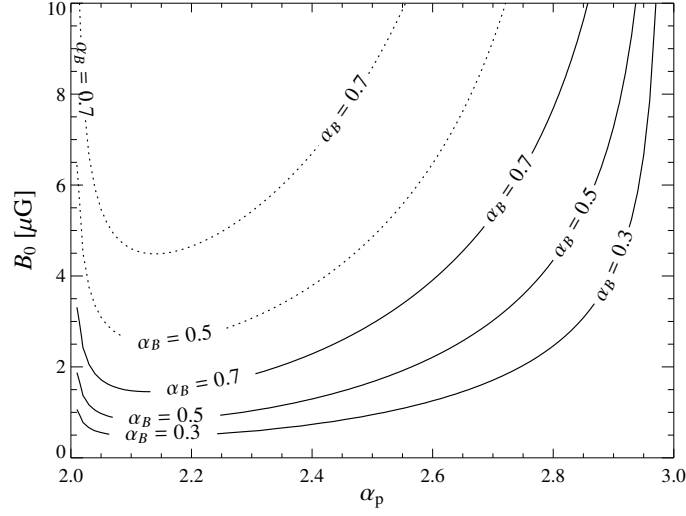
Figure 6.6.: Parameter study on the ability of hadronically originating CRe to generate the radio halo of Coma. Shown are contour lines of $X_{CRp}(r \leq 1\,h_{70}^{-1}\,Mpc) = 1$ (solid) and $X_{CRp}(r \leq 1\,h_{70}^{-1}\,Mpc) = 0.1$ (dotted) in parameter space spanned by α_p and B_0 for three choices of magnetic field morphology characterized by α_B. The contour line of $X_{CRp} = 0.1$ for $\alpha_B = 0.3$ has been omitted since it almost coincides with the contour of $X_{CRp} = 1$ for $\alpha_B = 0.7$. The lower right corner represents the region in parameter space, where the hadronic scenario faces challenges for explaining the observed radio halo of Coma.
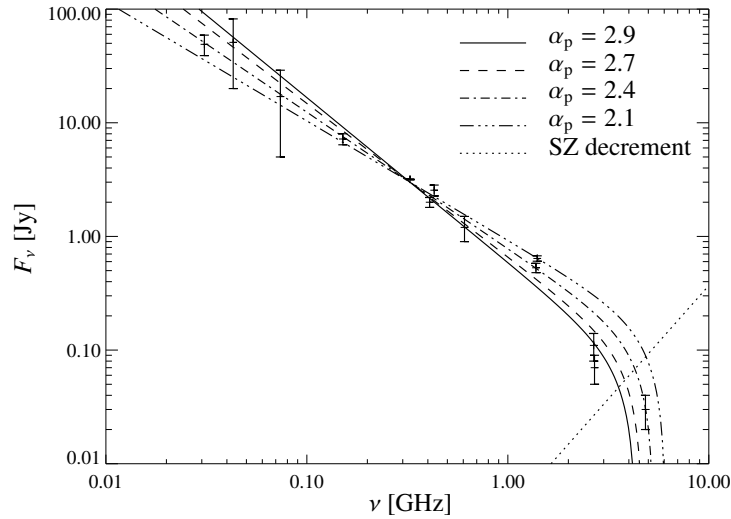
Figure 6.7.: Observed radio halo fluxes of the Coma cluster as compiled by Thierbach et al. (2003). Shown are synchrotron power-law spectra for different spectral indices $\alpha_\nu = \alpha_p/2$. The spectra are modified at higher frequencies by means of the SZ effect while the SZ decrement (a negative flux at the Rayleigh-Jeans part of the Planck spectrum) is also shown (dotted). The SZ flux is derived from the cluster volume up to the assumed position of the accretion shock.

6.5. Probing the cosmic ray population of the elliptical galaxy M 87

This section examines the cosmic ray proton (CRp) population within the giant elliptical galaxy M 87 using the TeV γ-ray detection of the HEGRA collaboration. In our scenario, the γ-rays are produced by decaying pions which result from hadronic CRp interactions with thermal gas of the interstellar medium of M 87.

6.5.1. Detection of γ-rays by the HEGRA collaboration: possible models

The giant elliptical galaxy M 87 is an intensively studied object in our direct extragalactic vicinity situated at a distance of 17 Mpc (Neilsen & Tsvetanov 2000). The announcement of the TeV γ-ray detection of M 87 at a 4-σ significance level by the HEGRA collaboration (Aharonian et al. 2003) using imaging atmospheric Čerenkov techniques was the first discovery of TeV γ-rays from a radio galaxy with a jet whose axis forms a relatively large angle with the line of sight of roughly $30° - 35°$ (Bicknell & Begelman 1996). On the basis of the limited event statistics the detected emission is inconclusive whether it originates from a point source or an extended source. Despite testing for burstlike behavior of M 87 no time variation of the TeV γ-ray flux has been found. This detection provides the unique possibility for probing different γ-ray emission scenarios and thus provides new astrophysical insight into high energy phenomena of this class of objects.

In the literature, there are three different types of model predicting γ-ray emission from objects like M 87: in the first scenario, the GeV/TeV γ-ray emission is generated by the active galactic nucleus (AGN), and possibly related to processed radiation of the relativistic outflow (Dermer et al. 1997). Particularly, inverse Compton (IC) scattering of cosmic microwave background photons off electrons within the jet which have been directly accelerated or reaccelerated as well as the Synchrotron Self Compton scenario could lead to γ-ray emission (Bai & Lee 2001). Secondly, dark matter annihilation or decay processes could be another conceivable source of γ-ray emission, such as the hypothetical neutralino annihilation (Baltz et al. 2000). Finally, hadronic cosmic ray proton (CRp) interactions with the thermal ambient gas would produce pion decay induced γ-rays as well as inverse Compton and synchrotron emission by secondary cosmic ray electrons (CRe) (Vestrand 1982). These processes are possible due to the long lifetimes of CRp comparable to the Hubble time (Völk et al. 1996), long enough to diffuse away from the production site and to maintain their distribution throughout the cluster volume. Because of the strong dependence of this hadronic process on particle density, the giant radio galaxy M 87, located inside the central cooling flow region of the Virgo cluster, is expected to be a major site of γ-ray emission (Pfrommer & Enßlin 2004a).

This work uses the hadronic scenario to model the resulting γ-ray emission. Thus it probes the CRp population by the recent TeV γ-ray observations yielding either an upper limit or a detection on the CRp population, provided this scenario applies. However, this approach only constrains the CRp within the central region of intracluster medium (ICM) of the Virgo cluster which is dominated by the interstellar medium (ISM) of the radio galaxy M 87. In the following, we use the term ICM for both. It should be emphasized that this hadronic scenario predicts stationary γ-ray emission and will be ruled out if the emission is found to be time-variable (barring the existence of a second component). This, however, would result in even tighter constraints on the CRp population owing to the absence of inescapably accompanying γ-ray emission.

6.5.2. Energy-integrated γ-ray fluxes: EGRET versus HEGRA

Provided the CRp population has a power-law spectrum, the relation of the hadronic γ-ray flux $\mathcal{F}_\gamma$ in different energy bands can easily be found using the analytic formulae for the integrated γ-ray source density, namely Eqns. (5.23) to (5.26),

$$\frac{\mathcal{F}_\gamma(E_1 < E_\gamma < E_2)}{\mathcal{F}_\gamma(E_3 < E_\gamma < E_4)} = \frac{\tilde{\mathcal{F}}_\gamma(E_1, E_2)}{\tilde{\mathcal{F}}_\gamma(E_3, E_4)}, \tag{6.29}$$

$$\text{where} \quad \tilde{\mathcal{F}}_\gamma(E_i, E_j) = \left[\mathcal{B}_x \left(\frac{\alpha_\gamma + 1}{2\delta_\gamma}, \frac{\alpha_\gamma - 1}{2\delta_\gamma} \right) \right]_{x_i}^{x_j} \text{and} \quad x_{i,j} = \left[1 + \left(\frac{m_{\pi^0} c^2}{2 E_{i,j}} \right)^{2\delta_\gamma} \right]^{-1}. \tag{6.30}$$

Here we introduced the abbreviation $[f(x)]_{x_1}^{x_2} = f(x_2) - f(x_1)$. This relation for hadronic γ-ray fluxes is independent of any specific model of CRp spatial distribution as long as the same physical mechanism governs the CRp distribution in both energy bands. In passing by, it should be noted that we use Dermer's model for the hadronically induced γ-ray emission, where $\alpha_\gamma = \alpha_p$.

Using the HEGRA γ-ray flux for M 87 of $\mathcal{F}_\gamma(E > 730 \text{ GeV}) = 9.6 \times 10^{-13}\,\gamma\,\text{cm}^{-2}\,\text{s}^{-1}$ (Aharonian et al. 2003), and requiring the expected γ-ray flux above 100 MeV to be smaller than the EGRET upper limit $\mathcal{F}_\gamma(E > 100 \text{ MeV}) = 2.18 \times 10^{-8}\,\gamma\,\text{cm}^{-2}\,\text{s}^{-1}$ (Reimer et al. 2003), we are able to constrain the CRp spectral index to $\alpha_p < 2.275$. For this calculation, we assume a constant CRp spectral index $\alpha_{\text{GeV}}^{\text{TeV}}$ extending from the GeV to TeV energy regime. In the case of steeper spectra in the TeV region, the CRp spectrum needs to be bent in a convex fashion or to exhibit a low energy cutoff in order to meet the requirement imposed by EGRET.

6.5.3. Modification of the spatial diffusion model of CRp

In this section, we also examine three models for the spatial distribution of CRp within the ICM. The isobaric and the adiabatic model for the spatial CRp distribution does not specify their origin, but the CRp may be accelerated by shock waves of cluster mergers, accretion shocks, or result from supernova driven galactic winds. Due to the better spatial resolution of the γ-ray detection of M 87 compared to the EGRET limits, it is necessary to modify our model for the spatial diffusion of the CRp population to include a parameter governing the lifetime of the AGN source.

The relativistic plasma bubbles produced by M 87 likely contain relativistic protons, which can partly escape into the thermal ICM (Enßlin 2003). Most of the CRp that have been injected into the cluster center are either diffusively transported into the surrounding ICM or form relativistic bubbles which rise in the gravitational potential of the cluster due to buoyant forces (Churazov et al. 2001, and references therein).

Momentum dependent CRp diffusion in a turbulent magnetic field with a Kolmogorov-type spectrum on small scales would result in spectral steepening and therefore would violate the limits on the spectral index $\alpha_{\text{GeV}}^{\text{TeV}}$ obtained in Sect. 6.5.2 provided there is no sharp upper cutoff in the CRp spectrum. Thus we adopt for simplicity the scenario of passive advective transport of CRp in a turbulent flow with a diffusion coefficient κ independent of momentum. The time-dependent CRp distribution function reads for short (duration Δt) point-like injection with CRp injection rate $Q(p_p)$ at time $t = 0$

$$f_p(r, p_p, t) = \frac{Q(p_p)\,\Delta t}{(4\pi\,t\,\kappa)^{3/2}}\,\exp\left(-\frac{r^2}{4\,t\,\kappa}\right). \tag{6.31}$$

In a quasi-stationary situation, which is a valid approximation for timescales longer than the typical CRp diffusion timescale in the case of a stationary or short-term intermittent CRp source, the integrated CRp distribution function is approximately given by

$$f_p(r, p_p) = \int_0^t \mathrm{d}t'\, f_p(r, p_p, t') = \frac{Q(p_p)}{4\pi\,r\,\kappa}\,\text{erfc}\left(\frac{r}{\sqrt{4\,t\,\kappa}}\right), \tag{6.32}$$

where $\text{erfc}(x)$ denotes the complementary error function which is responsible for the spatial cutoff at the characteristic diffusion scale $R_{\text{diff}} = \sqrt{6\,t\,\kappa}$. While assuming a power-law shaped $Q(p_p)$, the CRp distribution of Eqn. (5.6) can be written within the framework set by this model as

$$f_p(r, p_p) = \frac{\tilde{n}_{\text{CRp},0}\,c}{\text{GeV}}\left(\frac{r}{\text{kpc}}\right)^{-1}\text{erfc}\left(\frac{r}{\sqrt{4\,t\,\kappa}}\right)\left(\frac{p_p\,c}{\text{GeV}}\right)^{-\alpha_p}. \tag{6.33}$$

Following Sect. 6.2.3, the averaged CRp luminosity of M 87 can be estimated to be

$$\frac{L_{\text{CRp}}}{\kappa} = \frac{4\pi\,m_p c^2\,\tilde{n}_{\text{CRp},0}\,\text{kpc}}{2\,(\alpha_p - 1)}\left(\frac{m_p c^2}{\text{GeV}}\right)^{1-\alpha_p}\mathcal{B}\left(\frac{\alpha_p - 2}{2}, \frac{3 - \alpha_p}{2}\right). \tag{6.34}$$

Considering an energy dependent mean-free-path for diffusion would require fine-tuning of this model while simultaneously enlarging the accessible parameter space. While the resulting profiles should only be slightly affected by this change, this could possibly alter our conclusions concerning the normalization $\tilde{n}_{\text{CRp},0}$. However, this would only add further uncertainty to $\tilde{n}_{\text{CRp},0}$ which already depends on two unknown parameters, the lifetime of the source t and the diffusion coefficient κ.

6.5.4. Modeled γ-ray profiles

The γ-ray flux profiles $f_\gamma(r_\perp, E_\gamma > E_{\text{thr}})$ are obtained by integrating the γ-ray source function $q_\gamma(r, E_\gamma)$ of Eqn. (5.18) above a threshold energy E_{thr}, successively projecting and convolving the spherically symmetric profiles with the
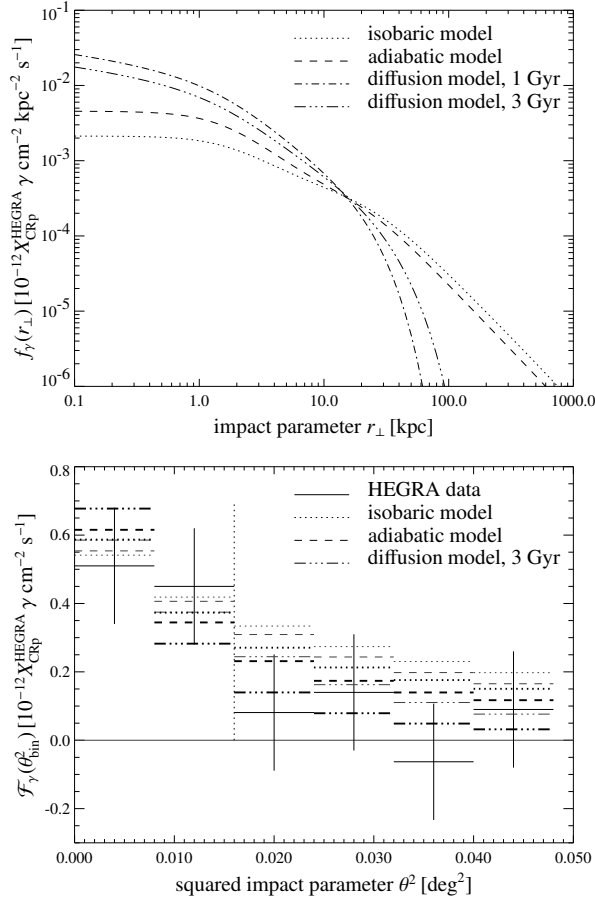
Figure 6.8.: *Top:* Modeled γ-ray surface flux profiles $f_\gamma(r_\perp)$ as function of impact parameter $r_\perp$ in our three different models for the spatial distribution of the CRp population. They are normalized by comparing the integrated γ-ray flux above 730 GeV to HEGRA data of M 87 within the innermost two data points. *Bottom:* Comparison of detected to integrated γ-ray flux $\mathcal{F}_\gamma(\theta^2)$ within the central aperture and the innermost annuli for different models of spatial CRp distribution as well as two different widths of the PSF. The thick black lines correspond to $\sigma = 0.05°$ whereas the thin grey lines are calculated for $\sigma = 0.08°$. The vertical dashed line separates the data from the noise level at a position corresponding to $r_\perp = 37.5$ kpc.

point spread function (PSF) of HEGRA, $\mathrm{PSF}(r_\perp) = \exp[-r_\perp^2/(2\,\sigma^2)]/(2\,\pi\,\sigma^2)$. Resolution studies based on observations of the Crab Nebula with HEGRA indicate a width of $\sigma = 0.08°$, assuming a differential spectral index of $\alpha_\gamma = 2.7$ (Daum et al. 1997). However, for flatter power-law spectra being preferred by our hadronic γ-ray model (see Eqn. (6.29)), the width will be smaller owing to increasing mean γ-ray energy. This leads to an increase of γ-ray induced particles of the air shower and therefore better quality of shower reconstruction according to a smaller relative Poissonian error. For a rough estimate, we rescaled the width of the PSF using the scaling of the mean γ-ray energies above the instrumental threshold, yielding $\sigma = 0.05°$ with $\alpha_\gamma = 2.2$.

The line-of-sight integration was performed out to a radius of $R_{\max} \simeq 3$ Mpc which corresponds to the characteristic distance where the β-model of electron densities is no longer applicable due to accretion shocks of the cluster. The resulting γ-ray profiles are shown in Fig. 6.8. The normalization of the surface fluxes depends on the assumed scaling between CRp and thermal energy density, which is fixed by comparing the integrated flux above 730 GeV to the innermost two γ-ray flux data points of HEGRA (Aharonian et al. 2003) corresponding to $\theta = 0.126°$ or $r_\perp = 37.5$ kpc. Although there are distinct morphological differences visible in the three spatial CRp models, the convolution with the PSF leads to very similar profiles for the expected HEGRA γ-ray counts within the uncertainties. To demonstrate this, we compare the integrated γ-ray flux $F_\gamma(E_\gamma > E_{\mathrm{thr}})$ for different annuli of equal solid

Table 6.2.: Consequences for the CRp scaling parameter X_{CRp} and $\tilde{n}_{CRp,0}$ by comparing the integrated flux above 730 GeV to HEGRA data of the radio galaxy M 87 within the innermost two data points corresponding to $\theta = 0.126°$. The spatial distribution of CRp is given by the isobaric, the adiabatic, and the diffusion model, respectively (see Sect. 6.2). In the first two cases the values are calculated for a CRp population with and without lower cutoff p_{min} while in the latter case two different lifetimes of the source have been considered. Note that the averaged CRp luminosity L_{CRp} scales with $\kappa_{29} = \kappa/(10^{29} \text{ cm}^2 \text{ s}^{-1})$.

α_{GeV}^{TeV}	$X_{CRp}^{isobaric}$	$X_{CRp}^{adiabatic}$	$\tilde{n}_{CRp,0}$ [cm^{-3}]	L_{CRp} [κ_{29} erg/s]
	$p_{min} = 0 \text{ GeV}c^{-1}$:		$t = 1 \text{ Gyr } \kappa_{29}^{-1}$:	
2.1	0.47	0.31	1.8×10^{-7}	1.1×10^{43}
2.2	0.65	0.43	5.0×10^{-7}	1.6×10^{43}
2.27	0.99	0.64	1.0×10^{-6}	2.4×10^{43}
	$p_{min} = 2 \text{ GeV}c^{-1}$:		$t = 3 \text{ Gyr } \kappa_{29}^{-1}$:	
2.1	0.42	0.28	1.2×10^{-7}	7.6×10^{42}
2.2	0.52	0.34	3.4×10^{-7}	1.1×10^{43}
2.27	0.73	0.47	6.8×10^{-7}	1.6×10^{43}

angle elements centered on the source to the HEGRA data for the two different widths of the PSF discussed above (Fig. 6.8).

6.5.5. Consequences and predictions for the CRp population in M 87

By employing the technique described in Sect. 6.5.4, we explore the consequences for the CRp scaling parameters X_{CRp} and $\tilde{n}_{CRp,0}$ in the particular models of CRp spatial distributions. The resulting values, shown in Table 6.2, have been obtained using a PSF of width $\sigma = 0.05°$, however there are no significant changes in X_{CRp} for $\sigma = 0.08°$. The values of the CRp scaling parameter X_{CRp} inferred from M 87 are comparable to the one in our Galaxy, which is of order unity (Parker 1969). Since the HEGRA γ-ray measurements probe only the central region of the Virgo cluster which is dominated by the elliptical radio galaxy M 87, a composition of ISM and ICM is observed, potentially mixed by convective motion within the cooling flow (Churazov et al. 2001). Therefore we expect X_{CRp} to be smaller than in our Galaxy, but significantly higher than upper limits obtained in nearby cooling flow clusters, which are less than 20% (Pfrommer & Enßlin 2004a).

In the case of diffusion of CRp away from M 87, we are able to constrain the averaged CRp luminosity L_{CRp} of the central AGN by assuming a plausible value for the diffusion coefficient κ. The inferred values are of the same order as instantaneous jet power estimates of M 87, $L_{jet} \simeq 10^{43}$ erg s^{-1} (Bicknell & Begelman 1996). Thus, we limit a combination of diffusion efficiency of CRp into the ambient thermal medium and average jet power by this approach.

Because of the scaling behavior of X_{CRp} in the isobaric and adiabatic models, we quantify the influence of a lower cutoff p_{min} on the population of CRp due to Coulomb interactions in the plasma by taking the ratio of CRp energy densities $\varepsilon_{CRp}(p_{min})$ with and without lower cutoff (see Eqn. (5.14)). Such a cutoff yields lower values of X_{CRp} and therefore smaller contribution to the γ-ray flux in the energy range of EGRET once the CRp momentum cutoff p_{min} exceeds the kinematic threshold $p_{thr} = 0.78 \text{ GeV}c^{-1}$ of the hadronic interaction. Thus, cooling of the CRp population allows for steeper power-law distributions.

6.5.5.1. Synchrotron emission by hadronic CRe

Following the formalism described in Pfrommer & Enßlin (2004a), we compute the synchrotron emission of CRe resulting from hadronic CRp interactions. Integrating the expected radio surface brightness profiles over the solid angle element corresponding to the γ-ray emission region and assuming magnetic fields of the form $B(r) = 10 \,\mu\text{G} \, [n_e(r)/n_e(0)]^{0.5}$, we expect hadronic synchrotron fluxes $F_\nu = F_0 \, [\nu/(1.4 \text{ GHz})]^{-\alpha_p/2}$, where $F_0 = 11$ Jy and 16 Jy for $\alpha_p = 2.1$ and 2.2. However, this hypothetical radio mini-halo is outshone by the synchrotron emission

of the relativistic jet, which shows a flux level of $F_{1.4\,\mathrm{GHz}} = (220 \pm 11)$ Jy (Kuehr et al. 1981). The hadronic radio surface profiles which are characterized by a smooth morphology fall short by roughly one order of magnitude even at impact parameters of some arc minutes compared to observed profiles of Rottmann et al. (1996).

6.5.5.2. Predictions for next generation Čerenkov telescopes and GLAST

There are three different scenarios predicting γ-ray emission from objects like M 87, namely processed radiation of the relativistic outflow, dark matter annihilation, and the hadronic scenario. The predictions of these types of model differ predominantly in morphology, existing time-variability, and spectral signatures. The radio galaxy M 87 which is well within the field of view of the next generation Čerenkov telescopes MAGIC[3], HESS[4], and VERITAS[5] should therefore serve as a unique source for testing these scenarios. While the angular resolution of these telescopes is comparable to the previously attained resolution, the flux sensitivities have strongly improved. These developments should allow for γ-ray spectroscopy by Čerenkov experiments in the near future, providing the opportunity of scrutinizing existing time-variation, and thus being able to constrain different γ-ray emission scenarios.

The LAT instrument onboard GLAST[6] will complement this research to even lower energies ranging from 20 MeV up to 300 GeV. Given a CRp population described by a single power-law spectral index $\alpha_{\mathrm{p}} = \alpha_{\mathrm{GeV}}^{\mathrm{TeV}}$ extending from the GeV to TeV energy regime as well as a CRp scaling parameter X_{CRp} of Table 6.2, we calculated the expected integrated γ-ray flux above 20 MeV. In the isobaric model, the γ-ray flux estimates are $\mathcal{F}_{\gamma}(> 20\,\mathrm{MeV})/(\gamma\,\mathrm{cm}^{-2}\,\mathrm{s}^{-1}) = 6.0 \times 10^{-8}, 1.3 \times 10^{-7}$, and 2.3×10^{-7} for $\alpha_{\mathrm{GeV}}^{\mathrm{TeV}} = 2.1, 2.2$, and 2.27, respectively. This is well above the sensitivity limit of GLAST. The energy resolution of GLAST will even provide the possibility to disentangle the pion decay induced signature from inverse Compton emission of high-energetic electrons or positrons due to the energy resolution which is better than 10% and is sufficient to resolve the pion decay induced peak in the γ-ray spectrum.

6.6. Detectability of γ-rays by future satellite missions and Čerenkov telescopes

Based on the previous results we discuss the detectability of IC emission by secondary CRe and pion decay induced γ-ray emission by current and future satellite missions as well as operating and future Čerenkov telescopes.

6.6.1. Detectability of pion decay induced γ-ray and IC emission with INTEGRAL

The imager IBIS which is the Imager on Board the "INTErnational Gamma-Ray Astrophysics Laboratory" (INTE-GRAL)[7] Satellite covers an energy range from 15 keV up to 10 MeV and is capable of high resolution imaging (12′ FWHM) and source identification. Its spectral sensitivity reaches down to $5 \times 10^{-8}\,\gamma\,\mathrm{s}^{-1}\,\mathrm{cm}^{-2}\,\mathrm{keV}^{-1}$ ($3\,\sigma$ in 10^{6} s, $\Delta E = E/2$) to the continuum at 10 MeV. However, this is most probably not sufficient in order to detect the pion decay induced γ-rays of a particular cluster (compare Fig. 5.3). Assuming a CRp spectral index of $\alpha_{\mathrm{p}} = 2.3$ and taking the results of Table 6.1 we expect an IC emission of hadronically originating CRe in the Perseus cluster of

$$\frac{\mathrm{d}\mathcal{F}}{\mathrm{d}E}(20\,\mathrm{keV}) = \mathcal{F}_{\mathrm{IC}}\,10^{-7}\,\gamma\,\mathrm{cm}^{-2}\,\mathrm{s}^{-1}\,\mathrm{keV}^{-1}, \tag{6.35}$$

with $\mathcal{F}_{\mathrm{IC}} = 8.4, 4.2$, and 2.3 for $B_0 = 5\,\mu\mathrm{G}, 10\,\mu\mathrm{G}$, and $20\,\mu\mathrm{G}$. Comparing these results to the *post-launch* spectral sensitivity of $4 \times 10^{-6}\,\gamma\,\mathrm{s}^{-1}\,\mathrm{cm}^{-2}\,\mathrm{keV}^{-1}$ to the continuum at 20 keV for an observation time of 10^{6} s ($3\,\sigma$ detection) there is only a minor chance to detect IC emission of CRe. However, for steeper spectral indices or a strongly inhomogeneously magnetized environment, IC fluxes can be enhanced at the expense of synchrotron emission according to Enßlin et al. (1999).
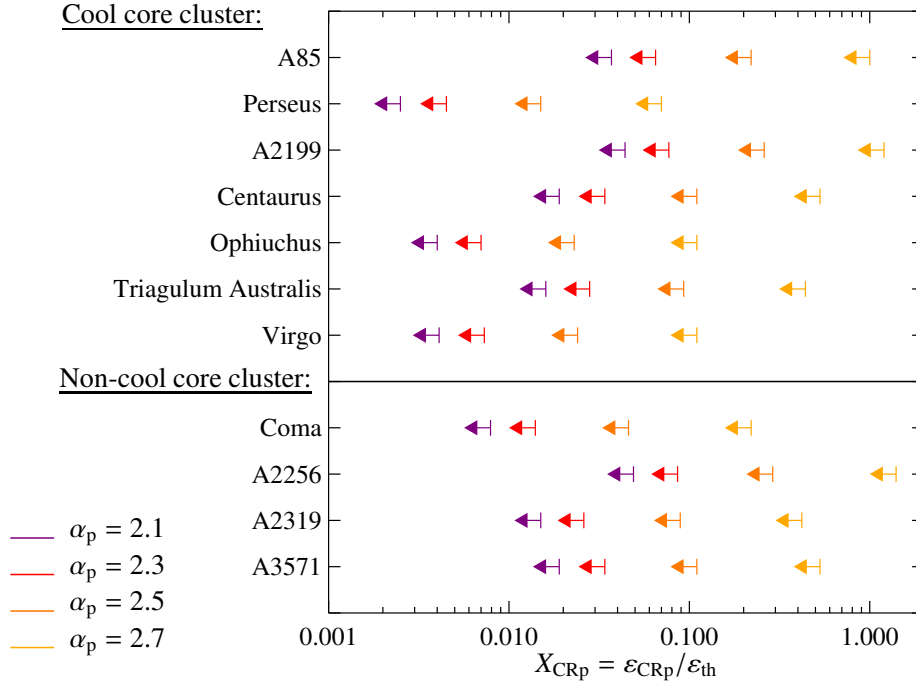
---

[3] http://hegra1.mppmu.mpg.de/MAGICWeb/
[4] http://www.mpi-hd.mpg.de/hfm/HESS/HESS.html
[5] http://veritas.sao.arizona.edu/
[6] http://glast.gsfc.nasa.gov/science/
[7] http://astro.esa.int/Integral/

Figure 6.9.: Expected limits on the CRp scaling parameter X_{CRp} in the isobaric model by comparing the integrated pion decay induced γ-ray flux above 100 GeV to sensitivity limits of Čerenkov telescopes of $\mathcal{F}_{\gamma,\exp}(E > E_{thr}) = 10^{-12}\,\gamma\,\mathrm{cm}^{-2}\,\mathrm{s}^{-1}\,(E_{thr}/100\,\mathrm{GeV})^{1-\alpha_\gamma}$ assuming a γ-ray spectral index in Dermer's model $\alpha_\gamma = \alpha_p$. Note that limits on X_{CRp} roughly $\lesssim 0.01$ for $\alpha_p = 2.3$ in the isobaric model provide good chances to detect γ-rays in these particular clusters with new generation Čerenkov telescopes.

6.6.2. Possibility of pion decay induced γ-ray detection by GLAST

The "Large Area Telescope" (LAT) onboard the "Gamma-ray Large Area Space Telescope" (GLAST)[8] scheduled to be launched in 2006 has an angular resolution smaller than 3.5° at 100 MeV while covering an energy range of 20 MeV up to 300 GeV with an energy resolution smaller than 10%. Assuming a photon spectral index of $\alpha_\gamma = 2$ for the γ-ray background the point source sensitivity at high galactic latitude in an one year all-sky survey is better than $6 \times 10^{-9}\,\mathrm{cm}^{-2}\,\mathrm{s}^{-1}$ for energies integrated above 100 MeV. Assuming the radio-mini halo in the Perseus cluster mainly to originate from secondary electrons emitting synchrotron radiation then we expect the CRp scaling parameter to be typically one order of magnitude below the upper limits obtained by comparing to EGRET data. This immediately would imply a good possibility to detect pion decay induced γ-ray emission by GLAST preferentially in nearby cooling flow clusters like Perseus and Virgo. Specifically for our secondary model of the radio mini-halo of Perseus, while assuming $\alpha_p = 2.3$ in the CRp isobaric model we expect an integrated γ-ray flux above 100 MeV from Perseus of $\mathcal{F}_\gamma(> 100\,\mathrm{MeV})/(\gamma\,\mathrm{cm}^{-2}\,\mathrm{s}^{-1}) = 1.3 \times 10^{-8}, 7.4 \times 10^{-9}$, and 5.6×10^{-9} for $B_0 = 5\mu\mathrm{G}, 10\mu\mathrm{G}$, and $20\mu\mathrm{G}$. The expected γ-ray flux is ever higher when including lower energetic photons.

6.6.3. Expected γ-ray flux for Čerenkov telescopes

In the near future there will be different Čerenkov telescope experiments operating with several telescopes simultaneously and therefore allowing stereoscopic observations. On the southern hemisphere there are the "Collaboration between Australia and Nippon for a Gamma Ray Observatory in the Outback" (CANGAROO)[9] in Aus-

---

[8]http://glast.gsfc.nasa.gov/science/
[9]http://www.physics.adelaide.edu.au/astrophysics/

tralia and the "High Energy Stereoscopic System" (HESS)[10] in Namibia. On the northern hemisphere there will be the "Very Energetic Radiation Imaging Telescope Array System" (VERITAS)[11] in Arizona. All these telescopes have comparable lower energy thresholds of $E_{thr} = 100$ GeV and provide flux sensitivities better than $\mathcal{F}_{\gamma,exp}(E > 100 \text{ GeV}) = 10^{-12} \gamma \text{ cm}^{-2} \text{ s}^{-1}$. On the northern hemisphere there will also be the "Major Atmospheric Gamma-ray Imaging Čerenkov detector" (MAGIC)[12] on the Canary Islands observing with a single dish telescope of 234 m^2 providing an even lower energy threshold of $E_{min} = 30$ GeV.

Following the formalism described in Sect. 6.3.2 and comparing the resulting γ-ray flux $\mathcal{F}_\gamma(E > E_{thr})$ to expected flux sensitivities of Čerenkov telescopes $\mathcal{F}_{\gamma,exp}(E > E_{thr})$, we obtain possible upper limits on the CRp scaling parameter X_{CRp} for an integrated volume out to a radial distance of $3\,h_{70}^{-1}$ Mpc. Table C.5 shows constraints for X_{CRp} using the isobaric and the adiabatic model of CRp described in Sect. 6.2. For the sake of better comparison, Fig. 6.9 additionally illustrates these limits using the isobaric model of CRp. By comparing these limits to those obtained by analyzing synchrotron emission in the Perseus and Coma cluster (see Table 6.1) and assuming a substantial contribution of hadronically originating CRe to these radio halos there is a realistic chance to detect extragalactic pion decay induced γ-ray emission in clusters like Perseus (A 426), Virgo, Ophiuchus, and Coma (A 1656).

6.7. Conclusions

We investigated hadronic CRp-p interactions in the ICM of clusters and simulated the resulting emission mechanisms in radio, X-rays, and γ-rays assuming spherical symmetry. By applying this technique to a sample of prominent clusters of galaxies including cooling flow clusters we succeeded in constraining the population of CRp. Especially cooling flow regions are perfectly suited for constraining non-thermal ICM components due to their high gas density and magnetic field strength.

6.7.1. The cosmic ray population of nearby galaxy clusters: EGRET constraints

From the literature we collected electron density and temperature profiles of seven cooling flow clusters and four non-cooling flow clusters using our analytic scaling relation between the γ-ray and bolometric X-ray fluxes to obtain observationally promising candidates.

In order to apply this method to our sample of clusters of galaxies we introduced three specific models for the spatial distribution of CRp within cooling flow cluster. In our first two scenarios we characterized the kinetic CRp energy density $\varepsilon_{CRp}(r)$ to be a constant fraction of the thermal energy density $\varepsilon_{th}(r)$ of the ICM parametrized by X_{CRp}. The CRp isobaric model assumes the average pressure of CRp not to change during the formation of the cooling flow while the adiabatic model hypothesizes this proportionality prior to transition because the CRp experience adiabatic compression during the relaxation phase. In our third scenario we modeled the resulting distribution of CRp diffusion from a central source. By modeling the particular γ-ray emission of our cluster sample and comparing to EGRET upper limits we obtained upper bounds on the CRp scaling parameter $X_{CRp} = \varepsilon_{CRp}(r)/\varepsilon_{th}(r)$. For Perseus and Virgo we infer the strongest upper limits which lie in the range $X_{CRp} \in [0.08, 0.18]$ for different choices of the CRp spectral index $\alpha_p \in [2.1, 2.7]$.

6.7.2. Radio synchrotron emission by hadronically produced relativistic electrons

Furthermore, the radio emission due to hadronically produced secondary electrons emitting synchrotron radiation was calculated and resulting radio brightness profiles were compared to measured data of the radio-mini halo of Perseus as well as the radio halo of Coma. In the case of Coma our CRp profiles characterized by a flat CRp scaling parameter X_{CRp} are not able to reproduce the observed radio profiles particularly in the peripheral regions of the cluster. In the following we adjusted the radial behavior of $X_{CRp}(r)$ such that the synchrotron emission resulting from hadronic CRe is able to account for the observed radio surface brightness profile and thus allowing for an additional degree of freedom. The resulting increase of $X_{CRp}(r)$ for larger radii could be due to adiabatic compression which increases the thermal energy density at a higher rate than the CRp energy density. Even more

---

[10] http://www.mpi-hd.mpg.de/hfm/HESS/HESS.html
[11] http://veritas.sao.arizona.edu/
[12] http://hegra1.mppmu.mpg.de/MAGICWeb/

important, the aspherical Coma cluster morphology reduces the required radial increase in $X_{\mathrm{CRp}}(r)$. By exploring the accessible parameter space spanned by parameters describing the magnetic field and the spectral index of the CRp population we identify regions where the hadronic scenario is able to reproduce the observed radio profiles preferentially for an energy density of the magnetic field which declines shallower than the thermal energy density. We conclude that the secondary model for radio halos is still viable.

In the case of the Perseus mini-radio halo, we conclude upper limits on X_{CRp} which are ranging for the isobaric model of CRp within the interval $X_{\mathrm{CRp}} \in [0.01, 0.1]$ for conservative combinations of values of the magnetic field B and the CRp spectral index α_{p} while upper limits for the CRp adiabatic model are typically half an order of magnitude below. By comparing calculated radio brightness profiles to measured data of the radio-mini halo in Perseus, we found excellent morphological agreement between the CRp isobaric model and the radio data especially for the choice of $B_0 = 10$ μG, $\alpha_B = 0.5$, and $\alpha_{\mathrm{p}} = 2.3$. In the course of this chapter we argued that this specific choice of parameters for the magnetic fields in cooling flow clusters is also preferred by experiments like Faraday rotation measurements and cosmological cluster simulations including magnetic fields. A discussion of different acceleration mechanisms of CRp such as structure formation shocks, supernovae remnants, and injection by active radio galaxies supports also a value of α_{p} close to the inferred one. Because of the required moderate CRp energy density we propose synchrotron radiation by non-thermal secondary electrons from hadronic interactions as a likely explanation of radio mini-halos. In order to scrutinize this model we provide predictions of γ-ray fluxes for Čerenkov telescopes as well as the INTEGRAL and GLAST satellites.

6.7.3. The cosmic ray population of the giant elliptical galaxy M 87

Using TeV γ-ray detections of M 87 by the HEGRA collaboration, it is for the first time possible to constrain the CRp population of an elliptical galaxy. By comparing to EGRET upper limits on the γ-ray emission, we constrain the CRp spectral index to $\alpha_{\mathrm{GeV}}^{\mathrm{TeV}} < 2.275$, provided the γ-ray emission is of hadronic origin and the population is described by a single power-law ranging from the GeV to TeV energy regime.

By investigating three different models for the spatial distribution of the CRp and applying those to realistic electron density and temperature profiles obtained from X-ray observations, we calculate γ-ray flux profiles resulting from hadronic CRp interactions with the thermal ambient gas using an analytic formalism. After convolving with the HEGRA point spread function, we compare the integrated γ-ray flux $F_\gamma(E_\gamma > 730$ GeV) for different annuli of equal solid angle elements centered on the source. Based on the available data we find good morphological agreement of all our models with these HEGRA Čerenkov observations.

In the isobaric and adiabatic CRp model, the consequences for the CRp scaling parameter X_{CRp} drawn from normalization of our γ-ray flux profiles to HEGRA observations yield slightly smaller values when comparing to our Galaxy with $X_{\mathrm{CRp}} \sim 1$, depending on the CRp spectral index. This is because of the sensitivity of the observations to both the ISM of M 87 and the ICM of the central cooling flow region of Virgo, where $X_{\mathrm{CRp}} \lesssim 0.2$ (cf. Fig. 6.1). Especially for $\alpha_{\mathrm{GeV}}^{\mathrm{TeV}} \simeq 2.1$ or lower momentum cutoffs of the CRp population due to Coulomb cooling processes, we obtain smaller contributions of CRp pressure to the ambient medium. By exploring our diffusion model and comparing our constraints on the CRp luminosity L_{CRp} to mechanical jet power estimates of M 87, we show the ability of TeV γ-ray observations to constrain a combination of energy fraction of CRp escaping from the radio plasma and average jet power of the AGN.

The expected radio emission by hadronically produced CRe is roughly one order of magnitude smaller compared to the synchrotron emission of the jet. Therefore it will be a challenge for future radio observations to disentangle the hadronic and jet emission components. Future Čerenkov observations should at least be able to severely constrain the parameter space of different γ-ray emission scenarios. Investigating the γ-ray flux in the energy regime of GLAST, we predict values which should allow to scrutinize this hadronic model in contrast to other scenarios.

6.7.4. Predictions for next generation Čerenkov telescopes and GLAST

Finally, we analyzed the possibility of detecting such pion decay induced γ-ray and IC emission by current and future satellite missions as well as new generation Čerenkov telescopes. Depending on the CRp spectral index, the fragmentation of the spatial distribution of the magnetic field as well as its field strength, it will be difficult for INTEGRAL to detect the IC emission of the hadronically originating secondary CRe while GLAST has the potentiality to detect the distinct signature of the pion decay induced γ-ray emission preferentially in nearby cooling flow clusters. By investigating the opportunity of detecting extragalactic γ-rays by Čerenkov telescopes we argued

in favor of four candidate clusters (Perseus (A 426), Virgo, Ophiuchus, and Coma (A 1656)) which are especially suited to detect hadronically originating γ-ray emission. These future experiments have the potential of entering a new era of precision high energy cluster physics.

The results of this chapter were worked out in collaboration with T.A. Enßlin. This chapter includes two publications: the second part of the paper entitled "Constraining the population of cosmic ray protons in cooling flow clusters with γ-ray and radio observations: Are radio mini-halos of hadronic origin?" *which has been published in the journal* Astronomy & Astrophysics (Pfrommer & Enßlin, 2004, A&A, 413, 17) *and the letter entitled* "Probing the cosmic ray population of the giant elliptical galaxy M 87 with observed TeV γ-rays" *which has been published in the journal* Astronomy & Astrophysics (Pfrommer & Enßlin, 2003, A&A, 407, L73).

7. Estimating galaxy cluster magnetic fields by minimum energy criteria

Abstract

This chapter estimates magnetic field strengths of radio emitting galaxy clusters by minimizing the non-thermal energy density contained in cosmic ray electrons (CRe), protons (CRp), and magnetic fields. The *classical* minimum energy estimate can be constructed independently of the origin of the radio synchrotron emitting CRe yielding thus an absolute minimum of the non-thermal energy density. Provided the observed synchrotron emission is generated by a CRe population originating from hadronic interactions of CRp with the ambient thermal gas of the intra-cluster medium, the parameter space of the *classical* scenario can be tightened by means of the *hadronic* minimum energy criterion. For both approaches, we derive the theoretically expected tolerance regions for the inferred minimum energy densities. Application to the radio halo of the Coma cluster and the radio mini-halo of the Perseus cluster yields equipartition between cosmic rays and magnetic fields within the expected tolerance regions. In the hadronic scenario, the inferred central magnetic field strength ranges from 2.4 µG (Coma) to 8.8 µG (Perseus), while the optimal CRp energy density is constrained to 2% ± 1% of the thermal energy density (Perseus). We discuss the possibility of a hadronic origin of the Coma radio halo while current observations favor such a scenario for the Perseus radio mini-halo. Combining future expected detections of radio synchrotron, hard X-ray inverse Compton, and hadronically induced γ-ray emission should allow an estimate of volume averaged cluster magnetic fields and provide information about their dynamical state.

7.1. Introduction

Clusters of galaxies harbor magnetized plasma. In particular, the detection of diffuse synchrotron radiation from radio halos or relics provides evidence for the existence of magnetic fields within the intra-cluster medium (ICM) (for a review, see Carilli & Taylor 2002). Since the detection rate of radio halos in galaxy clusters seems to be of the order of 30% for X-ray luminous clusters (Giovannini et al. 1999), the presence of magnetic fields appears to be common. Based on these observations, Enßlin & Röttgering (2002) developed a redshift dependent radio halo luminosity function and predicted large numbers of radio halos to be detected with future radio telescopes.

A different piece of evidence comes from Faraday rotation which arises owing to the birefringent property of magnetized plasma causing the plane of polarization to rotate for a nonzero magnetic field component along the propagation direction of the photons (Clarke et al. 2001). However, the accessible finite windows given by the extent of the sources emitting polarized radiation are a limitation of this method. The derived magnetic field strengths depend on the unknown magnetic field autocorrelation length which has to be deprojected from the observed two dimensional Faraday rotation measure maps using certain assumptions (see, however, Enßlin & Vogt 2003, Vogt & Enßlin 2003). A different approach is given by the energy equipartition argument if a particular cluster exhibits diffuse radio synchrotron emission. The method assumes equal energy densities of cosmic ray electrons and magnetic fields in order to estimate volume averaged magnetic field strengths.

The minimum energy criterion is a complementary method. It is based on the idea of minimizing the non-thermal energy density contained in cosmic ray electrons (CRe), protons (CRp), and magnetic fields by varying the magnetic field strength. As one boundary condition, the implied synchrotron emissivity is required to match the observed value. Additionally, a second boundary condition is required mathematically which couples CRp and CRe. For the classical case, a constant scaling factor between CRp and CRe energy densities is assumed. However, if the physical connection between CRp and CRe is known or assumed, a physically better motivated criterion can be formulated. As such a case, we introduce the minimum energy criterion within the scenario of hadronically generated CRe.

Classically, the equipartition/minimum energy formulae use a fixed interval in radio frequency in order to estimate

the total energy density in cosmic ray electrons (CRe), a purely observationally motivated procedure (Burbidge 1956, Pacholczyk 1970). However, this approach has a drawback when comparing different field strengths between galaxy clusters because a given frequency interval corresponds to different CRe energy intervals depending on the magnetic field strengths (Beck 2001). For this reason, variants of the minimum energy criterion have been studied in order to place the magnetic field estimates on more physical grounds, based then on assumptions such as the fixed interval in CRe energy (Pohl 1993, Beck et al. 1996, Brunetti et al. 1997). The modified classical minimum energy criterion does not specify a particular energy reservoir of the CRe. However, this apparent model-independence is bought dearly at the cost of the inferred magnetic field strength depending on unknown parameters like the lower energy cutoff of the CRe population or the unknown contribution of CRp to the non-thermal energy density. In the following, we use the term *classical minimum energy criterion* in its modified version, including e.g. a fixed interval in CRe energy.

Natural candidates for acceleration mechanisms providing a highly-relativistic particle population are strong structure formation and merger shocks (e.g., Harris et al. 1980, Sarazin 1999) or reacceleration processes of 'mildly' relativistic CRe ($\gamma_e \simeq 100 - 300$) being injected over cosmological timescales into the ICM. Owing to their long lifetimes of a few times 10^9 years, these mildly relativistic CRe can accumulate within the ICM (see Sarazin 2002, and references therein), until they experience continuous in-situ acceleration via resonant pitch angle scattering by turbulent Alfvén waves as originally proposed by Jaffe (1977) and reconsidered by Schlickeiser et al. (1987), Brunetti et al. (2001), Ohno et al. (2002), Gitti et al. (2002), and Kuo et al. (2003). However, this reacceleration scenario also faces challenges as recent results imply: Brunetti et al. (2004b) show, that if the CRp-to-thermal energy density ratio were more than a few percent, Alfvén waves would be damped efficiently such that the reacceleration mechanism of the electrons is inefficient. Because nearly all conceivable electron acceleration mechanisms produce a population of CRp which accumulates within the clusters volume, this represents an efficient damping source of Alfvén waves.[1] Kuo et al. (2004) presented an interesting line of argumentation to investigate the nature of radio halos by comparing the observed and statistically predicted population. This approach might allow to measure the life time of radio halos and thus help to conclude their physical origin with a future flux-limited, controlled, and homogeneous radio halo sample.

In this work, we examine a minimum energy criterion within another specific model for the observed extended radio halos of ∼ Mpc size: hadronic interactions of CRp with the ambient thermal gas produce secondary electrons, neutrinos, and γ-rays by inelastic collisions taking place throughout the cluster volume. These secondary CRe would generate radio halos through synchrotron emission (Dennison 1980, Vestrand 1982, Blasi & Colafrancesco 1999, Dolag & Enßlin 2000, Miniati et al. 2001, Pfrommer & Enßlin 2004a). This scenario is motivated by the following argument: The radiative lifetime of a CRe population in the ICM, generated by direct shock acceleration, is of the order of 10^8 years for $\gamma_e \sim 10^4$. This is relatively short compared to the required diffusion timescale needed to account for such extended radio phenomena (Brunetti 2002). On the other hand, the CRp are characterized by lifetimes of the order of the Hubble time, which is long enough to diffuse away from the production site and to be distributed throughout the cluster volume to which they are confined by magnetic fields (Völk et al. 1996, Enßlin et al. 1997, Berezinsky et al. 1997). The magnetic field strength within this scenario is obtained by analogy with the classical minimum energy criterion while combining the CRp and CRe energy densities through their physically connecting process. Apart from relying on the particular model, the inferred magnetic field strengths do not depend strongly on unknown parameters in this model.[2]

The philosophy of these approaches is to provide a criterion for the energetically least expensive radio synchrotron emission model possible for a given physically motivated scenario. To our knowledge, there is no first principle enforcing this minimum state to be realized in Nature. However, our minimum energy estimates are interesting in two respects: first, these estimates allow scrutinizing the hadronic model for extended radio synchrotron emission in clusters of galaxies. If it turns out that the required minimum non-thermal energy densities are too large compared to the thermal energy density, the hadronic scenario will become implausible to account for the extended diffuse radio emission. For the classical minimum energy estimate, such a comparison can yield constraints on the accessible parameter space spanned by lower energy cutoff of the CRe population or the contribution of CRp to the non-thermal energy density. Secondly, should the hadronic scenario be confirmed, the minimum energy estimates allow testing

---

[1] Indeed, there are first hints for the existence of a 10 MeV - 100 MeV CRp population deriving from the detection of excited gamma-ray lines from the clusters Coma and Virgo (Iyudin et al. 2004). If verified, that would make a high energy (GeV) CRp population very plausible.

[2] Likewise the minimum energy criterion within the reacceleration scenario of mildly relativistic CRe ($\gamma_e \simeq 100 - 300$) can be obtained by minimizing the sum of magnetic, mildly relativistic CRe, and turbulent energy densities while allowing for constant synchrotron emission.

for the realization of the minimum energy state for a given independent measurement of the magnetic field strength.

This chapter is organized as follows: after introducing synchrotron radiation of CRe (Sect. 7.2.1), analytic formulae for hadronically induced emission processes are presented (Sect. 7.2.2). The classical and hadronic minimum energy criteria are then derived, the theoretically expected tolerance regions are given, and limiting cases are discussed (Sect. 7.3). In Sect. 7.4, we examine whether future observations of inverse Compton emission and hadronically induced γ-ray emission can serve as tests for the verification of the minimum energy criterion. Magnetic and cosmic ray energy densities and their tolerance regions are inferred from application of the minimum energy arguments in the Coma and Perseus cluster for both scenarios (Sect. 7.5). This chapter concludes with formulae which provide recipes for estimating the magnetic field strength in typical observational situations (Sect. 7.6). Throughout this chapter we use the present Hubble constant $H_0 = 70\ h_{70}$ km s^{-1} Mpc^{-1}, where h_{70} indicates the scaling of H_0.

7.2. Theoretical background

This section presents our definitions and the theoretical background for this work. After introducing characteristics of the CRe population and the synchrotron emission formulae, we focus on specifications of the CRp population. Finally, the section concludes with analytic formulae describing the hadronically induced γ-ray and radio synchrotron emission processes.

7.2.1. Cosmic ray electrons and synchrotron emission

The differential number density distribution of a CRe population above a MeV is often represented by a power-law in energy E_e,

$$f_e(\boldsymbol{r}, E_e)\, dE_e\, dV = \tilde{n}_{\mathrm{CRe}}(\boldsymbol{r}) \left(\frac{E_e}{\mathrm{GeV}}\right)^{-\alpha_e} \left(\frac{dE_e}{\mathrm{GeV}}\right) dV. \tag{7.1}$$

where the tilde indicates that $\tilde{n}_{\mathrm{CRe}}$ is not a real CRe number density although it exhibits the appropriate dimensions. The normalization $\tilde{n}_{\mathrm{CRe}}(\boldsymbol{r})$ might be determined by assuming that the kinetic CRe energy density $\varepsilon_{\mathrm{CRe}}(\boldsymbol{r})$ is expressed in terms of the thermal energy density $\varepsilon_{\mathrm{th}}(\boldsymbol{r})$,

$$\varepsilon_{\mathrm{CRe}}(\boldsymbol{r}) = X_{\mathrm{CRe}}(\boldsymbol{r})\, \varepsilon_{\mathrm{th}}(\boldsymbol{r}) = A_{E_e}\, \tilde{n}_{\mathrm{CRe}}(\boldsymbol{r}), \tag{7.2}$$

$$A_{E_e}(\alpha_e) = \frac{\mathrm{GeV}}{2 - \alpha_e} \left[\left(\frac{E_e}{\mathrm{GeV}}\right)^{2-\alpha_e}\right]_{E_1}^{E_2}. \tag{7.3}$$

Here we introduced the abbreviation $[f(x)]_{x_1}^{x_2} = f(x_2) - f(x_1)$. in order to account for cutoffs of the CRe population. If the CRe population had time to lose energy by means of Coulomb interactions (Gould 1972), the low energy part of the spectrum would be modified. This modification, which impacts on the CRe distribution function $f_e(\boldsymbol{r}, E_e)$ and thus on $A_{E_e}(\alpha_e)$, can be approximately treated by imposing a time dependent lower energy cutoff on the CRe population as described in Pfrommer & Enßlin (2004a).

While the functional dependence of the CRe scaling parameter $X_{\mathrm{CRe}}(\boldsymbol{r})$ is a priori unknown, its radial behavior will be adjusted such that it obeys the minimum energy criterion. The thermal energy density of the ICM $\varepsilon_{\mathrm{th}}$ is given by

$$\varepsilon_{\mathrm{th}}(\boldsymbol{r}) = \frac{3}{2}\, d_e\, n_e(\boldsymbol{r})\, kT_e(\boldsymbol{r}), \tag{7.4}$$

$$\text{where} \quad d_e = 1 + \frac{1 - \frac{3}{4}X_{\mathrm{He}}}{1 - \frac{1}{2}X_{\mathrm{He}}} \tag{7.5}$$

counts the number of particles per electron in the ICM using the primordial ^{4}He mass fraction $X_{\mathrm{He}} = 0.24$. T_e and n_e denote the electron temperature and number density, respectively.

The synchrotron emissivity j_ν at frequency ν and per steradian of such a CRe population (7.1), which is located in an isotropic distribution of magnetic fields (Eqn. (6.36) in Rybicki & Lightman 1979), is obtained after averaging

over an isotropic distribution of electron pitch angles yielding

$$j_\nu(\boldsymbol{r}) \quad = \quad A_{E_{\mathrm{syn}}}(\alpha_{\mathrm{e}})\,\tilde{n}_{\mathrm{CRe}}(\boldsymbol{r})\left[\frac{\varepsilon_B(\boldsymbol{r})}{\varepsilon_{B_{\mathrm{c}}}}\right]^{(\alpha_\nu+1)/2} \propto \varepsilon_{\mathrm{CRe}}(\boldsymbol{r})\,B(\boldsymbol{r})^{\alpha_\nu+1}\nu^{-\alpha_\nu}, \tag{7.6}$$

$$B_{\mathrm{c}} \quad = \quad \sqrt{8\pi\,\varepsilon_{B_{\mathrm{c}}}} = \frac{2\pi\,m_{\mathrm{e}}^3\,c^5\,\nu}{3\,e\,\mathrm{GeV}^2} \simeq 31\left(\frac{\nu}{\mathrm{GHz}}\right)\,\mu\mathrm{G}, \tag{7.7}$$

$$A_{E_{\mathrm{syn}}} \quad = \quad \frac{\sqrt{3\pi}}{32\pi}\frac{B_{\mathrm{c}}\,e^3}{m_{\mathrm{e}}c^2}\frac{\alpha_{\mathrm{e}}+\frac{7}{3}}{\alpha_{\mathrm{e}}+1}\frac{\Gamma\left(\frac{3\alpha_{\mathrm{e}}-1}{12}\right)\Gamma\left(\frac{3\alpha_{\mathrm{e}}+7}{12}\right)\Gamma\left(\frac{\alpha_{\mathrm{e}}+5}{4}\right)}{\Gamma\left(\frac{\alpha_{\mathrm{e}}+7}{4}\right)}, \tag{7.8}$$

where $\Gamma(a)$ denotes the Gamma-function (Abramowitz & Stegun 1965) and $\alpha_\nu = (\alpha_{\mathrm{e}}-1)/2$. Note that for later convenience, we introduce a (frequency dependent) characteristic magnetic field strength B_{c} which implies a characteristic magnetic energy density $\varepsilon_{B_{\mathrm{c}}}$. Line-of-sight integration of the radio emissivity $j_\nu(\boldsymbol{r})$ yields the surface brightness of the radio emission $S_\nu(\boldsymbol{r}_\perp)$.

7.2.2. Cosmic ray protons

7.2.2.1. CRp population

In contrast to the previously introduced CRe population and owing to the higher rest mass of protons, we assume the differential number density distribution of a CRp population to be described by a power-law in momentum p_{p} which for instance is motivated by shock acceleration studies:

$$f_{\mathrm{p}}(\boldsymbol{r}, p_{\mathrm{p}})\,\mathrm{d}p_{\mathrm{p}}\,\mathrm{d}V = \tilde{n}_{\mathrm{CRp}}(\boldsymbol{r})\left(\frac{p_{\mathrm{p}}\,c}{\mathrm{GeV}}\right)^{-\alpha_{\mathrm{p}}}\left(\frac{c\,\mathrm{d}p_{\mathrm{p}}}{\mathrm{GeV}}\right)\mathrm{d}V. \tag{7.9}$$

The normalization $\tilde{n}_{\mathrm{CRp}}(\boldsymbol{r})$ can be determined in such a way that the kinetic CRp energy density $\varepsilon_{\mathrm{CRp}}(\boldsymbol{r})$ is expressed in terms of the thermal energy density $\varepsilon_{\mathrm{th}}(\boldsymbol{r})$ of the ICM,

$$\varepsilon_{\mathrm{CRp}}(\boldsymbol{r}) \quad = \quad X_{\mathrm{CRp}}(\boldsymbol{r})\,\varepsilon_{\mathrm{th}}(\boldsymbol{r}) = A_{E_{\mathrm{p}}}\,\tilde{n}_{\mathrm{CRp}}(\boldsymbol{r}), \tag{7.10}$$

$$A_{E_{\mathrm{p}}}(\alpha_{\mathrm{p}}) \quad = \quad \frac{m_{\mathrm{p}}\,c^2}{2\,(\alpha_{\mathrm{p}}-1)}\left(\frac{m_{\mathrm{p}}\,c^2}{\mathrm{GeV}}\right)^{1-\alpha_{\mathrm{p}}}\mathcal{B}\left(\frac{\alpha_{\mathrm{p}}-2}{2}, \frac{3-\alpha_{\mathrm{p}}}{2}\right). \tag{7.11}$$

$\mathcal{B}(a,b)$ denotes the Beta-function (Abramowitz & Stegun 1965).

Aging imprints a modulation on the low energy part of the CRp spectrum by Coulomb losses in the plasma. This modification, which impacts on the CRp distribution function $f_{\mathrm{p}}(\boldsymbol{r}, p_{\mathrm{p}})$ and thus on $A_{E_{\mathrm{p}}}(\alpha_{\mathrm{p}})$, can be treated approximately by imposing a lower momentum cutoff as described in Pfrommer & Enßlin (2004a). On the other side, highly energetic CRp with energies beyond 2×10^7 GeV are able to escape from the galaxy cluster assuming momentum dependent CRp diffusion in a turbulent magnetic field with a Kolmogorov-type spectrum on small scales (Berezinsky et al. 1997). The finite lifetime and size of particle accelerating shocks also give rise to high-energy breaks in the CRp spectrum. These low and high momentum cutoffs are always present in the CRp population. However, for CRp spectral indices between $2 \lesssim \alpha_{\mathrm{p}} \lesssim 3$ these spectral breaks have negligible influence on the CRp energy density. If the breaks are neglected, the CRp energy density would diverge for $\alpha_{\mathrm{p}} \lesssim 2$ at the high-energy and for $3 \lesssim \alpha_{\mathrm{p}}$ at the low-energy part of the spectrum. In these cases, breaks have to be included by replacing $A_{E_{\mathrm{p}}}$ in Eqn. (7.10) with

$$\tilde{A}_{E_{\mathrm{p}}}(\alpha_{\mathrm{p}}) \quad = \quad \frac{m_{\mathrm{p}}\,c^2}{2\,(\alpha_{\mathrm{p}}-1)}\left(\frac{m_{\mathrm{p}}\,c^2}{\mathrm{GeV}}\right)^{1-\alpha_{\mathrm{p}}}\left[\mathcal{B}_{x(\tilde{p})}\left(\frac{\alpha_{\mathrm{p}}-2}{2}, \frac{3-\alpha_{\mathrm{p}}}{2}\right) + 2\,\tilde{p}^{1-\alpha_{\mathrm{p}}}\left(\sqrt{1+\tilde{p}^2}-1\right)\right]_{\tilde{p}_2}^{\tilde{p}_1}, \tag{7.12}$$

$$x(\tilde{p}) \quad = \quad (1+\tilde{p}^2)^{-1}, \text{ and } \tilde{p} = \frac{p_{\mathrm{p}}}{m_{\mathrm{p}}c}, \tag{7.13}$$

where $\mathcal{B}_x(a,b)$ denotes the incomplete Beta-function (Abramowitz & Stegun 1965) and $\tilde{p}_1$ and $\tilde{p}_2$ are the lower and higher break momenta, respectively.

7.2.2.2. Hadronically induced γ-ray emission

The CRp interact hadronically with the ambient thermal gas and produce pions, provided their momentum exceeds the kinematic threshold $p_{thr} = 0.78$ GeV c^{-1} for the reaction. The neutral pions decay into γ-rays while the charged pions decay into secondary electrons (and neutrinos):

$$
\begin{aligned}
\pi^{\pm} &\rightarrow \mu^{\pm} + \nu_{\mu}/\bar{\nu}_{\mu} \rightarrow e^{\pm} + \nu_e/\bar{\nu}_e + \nu_{\mu} + \bar{\nu}_{\mu} \\
\pi^0 &\rightarrow 2\gamma \,.
\end{aligned}
$$

Only the CRp population above the kinematic threshold p_{thr} is visible through its decay products in γ-ray and synchrotron emission.

An analytic formula describing the omnidirectional (i.e. integrated over 4π solid angle) differential γ-ray source function resulting from π^0-decay of a power-law CRp population is given in Pfrommer & Enßlin (2004a):

$$
q_{\gamma}(\boldsymbol{r}, E_{\gamma})\, dE_{\gamma}\, dV \simeq \sigma_{pp}\, c\, n_N(\boldsymbol{r})\, 2^{2-\alpha_{\gamma}}\, \frac{\tilde{n}_{CRp}(\boldsymbol{r})}{\text{GeV}}\, \frac{4}{3\,\alpha_{\gamma}} \left(\frac{m_{\pi^0}\, c^2}{\text{GeV}}\right)^{-\alpha_{\gamma}} \left[\left(\frac{2\, E_{\gamma}}{m_{\pi^0}\, c^2}\right)^{\delta_{\gamma}} + \left(\frac{2\, E_{\gamma}}{m_{\pi^0}\, c^2}\right)^{-\delta_{\gamma}}\right]^{-\alpha_{\gamma}/\delta_{\gamma}} dE_{\gamma}\, dV, \quad (7.14)
$$

where $n_N(\boldsymbol{r}) = d_{tar}\, n_e(\boldsymbol{r}) = n_e(\boldsymbol{r})/(1 - \frac{1}{2}X_{He})$ denotes the target nucleon density in the ICM while assuming primordial element composition with $X_{He} = 0.24$, which holds approximately. The formalism also includes the detailed physical processes at the threshold of pion production like the velocity distribution of CRp, momentum dependent inelastic CRp-p cross section, and kaon decay channels. The shape parameter δ_{γ} and the effective cross section σ_{pp} depend on the spectral index of the γ-ray spectrum α_{γ} according to

$$
\delta_{\gamma} \simeq 0.14\, \alpha_{\gamma}^{-1.6} + 0.44 \qquad \text{and} \tag{7.15}
$$

$$
\sigma_{pp} \simeq 32 \cdot \left(0.96 + e^{4.4 - 2.4\,\alpha_{\gamma}}\right) \text{ mbarn}. \tag{7.16}
$$

There is a detailed discussion in Pfrommer & Enßlin (2004a) how the γ-ray spectral index α_{γ} relates to the spectral index of the parent CRp population α_p. In Dermer's model, which is motivated by accelerator experiments, the pion multiplicity is independent of energy yielding the relation $\alpha_{\gamma} = \alpha_p$ (Dermer 1986a,b).

Provided the CRp population has a power-law spectrum, the integrated γ-ray source density λ_{γ} for pion decay induced γ-rays can be obtained by integrating the γ-ray source function $q_{\gamma}(\boldsymbol{r}, E_{\gamma})$ in Eqn. (7.14) over an energy interval yielding

$$
\lambda_{\gamma}(\boldsymbol{r}, E_1, E_2) = \int_{E_1}^{E_2} dE_{\gamma}\, q_{\gamma}(\boldsymbol{r}, E_{\gamma}) = A_{\gamma}(\alpha_p)\, A_{E_p}^{-1}(\alpha_p)\, X_{CRp}(\boldsymbol{r})\, n_e^2(\boldsymbol{r})\, kT_e(\boldsymbol{r}), \tag{7.17}
$$

$$
\text{where } A_{\gamma}(\alpha_p) = \frac{\sigma_{pp}(\alpha_p)\, c\, d_e\, d_{tar} \left[\mathcal{B}_x\left(\frac{\alpha_{\gamma}+1}{2\,\delta_{\gamma}}, \frac{\alpha_{\gamma}-1}{2\,\delta_{\gamma}}\right)\right]_{x_1}^{x_2}}{\left(\frac{m_{\pi^0}\, c^2}{\text{GeV}}\right)^{\alpha_{\gamma}-1}\, 2^{\alpha_{\gamma}-1}\, \alpha_{\gamma}\, \delta_{\gamma}}, \tag{7.18}
$$

$$
\text{and } x_i = \left[1 + \left(\frac{m_{\pi^0}\, c^2}{2\, E_i}\right)^{2\,\delta_{\gamma}}\right]^{-1} \text{ for } i \in \{1, 2\}. \tag{7.19}
$$

The γ-ray number flux $\mathcal{F}_{\gamma}$ is derived by means of volume integration over the emission region and correct accounting for the growth of the area of the emission sphere on which the photons are distributed:

$$
\mathcal{F}_{\gamma}(E_1, E_2) = \frac{1+z}{4\pi\, D^2} \int dV\, \lambda_{\gamma}[\boldsymbol{r}, (1+z)E_1, (1+z)E_2]. \tag{7.20}
$$

Here D denotes the luminosity distance and the additional factors of $1 + z$ account for the cosmological redshift of the photons.

7.2.2.3. Hadronically induced synchrotron emission

Following for instance Dolag & Enßlin (2000) and Pfrommer & Enßlin (2004a), the steady-state CRe spectrum is governed by injection of secondaries and cooling processes so that it can be described by the continuity equation

$$
\frac{\partial}{\partial E_e}\left(\dot{E}_e(\boldsymbol{r}, E_e) f_e(\boldsymbol{r}, E_e)\right) = q_e(\boldsymbol{r}, E_e)\,. \tag{7.21}
$$

For $\dot{E}_e(\boldsymbol{r}, p) < 0$ this equation is solved by

$$f_e(\boldsymbol{r}, E_e) = \frac{1}{|\dot{E}_e(\boldsymbol{r}, E_e)|} \int_{E_e}^{\infty} dE_e' \, q_e(\boldsymbol{r}, E_e') \,. \tag{7.22}$$

For the energy range of interest, the cooling of the radio emitting CRe is dominated by synchrotron and inverse Compton losses:

$$-\dot{E}_e(\boldsymbol{r}, E_e) = \frac{4 \, \sigma_T \, c}{3 \, m_e^2 \, c^4} \left[\varepsilon_B(\boldsymbol{r}) + \varepsilon_{CMB} \right] E_e^2 \,, \tag{7.23}$$

where σ_T is the Thomson cross section, $\varepsilon_B(\boldsymbol{r})$ is the local magnetic field energy density, and $\varepsilon_{CMB} = B_{CMB}^2/(8\pi)$ is the energy density of the cosmic microwave background expressed by an equivalent field strength $B_{CMB} = 3.24 \, (1 + z)^2 \, \mu G$. Assuming that the parent CRp population is represented by a power-law (7.9), the CRe population above a GeV is therefore described by a power-law spectrum

$$f_e(\boldsymbol{r}, E_e) \;\; = \;\; \frac{\tilde{n}_{CRe}(\boldsymbol{r})}{GeV} \left(\frac{E_e}{GeV} \right)^{-\alpha_e}, \tag{7.24}$$

$$\text{and} \;\; \tilde{n}_{CRe}(\boldsymbol{r}) \;\; = \;\; A_{\varepsilon_{eff}}(\boldsymbol{r}) \frac{\tilde{n}_{CRp}(\boldsymbol{r})}{\varepsilon_B(\boldsymbol{r}) + \varepsilon_{CMB}}, \tag{7.25}$$

$$A_{\varepsilon_{eff}}(\boldsymbol{r}) \;\; = \;\; \frac{16^{-(\alpha_e - 2)}}{\alpha_e - 2} \frac{\sigma_{pp} \, m_e^2 \, c^4 \, n_N(\boldsymbol{r})}{\sigma_T \, GeV} \,, \tag{7.26}$$

where the effective CRp-p cross section σ_{pp} is given by Eqn. (7.16).

The hadronically induced synchrotron emissivity j_ν at frequency ν and per steradian of such a CRe population (7.24) which is located in an isotropic distribution of magnetic fields within the halo volume is given by Eqn. (7.6). However, the normalization $\tilde{n}_{CRe}(\boldsymbol{r})$ of the CRe population is given by Eqn. (7.25). The spectral index of the synchrotron emission is related to the CRp spectral index by $\alpha_\nu = (\alpha_e - 1)/2 = \alpha_p/2$.

7.3. Minimum energy criteria

This section develops minimum energy criteria in order to estimate the magnetic field and studies the tolerance region of the obtained estimates. As described in Sect. 7.1, we discuss two different approaches when requiring the non-thermal energy density of the source to be minimal for a particular (observed) synchrotron emission. The classical minimum energy criterion used in radio astronomy (Pohl 1993, Beck et al. 1996, Brunetti et al. 1997) can be applied irrespective of the particular acceleration process of CRe, but unfortunately it relies on uncertain assumptions or parameters. Provided the hadronic scenario of synchrotron emission applies, these dependencies can be softened. The resulting minimum energy argument needs to be changed accordingly.

The philosophy of these approaches is to provide an estimate of the energetically least expensive radio emission model possible in each of these physically motivated scenarios. Thus, the obtained minimum energy estimates should not be taken literally in a sense that they are necessarily realized in Nature. However, the minimum energy estimates allow scrutinizing the hadronic model for extended radio synchrotron emission in clusters of galaxies by comparing to the thermal energy density. For the classical minimum energy estimate, such a comparison can yield important constraints on the accessible parameter space.

The non-thermal energy density in the intra-cluster medium (ICM), which is the quantity to be minimized, is composed of the sum of the energy densities in magnetic fields, CRp and CRe:

$$\varepsilon_{NT} = \varepsilon_B + \varepsilon_{CRp} + \varepsilon_{CRe}. \tag{7.27}$$

The CRp population also includes higher mass nuclei in addition to protons. For convenience, we introduce canonical dimensionless energy densities by means of scaling with the critical magnetic energy density $\varepsilon_{B_c} = B_c^2/(8\pi)$, where B_c is defined in Eqn. (7.7):

$$x_{NT}(\boldsymbol{r}) \equiv \frac{\varepsilon_{NT}(\boldsymbol{r})}{\varepsilon_{B_c}} \,, \;\; x_{CRp}(\boldsymbol{r}) \equiv \frac{\varepsilon_{CRp}(\boldsymbol{r})}{\varepsilon_{B_c}} \,, \;\; x_{CRe}(\boldsymbol{r}) \equiv \frac{\varepsilon_{CRe}(\boldsymbol{r})}{\varepsilon_{B_c}} \,, \tag{7.28}$$

$$x_B(\boldsymbol{r}) \equiv \frac{\varepsilon_B(\boldsymbol{r})}{\varepsilon_{B_c}} \,, \;\; x_{th}(\boldsymbol{r}) \equiv \frac{\varepsilon_{th}(\boldsymbol{r})}{\varepsilon_{B_c}} \,, \;\; \text{and} \;\; x_{CMB} \equiv \frac{\varepsilon_{CMB}}{\varepsilon_{B_c}} \,. \tag{7.29}$$

After presenting the conceptually simpler classical minimum energy criterion, we will subsequently discuss the hadronic minimum energy criterion.

7.3.1. Classical minimum energy criterion

This section presents the classical minimum energy criterion from a physically motivated point of view, probing synchrotron emission from CRe characterized by a power-law distribution function without specifying their origin. This approach implies putting up with a dependence of the inferred magnetic field strength on unknown parameters like the lower energy cutoff of the CRe population or the unknown contribution of CRp to the non-thermal energy density.

7.3.1.1. Derivation

Assuming a proportionality between the CRe and CRp energy densities, i.e. $x_{CRp} = k_p x_{CRe}$, the non-thermal energy composition equation (7.27) can be written as

$$x_{NT} = x_B + (1 + k_p) x_{CRe}. \tag{7.30}$$

This assumption is reasonable if for instance the thermal electron population and the CRp were energized by the same shock wave assuming that there is a constant fraction of energy going into the CRp population by such an acceleration process, provided injection processes alone determine the energies. In order to proceed, we need an expression for j_ν (given by Eqn. (7.6)) as a function of the dimensionless energy densities considered here:

$$j_\nu(\boldsymbol{r}) = \frac{A_{E_{syn}}(\alpha_e)\,\varepsilon_{B_c}}{A_{E_e}}\, x_{CRe}(\boldsymbol{r})\, x_B(\boldsymbol{r})^{1+\delta}, \quad \text{where} \tag{7.31}$$

$$\delta = \frac{\alpha_\nu - 1}{2} = \frac{\alpha_e - 3}{4}. \tag{7.32}$$

For consistency reasons, which will become clear in Sect. 7.3.2, we introduce δ as a parameterization of the spectral index. For typical radio (mini-)halos, δ is a small quantity: the synchrotron spectral index $\alpha_\nu = 1$ corresponds to $\delta = 0$. Solving Eqn. (7.31) for the CRe energy density yields

$$x_{CRe} = C_{class}(\boldsymbol{r})\, x_B(\boldsymbol{r})^{-1-\delta}, \quad \text{where} \tag{7.33}$$

$$C_{class}(\boldsymbol{r}) \equiv \frac{A_{E_e}\, j_\nu(\boldsymbol{r})}{A_{E_{syn}}\, \varepsilon_{B_c}} \propto \frac{j_\nu}{\nu^3} \tag{7.34}$$

is a convenient auxiliary variable. Combining Eqns. (7.30) and (7.33) yields the non-thermal energy density solely as a function of the magnetic energy density

$$x_{NT} = x_B + (1 + k_p)\, C_{class}(\boldsymbol{r})\, x_B(\boldsymbol{r})^{-1-\delta}. \tag{7.35}$$

Requesting this energy density to be minimal for a given synchrotron emissivity yields the energetically least expensive radio emission model possible in this approach:

$$\left(\frac{\partial x_{NT}}{\partial x_B} \bigg|_{j_\nu} \right) = 1 - (1 + k_p)(1 + \delta)\, C_{class}(\boldsymbol{r}) x_B(\boldsymbol{r})^{-2-\delta} \stackrel{!}{=} 0. \tag{7.36}$$

The corresponding CRp, CRe and magnetic energy densities are given by

$$x_{B_{min}}(\boldsymbol{r}) = \left[(1 + k_p)(1 + \delta)\, C_{class}(\boldsymbol{r}) \right]^{1/(2+\delta)}, \tag{7.37}$$

$$x_{CRe_{min}}(\boldsymbol{r}) = C_{class}(\boldsymbol{r}) \left[(1 + k_p)(1 + \delta)\, C_{class}(\boldsymbol{r}) \right]^{-(1+\delta)/(2+\delta)}, \tag{7.38}$$

$$x_{CRp_{min}}(\boldsymbol{r}) = k_p\, x_{CRe_{min}}(\boldsymbol{r}). \tag{7.39}$$

Note that these formulae deviate from Pacholczyk (1970), since we use a fixed interval in CRe energy rather than in radio frequency (cf. Sect. 7.1). However, they are equivalent to those obtained by Brunetti et al. (1997).

7.3.1.2. Localization of classical minimum energy densities

We wish to quantify how tight our statements about the inferred minimum energy densities are, i.e. to assign a tolerance region to the minimum energy estimates. This region would have the meaning of a quasi-optimal realization of the particular energy densities. The curvature radius at the extremal value is one possible way of characterizing the 'sharpness' of the minimum:[3]

$$\sigma_{x_B, \text{Gauss}} \equiv \left(\frac{1}{x_{\text{NT}}} \frac{\partial^2 x_{\text{NT}}}{\partial x_B^2} \Bigg|_{x_{B_{\min}}} \right)^{-1/2}. \tag{7.40}$$

In order to avoid unphysical negative values for the lower tolerance level of $x_{B_{\min}}$ we rather adopt the following logarithmic measure of the curvature:

$$\sigma_{\ln x_B} \equiv \left(\frac{\partial^2 \ln x_{\text{NT}}}{\partial (\ln x_B)^2} \Bigg|_{x_{B_{\min}}} \right)^{-1/2}. \tag{7.41}$$

Considering the linear representation of x_B, this definition explicitly implies tolerance levels which are given by $\exp(\ln x_B \pm \sigma_{\ln x_B})$. Applying this definition to Eqn. (7.35) yields the theoretical tolerance level of the estimated minimum magnetic energy density,

$$\sigma_{\ln x_B}(\boldsymbol{r}) = \left\{ \frac{x_{B_{\min}}^{-2-\delta} \left[C_{\text{class}} \left(1 + k_{\text{p}} \right) + x_{B_{\min}}^{2+\delta} \right]^2}{C_{\text{class}} \left(1 + k_{\text{p}} \right) (2 + \delta)^2} \right\}^{1/2} (\boldsymbol{r}). \tag{7.42}$$

The tolerance level of the estimated minimum CRp energy density is given by

$$\sigma_{\ln x_{\text{CRp}}} \equiv \left| \frac{\partial \ln x_{\text{CRp}}}{\partial \ln x_B} \right|_{x_{B_{\min}}} \sigma_{\ln x_B}, \tag{7.43}$$

while the theoretical tolerance level of the estimated minimum CRe energy density can be obtained likewise. Applying this Gaussian error propagation to Eqn. (7.33), we obtain following general result:

$$\sigma_{\ln x_{\text{CRp}}} = \sigma_{\ln x_{\text{CRe}}} = (1 + \delta) \sigma_{\ln x_B}. \tag{7.44}$$

7.3.1.3. Equipartition condition

In order to investigate under which conditions the classical minimum energy criterion implies exact equipartition, we examine the special case $\delta = 0$ of Eqn. (7.37). The resulting minimal magnetic and CRp energy densities read

$$x_{B_{0,\min}}(\boldsymbol{r}) = \sqrt{(1 + k_{\text{p}}) C_{\text{class}}(\boldsymbol{r})}, \tag{7.45}$$

$$x_{\text{CRp}_{0,\min}}(\boldsymbol{r}) = \sqrt{\frac{k_{\text{p}}^2 C_{\text{class}}(\boldsymbol{r})}{(1 + k_{\text{p}})}} \quad \overset{k_{\text{p}} \gg 1}{\longrightarrow} \quad x_{B_{0,\min}}(\boldsymbol{r}). \tag{7.46}$$

This comparison shows that there exists exact equipartition between the CRp and magnetic energy densities if $\delta = 0$ and $k_{\text{p}} \gg 1$! In our Galaxy $k_{\text{p}} \simeq 100$ (Beck et al. 1996) and $\alpha_\nu = \alpha_{\text{GHz}} = 0.8$ suggesting $\delta = -0.1$ (Beuermann et al. 1985), which implies that these equipartition conditions are well fulfilled. Comparing this result with studies that are using a combination of synchrotron emission, the local CRe density, and diffuse continuum γ-rays, Strong et al. (2000) interestingly imply the same magnetic field strength as inferred from equipartition arguments (Beck et al. 1996). The corresponding minimal CRe energy density is given by

$$x_{\text{CRe}_{0,\min}}(\boldsymbol{r}) = \sqrt{\frac{C_{\text{class}}(\boldsymbol{r})}{(1 + k_{\text{p}})}} \quad \overset{k_{\text{p}} \ll 1}{\longrightarrow} \quad x_{B_{0,\min}}(\boldsymbol{r}). \tag{7.47}$$

The classical minimum energy densities in CRe and magnetic fields are in exact equipartition if $\delta = 0$ and $k_{\text{p}} \ll 1$! In the limiting case $\delta = 0$, the theoretical tolerance levels of the estimated classical minimum energy densities read

$$\sigma_{\ln x_{B_0}} = \sigma_{\ln x_{\text{CRp}_0}} = \sigma_{\ln x_{\text{CRe}_0}} = 1. \tag{7.48}$$

---

[3]One could picture this approach by assuming Gaussian statistics for the distribution of non-thermal energy densities. The curvature radius at the minimum would then correspond to the width σ_B and thus yielding the 68%-confidence level with respect to this extremal value.

7.3.2. Hadronic minimum energy criterion

This section deals with the hadronic minimum energy criterion and thus probes hadronically induced synchrotron emission. If a significant part of the CRe population is known to be generated by hadronic interactions, the minimum energy estimate allows testing for the realization of the minimum energy state for a given independent measurement of the magnetic field strength. Thus, the proposed minimum energy criterion would provide information about the dynamical state of the magnetic field.

7.3.2.1. Derivation

To derive the hadronic minimum energy criterion, we need an expression for the CRp energy density as a function of the magnetic energy density which is obtained by combining Eqns. (7.6) and (7.25):

$$x_{\mathrm{CRp}}(\boldsymbol{r}) = C_{\mathrm{hadr}}(\boldsymbol{r})\left[x_B(\boldsymbol{r}) + x_{\mathrm{CMB}}\right] x_B(\boldsymbol{r})^{-1-\delta}, \tag{7.49}$$

$$C_{\mathrm{hadr}}(\boldsymbol{r}) \equiv \frac{A_{E_{\mathrm{p}}}}{A_{E_{\mathrm{syn}}}} \frac{j_\nu(\boldsymbol{r})}{A_{\varepsilon_{\mathrm{eff}}}(\boldsymbol{r})} \propto \frac{j_\nu(\boldsymbol{r})}{\nu\, n_{\mathrm{N}}(\boldsymbol{r})}, \tag{7.50}$$

$$\delta = \frac{\alpha_\nu - 1}{2} = \frac{\alpha_{\mathrm{e}} - 3}{4} = \frac{\alpha_{\mathrm{p}} - 2}{4}. \tag{7.51}$$

The parameter $C_{\mathrm{hadr}}(\boldsymbol{r})$ has the meaning of a hadronic synchrotron emissivity per target nucleon density and per frequency. Its value decreases for any existing cutoff in the parent CRp population as described by Eqn. (7.12). For convenience we introduce the parameter δ which ranges within $[-0.1, 0.2]$ for conceivable CRp spectral indices $\alpha_{\mathrm{p}} = [1.6, 2.8]$.

Assuming the hadronic electron source to be dominant, we can neglect the primary CRe population. In any case, the energy density of hadronically generated CRe is negligible compared to the energy density of the parent CRp population: Above energies of $\sim$ GeV the differential hadronic $\tilde{k}_{\mathrm{p}} = \tilde{n}_{\mathrm{CRp}}/\tilde{n}_{\mathrm{CRe}}$ has typically values ranging between $\tilde{k}_{\mathrm{p}} \sim 100$ (Perseus) and $\tilde{k}_{\mathrm{p}} \sim 300$ (Coma), where we inserted the typical values of the central density and magnetic field strength. The tilde in $\tilde{k}_{\mathrm{p}}$ indicates the slightly modified definition compared to the previous classical case. Requiring minimum non-thermal energy density within the hadronic framework for a given synchrotron emissivity yields

$$\left(\frac{\partial x_{\mathrm{NT}}}{\partial x_B}\bigg|_{j_\nu}\right) = 1 + \frac{\partial x_{\mathrm{CRp}}}{\partial x_B}\bigg|_{j_\nu} \overset{!}{=} 0. \tag{7.52}$$

By using Eqn. (7.49) we obtain the following implicit equation for the minimum magnetic energy density:

$$\left[(1 + \delta)\, x_{\mathrm{CMB}} + \delta x_{B_{\min}}(\boldsymbol{r})\right] x_{B_{\min}}(\boldsymbol{r})^{-2-\delta} = C_{\mathrm{hadr}}^{-1}(\boldsymbol{r}). \tag{7.53}$$

The definition of $C_{\mathrm{hadr}}(\boldsymbol{r})$ (7.50) reveals an implicit dependence on the parametrized spectral index δ. However, the right hand side of the minimum energy criterion (7.53) is uniquely determined for a given spectral index and an observed synchrotron emissivity at a particular frequency. Thus, the minimum energy density of the magnetic field giving rise to an observed synchrotron emission in the hadronic model can either be obtained by solving Eqn. (7.53) numerically or applying the asymptotic expansion which will be developed in Sect. 7.3.2.2.

7.3.2.2. Asymptotic expansion for $\delta \neq 0$

The asymptotic expansion of the magnetic field energy density as a function of the small parameter δ follows from the minimum energy criterion (7.53):

$$x_{B_{\min}}(\boldsymbol{r}) = x_{B_0}(\boldsymbol{r}) + \delta x_{B_1}(\boldsymbol{r}) + \delta^2 x_{B_2}(\boldsymbol{r}) + O(\delta^3), \tag{7.54}$$

$$x_{B_0}(\boldsymbol{r}) = \sqrt{C_{\mathrm{hadr}}(\boldsymbol{r})\, x_{\mathrm{CMB}}}, \tag{7.55}$$

$$x_{B_1}(\boldsymbol{r}) = \frac{x_{B_0}}{2}\left(1 - \ln x_{B_0} + \frac{x_{B_0}}{x_{\mathrm{CMB}}}\right)(\boldsymbol{r}), \tag{7.56}$$

$$x_{B_2}(\boldsymbol{r}) = \frac{x_{B_0}}{2}\left[-\frac{1}{2}\left(\ln x_{B_0}\right)^2 - \frac{x_{B_1}}{x_{B_0}}\left(2 + \ln x_{B_0}\right) + \frac{x_{B_1}^2}{x_{B_0}^2}\right]. \tag{7.57}$$
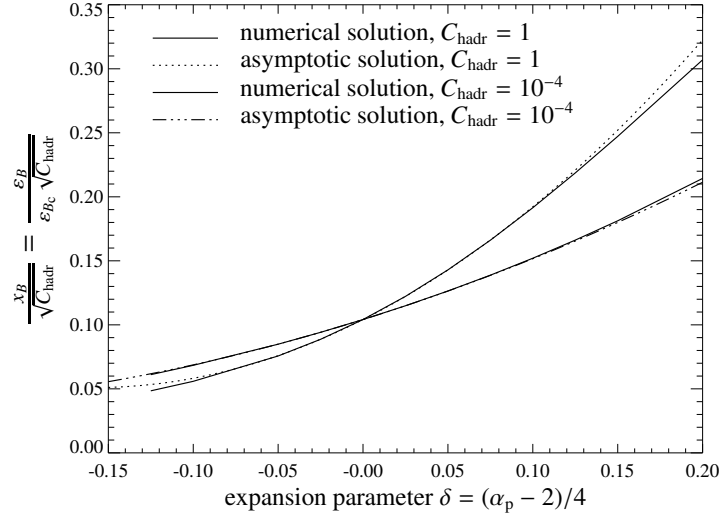
Figure 7.1.: Comparison between the numerical solution and the second order asymptotic expansion for $C_{\text{hadr}} = 1$ (cool core cluster, formerly referred to as cooling flow cluster) and $C_{\text{hadr}} = 10^{-4}$ (cluster without a cool core). The perfect match indicates a fast convergence of the asymptotic solution for the range of δ being considered.

A comparison between the numerical solution and the asymptotic solution for two different values of the parameter C_{hadr} is shown in Fig. 7.1. The particular values of the parameter C_{hadr} will be motivated in Sect. 7.5.2. This figure should serve as mathematical illustration of the convergence behavior of the asymptotic expansion while keeping the parameter C_{hadr} fixed. The second order asymptotic solution perfectly agrees with the exact solution for the range $\delta = [-0.15, 0.2]$ of conceivable CRp spectral indices $\alpha_{\text{p}} = [1.6, 2.8]$.

7.3.2.3. Localization of hadronic minimum energy densities

Considering the accuracy of the estimated minimum energy densities in the hadronic scenario, we can also apply the logarithmic measure of the theoretical tolerance level as defined in Eqn. (7.41):

$$
\begin{aligned}
\sigma_{\ln x_B}(\boldsymbol{r}) &= \left[x_{B_{\min}}^{2+\delta} + C_{\text{hadr}} \left(x_{B_{\min}} + x_{\text{CMB}} \right) \right] \left(C_{\text{hadr}} \, x_{B_{\min}} \right)^{-1/2} \\
&\quad \times \left\{ C_{\text{hadr}} \, x_{\text{CMB}} + x_{B_{\min}}^{1+\delta} \left[(1+\delta)^2 x_{B_{\min}} + (2+\delta)^2 x_{\text{CMB}} \right] \right\}^{-1/2} (\boldsymbol{r}).
\end{aligned}
\tag{7.58}
$$

The corresponding tolerance level for the minimum CRp energy density is obtained by applying Gaussian error propagation (7.43):

$$
\sigma_{\ln x_{\text{CRp}}}(\boldsymbol{r}) = \left(\frac{x_{\text{CMB}}}{x_{B_{\min}}(\boldsymbol{r}) + x_{\text{CMB}}} + \delta \right) \sigma_{\ln x_B}(\boldsymbol{r}).
\tag{7.59}
$$

The consequences of these rather unwieldy formulae will become intuitively clear in the next section where characteristic limiting cases are investigated.

7.3.2.4. Special cases

In order to gain insight into the hadronic minimum energy criterion, we investigate special cases of Eqn. (7.53), namely $\delta \to 0$, $\varepsilon_B \gg \varepsilon_{\text{CMB}}$, and $\varepsilon_B \ll \varepsilon_{\text{CMB}}$, while simultaneously considering the resulting tolerance regions of the previous Sect. 7.3.2.3.

1. $\delta \to 0$: The limit of $\delta \to 0$ corresponds to a hard spectral CRp population described by a spectral index of $\alpha_{\text{p}} = 2.0$ and thus $\alpha_\nu = 1$. There the dimensionless magnetic field energy density reads

$$
x_{B_{0,\min}}(\boldsymbol{r}) = \sqrt{C_{\text{hadr}}(\boldsymbol{r}) \, x_{\text{CMB}}} \propto \left[\frac{j_\nu(\boldsymbol{r}) \, \varepsilon_{\text{CMB}}}{\nu \, n_{\text{N}}(\boldsymbol{r})} \right]^{1/2}.
\tag{7.60}
$$

We can formulate the corresponding dimensionless CRp energy density resulting from this minimizing argument:

$$x_{\mathrm{CRp_{0,min}}}(\boldsymbol{r}) = C_{\mathrm{hadr}}(\boldsymbol{r}) + \sqrt{C_{\mathrm{hadr}}(\boldsymbol{r})\, x_{\mathrm{CMB}}}. \tag{7.61}$$

It is interesting to note that there are two regimes for $x_{\mathrm{CRp_{0,min}}}$, namely

$$x_{\mathrm{CRp_{0,min}}}(\boldsymbol{r}) = \begin{cases} C_{\mathrm{hadr}}(\boldsymbol{r}), & \text{for } C_{\mathrm{hadr}}(\boldsymbol{r}) \gg 0.01\, \nu_{\mathrm{GHz}}^{-2}, \\ x_{B_{0,min}}(\boldsymbol{r}), & \text{for } C_{\mathrm{hadr}}(\boldsymbol{r}) \ll 0.01\, \nu_{\mathrm{GHz}}^{-2}. \end{cases} \tag{7.62}$$

Only in the limit of a small parameter $C_{\mathrm{hadr}}(\boldsymbol{r})$ and $\delta = 0$, there is an exact equipartition between the hadronic minimum energy densities in CRp and magnetic fields!

The tolerance regions of the estimated minimum energy densities are also more intuitive to understand in the limit $\delta = 0$ compared to the general case laid down in Eqn. (7.58):

$$\sigma_{\ln x_{B_0}}(\boldsymbol{r}) = \left(1 + \frac{x_{B_{0,min}}(\boldsymbol{r})}{2x_{\mathrm{CMB}}}\right)^{1/2}, \quad \text{implying two regimes:}$$

$$\sigma_{\ln x_{B_0}}(\boldsymbol{r}) = \begin{cases} 1, & \text{for } x_{B_{0,min}} \ll x_{\mathrm{CMB}}, \\ \left[\dfrac{x_{B_{0,min}}(\boldsymbol{r})}{2x_{\mathrm{CMB}}}\right]^{1/2}, & \text{for } x_{B_{0,min}} \gg x_{\mathrm{CMB}}. \end{cases} \tag{7.63}$$

In the previously studied classical case (7.48), the tolerance region remains constant for all conceivable magnetic energy densities. In contrast to this, the hadronic scenario shows a increasing tolerance region $\sigma_{\ln x_{B_0}}$ for strong magnetic field strengths ($B_{0,min} \gg 3.24\,(1+z)^2\,\mu\mathrm{G}$) which is explained by the following argument: in the limit of strong magnetic fields, the hadronically induced synchrotron emission with $\alpha_\nu = 1$ does not depend any more on the magnetic field strength but only on the CRp energy density. This is, because the inverse Compton cooling is negligible in this regime, implying that observed synchrotron emission is insensitive to any variation of the magnetic field strength since all injected CRe energy results in synchrotron emission. Therefore magnetic field estimates inferred from minimum energy arguments are rather uncertain in the limit of strong magnetic field strengths.

The tolerance levels of the corresponding CRp energy density, derived from Eqn. (7.59), shows two limiting regimes:

$$\sigma_{\ln x_{\mathrm{CRp_0}}}(\boldsymbol{r}) = \left(1 + \frac{x_{B_{0,min}}(\boldsymbol{r})}{x_{\mathrm{CMB}}}\right)^{-1}\left(1 + \frac{x_{B_{0,min}}(\boldsymbol{r})}{2x_{\mathrm{CMB}}}\right)^{1/2}, \quad \text{implying}$$

$$\sigma_{\ln x_{\mathrm{CRp_0}}}(\boldsymbol{r}) = \begin{cases} 1, & \text{for } x_{B_{0,min}} \ll x_{\mathrm{CMB}}, \\ \left[\dfrac{x_{\mathrm{CMB}}}{x_{B_{0,min}}(\boldsymbol{r})}\right]^{1/2}, & \text{for } x_{B_{0,min}} \gg x_{\mathrm{CMB}}. \end{cases} \tag{7.64}$$

The tolerance region of the inferred minimum CRp energy density decreases in the regime of strong magnetic fields which can be understood by the same token as above, i.e. synchrotron losses dominate over the inverse Compton cooling in this limit. Thus, the observed radio emission reflects accurately the CRp energy density in the strong magnetic field limit.

2. $\varepsilon_B \gg \varepsilon_{\mathrm{CMB}}$: In the limit of $\varepsilon_B \gg \varepsilon_{\mathrm{CMB}}$, the magnetic field energy density is an even stronger function of the synchrotron emissivity and the number density of the ambient gas:

$$x_{B_{min}}(\boldsymbol{r}) = [\delta\, C_{\mathrm{hadr}}(\boldsymbol{r})]^{1/(1+\delta)} \simeq \delta\, C_{\mathrm{hadr}}(\boldsymbol{r})^{1/(1+\delta)} \propto \delta \left[\frac{j_\nu(\boldsymbol{r})}{\nu\, n_{\mathrm{N}}(\boldsymbol{r})}\right]^{1/(1+\delta)}, \tag{7.65}$$

where we assumed $|\delta| \ll 1$ in the second step. In the limit of strong magnetic fields and small δ, exact equipartition of the magnetic and CRp hadronic minimum energy density does not occur, because

$$x_{\mathrm{CRp_{min}}}(\boldsymbol{r}) = \delta^{-\delta/(1+\delta)} C_{\mathrm{hadr}}(\boldsymbol{r})^{1/(1+\delta)} \simeq C_{\mathrm{hadr}}(\boldsymbol{r})^{1/(1+\delta)}(1 - \delta \ln \delta). \tag{7.66}$$

3. $\varepsilon_{CMB} \gg \varepsilon_B$: In the opposite limit, we obtain the following minimum energy criterion for the magnetic field energy density:

$$
\begin{align}
x_{B_{\min}}(\boldsymbol{r}) &= [(1+\delta)\, x_{CMB}\, C_{hadr}(\boldsymbol{r})]^{1/(2+\delta)} \tag{3.67a}\\[2mm]
&\simeq \left(1 + \frac{\delta}{2}\right) [x_{CMB} C_{hadr}(\boldsymbol{r})]^{1/(2+\delta)} \tag{3.67b}\\[2mm]
&\propto \left(1 + \frac{\delta}{2}\right) \left[\frac{j_\nu(\boldsymbol{r})\varepsilon_{CMB}}{\nu\, n_{N}(\boldsymbol{r})}\right]^{1/(2+\delta)}, \tag{3.67c}
\end{align}
$$

where we again assumed $\delta \ll 1$ in the second step. In contrast to the previous limit, there is exact equipartition between the magnetic and CRp hadronic minimum energy density to zeroth order in δ,

$$
\begin{align}
x_{CRp_{\min}}(\boldsymbol{r}) &= (1+\delta)^{-(1+\delta)/(2+\delta)} [x_{CMB} C_{hadr}(\boldsymbol{r})]^{1/(2+\delta)} \tag{3.68a}\\[2mm]
&\simeq \left(1 - \frac{\delta}{2}\right) [x_{CMB} C_{hadr}(\boldsymbol{r})]^{1/(2+\delta)}. \tag{3.68b}
\end{align}
$$

7.4. Future testing

This section will discuss possibilities of measuring the magnetic field strength, averaged over the cluster volume, in order to test for the realization of the energetically least expensive state given by the minimum energy criterion.

7.4.1. Inverse Compton emission

The CRe population seen in the radio band via synchrotron emission should also scatter photons of the cosmic microwave background (CMB), the local radiation field of elliptical galaxies, and the thermal X-ray emission of the ICM to different energy bands (Felten & Morrison 1966, Rees 1967). Combining measurements of inverse Compton (IC) and synchrotron emission eliminates the uncertainty in number density of the CRe population provided the inevitable extrapolation of the CRe power-law distribution for certain observed wavebands is justified. This enables the determination of the magnetic field strength B for an IC detection and a lower limit on B for a given non-detection of the IC emission.

The source function q_{IC} owing to IC scattering of CMB photons off an isotropic power law distribution of CRe (Eqn. (7.1)) is (derived from Eqn. (7.31) in Rybicki & Lightman 1979, in the case of Thomson scattering),

$$
\begin{align}
q_{IC}(\boldsymbol{r}, E_\gamma) &= \tilde{q}(\boldsymbol{r})\, f_{IC}(\alpha_e) \left(\frac{m_e\, c^2}{\text{GeV}}\right)^{1-\alpha_e} \left(\frac{E_\gamma}{kT_{CMB}}\right)^{-(\alpha_\nu+1)}, \tag{7.69}\\[2mm]
f_{IC}(\alpha_e) &= \frac{2^{\alpha_e+3}(\alpha_e^2 + 4\alpha_e + 11)}{(\alpha_e+3)^2(\alpha_e+5)(\alpha_e+1)} \Gamma\left(\frac{\alpha_e+5}{2}\right) \zeta\left(\frac{\alpha_e+5}{2}\right), \tag{7.70}\\[2mm]
\text{and}\quad \tilde{q}(\boldsymbol{r}) &= \frac{3\pi\,\sigma_T\,\tilde{n}_{CRe}(\boldsymbol{r})\,(kT_{CMB})^2}{h^3\,c^2}, \tag{7.71}
\end{align}
$$

where $\alpha_\nu = (\alpha_e - 1)/2$ denotes the spectral index, $\zeta(a)$ the Riemann ζ-function (Abramowitz & Stegun 1965), and $\tilde{n}_{CRe}(\boldsymbol{r})$ is given by Eqn. (7.2). After integrating over the considered energy interval and the IC emitting volume in the cluster, the particle flux $\mathcal{F}_\gamma(E_1, E_2)$ is obtained (cf. Eqn. (7.20)).

Enßlin & Biermann (1998) compiled non-detection limits of IC emission of different photon fields in various wavebands from the Coma cluster and obtained the tightest limits on B from the CMB photon field. The same CRe population emitting radio synchrotron radiation scatters CMB photons into the hard X-ray band. Non-detection of this IC emission by the OSSE experiment (Rephaeli et al. 1994) yields a lower limit on the central magnetic field strength of $B_{Coma}(0) > 0.2\ \mu G\ f_B^{-0.43}$, where f_B is the filling factor of the magnetic field in the volume occupied by CRe. Provided the CRe power-law distribution can be extrapolated to lower energies, the limit given by the EUV flux (Lieu et al. 1996) predicts a magnetic field strength stronger than $B_{Coma}(0) > 1.2\ \mu G\ f_B^{-0.43}$.

The reported high energy X-ray excess of the Coma cluster by the Beppo-Sax satellite (Fusco-Femiano et al. 1999) initiated other theoretical explanations about the origin of such an excess than IC up-scattering of CMB photons by relativistic electrons. One possibility implies the existence of a bremsstrahlung emitting supra-thermal

electron population between 10 and 100 keV which would also produce a unique Sunyaev-Zel'dovich signature (Enßlin et al. 1999, Enßlin & Kaiser 2000, Blasi et al. 2000, Blasi 2000, Liang et al. 2002, Colafrancesco et al. 2003). However, such a population is questioned on theoretical reasons (Petrosian 2001), and even the high X-ray excess of Coma itself is under debate (Rossetti & Molendi 2004, Fusco-Femiano et al. 2004). The data analysis of the RXTE observation of A 2256 yielded also evidence for a second spectral component (Rephaeli & Gruber 2003). On the basis of statistics alone, the detected emission is inconclusive as to whether it originates from a thermal multi-temperature fluid or an isothermal gas in combination with a non-thermal IC power-law emission. Future measurements with the IBIS instrument on-board the INTEGRAL satellite should provide even tighter upper limits respectively detections of the IC X-ray flux of a particular cluster and should therefore allow even tighter lower limits on the magnetic field strength.

7.4.2. γ-ray emission

This subsection outlines the method for estimating upper limits on the magnetic field strength using hadronic CRp interactions. The method is based on the idea of combining hadronically induced γ-ray and synchrotron emission to eliminate the uncertainty in number density of the CRp population. For this purpose, one necessarily needs to resolve the detailed broad spectral signature of γ-rays resulting from the π^0-decay (π^0-bump centered on $m_{\pi^0}c^2/2 \simeq$ 67.5 MeV) as laid down in Eqn. (7.17). This is to exclude other possible processes contributing to diffuse extended γ-ray emission like IC radiation or dark matter annihilation. Because of possible other additional contributions to the diffuse synchrotron emission from CRe populations, e.g. primarily accelerated electrons, we are only able to provide an upper limit on the magnetic field strength.

The proposed algorithm allows for different spatial resolutions of the γ-ray and synchrotron emission. The application, we have in mind, is the determination of intracluster magnetic fields. In this case, γ-ray observations of the π^0-decay induced γ-ray emission signature are only able to provide integrated γ-ray fluxes of the entire cluster due to their comparably large point spread function. γ-ray fluxes depend on the thermal electron density and temperature profiles which have to be derived from X-ray observations. However, if we assumed a comparable resolution in γ-ray and synchrotron emission the dependences on the thermal electron population could be eliminated (cf. Sect. 7.2.2). The algorithm consists of the following two steps:

1. Choosing a constant scaling parameter X_{CRp} for the CRp population and performing the volume integral of the energy integrated γ-ray source density λ_γ (7.17) yields the γ-ray flux according to Eqn. (7.20). The CRp parameter X_{CRp} is obtained by comparing the observed to the theoretically expected γ-ray flux.

2. Inserting X_{CRp} into the synchrotron emissivity j_ν (7.6) enables us to solve for the magnetic field strength as function of angle on the sky when comparing to radio surface brightness observations.

Once a detailed angular distribution of π^0-decay induced γ-ray emission from a particular astrophysical object is available this algorithm may be implemented for the average of pixels contained within a certain solid angle. In this case the spatial distribution of CRp may even be deprojected.

Is there a chance to apply this method to galaxy cluster magnetic fields with future γ-ray instruments? Because of the necessity of resolving the broad spectral signature of γ-rays resulting from the π^0-decay centered on ∼ 67.5 MeV, the imaging atmospheric Čerenkov technique with a lower energy cutoff above 10 GeV is not applicable. Contrarily, the LAT instrument on-board GLAST scheduled to be launched in 2007 has an angular resolution better than 3.5° at 100 MeV while covering an energy range from 20 MeV up to 300 GeV with an energy resolution better than 10%. Assuming a photon spectral index of $\alpha_\gamma = 2$ for the γ-ray background, the point-source sensitivity at high galactic latitude in a one year all-sky survey is better than 6×10^{-9} cm^{-2} s^{-1} for energies integrated above 100 MeV. Specifically, assuming a CRp spectral index $\alpha_p = 2.3$ and a flat X_{CRp} for simplicity, such a one year all-sky survey is able to constrain $X_{CRp} < 0.01$ (Perseus) and $X_{CRp} < 0.04$ (Coma). Taking additionally into account the γ-ray flux between 20 MeV and 100 MeV as well as a longer survey time will improve the sensitivities and yield even tighter limits on X_{CRp}. Comparing these limits with energetically favored values of $X_{CRp_{min}}$ which are obtained by applying hadronic minimum energy arguments to a given radio synchrotron emission (cf. Fig. 7.2) yields comparable values in the case of Perseus while the situation in Coma is less optimistic. However, a definitive answer to the applicability of this method can not be given on the basis of minimum energy arguments because such a minimum energy state is not necessarily realized in Nature.

Table 7.1.: Individual parameters describing the extended diffuse radio emission in the Coma and Perseus galaxy cluster according to Eqn. (7.72). The maximal radius to which these profiles are applicable is denoted by r_{max}. The radio data at 1.4 GHz are taken from Deiss et al. (1997) (Coma) and Pedlar et al. (1990) (Perseus) while the profile of the Coma cluster at 326 MHz is taken from Govoni et al. (2001) which is based on radio observations by Venturi et al. (1990).

Cluster	S_0 [Jy arcmin^{-2}]	r_c [h_{70}^{-1} kpc]	r_{max} [h_{70}^{-1} Mpc]	β
1.4 GHz observations:				
A1656 (Coma)	1.1×10^{-3}	450	1.0	0.78
A426 (Perseus)	2.3×10^{-1}	30	0.1	0.55
326 MHz observation:				
A1656 (Coma)	4.7×10^{-3}	850	0.7	1.07

7.5. Applications

In this section we apply the classical and hadronic minimum energy criterion to the radio (mini-)halos of the Coma and Perseus galaxy clusters. For simplicity, the CRp and CRe spectral indices are assumed to be independent of position and therefore constant over the cluster volume. If a radial spectral steepening as reported by Giovannini et al. (1993) in the case of the Coma radio halo will be confirmed by future radio observations evincing a better signal-to-noise ratio, the CRp and CRe spectral index distributions would have to embody this additional degree of freedom. We discuss in Sect. 7.5.3 that a moderate steepening would not significantly modify the hadronic minimum energy condition while a strong steepening would challenge the hadronic scenario.

7.5.1. Classical minimum energy criterion

In a first step we have to deproject the radio surface brightness and electron density profiles: in analogy to X-ray observations we assume the azimuthally averaged radio profile to be described by a β-model,

$$S_\nu(r_\perp) = S_0 \left[1 + \left(\frac{r_\perp}{r_c} \right)^2 \right]^{-3\beta + 1/2}. \tag{7.72}$$

Deprojecting this profile yields the radio emissivity (cf. Appendix A)

$$j_\nu(r) = \frac{S_0}{2\pi r_c} \frac{6\beta - 1}{\left(1 + r^2/r_c^2 \right)^{3\beta}} \mathcal{B}\left(\frac{1}{2}, 3\beta \right) = j_{\nu,0} \left(1 + r^2/r_c^2 \right)^{-3\beta}. \tag{7.73}$$

The individual parameters for the Coma radio halo and Perseus radio mini-halo are shown in Table 7.1. Both profiles describe the extended diffuse emission where all point sources have been subtracted. Particularly, the extremely bright flat-spectrum core owing to relativistic outflows of the radio galaxy NGC 1275 in the center of the Perseus cluster has been excluded from the fit. The electron density profiles are inferred from X-ray observations by Briel et al. (1992) (Coma) and Churazov et al. (2003) (Perseus).

In the following, we assume that the energy distribution of the CRe population above a MeV is represented by a power-law in energy E_e with a lower cutoff. As a word of caution, such an assumption might be a strong simplification in the case of turbulent acceleration models yielding more complex energy distributions which are considerably flatter at lower energies (Brunetti et al. 2001, Petrosian 2001, Ohno et al. 2002) . We assume a CRe spectral index of $\alpha_e = 3.3$ which translates into a synchrotron spectral index of $\alpha_\nu = 1.15$. This is consistent with radio data of Perseus and Coma; particularly when considering the spectral cutoff between 1 and 10 GHz owing to the Sunyaev-Zel'dovich flux decrement (Deiss et al. 1997, Enßlin 2002, Pfrommer & Enßlin 2004a).

Applying the classical minimum energy criterion to the diffuse synchrotron emission of the Coma cluster yields a central magnetic field strength of $B_{Coma}(r = 0) = 1.1^{+0.7}_{-0.4}$ µG. In the case of the Perseus radio mini-halo we obtain $B_{Perseus}(r = 0) = 7.2^{+4.5}_{-2.8}$ µG. The indicated tolerance levels derive from the logarithmic definition of the theoretical
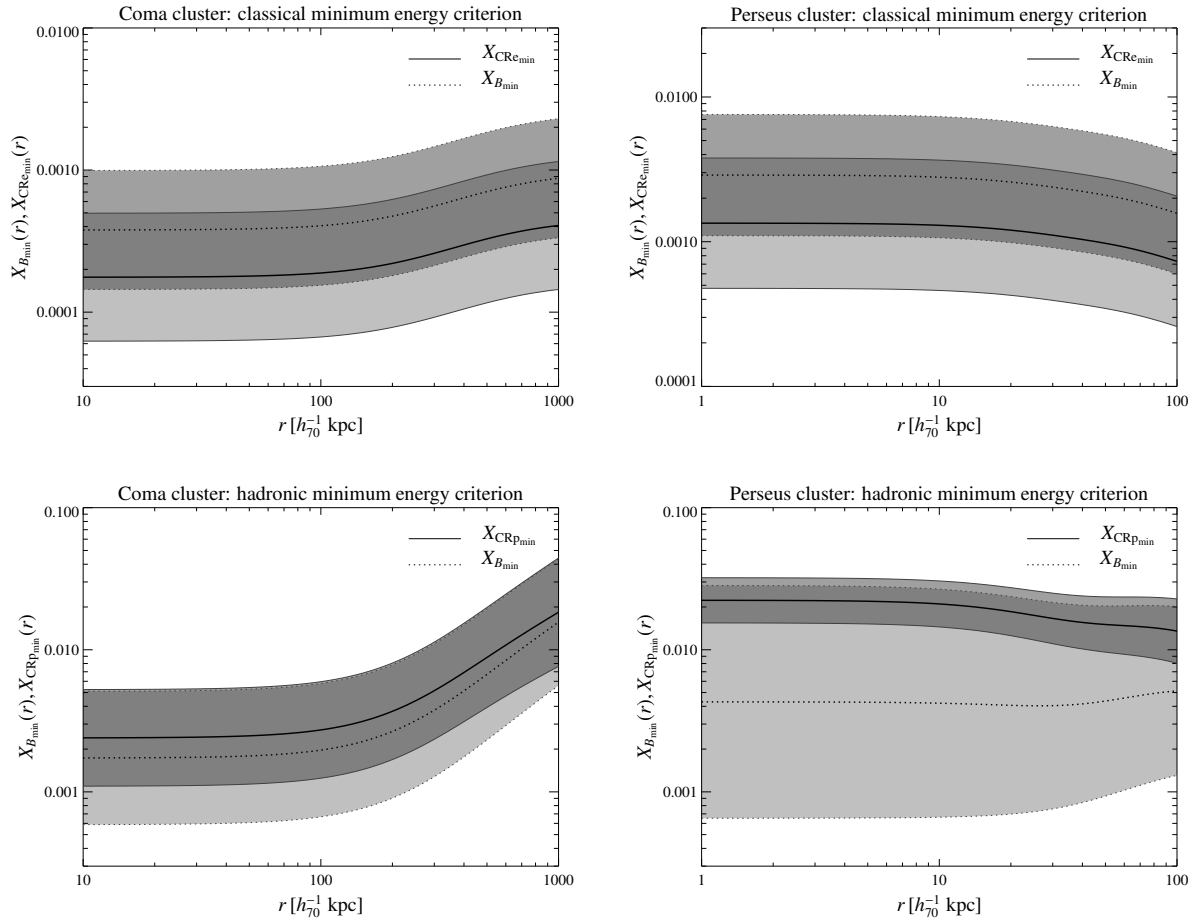
Figure 7.2.: Profiles of the CRe-to-thermal energy density $X_{\mathrm{CRe_{min}}}(r)$ (solid) and magnetic-to-thermal energy density $X_{B_{\mathrm{min}}}(r)$ (dotted) as a function of deprojected radius are shown. The different energy densities are obtained by means of the classical minimum energy criterion (*upper panels*) and the hadronic minimum energy criterion (*lower panels*). In the latter scenario, profiles of the scaled CRp energy density are shown instead of CRe profiles. The left hand side shows profiles of the Coma cluster while the right hand side represents profiles of the Perseus cluster. The light shaded areas represent the logarithmic tolerance regions of $X_{B_{\mathrm{min}}}(r)$ and $X_{\mathrm{CRe_{min}}}(r)$, respectively, while the dark shaded regions indicate the overlap and thus the possible equipartition regions in the quasi-optimal case.

accuracies of the minimum in Eqn. (7.41). However, these values are highly dependent on the lower energy cutoff of the CRe population, E_1, and the CRp proportionality parameter k_p. Following the philosophy of this chapter we adopt a physically motivated lower Coulomb cutoff of the CRe distribution of $E_1 = 0.1$ GeV corresponding to a relativistic γ factor of $\gamma_e \simeq 200$ (as suggested by Sarazin 1999). We also adopt a conservative choice of the proportionality constant between the CRe and CRp energy densities of $k_p = 1$. An increase of k_p would directly increase the magnetic field strength by approximately the square root of this factor.

For a cluster-wide comparison of energy densities of magnetic fields, CRe, and CRp, it is convenient to introduce a scaling with the thermal energy density by means of

$$X_B(\boldsymbol{r}) \equiv \frac{x_B(\boldsymbol{r})}{x_{\mathrm{th}}(\boldsymbol{r})} = \frac{\varepsilon_B(\boldsymbol{r})}{\varepsilon_{\mathrm{th}}(\boldsymbol{r})}, \text{ and} \tag{7.74}$$

$$X_{\mathrm{CRp,CRe}}(\boldsymbol{r}) \equiv \frac{x_{\mathrm{CRp,CRe}}(\boldsymbol{r})}{x_{\mathrm{th}}(\boldsymbol{r})} = \frac{\varepsilon_{\mathrm{CRp,CRe}}(\boldsymbol{r})}{\varepsilon_{\mathrm{th}}(\boldsymbol{r})}. \tag{7.75}$$

Profiles of the CRe-to-thermal energy density $X_{\mathrm{CRe_{min}}}(r)$ and magnetic-to-thermal energy density $X_{B_{min}}(r)$ are shown in Fig. 7.2 for the Coma and Perseus cluster and our different scenarios. The upper panels show the scaled energy densities in the acceleration model of CRe, obtained by the classical minimum energy criterion. While the optimal magnetic energy density is roughly a factor of two larger than the CRe energy density, they both can be in equipartition for the quasi-optimal case of their distribution of energy densities, as indicated by the dark shaded regions. In order to explain the observed synchrotron emission in the CRe acceleration scenario the CRe and magnetic energy densities are only required to be below one percent of the thermal energy density.

7.5.2. Hadronic minimum energy criterion

Assuming a CRp spectral index of $\alpha_p = 2.3$ when applying the hadronic minimum energy criterion to the diffuse synchrotron emission of the Coma cluster yields a central magnetic field strength of $B_{\mathrm{Coma}}(r = 0) = 2.4^{+1.7}_{-1.0}$ µG. In the case of the Perseus cluster we obtain $B_{\mathrm{Perseus}}(r = 0) = 8.8^{+13.8}_{-5.4}$ µG. Both inferred profiles of the magnetic field are relatively flat: while the magnetic field strength in the outer part of the radio mini-halo in Perseus ($r \simeq 100 \, h_{70}^{-1}$ kpc) declines to a value of 55% of its central value, the magnetic field in the outer region of the radio halo in Coma ($r \simeq 1 \, h_{70}^{-1}$ Mpc) only decreases to 72% of its central value.

As discussed in Sect. 7.3.2.4, the hadronic scenario shows an increasing tolerance region for strong magnetic field strengths which are expected to be present in the case of cool core clusters, such as Perseus (Taylor & Perley 1993, Carilli & Taylor 2002, Vogt & Enßlin 2003). In this limit, synchrotron losses dominate over inverse Compton cooling. This almost cancels the dependence of the synchrotron emissivity on the magnetic energy density. The lower panels of Fig. 7.2 show the scaled energy densities $X_{B_{min}}(r)$ and $X_{\mathrm{CRp_{min}}}(r)$ as inferred from the hadronic scenario. In both clusters the optimal CRp energy density is larger than the magnetic energy density within this model. However, both energy densities can be again in equipartition for the quasi-optimal case of their distribution, as indicated by the dark shaded regions.

Owing to the inverse dependence of $\sigma_{\ln x_B}$ and $\sigma_{\ln x_{\mathrm{CRp}}}$ on the magnetic energy density in the limit of strong magnetic fields (cf. Eqns. (7.63) and (7.64)), a large tolerance region of $X_{B_{min}}$ immediately implies a well defined localization of $X_{\mathrm{CRp_{min}}}$. In the Perseus cluster this results in a confinement for the CRp energy density of 2% ± 1% of the thermal energy density. On the other hand, in the Coma cluster $X_{B_{min}}(r)$ and $X_{\mathrm{CRp_{min}}}(r)$ are required to increase by less than one order of magnitude from the center to the outer parts of the cluster in order to account for the observed radio halo. This increase might be partly due to azimuthally averaging the aspheric electron density distribution of the Coma cluster (Pfrommer & Enßlin 2004a).

High values for the radio emissivity per target density and frequency C_{hadr} of order unity seem to reflect conditions in cool core clusters (formerly referred to as cooling flow cluster) whereas smaller values seem to represent conditions in clusters without cool cores as shown in the following:

$$C_{\mathrm{hadr}} \equiv \frac{A_{E_p}}{A_{E_{\mathrm{syn}}}} \frac{j_\nu}{A_{\varepsilon_{\mathrm{eff}}}} = C_{\mathrm{cluster}} \left(\frac{\nu}{1.4 \text{ GHz}} \right)^{-1} \left(\frac{n_e}{n_{e,0}} \right)^{-1} \left(\frac{j_\nu}{j_{\nu,0}} \right), \tag{7.76}$$

where $C_{\mathrm{Coma}} = 9.4 \times 10^{-4}$ and $C_{\mathrm{Perseus}} = 1.5 \times 10^{-1}$.

7.5.3. Possibility of a hadronic scenario in Perseus and Coma

7.5.3.1. Perseus radio mini-halo

The azimuthally averaged radio surface brightness profile of the Perseus mini-halo matches the expected emission by the hadronic scenario well on all radii (Pfrommer & Enßlin 2004a) while requiring almost flat profiles for CRp and magnetic energy densities relative to the thermal energy density, X_{CRp} and X_B, respectively. Moreover, the small amount of required energy density in cosmic ray protons ε_{CRp} ($\sim$ 2% relative to the thermal energy density) supports the hypothesis of a hadronic origin of the Perseus radio mini-halo not only because the hadronic minimum energy criterion predicts a close confinement of ε_{CRp} (see Sect. 7.5.2) but also because cosmological simulations carried out by Miniati et al. (2001) easily predict a CRp population at the clusters center of this order of magnitude.

7.5.3.2. Coma radio halo

The energetically favored radial profile for the magnetic field strength in the Coma cluster is almost flat as predicted by the hadronic minimum energy criterion (see Sect. 7.5.2). Provided these results would be realized in Nature, this apparently contradicts profiles of the magnetic field strength as inferred from numerical simulations which seem to follow the electron density $n_e(r)$ according to $B(r) \propto n_e(r)^{\alpha_B}$ with $\alpha_B \in [0.5, 0.9]$ (Dolag et al. 1999, 2001). It would also contradict theoretical considerations assuming the magnetic field to be frozen into the flow and isotropized, i.e. $\alpha_B = 2/3$ (Tribble 1993). Applying the flux freezing conditions to the electron density profile of Coma (Briel et al. 1992) yields an expected decline of the magnetic field strength from its central value to the magnitude at $1\,h_{70}^{-1}$ Mpc by a factor of $\sim$ 6.7.

However, there are other numerical, physical, and observational arguments indicating large uncertainties in the origin, amplification mechanism, and specific profile of the magnetic field strength, thus leaving the hadronic scenario as a viable explanation of the Coma radio halo: in contrast to the cited numerical simulations, there are other cosmological simulations (Miniati 2001, Miniati et al. 2001) which are able to produce giant radio halos in the hadronic scenario and therefore reasonably flat profiles of the magnetic field strength. From the physical point of view, there could be stronger shear flows or a larger number of weaker shocks in the outer parts of clusters which are unresolved or not accounted for in current simulations. This would imply stronger additional amplification of the magnetic field strength in the outer parts of clusters yielding a flatter profile of the magnetic field strength. Observationally, there are still uncertainties in the radio surface profiles which are increased by azimuthally averaging the diffuse synchrotron emission in the presence of non-centrally symmetric emission components such as the so-called radio-bridge in Coma around NGC 4839.

In order to account for the radio halo of Coma in the hadronic scenario, the product of X_{CRp} and X_B needs to increase by nearly two orders of magnitude towards the outskirts of the halo (cf. lower left panel of Fig. 7.2). Leaving aside the minimum energy criterion, this increase can be split arbitrarily among the magnetic and CRp energy density ratios. For instance a constant magnetic-to-thermal energy density ratio X_B, corresponding to $\alpha_B = 0.5$ in an isothermal cluster, is still consistent within the theoretically expected tolerance regions, i.e. within a quasi-optimal realization. However, the CRp-to-thermal energy density ratio X_{CRp} would have to compensate for this by increasing nearly two orders of magnitude towards the outskirts of the halo.[4] This choice of the magnetic field morphology ($\alpha_B = 0.5$) has been adopted in Fig. 7.3 which represents a parameter study on the ability of hadronically originating CRe to generate the radio halo of Coma. Contour lines of $\max(X_{CRp}) = (1, 0.3, 0.1, 0.03, 0.01)$ for the range $r \leq 1\,h_{70}^{-1}$ Mpc are shown in parameter space spanned by α_p and B_0. The gradient of the maximum of X_{CRp} points downwards in Fig. 7.3 and thus leaves the upper region of parameter space where the hadronic scenario is energetically able to account for the observed radio halo. For the choice of $\alpha_p = 2.3$ and $X_B = 0.01$ the maximum of the CRp-to-thermal energy density X_{CRp} is smaller than 3% for the entire range of the radio halo. Conservative choices for CRp spectral breaks have been adopted by means of Eqn. (7.12): we assume a high-momentum break of $p_2 \sim 2 \times 10^7$ GeVc^{-1} being derived from CRp diffusion (Berezinsky et al. 1997) while the lower momentum cutoff assumes the CRp to be accelerated from a thermal Maxwellian distribution, $p_1 \sim 3\sqrt{2m_p k T_{Coma}} = 0.01$ GeVc^{-1} (Miniati 2001). This choice of the lower cutoff represents the energetically tightest constraint because taking into account Coulomb losses would only weaken the energetic requirements. Moving away from the minimum energy solution, especially in the inner parts of the cluster, the presented energetic considerations show that the hadronic

---

[4]Though, some part of this apparent increase is an artifact owing to azimuthally averaging the non-centrally symmetric synchrotron brightness distribution (for a more detailed discussion on this topic, see Pfrommer & Enßlin 2004a).
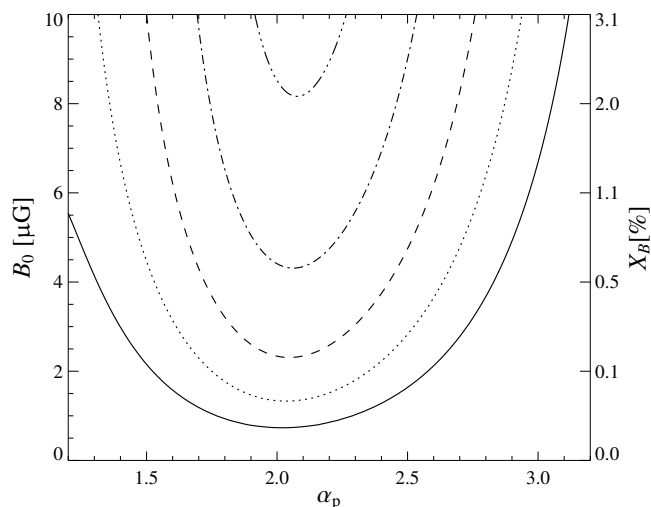
Figure 7.3.: Parameter study on the ability of hadronically originating CRe to account for the radio halo of Coma. Assuming the profile of the magnetic field to scale with the square root of the electron density yields a flat magnetic-to-thermal energy density ratio X_B. Shown are contour lines from the bottom to the top of $\max(X_{CRp}) = (1, 0.3, 0.1, 0.03, 0.01)$ for the range $r \leq 1\, h_{70}^{-1}$ Mpc in parameter space spanned by α_p and B_0. Conservative choices for CRp spectral breaks have been assumed. The lower part represents the region in parameter space, where the hadronic scenario faces serious challenges for explaining the observed radio halo of Coma.

scenario is a viable explanation of the Coma radio halo as long as the spatially constant CRp spectral index is between $1.4 \lesssim \alpha_p \lesssim 2.8$.

Giovannini et al. (1993) found a strong radial spectral steepening from $\alpha_\nu = 0.8 - 1.8$ which would translate within the hadronic scenario into a CRp spectral index steepening of $\alpha_p = 1.6 - 3.6$. If the strong steepening will be confirmed, the hadronic scenario will face serious challenges even when including conservative CRp spectral breaks. However, an absent or weaker steepening of the CRp spectral index e.g. from $\alpha_p = 2.3$ in the cluster center to $\alpha_p = 2.8$ at the outskirts of the radio halo would only double the CRp energy density required to explain the radio halo in the hadronic scenario. The studies of Giovannini et al. (1993) are based on two synthesis aperture radio maps obtained with different radio telescopes. The technique of interferometric radio observations generally suffers from missing short-baseline information leading to an uncertainty of emission from larger structures: the so-called "missing zero spacing"-problem. This uncertainty of the surface brightness distribution at a single frequency is even increased for spatial distributions of the spectral index which represent a ratio of surface brightness distributions yielding to possible observational artifacts at the outskirts of the radio halo. Thus, future observations are required to decide whether the strong spectral steepening as a function of radius is an observational artifact or a real characteristic of the radio halo.

Figure 7.4 compares radio synchrotron profiles of the Coma radio halo by Govoni et al. (2001) which is based on observations by Venturi et al. (1990) using a synthesis aperture telescope with observations by Deiss et al. (1997) using a single-dish telescope. The statistical variance given by Govoni et al. (2001) represents the rms scatter within concentric annuli (shown in light grey) which is composed of measurement uncertainties and non-sphericity of the underlying radio profile. Rescaling with the square root of the number of independent beams within concentric annuli yields statistical uncertainties (black) however without taking into account systematics.[5] The top panel shows a comparison of the different profiles by Govoni et al. (2001) and Deiss et al. (1997) (rescaled from its original observational frequency $\nu = 1.4$ GHz to 326 MHz using the synchrotron spectral index $\alpha_\nu = 1.15$). There seems to be an indication of spectral steepening as reported by Giovannini et al. (1993). However, for simplicity we use a spatially constant CRp spectral index. Because of the more extended profile of the radio halo of the

---

[5]Due to the interferometric nature of the measurement and due to the non-completely synthesized aperture, we expect the true error bars to be larger than the estimates given here suggest. However, a detailed discussion of this topic is beyond the scope of this work.
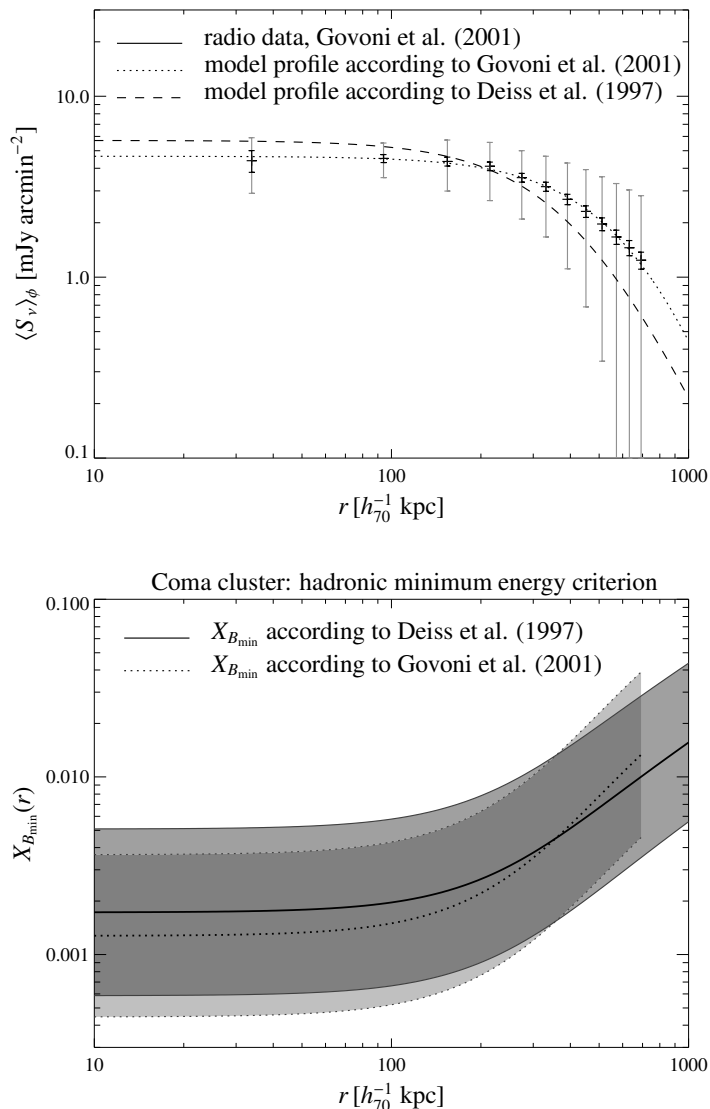
Figure 7.4.: *Top panel:* Azimuthally averaged radio brightness profile of the radio halo in the Coma cluster as a function of impact parameter $r_\perp$. Shown are the radio data at 326 MHz (Govoni et al. 2001) in combination with the 1σ-error bars (black) and the surface brightness fluctuations within concentric annuli (grey) which are based on observations by Venturi et al. (1990). Also presented is the model profile according to Govoni et al. (2001) (dotted) and the model profile according to Deiss et al. (1997) (dashed) which is rescaled to 326 MHz using the synchrotron spectral index $\alpha_\nu = 1.15$ (cf. Table 7.1). *Lower panel:* Profiles of the magnetic-to-thermal energy density $X_{B_{\min}}(r)$ in the Coma cluster as a function of deprojected radius are shown within the hadronic minimum energy criterion. A comparison of the used synchrotron profiles by Deiss et al. (1997) (solid, tolerance region medium grey shaded) and Govoni et al. (2001) (dotted, tolerance region light grey shaded) shows no significant difference within the allowed logarithmic tolerance regions (overlap is shown dark shaded).

single-dish observation, we decided to adopt the profile obtained by Deiss et al. (1997) in our analysis shown in Fig. 7.2. Nevertheless, the lower panel of Fig. 7.4 shows a comparison of the energetically favored magnetic-to-thermal energy density $X_{B_{\min}}(r)$ as a function of deprojected radius within the hadronic minimum energy criterion for both data sets. The tolerance regions of $X_{B_{\min}}$ are drawn light shaded while the overlap of $X_{B_{\min}}$ using the different synchrotron profiles is shown dark shaded. There is no significant difference within the allowed tolerance regions. Together with the previous considerations about spectral steepening, this indicates that a moderate radially dependent spectral index does not significantly modify the hadronic minimum energy condition while a strong steepening would challenge the hadronic scenario.

7.6. Minimum energy criteria in a nutshell

This section provides self-consistent recipes for applying the classical and hadronic minimum energy criterion in typical observational situations. We present formulae for inferring magnetic field strengths solely as a function of observed flux per frequency, $\mathcal{F}_\nu$, luminosity distance to the galaxy cluster, D, extent of the cluster measured in core radius, r_c, observed frequency, ν, and spectral index of the diffuse synchrotron emission, α_ν, where the emissivity scales as $j_\nu \propto \nu^{-\alpha_\nu}$.

The omnidirectional (i.e. integrated over 4π solid angle) luminosity per frequency is given by the volume integral of the synchrotron emissivity, j_ν,

$$\mathcal{L}_\nu = 4\pi \int dV\, j_\nu. \tag{7.77}$$

We choose a reference luminosity $\mathcal{L}_{\nu(1+z),0} = 4\pi D^2 (1+z)^{-1} \mathcal{F}_{\nu,0}$ which corresponds to a flux at $\nu = 1$ GHz of $\mathcal{F}_{\nu,0} = 1$ Jy for a source at a luminosity distance of $D = 100\, h_{70}^{-1}$ Mpc. This corresponds to a cluster like Coma which is characterized by a core radius of $r_{c,0} \sim 300\, h_{70}^{-1}$ kpc.

7.6.1. Classical minimum energy criterion in a nutshell

Applying the classical minimum energy criterion, we infer an optimal magnetic field strength by rewriting Eqn. (7.37),

$$B_{\min}^{\text{class}} = B_{\min,0}^{\text{class}}(\alpha_\nu)\,\mu\text{G} \left[\frac{1+k_p}{2} \frac{\mathcal{L}_\nu}{\mathcal{L}_{\nu,0}} \left(\frac{r_c}{r_{c,0}}\right)^{-3} f_B^{-1} \left(\frac{\nu}{1\text{ GHz}}\right)^{\alpha_\nu} \left(\frac{E_1}{0.1\text{ GeV}}\right)^{1-2\alpha_\nu} \right]^{1/(\alpha_\nu+3)}. \tag{7.78}$$

Here $B_{\min,0}^{\text{class}}(\alpha_\nu)$ is given by Table 7.2, k_p denotes the ratio between CRp and CRe energy densities, E_1 denotes the lower cutoff of the CRe population, and f_B denotes the filling factor of the magnetic field in the volume occupied by CRe, which is thought to be of order unity. While deriving Eqn. (7.78) we implicitly assumed that $E_2 \gg E_1$. We also applied a lower Coulomb cutoff to the CRe distribution of $E_1 = 0.1$ GeV (as suggested by Sarazin 1999), and adopt a conservative choice for the cosmic ray energy scaling of $k_p = 1$.

In the case of the classical minimum energy criterion the tolerance region of the magnetic field strength is given by Eqn. (7.42). The following substitutions might be useful when computing the tolerance levels of the magnetic field, $\sigma_{\ln B} = \sigma_{\ln x_B}/2$, which are equally spaced in logarithmic units of B. In linear representation of B, this definition explicitly implies the tolerance levels given by $\exp(\ln B \pm \sigma_{\ln B})$. The scaled synchrotron index is given by $\delta = (\alpha_\nu - 1)/2$, while the dimensionless magnetic energy density $x_{B_{\min}}^{\text{class}}$ and the constant $C_{\text{class}}(\alpha_\nu)$ are denoted by

$$x_{B_{\min}}^{\text{class}} = \left(\frac{B_{\min}^{\text{class}}}{B_c}\right)^2 = \left(\frac{B_{\min}^{\text{class}}}{31\,\mu\text{G}}\right)^2 \left(\frac{\nu}{1\text{ GHz}}\right)^{-2}, \tag{7.79}$$

$$C_{\text{class}}(\alpha_\nu) = f_{\text{class}}(\alpha_\nu)\, f_B^{-1} \frac{\mathcal{L}_\nu}{\mathcal{L}_{\nu,0}} \left(\frac{r_c}{r_{c,0}}\right)^{-3} \left(\frac{\nu}{1\text{ GHz}}\right)^{-3}, \tag{7.80}$$

where $f_{\text{class}}(\alpha_\nu)$ is given by Table 7.2.

7.6.2. Hadronic minimum energy criterion in a nutshell

In the case of the hadronic scenario the energetically favored magnetic field strength $B_{\min,0}^{\text{hadr}}$ is given by

$$B_{\min,0}^{\text{hadr}} = \sqrt{x_{B_{\min}}}\, B_c = 31\,\mu\text{G}\,\sqrt{x_{B_{\min}}} \left(\frac{\nu}{1\text{ GHz}}\right), \tag{7.81}$$

Table 7.2.: Useful numerical values for particular choices of the synchrotron spectral index α_ν in the framework of the minimum energy criterion in a nutshell are given for both scenarios. Note, that a priori, we assume no cutoff in the CRp distribution. For spectral indices $\alpha_\nu \leq 1$ within the hadronic scenario, an upper cutoff needs to be introduced for deducing an equipartition magnetic field strength in order to meet the requirements of the regularity conditions.

α_ν	α_e	$B^{\text{class}}_{\text{min},0}$ [μG]	f_{class}	$B^{\text{hadr}}_{\text{min},0}$ [μG]	f_{hadr}
0.65	2.3	0.6	3.3×10^{-7}		
0.75	2.5	0.7	3.6×10^{-7}		
0.85	2.7	0.8	4.7×10^{-7}		
0.95	2.9	1.0	6.4×10^{-7}		
1.05	3.1	1.2	9.2×10^{-6}	4.0	2.1×10^{-2}
1.15	3.3	1.4	1.3×10^{-6}	4.2	1.9×10^{-2}
1.25	3.5	1.7	2.0×10^{-6}	5.3	3.4×10^{-2}
1.35	3.7	2.0	3.0×10^{-6}	7.3	8.2×10^{-2}
1.45	3.9	2.4	4.5×10^{-6}	13.0	3.9×10^{-1}

where $x_{B_{\min}}$ is given by Eqns. (7.54) through (7.57). $B^{\text{hadr}}_{\text{min},0}$ is specified in Table 7.2 for a few spectral indices α_ν where we assumed no cutoff of the CRp distribution. Provided the synchrotron index $\alpha_\nu \leq 1$, there must be an upper cutoff of the CRp distribution in order to ensure a non-divergent CRp energy density. This might be obtained by means of Eqn. (7.12). Owing to the non-analytic structure of the hadronic minimum energy criterion (7.53) in $x_{B_{\min}}$, we were forced to carry out an asymptotic expansion for $x_{B_{\min}}$ which does not admit a comparable simple scaling of the magnetic field as in the classical case (7.78).

The theoretically expected tolerance levels of the magnetic field, $\sigma_{\ln B} = \sigma_{\ln x_B}/2$, are given by Eqn. (7.58) while neglecting the radial dependence in the nutshell approach. The following substitutions might be useful when computing the magnetic field strength $B^{\text{hadr}}_{\text{min},0}$ and the corresponding tolerance region. The scaled synchrotron index is given by $\delta = (\alpha_\nu - 1)/2$, while the dimensionless energy density of the CMB, x_{CMB}, and the constant $C_{\text{hadr}}(\alpha_\nu)$ are denoted by

$$x_{\text{CMB}} \;=\; \frac{B^2_{\text{CMB}}}{B^2_{\text{c}}} = 1.08 \times 10^{-2} \left(\frac{\nu}{1\,\text{GHz}}\right)^{-2} (1+z)^4, \tag{7.82}$$

$$C_{\text{hadr}}(\alpha_\nu) \;=\; f_{\text{hadr}}(\alpha_\nu)\, f_B^{-1}\, \frac{\mathcal{L}_\nu}{\mathcal{L}_{\nu,0}} \left(\frac{r_{\text{c}}}{r_{\text{c},0}}\right)^{-3} \left(\frac{n_{\text{e}}}{n_{\text{e},0}}\right)^{-1} \left(\frac{\nu}{1\,\text{GHz}}\right)^{-3}, \tag{7.83}$$

where $f_{\text{hadr}}(\alpha_\nu)$ is given by Table 7.2, and $n_{\text{e},0} = 10^{-3}\,\text{cm}^{-3}$.

7.7. Conclusions

We investigated the minimum energy criterion of radio synchrotron emission in order to estimate the energy density of magnetic fields with the main focus on the underlying physical scenario. The classical scenario might find application for cosmic ray electrons (CRe) originating either from primary shock acceleration or in-situ reacceleration processes while the hadronic model assumes a scenario of inelastic cosmic ray proton (CRp) interactions with the ambient gas of the intra-cluster medium (ICM) and thus leads to extended diffuse synchrotron and γ-ray emission.

Generally, the hadronic minimum energy estimates allow testing the hadronic model for extended radio synchrotron emission in clusters of galaxies. If it turns out that the required minimum non-thermal energy densities are too large compared to the thermal energy density, the hadronic scenario has to face serious challenges. For the classical minimum energy estimate, such a comparison can yield constraints on the accessible parameter space spanned by the lower energy cutoff of the CRe population or the unknown contribution of CRp to the non-thermal energy density.

For the first time we examine the localization of the predicted minimum energy densities and provide a measure of the theoretically expected tolerance regions of these energetically favored energy densities. The tolerance regions

of the particular energy densities inferred from the classical minimum energy criterion are approximately constant for varying magnetic field strength ε_B. On the contrary, the hadronic minimum energy criterion predicts constant energy densities for varying magnetic field strength in the case of low ε_B compared to ε_{CMB}, while the tolerance region of the CRp energy density decreases at the same rate as the tolerance region of ε_B increases for high ε_B.

Future observations should shed light on the hypothetical realization of such an optimal distribution of energy densities in Nature: combining upper limits on the inverse Compton (IC) scattering of cosmic microwave background photons off CRe within the ICM provides lower limits on the magnetic field strength. Unambiguous detection of the π^0-decay induced γ-ray emission owing to hadronic CRp interactions in the ICM together with the observed radio synchrotron emission yields strong upper limits on the magnetic field strength. These are only upper limits because the inevitably accompanying hadronically generated CRe could have a non-hadronic counterpart CRe population which also contributes to the observed synchrotron emission. A combination of IC detection in hard X-rays, radio synchrotron emission, and hadronically induced γ-ray emission therefore simultaneously enables the determination of the CRp population as well as a bracketing of the total magnetic field strength and the CRe population. Applying the appropriate minimum energy arguments would yield information about both the dynamical state as well as the fragmentation of the spatial distribution of the magnetic field.

Requiring the sum of cosmic ray and the magnetic field energy densities to be minimal for the observed synchrotron emission of the radio halo of the Coma cluster and the radio mini-halo of the Perseus cluster yields interesting results: within the theoretically expected tolerance regions, equipartition is possible between the energy densities of CRp and magnetic fields, i.e. the minimum energy criterion always seems to choose equipartition to be a quasi-optimal case. Applying the hadronic minimum energy criterion to the diffuse synchrotron emission of the Coma cluster yields a central magnetic field strength of $B_{Coma} = 2.4^{+1.7}_{-1.0}$ µG while in the case of the cool core cluster Perseus we obtain $B_{Perseus} = 8.8^{+13.8}_{-5.4}$ µG. These values agree with magnetic field strengths inferred from Faraday rotation which range in the case of clusters without cool cores within [3 µG, 6 µG] while cool core clusters yield values of ~ 12 µG (Vogt & Enßlin 2003). Within the hadronic model for the radio mini-halo in the Perseus cluster, this results in a confinement for the CRp energy density of 2% ± 1% of the thermal energy density while the magnetic energy density reaches only 0.4% of the thermal energy density within large uncertainties. These energetic considerations show that the hadronic scenario is a very attractive explanation of cluster radio mini-halos.

In order to account for the radio halo of Coma in the hadronic scenario, the product of ε_{CRp} and ε_B needs to increase by nearly two orders of magnitude relative to the square of the thermal energy density ε_{th} towards the outskirts of the halo. Moving away from the minimum energy solution and adopting for instance a constant magnetic-to-thermal energy density, it is energetically possible to explain the observed synchrotron emission hadronically by only requiring the magnetic and CRp energy density to be a few per cent relative to the thermal energy density (and even less for the CRp in the cluster center, provided $\alpha_p \sim 2.3$ and the cluster is isothermal). Such a magnetic energy density corresponds to a central magnetic field strength of 6 µG. Assuming a lower magnetic field strength of 3 µG corresponding to a magnetic-to-thermal energy density of approximately 0.5% requires the CRp energy density to be lower than 10% for the entire range of the radio halo.

The considered hadronic scenario assumes a CRp spectral index which is independent of position and thus the radio emission does not show any spatial variations over the clusters volume. In principle, one could allow for radial spectral variations of the CRp and thereby for the radio emission by adopting a particular history of this population. For instance, one possible scenario would be given by continuous in-situ acceleration of CRp via resonant pitch angle scattering by turbulent Alfvén waves. We discuss that a moderate radial steepening would not significantly modify the hadronic minimum energy condition while a confirmation of the strong steepening reported by Giovannini et al. (1993) would seriously challenge the hadronic scenario.

As a caveat, it should be stressed that the inferred values for the particular energy densities only represent the energetically least expensive radio synchrotron emission model possible for a given physically motivated scenario. This minimum is not necessarily realized in Nature. Nevertheless, our minimum energy estimates are also interesting in a dynamical respect: should the hadronic scenario of extended radio synchrotron emission be confirmed, the minimum energy estimates allow testing for the realization of the minimum energy state for a given independent measurement of the magnetic field strength. Within the tolerance regions, our minimum energy estimates in Perseus and Coma agree well with magnetic field strengths inferred from Faraday rotation. Under the hypotheses of correctness of the hadronic scenario, such a possible realization of the minimum energy state would seek an explanation of a first principle enforcing this extremal value to be realized in Nature.

The results of this chapter were worked out in collaboration with T.A. Enßlin. A paper entitled "Estimating galaxy cluster magnetic fields by the classical and hadronic minimum energy criterion" *has been published in the journal*

Monthly Notices of the Royal Astronomical Society *with the reference:* Pfrommer & Enßlin, 2004, MNRAS, 352, 76.

8. Unveiling the composition of plasma bubbles in galaxy clusters with the SZ effect

Abstract

The *Chandra* X-ray Observatory is finding a large number of cavities in the X-ray emitting intra-cluster medium which often coincide with the lobes of the central radio galaxy. We propose high-resolution Sunyaev-Zel'dovich (SZ) observations to infer the yet unknown dynamically dominant component of the radio plasma bubbles. This chapter calculates the thermal and relativistic SZ emission of different compositions of these plasma bubbles while simultaneously allowing for the cluster's kinetic SZ effect. As examples, we present simulations of an *Atacama Large Millimeter Array (ALMA)* observation and of a *Green Bank Telescope (GBT)* observation of the cores of the Perseus cluster and Abell 2052. We predict a 5σ detection of the southern radio bubble of Perseus in a few hours with the *GBT* and *ALMA* while assuming a relativistic electron population within the bubble. In Abell 2052, a similar detection would require a few tens of hours with either telescope, the longer exposures mainly being the result of the higher redshift and the lower central temperature of this cluster. Future high-sensitivity multi-frequency SZ observations will be able to infer the energy spectrum of the dynamically dominant electron population in order to measure its temperature or spectral characteristics. This knowledge can yield indirect indications for an underlying radio jet model.

8.1. Introduction

The *Chandra* X-ray Observatory is detecting numerous X-ray cavities in clusters of galaxies, confirming pioneering detections of the *ROSAT* satellite. Prominent examples include the Perseus cluster (Böhringer et al. 1993, Fabian et al. 2000), the Cygnus-A cluster (Carilli et al. 1994), the Hydra-A cluster (McNamara et al. 2000), Abell 2597 (McNamara et al. 2001), Abell 4059 (Huang & Sarazin 1998, Heinz et al. 2002), Abell 2199 (Fabian 2001), Abell 2052 (Blanton et al. 2001), the vicinity of M84 in the Virgo cluster (Finoguenov & Jones 2001), the RBS797 cluster (Schindler et al. 2001), and the MKW3s cluster (Mazzotta et al. 2002). They are produced by the release of radio plasma from active galactic nuclei (AGN) which are typically hosted by a cD galaxy located at the cluster center and mainly reside within the cool cores of galaxy clusters.

While radio synchrotron emission provides evidence for the existence of cosmic ray electrons (CRes) and magnetic fields, the detailed composition of the plasma bubble governing its dynamics is still unknown. Minimum energy or equipartition estimates of the nonthermal pressure in the radio bubbles give values which are typically a factor of ten smaller than the pressures required to inflate and maintain the bubbles as determined from the surrounding X-ray gas (e.g., Blanton et al. 2001). This indicates that the standard minimum energy or equipartition radio arguments are missing the main component of the pressure and energy content of the radio lobes. Possibilities include magnetic fields, cosmic ray proton (CRp) or CRe power-law distributions, or very hot thermal gas. Solving this enigma would yield further insight into physical processes within cool cores (De Young 2003) as well as provide hints about the composition of relativistic outflows of radio galaxies because plasma bubbles represent the relic fluid of jets (e.g. Celotti et al. 1998, Hirotani et al. 1998, Sikora & Madejski 2000).

Additionally, some of the clusters exhibit cavities in the X-ray emitting intra-cluster medium (ICM) without detectable high frequency radio emission, for instance in Perseus, Abell 2597, Abell 4059, and the MKW3s cluster. This category of X-ray cavities is also believed to be filled with radio plasma, but during the buoyant rise of the light radio plasma bubble in the cluster's potential (Gull & Northover 1973, Churazov et al. 2000, 2001, Brüggen & Kaiser 2001) the resulting adiabatic expansion and synchrotron/inverse Compton losses dwindles the observable radio emitting electron population producing a so-called *ghost cavity* or *radio ghost* (Enßlin 1999). Possible entrainment of the ICM into the plasma bubble and subsequent Coulomb heating by CRes generates further uncertainty of the composition of the ghost cavity.

If the radio bubbles contain a significant amount of very hot thermal gas, this might be detected by X-ray observations. However, this is quite difficult (e.g., Blanton et al. 2003) due to the projected foreground and background cluster emission, and the fact that the X-ray emissivity is proportional to the square of the density. If most of the pressure in the radio bubbles were due to the very hot, low density thermal gas, it would have a very low X-ray emissivity. Observationally, there has been a claim by Mazzotta et al. (2002) to have seen hot X-ray emitting gas within the ghost cavity of the MKW3s cluster. Obviously, it might be more useful to observe the radio bubbles with a technique which was sensitive to thermal gas pressure, rather than density squared, as pressure is the quantity which is missing. For this reason, in this chapter we propose high resolution Sunyaev-Zel'dovich (SZ) radio observations of the radio bubbles and radio ghosts in clusters, as the thermal SZ effect directly measures the thermal electron pressure in the gas. The thermal SZ effect arises because photons of the cosmic microwave background (CMB) experience inverse Compton collisions with thermal electrons of the hot plasma inside clusters of galaxies and are spectrally redistributed (e.g. Sunyaev & Zel'dovich 1972, Sunyaev & Zeldovich 1980, Rephaeli 1995a). The proposed measurement is able to infer directly the composition of radio plasma bubbles and radio ghosts while indirectly obtaining indications for a specific underlying jet model.

This chapter is organized as follows: after basic definitions concerning the thermal, kinetic, and relativistic SZ effect in Sect. 8.2, we introduce a toy model in Sect. 8.3 describing projected maps of the SZ flux decrement with spherically symmetric radio plasma bubbles. The models for the cool core regions of the Perseus cluster and Abell 2052 are described in Sect. 8.4. Simulating an *Atacama Large Millimeter Array (ALMA)* and a *Green Bank Telescope (GBT)* observation of both clusters in Sect. 8.5, we examine whether the plasma bubbles are detectable by the SZ flux decrement. Five physically different scenarios for the plasma composition of the bubbles are investigated exemplarily using three characteristic SZ frequencies in Sects. 8.6 and 8.7. Finally, we discuss observing strategies for *ALMA* and *GBT*. Throughout the chapter, we assume a ΛCDM cosmology and the Hubble parameter at the present time of $H_0 = 70\,h_{70}$ km s^{-1} Mpc^{-1}.

8.2. Sunyaev-Zel'dovich effect

The SZ effect arises because CMB photons experience inverse Compton (IC) scattering off electrons of the dilute intra-cluster plasma (for a comprehensive review, see Birkinshaw 1999). At the angular position of galaxy clusters, the CMB spectrum is modulated as photons are redistributed from the low-frequency part of the spectrum below a characteristic crossover frequency ν_c to higher frequencies. For non-relativistic electron populations, $\nu_c \simeq 217$ GHz, while this characteristic frequency shifts towards higher values for more relativistic scattering electrons.

The relative change $\delta i(x)$ in flux density as a function of dimensionless frequency $x = h\nu/(kT_{\mathrm{CMB}})$ for a line-of-sight through a galaxy cluster is given by

$$\delta i(x) = g(x)\,y_{\mathrm{gas}}\,[1 + \delta(x, T_{\mathrm{e}})] - h(x)\,w_{\mathrm{gas}} + [j(x) - i(x)]\,\tau_{\mathrm{rel}}\,, \tag{8.1}$$

with the Planckian distribution function of the CMB

$$I(x) = i_0 i(x) = i_0 \frac{x^3}{\mathrm{e}^x - 1}\,, \tag{8.2}$$

and $i_0 = 2(kT_{\mathrm{CMB}})^3/(hc)^2$ where $T_{\mathrm{CMB}} = 2.725$ K, k, h and c denote the average CMB temperature, Boltzmann's constant, Planck's constant, and the speed of light, respectively.

The first term in Eqn. (8.1) arises because of the thermal motion of non-relativistic electrons (thermal SZ effect) and gives the spectral distortion

$$g(x) = \frac{x^4 \mathrm{e}^x}{(\mathrm{e}^x - 1)^2}\left(x\,\frac{\mathrm{e}^x + 1}{\mathrm{e}^x - 1} - 4\right). \tag{8.3}$$

The amplitude of the thermal SZ effect is known as the thermal Comptonization parameter y_{gas} that is defined as the line-of-sight integration of the temperature weighted thermal electron density from the observer to the last scattering surface of the CMB at redshift $z = 1100$:

$$y_{\mathrm{gas}} \equiv \frac{\sigma_{\mathrm{T}}}{m_{\mathrm{e}}c^2} \int \mathrm{d}l\, n_{\mathrm{e,gas}}\, kT_{\mathrm{e}}. \tag{8.4}$$

Here, σ_{T} denotes the Thompson cross section, m_{e} the electron rest mass, T_{e} and $n_{\mathrm{e,gas}}$ are electron temperature and thermal electron number density, respectively. For non-relativistic electrons the relativistic correction term is

zero, $\delta(x, T_e) = 0$, but for hot clusters even the thermal electrons have relativistic corrections, which will modify the thermal SZ effect (Wright 1979). These corrections have been calculated in the literature (see e.g. Rephaeli 1995b, Enßlin & Kaiser 2000, Dolgov et al. 2001, Itoh & Nozawa 2004), and can be used to measure the cluster temperature purely from SZ observations (e.g. Hansen et al. 2002).

The second term in Eqn. (8.1) describes an additional spectral distortion of the CMB spectrum due to the Doppler effect of the bulk motion of the cluster itself relative to the rest frame of the CMB. If the component of the cluster's peculiar velocity is projected along the line-of-sight, then the Doppler effect leads to a spectral distortion referred to as the kinetic SZ effect with the spectral signature

$$h(x) = \frac{x^4 \, e^x}{(e^x - 1)^2}. \tag{8.5}$$

The amplitude of the kinetic SZ effect depends on the kinetic Comptonization parameter w_{gas} that is defined as

$$w_{gas} \equiv \bar{\beta}_{gas} \, \tau_{gas} = \sigma_T \int dl \, n_{e,gas} \bar{\beta}_{gas}, \tag{8.6}$$

where τ_{gas} is the Thomson optical depth, $\bar{v}_{gas}$ is the average line-of-sight streaming velocity of the thermal gas, $\bar{\beta}_{gas} \equiv \bar{v}_{gas}/c$, and $\bar{\beta}_{gas} < 0$ if the gas is approaching the observer.

Finally, the third term in Eqn. (8.1) takes account of Compton scattering with relativistic electrons that exhibit an optical depth of

$$\tau_{rel} = \sigma_T \int dl \, n_{e,rel}. \tag{8.7}$$

The flux scattered to other frequencies is $i(x)\tau_{rel}$ while $j(x)\tau_{rel}$ is the flux scattered from other frequencies to $x = h\nu/(kT_{CMB})$. It is worth noting, that in the limit of ultra-relativistic electrons and for $x < 10$, one can neglect the scattered flux, because $j(x) \ll i(x)$. In the following, we drop this approximation and consider the general case. The scattered flux can be expressed in terms of the photon redistribution function for a mono-energetic electron distribution $P(t; p)$, where the frequency of a scattered photon is shifted by a factor t:

$$j(x) = \int_0^\infty dt \int_0^\infty dp \, f_e(p) \, P(t; p) \, i(x/t). \tag{8.8}$$

For a given electron spectrum $f_e(p) \, dp$ with the normalized electron momentum $p = \beta_e \gamma_e$ and $\int dp \, f_e(p) = 1$, this redistribution function can be derived following the kinematic considerations of Wright (1979) of the IC scattering in the Thomson regime, where $\gamma_e \, h\nu \ll m_e c^2$ is valid. We use the compact formula for the photon redistribution function which was derived by Enßlin & Kaiser (2000):

$$\begin{aligned}
P(t; p) &= -\frac{3|1 - t|}{32p^6 t} \left[1 + (10 + 8p^2 + 4p^4)t + t^2 \right] \\
&+ \frac{3(1 + t)}{8p^5} \left\{ \frac{3 + 3p^2 + p^4}{\sqrt{1 + p^2}} - \frac{3 + 2p^2}{2p} \left[2\,\mathrm{arcsinh}(p) - |\ln(t)| \right] \right\}.
\end{aligned} \tag{8.9}$$

The allowed range of frequency shifts is restricted to

$$|\ln(t)| \le 2\,\mathrm{arcsinh}(p), \tag{8.10}$$

and thus $P(t; p) = 0$ for $|\ln(t)| > 2\,\mathrm{arcsinh}(p)$. Similar expressions for the photon redistribution function using different variables can be found in the literature (Rephaeli 1995b, Enßlin & Biermann 1998, Sazonov & Sunyaev 2000).

The spectral distortions owing to the relativistic SZ effect can be rewritten to include a relativistic Comptonization parameter $\tilde{y}$,

$$\delta i_{rel}(x) = [j(x) - i(x)]\tau_{rel} = \tilde{g}(x)\tilde{y}, \tag{8.11}$$

where

$$\tilde{y} \;=\; \frac{\sigma_{\mathrm{T}}}{m_{\mathrm{e}} c^2} \int \mathrm{d}l \, n_{\mathrm{e}} \, k\tilde{T}_{\mathrm{e}} \,, \tag{8.12}$$

$$k\tilde{T}_{\mathrm{e}} \;=\; \frac{P_{\mathrm{e}}}{n_{\mathrm{e}}} \,, \tag{8.13}$$

$$\tilde{g}(x) \;=\; [j(x) - i(x)] \, \tilde{\beta}(k\tilde{T}_{\mathrm{e}}) \,, \tag{8.14}$$

$$\tilde{\beta}(k\tilde{T}_{\mathrm{e}}) \;=\; \frac{m_{\mathrm{e}} c^2}{\langle k\tilde{T}_{\mathrm{e}} \rangle} = \frac{m_{\mathrm{e}} c^2 \int \mathrm{d}l \, n_{\mathrm{e}}}{\int \mathrm{d}l \, n_{\mathrm{e}} k\tilde{T}_{\mathrm{e}}} \,. \tag{8.15}$$

We introduced the normalized pseudo-thermal beta-parameter $\tilde{\beta}(k\tilde{T}_{\mathrm{e}})$ and the pseudo-temperature $k\tilde{T}_{\mathrm{e}}$ which are both equal to its thermodynamic analog in the case of a thermal electron distribution. If the CRe population is described by the power-law distribution (8.33), the CRe pressure is given by

$$P_{\mathrm{CRe}} = \frac{m_{\mathrm{e}} c^2}{3} \int_0^\infty \mathrm{d}p \, f(p) \beta_{\mathrm{e}} \, p = \frac{n_{\mathrm{CRe}} m_{\mathrm{e}} c^2 (\alpha - 1)}{6 \left[p^{1-\alpha} \right]_{p_2}^{p_1}} \left[\mathcal{B}_{\frac{1}{1+p^2}} \left(\frac{\alpha - 2}{2}, \frac{3 - \alpha}{2} \right) \right]_{p_2}^{p_1} \,, \tag{8.16}$$

where $\beta_{\mathrm{e}} \equiv \upsilon/c = p/\sqrt{1 + p^2}$ is the dimensionless velocity of the electron, $\mathcal{B}_q(a, b)$ denotes the incomplete Beta function (Abramowitz & Stegun 1965). In this case, the normalization of the CRe distribution function $f(p)\mathrm{d}p$ is determined by the CRe number density, $n_{\mathrm{CRe}} = \int \mathrm{d}p f(p)$. Here, we introduced the abbreviation

$$[F(p)]_{p_2}^{p_1} = F(p_1) - F(p_2) \tag{8.17}$$

in order to account for the lower and upper cutoff p_1 and p_2 of the CRe population.

8.3. Model for plasma bubbles

This section adopts an analytical formalism to describe buoyant plasma bubbles which was developed for the analysis of X-ray and radio emission by Enßlin & Heinz (2002). After a phase of supersonic propagation of the radio plasma into the ambient ICM, the radio lobes quickly reach pressure equilibrium with the surrounding medium once the AGN activity has terminated. During this stage, the bubble rises with constant velocity governed by the balance of buoyancy and drag forces while the volume of the bubble expands adiabatically. Meanwhile, the surrounding gas is approximately in hydrostatic equilibrium with the underlying dark matter potential. Synchrotron, inverse Compton, and adiabatic losses diminish the observable radio emitting electron population within the plasma bubble producing a so-called ghost cavity.

As an analytically feasible toy model, we assume spherical geometry of the plasma bubble and adopt the general n-fold β-profile for the electron pressure of the ICM which might find application for cool-core clusters:

$$P_{\mathrm{e}}(r) = n_{\mathrm{e}}(r) k T_{\mathrm{e}}(r) = \sum_{i=1}^N P_i \left[1 + \left(\frac{r}{r_{y,i}} \right)^2 \right]^{-3\beta_{y,i}/2} \,. \tag{8.18}$$

The origin of our coordinate system coincides with the cluster center while the x_1- and x_2-axes define the image plane, and the z-axis the line-of-sight to the observer. We choose the direction of the x_1-axis such that the bubble center is located in the x_1-z plane at $\boldsymbol{r}_{\mathrm{c}} = (r_{\mathrm{c}} \cos\theta, 0, r_{\mathrm{c}} \sin\theta)$. Its projected distance from the cluster center amounts to $R_{\mathrm{c}} = \mu r_{\mathrm{c}}$ with $\mu = \cos\theta$, while the radius of the bubble is denoted by r_{b}. For an unperturbed line-of-sight which is not intersecting the bubble, the observed thermal Comptonization parameter $y_{\mathrm{cl}}(x_1, x_2)$ of the cluster is given by

$$y_{\mathrm{cl}}(x_1, x_2) = \sum_{i=1}^N y_i \left(1 + \frac{x_1^2 + x_2^2}{r_{y,i}^2} \right)^{-(3\beta_{y,i}-1)/2} + y_{\mathrm{bg}}, \tag{8.19}$$

where $y_i = \sigma_{\mathrm{T}} (m_{\mathrm{e}} c^2)^{-1} P_i r_{y,i} \mathcal{B} \left(\frac{3\beta_{y,i}-1}{2}, \frac{1}{2} \right)$ is the central thermal Compton parameter of the respective individual β-profile and y_{bg} is the background contribution to the Comptonization which we set to zero in our analysis. In the case of a line-of-sight intersecting the surface of the bubble, the two intersection points are $(x_1, x_2, z_\pm)$ with

$$z_\pm = r_{\mathrm{c}} \sqrt{1 - \mu^2} \pm \sqrt{r_{\mathrm{b}}^2 - x_2^2 - (x_1 - r_{\mathrm{c}}\mu)^2}. \tag{8.20}$$

The thermal Comptonization parameter $y(x_1, x_2)$ for the area covered by the bubble is given by

$$y_{\rm b}(x_1, x_2) = y_{\rm cl}(x_1, x_2) - \sum_{i=1}^{N} y_i \left(1 + \frac{x_1^2 + x_2^2}{r_{y,i}^2}\right)^{-(3\beta_{y,i}-1)/2} \left[\frac{{\rm sgn}(z)}{2} \mathcal{I}_{q_{y,i}(z)}\left(\frac{1}{2}, \frac{3\beta_{y,i}-1}{2}\right)\right]_{z_-}^{z_+}, \qquad (8.21)$$

where $\mathcal{I}_q = \mathcal{B}_q(a, b)/\mathcal{B}(a, b)$ denotes the regularized Beta function and $q_{y,i}(z) \equiv z^2/(r_{y,i}^2 + x_1^2 + x_2^2 + z^2)$.

The amplitude of the kinetic SZ effect is proportional to the line-of-sight integrated electron density for which we also assume a general n-fold β-profile:

$$n_{\rm e}(r) = \sum_{i=1}^{N} n_i \left[1 + \left(\frac{r}{r_{w,i}}\right)^2\right]^{-3\beta_{w,i}/2}. \qquad (8.22)$$

To avoid confusion, we adopt the notation $r_{w,i}$ and $\beta_{w,i}$ for the usual core radii and the β-parameters in analogy to the thermal SZ effect. For an unperturbed line-of-sight which is not intersecting the bubble, the observed kinetic Comptonization parameter $w_{\rm cl}(x_1, x_2)$ of the cluster is given by

$$w_{\rm cl}(x_1, x_2) = \sum_{i=1}^{N} w_i \left(1 + \frac{x_1^2 + x_2^2}{r_{w,i}^2}\right)^{-(3\beta_{w,i}-1)/2}, \qquad (8.23)$$

where $w_i = \bar{\beta}_{\rm gas} \sigma_{\rm T} n_i r_{w,i} \mathcal{B}\left(\frac{3\beta_{w,i}-1}{2}, \frac{1}{2}\right)$ is the central kinetic Compton parameter of the respective individual β-profile. The kinetic Comptonization parameter $w(x_1, x_2)$ for the area covered by the bubble is obtained by analogy to the previous case:

$$w_{\rm b}(x_1, x_2) = w_{\rm cl}(x_1, x_2) - \sum_{i=1}^{N} w_i \left(1 + \frac{x_1^2 + x_2^2}{r_{w,i}^2}\right)^{-(3\beta_{w,i}-1)/2} \left[\frac{{\rm sgn}(z)}{2} \mathcal{I}_{q_{w,i}(z)}\left(\frac{1}{2}, \frac{3\beta_{w,i}-1}{2}\right)\right]_{z_-}^{z_+}. \qquad (8.24)$$

where $q_{w,i}(z) \equiv z^2/(r_{w,i}^2 + x_1^2 + x_2^2 + z^2)$.

8.4. Plasma bubbles of Perseus and Abell 2052

Two of the most prominent examples of radio plasma bubbles in nearby galaxy clusters can be observed within the cool core regions of the Perseus cluster (redshift $z_{\rm Perseus} = 0.0179$) and Abell 2052 ($z_{\rm A2052} = 0.0348$). Their proximity makes both clusters suitable targets for plasma bubble observations. Both clusters each host two bubbles which reflect the relic plasma of a past cycle of jet activity in the cD galaxy at the cluster center. At the current stage, the two radio lobes are in approximate pressure equilibrium with the surrounding medium and rise with a velocity governed by the balance of buoyancy and drag forces while the volume of the bubbles expands adiabatically.

As in the previous section, the coordinate origin coincides with the cluster center and the new direction of the x_1-axis points towards positive values of the relative right ascension. Assuming spherical symmetry of the plasma bubbles, their three dimensional position relative to the cluster center is degenerate because of projection effects. Together with the cluster center, the center of the bubbles form a plane which we assume to be perpendicular to the line-of-sight z. The azimuthal angle to the bubble center ϕ is measured from the x_1-axis.

8.4.1. Perseus

Using deprojected electron density and temperature profiles derived from X-ray observations (Churazov et al. 2003), we obtain a pressure profile by fitting a double β-profile according to Eqn. (8.18). In principle, we want the X-ray pressure profile in the absence of the radio bubbles. Since the observed X-ray surface brightness profile was derived assuming spherical symmetry including the region of the bubbles and does not extend into the very center of the cluster due to the AGN at the center and the *XMM/Newton* point spread function, our calculations somewhat underestimate the SZ effect of the bubbles. Table C.6 shows the individual parameters of the two plasma bubbles which are measured from the X-ray image of the central region of Perseus (Fabian et al. 2000).

In our model, we adopt the peculiar velocity of the Perseus cluster of $\bar{v}_{gas} = -136\ \text{km s}^{-1}$ with respect to the rest frame of the CMB and approaching the observer (Hudson et al. 1997).[1] The induced kinetic SZ effect gives rise to a small attenuation of the SZ decrement at our fiducial frequency. However, it also leads to an interesting effect at the crossover frequency $\nu_c \simeq 217\ \text{GHz}$, and produces an enhancement of the SZ increment at higher frequencies (cf. Sect. 8.7).

8.4.2. Abell 2052

Despite the lower central pressure of Abell 2052 compared to Perseus, Abell 2052 lies at higher Galactic latitudes. Thus, SZ flux confusion with Galactic dust emission is negligible in this case, which might be an observational advantage.

The electron density profile of Abell 2052 is obtained by deprojecting the X-ray surface brightness profile of Mohr et al. (1999) by means of the deprojection formula given in Appendix A of Pfrommer & Enßlin (2004a). Since the X-ray surface brightness is represented by a double β-model, the resulting density profile equals the square root of two single β-profiles added in quadrature. Refitting this electron density profile to match the profile defined by Eqn. (8.22) yields the parameters given in Table C.6.

In order to model the temperature profiles $T_e(r)$ for Abell 2052, we applied the universal temperature profile for cool core clusters proposed by Allen et al. (2001) to data taken from Blanton et al. (2001),

$$T_e(r) = T_0 + (T_1 - T_0) \left[1 + \left(\frac{r}{r_{temp}} \right)^{-\eta_{temp}} \right]^{-1}, \tag{8.25}$$

where $T_0 = 1.31\ \text{keV}$, $T_1 = 3.34\ \text{keV}$, $r_{temp} = 20.6\ h_{70}^{-1}\ \text{kpc}$, and $\eta_{temp} = 4.5$. This equation matches the temperature profile well up to radii of $\sim 0.3\ r_{vir}$, which is sufficient for our purposes since we are especially interested in the core region of Abell 2052. Combining the electron density and temperature profiles yields the radial variation in the gas pressure, which we represent as a triple β-profile (Table C.6); for two of the components, the normalization is negative. As noted for Perseus, what we really need is the pressure profile in the absence of the radio bubbles. The observed X-ray surface brightness profile was derived assuming spherical symmetry including the region of the bubbles. Probably as a result of this, the adopted pressure profile has more structure and a lower central pressure than would be true of the pressure profile in the absence of the radio bubbles. Thus, our calculations somewhat underestimate the SZ effect of the bubbles in Abell 2052. Since the southern bubble has a mushroom shape, we decided to model it using a half-sphere with the line-of-sight grazing the face.

For our simulation, Abell 2052 is taken to be at rest in the CMB rest frame owing to the large uncertainties of the velocity determination with the fundamental plane method to measure the Malmquist bias-corrected distance to early-type galaxies (Hudson et al. 2004, Hudson 2004).[2]

8.5. Synthetic observations

8.5.1. Atacama Large Millimeter Array

To simulate an *ALMA* observation of the central region of Perseus, we compute the frequency band-averaged SZ flux decrement $\langle \delta I \rangle_{\nu_0}$ which is defined by

$$\langle \delta I \rangle_{\nu_0} = \frac{\int d\nu\, \delta I(\nu) R_{\nu_0}(\nu)}{\int d\nu\, R_{\nu_0}(\nu)}. \tag{8.26}$$

---

[1] Using the fundamental plane, Hudson et al. (1997) measure the Malmquist bias-corrected distance to early-type galaxies of the Perseus cluster. Comparing these distances to the mean of the individual galaxy redshifts, they infer the peculiar velocity of the galaxy cluster, $v_{pec} = (-136 \pm 307)\ \text{km s}^{-1}$, where the uncertainty derives from the distance error added in quadrature with the cluster mean redshift error. On the other hand, the predicted peculiar velocity derived from the IRAS redshift survey density field yields $v_{pec} = +180\ \text{km s}^{-1}$ where the velocity field was smoothed on a scale of $8\ h^{-1}$ Mpc which corresponds to the scale from which the clusters collapsed.

[2] Hudson et al. (2004) have only 5 galaxies of Abell 2052 in their sample and infer a peculiar cluster velocity of $v_{pec} = (-494 \pm 1062)\ \text{km s}^{-1}$ where the error is dominated by the error in the distance but also includes redshift uncertainties and systematic effects such as extinction. On the other hand, the predicted peculiar velocity of Abell 2052 according the IRAS redshift survey density field is $v_{pec} = +208\ \text{km s}^{-1}$.
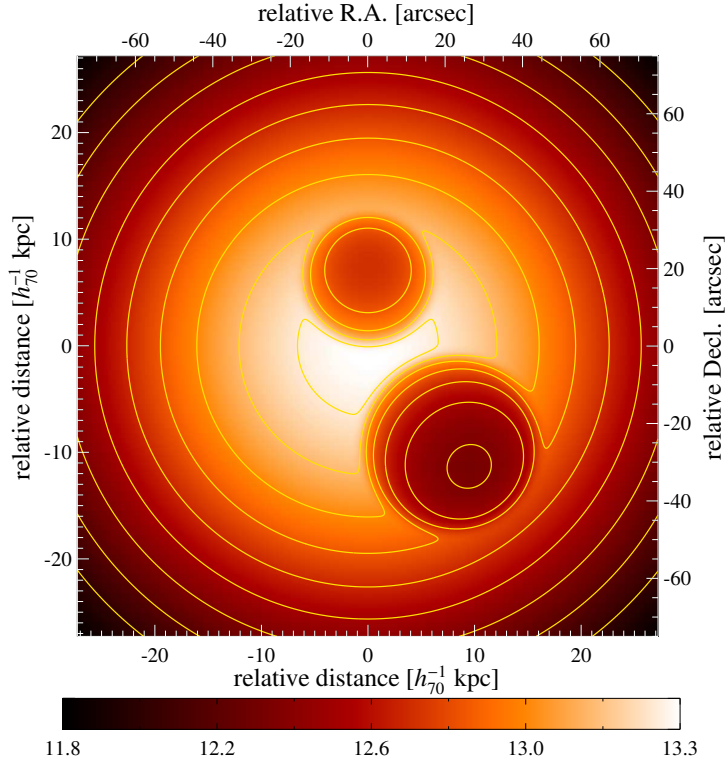
ALMA: Perseus cluster

Figure 8.1.: Synthetic *ALMA* observation of the cool core region of Perseus at the frequency band centered on 144 GHz. The simulated SZ flux decrement of radio plasma bubbles is shown in units of mJy/arcmin^2 assuming an ultra-relativistic electron population within the bubbles (scenario 1). The image is smoothed to the resolution of the *ALMA* compact core configuration (FWHM $\simeq 2.9''$). The contour lines have a linear spacing of 0.16 mJy/arcmin^2. For comparison, the size of the *ALMA* field of view at this frequency is FWHM$_{\text{fov}} \simeq 36''$.

Here, $R_{\nu_0}(\nu)$ denotes the frequency response of the *ALMA* receivers centered on a fiducial frequency ν_0 which we assume to be described by a top-hat function:

$$R_{\nu_0}(\nu) = \begin{cases} 1, & \nu \in [\nu_0 - \Delta\nu/2, \nu_0 + \Delta\nu/2] \\ 0, & \nu \notin [\nu_0 - \Delta\nu/2, \nu_0 + \Delta\nu/2] \end{cases} \tag{8.27}$$

We choose the *ALMA* frequency band 4 which samples the extremum of the SZ flux decrement and is characterized by $\nu_0 = 144$ GHz and $\Delta\nu = 38$ GHz (Brown et al. 2000). The requirement of obtaining the highest flux sensitivity to the largest scales comparable to the field of view at this frequency (FWHM$_{\text{fov}} \simeq 36''$) calls for the most compact configuration *ALMA E* with a maximal baseline of $d_{\text{bl}} = 150$ m. Thus, we convolve the simulated SZ flux decrement with a Gaussian to obtain the resolution of this configuration, FWHM $\simeq c/(\nu\, d_{\text{bl}}) \simeq 2.9''$. Since Perseus lies at more than 40 degrees of declination and is a Northern object, *ALMA* will be challenged to observe it, reaching only up to 25 degrees elevation. However, for the North-South elongated *ALMA* configuration of about a factor of $(\cos 65°)^{-1} \simeq 2.4$, the beam will be almost round. Assuming an ultra-relativistic electron population within the bubbles yields the SZ flux decrement as shown in Fig. 8.1 which is similar in morphology to the X-ray image.

To investigate whether the plasma bubbles are detectable in the SZ flux decrement, we define the SZ flux contrast ρ:

$$\rho = \frac{I_A - I_B}{I_A + I_B}. \tag{8.28}$$

Here, I_A and I_B denote the mean SZ flux decrement of two equally sized solid angle elements within the field of view, one of which measures the SZ flux inside and the other one outside the bubble. Prior information about

Table 8.1.: Summary of predicted exposure times to obtain a 5σ detection of the plasma bubble (assuming an ultra-relativistic electron population within the bubble) for the different combinations of telescopes and clusters. I_A and I_B denote the mean SZ flux decrement of two equally sized solid angle elements within the field of view, one of which measures the SZ flux outside and the other one inside the bubble.

Telescope: cluster	I_A [mJy amin^{-2}]	I_B [mJy amin^{-2}]	exposure [hours]
ALMA: Perseus	13.25	12.70	5.1
ALMA: Abell 2052	3.930	3.698	38
GBT: Perseus	11.31	10.85	2.1
GBT: Abell 2052	3.272	3.138	31

the angular position of the X-ray cavities allows one to maximize the SZ flux contrast. Adopting Gaussian error propagation and introducing *ALMA*'s sensitivity per beam in terms of flux density, σ_{ALMA}, yields the uncertainty in ρ,

$$\sigma_\rho = \sqrt{\left(\frac{\partial \rho}{\partial I_A}\right)^2 + \left(\frac{\partial \rho}{\partial I_B}\right)^2} \, \frac{\sigma_{ALMA}}{\sqrt{N_{\text{beam}}}} \tag{8.29}$$

$$= \frac{2\sqrt{I_A^2 + I_B^2}}{(I_A + I_B)^2} \, \frac{\sigma_{ALMA}}{\sqrt{N_{\text{beam}}}}. \tag{8.30}$$

Here, $N_{\text{beam}} = f \, A_{\text{beam}}/(2 A_{\text{fov}})$ is the number of statistically independent beams per flux averaged solid angle element, $f \leq 0.5$ measures the fraction of the solid angle of the bubble within the field of view, and the factor of $A_{\text{beam}}/(2 A_{\text{fov}})$ accounts for the statistically independent degrees of freedom within the field of view. Combining Eqns. (8.28) and (8.30) yields the signal-to-noise for the 5σ detection of the bubble[3]:

$$\frac{S}{N} \equiv \frac{\rho}{\sigma_\rho} = \frac{\sqrt{N_{\text{beam}}} \left(I_A^2 - I_B^2\right)}{2\sigma_{ALMA} \sqrt{I_A^2 + I_B^2}} \geq 5. \tag{8.32}$$

We choose the field of view to be centered on the inner rim of the southern bubble such that equal solid angle elements fall inside and outside the bubble, respectively. The simulated mean SZ flux decrements within the two solid angle elements of the primary beam require only an integration time of 5.1 hours in order to obtain a 5σ detection of the plasma bubble assuming an ultra-relativistic electron population within the bubble. Uncertainties in the amplitude of the kinetic SZ effect and the geometrical arrangement and shape of the bubbles may slightly modify this result. As a word of caution, this observation time allows a single bubble to be observed in a single pointing while it might be advisable to map the entire central region including both bubbles to get a clearer picture of the structure, and to be convinced that any holes seen in the SZ map at the radio bubbles were not just fluctuations also seen elsewhere in the cluster center away from the radio bubbles.

The corresponding observation of Abell 2052 would require an integration time of 38 hours in order to obtain a 5σ detection of the plasma bubble for the same plasma bubble content, the longer exposures mainly being the result of the higher redshift and the lower central temperature of this cluster.

---

[3]The flux density sensitivity σ_{ALMA} for point sources, which should be approximately applicable in the case of the compact core configuration, is given by Butler et al. (1999):

$$\sigma_{ALMA} = \frac{\sqrt{2} \, k T_{\text{sys}}}{\eta \, A_{\text{dish}} \, A_{\text{beam}} \, \sqrt{\Delta t \, \Delta \nu \, N_{\text{bl}}}}. \tag{8.31}$$

Here, $T_{\text{sys}} \simeq 65$ K denotes the system temperature, $A_{\text{dish}} = \pi D^2/4$ the collecting area of each dish ($D = 12$ m), $\eta = 0.75$ the aperture efficiency, $A_{\text{beam}} = 1.13 \, \text{FWHM}^2 \simeq 9.3 \, \text{arcsec}^2$ the area of the secondary beam, Δt the integration time, $\Delta \nu = 38$ GHz the bandwidth, and $N_{\text{bl}} = n(n-1)/2$ the number of baselines, $n = 64$ being the number of antennas.
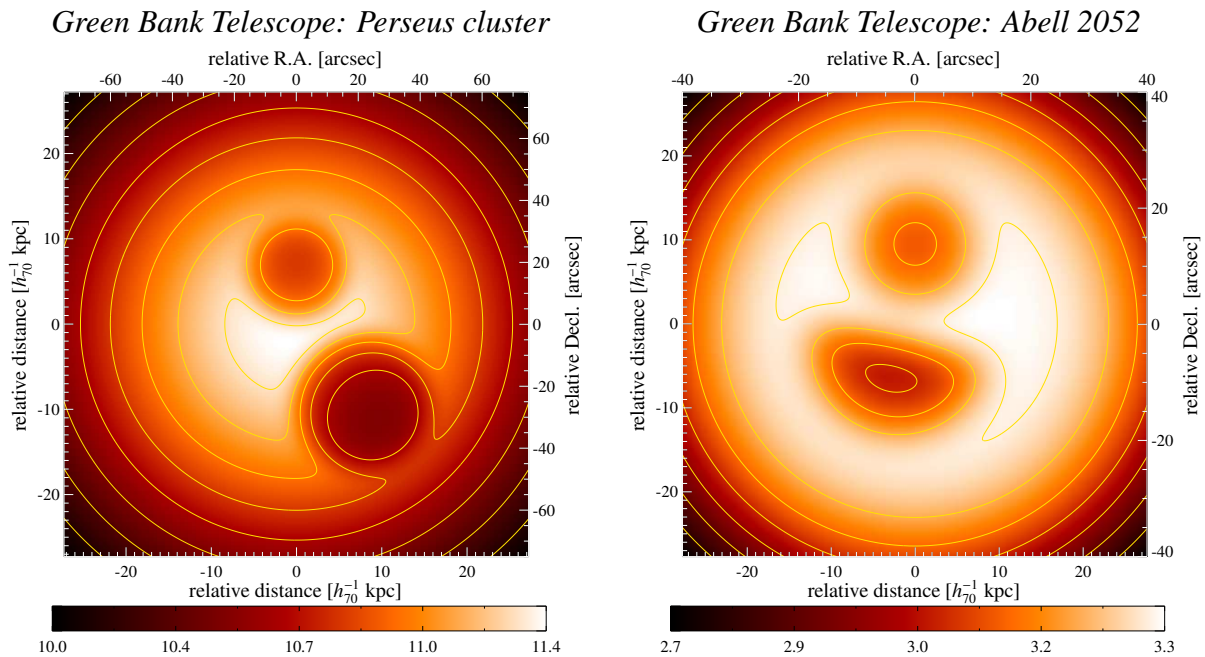
Green Bank Telescope: Perseus cluster   *Green Bank Telescope: Abell 2052*

Figure 8.2.: Synthetic *GBT* observations of the cool core regions of Perseus (*left panel*) and Abell 2052 (*right panel*) at the frequency band centered on 90 GHz. The simulated SZ flux decrement of radio plasma bubbles is shown in units of mJy/arcmin^2 assuming an ultra-relativistic electron population within the bubbles (scenario 1). The images are smoothed to the resolution the *GBT* 3 mm receiver (FWHM $\simeq 8.0''$). The contour lines have a linear spacing of 0.16 mJy/arcmin^2 (*left panel*) and 0.08 mJy/arcmin^2 (*right panel*). For comparison, the size of the *GBT* field of view at this frequency is $32'' \times 32''$.

8.5.2. Green Bank Telescope

To simulate a *GBT* observation of the central region of both clusters, we compute the frequency band-averaged SZ flux decrement $\langle \delta I \rangle_{\nu_0}$ in the frequency interval [86 GHz, 94 GHz]. The resulting simulated SZ flux decrement was convolved with a Gaussian of width $\sigma \simeq 3.4''$ to obtain the resolution of the *GBT* 3 mm receiver. Assuming an ultra-relativistic electron population within the bubbles yields the SZ flux decrement as shown in Fig. 8.2.

To investigate whether the plasma bubbles are detectable in the SZ flux decrement, we adopt the concept of SZ flux contrast of the previous section. The sensitivity of the upcoming *GBT* Penn Array Receiver in terms of flux density is given by $\sigma_{GBT} = 0.25 \, (\Delta t)^{-1/2}$ mJy arcmin^{-2}, where Δt is the integration time in hours (Mason 2004). We choose the $32'' \times 32''$ field of view of the *GBT* to be centered on the inner rim of the southern bubble of Perseus as described above. Assuming an ultra-relativistic electron population within the bubble, we predict a 5σ detection of the plasma bubble after an integration time of 2.1 hours owing to the better sensitivity of the bolometric receivers on the *GBT*. This observation time assumes a proper foreground subtraction of the Galactic emission components.

The corresponding observation of Abell 2052 would require an integration time of 31 hours in order to obtain a 5σ detection of the plasma bubble for the same plasma bubble content. Again, the integration times correspond to a single pointing on the southern bubble while mapping the entire central region would take respectively longer.

8.6. Composition study of plasma bubbles

In the following, we study exemplarily five physically different scenarios of the composition of the plasma bubble which is as a whole in approximate pressure equilibrium with the ambient ICM. Although these scenarios might not be realized in nature in these pure forms, a realistic SZ flux decrement can be obtained by linearly combining the different scenarios due to the superposition property of the pressure of different populations:

1. The internal pressure is either dominated by CRps, magnetic fields, or ultra-relativistic CRes being characterized by a mean momentum of $\langle p \rangle \gg 1$ in this scenario. This is the most positive case for the detection of the plasma bubbles in the SZ flux decrement, as the bubble volume does not contribute to the SZ flux decrement significantly. Although this is the most positive scenario, it also is the one adopted by most analyses of radio lobes.

2. This scenario assumes the internal pressure to be dominated by a compound of CRp and CRe populations where the latter is described by a power-law distribution:

$$f_{\mathrm{CRe}}(p, \alpha, p_1, p_2) = \frac{(\alpha - 1)p^{-\alpha}}{p_1^{1-\alpha} - p_2^{1-\alpha}}. \tag{8.33}$$

   The distribution function is normalized such that its integral over momentum space yields unity. The choice of $p_1 = 1$, $p_2 = 10^3$, and $\alpha = 2$ implies a mean momentum of $\langle p \rangle \simeq 6.9$ as well as a pseudo-temperature of $k\tilde{T}_{\mathrm{CRe}} \simeq 2.2\, m_{\mathrm{e}}c^2 \simeq 1.1$ MeV and represents a plausible scenario for the relativistic composition of the bubble. The CRp and CRe populations each contribute equally to the internal pressure of the bubble representing a remnant plasma originating from the hadronic jet scenario.

3. The dynamically dominant internal pressure support is contributed to equal amounts by relativistic electron and positron populations, respectively. Taking the same parameters for the CRe distribution of the previous scenario, this approach represents the remnant radio plasma originating from the electron-positron jet scenario.

4. A trans-relativistic thermal proton and electron distribution with $kT_{\mathrm{e}} = 50$ keV dominates dynamically over the other non-thermal components:

$$f_{\mathrm{e,th}}(p, \beta_{\mathrm{th}}) = \frac{\beta_{\mathrm{th}}}{K_2(\beta_{\mathrm{th}})} p^2 \exp\left(-\beta_{\mathrm{th}}\sqrt{1 + p^2}\right). \tag{8.34}$$

   K_2 denotes the modified Bessel function of the second kind (Abramowitz & Stegun 1965) which takes care of the proper normalization and $\beta_{\mathrm{th}} = m_{\mathrm{e}}c^2/(kT_{\mathrm{e}})$ is the normalized thermal beta-parameter. The mean momentum of this distribution amounts to $\langle p \rangle \simeq 0.55$.

5. This scenario assumes a dynamically dominant hot thermal proton and electron distribution with $kT_{\mathrm{e}} = 20$ keV which exhibits a mean momentum of $\langle p \rangle \simeq 0.33$.

In all cases, the bubble's sound velocity and thus the barometric scale height are much higher than the corresponding values of the ambient ICM which implies a flat pressure distribution within the plasma bubble. This leads to a reduced internal pressure with respect to the ambient ICM at the inner rim of the bubble and an excess pressure at the outer rim of the bubble, which is responsible for the buoyant rise of the bubble in the cluster atmosphere.

Figure 8.3 shows the spectral distortions due to the thermal SZ effect $g(x)$, kinetic SZ effect $h(x)$, and relativistic SZ effect of the various scenarios for the relativistic populations of the bubble composition. The spectral distortions of the relativistic SZ effect are given by $\tilde{g}(x)$ which have been defined in Eqns. (8.11) through (8.15). Please note, that the scenarios 2 and 3 exhibit the same spectral distortion $\tilde{g}_{\mathrm{CRe}}$ and that the amplitude of the kinetic SZ effect w_{gas} is typically one order of magnitude smaller than the amplitude of the thermal SZ effect y_{gas}.

The left panel of Fig. 8.4 shows the unconvolved SZ flux decrement along an impact parameter through the center of the southern bubble of Perseus at the *ALMA* frequency band centered on $\nu_0 = 144$ GHz. While the northern bubble of Perseus would evince qualitatively the same behavior, it shows a shallower depth of its SZ cavity due to its smaller geometrical size resulting in a weaker SZ flux contrast (cf. Fig. 8.1). The depth of the SZ cavity at this frequency range is a measure how relativistic the respective electron population is, i.e. a deeper SZ cavity indicates a higher mean momentum of the electron population. Our studies show a strong signature of the different bubble compositions on the SZ flux decrement. Thus, the combination of X-ray and SZ observations allows one to circumvent the degeneracy between the effects of the bubble composition and of the bubble extent along the line-of-sight on the SZ measurement. This enables us to distinguish a relativistic from a thermal electron population inside the bubble using only a single frequency SZ observation by either a detection or non-detection of the bubble, respectively.
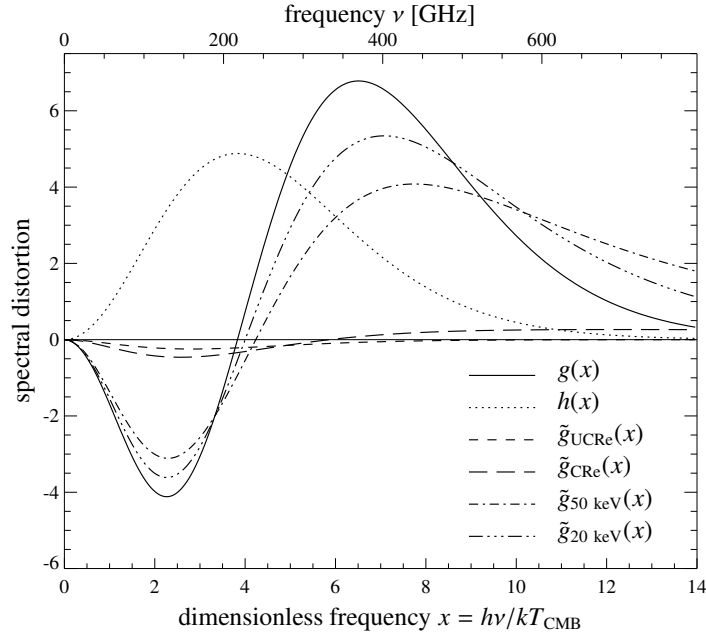
Figure 8.3.: Spectral distortions due to the thermal SZ effect $g(x)$, kinetic SZ effect $h(x)$, relativistic SZ effect due to a population of ultra-relativistic CRes, $\tilde{g}_{\mathrm{UCRe}} = -i(x)\tilde{\beta}_{\mathrm{UCRe}}$ (with $p_1 = 3$, $p_2 = 10^3$, and $\alpha = 2$), relativistic SZ effect due to a population of power-law CRes, $\tilde{g}_{\mathrm{CRe}} = [j(x) - i(x)]\tilde{\beta}_{\mathrm{CRe}}$ (with $p_1 = 1$, $p_2 = 10^3$, and $\alpha = 2$), and the relativistic SZ effect due to a population of trans-relativistic thermal electrons, $\tilde{g}_{50\ \mathrm{keV}} = [j(x) - i(x)]\beta_{\mathrm{th}}(50\ \mathrm{keV})$, as well as due to electrons with $kT_{\mathrm{e}} = 20$ keV, respectively.

8.7. Kinetic Sunyaev-Zel'dovich effect

8.7.1. General considerations

If the cluster is moving towards the observer, the CMB temperature in this direction is increased due to the Doppler effect of the bulk motion of the cluster relative to the rest frame of the CMB (in this case, our convention is such that $\bar{v}_{\mathrm{gas}} < 0$). This enhanced SZ emission implies a reduced SZ flux decrement for frequencies below the crossover frequency of the thermal SZ effect at $\nu_{\mathrm{c}} \simeq 217$ GHz (for the non-relativistic case). Cosmologically, line-of-sight cluster velocities follow a Gaussian distribution with vanishing mean since the large scale structure is at rest in the comoving CMB-frame and with a standard deviation of $\sigma_{\mathrm{vel}} \simeq 310$ km s^{-1} as derived from a cosmological structure formation simulation comprising the Hubble volume (Jenkins et al. 2001, Schäfer et al. 2004).

Theoretically, the turbulent motions of the ICM should also contribute to the kinetic SZ effect. The largest impact is caused by two merging clusters along the line-of-sight which induces a bimodal streaming flow pattern on the sky. However, radio plasma bubbles are mainly observed within cool-core clusters which represent relaxed clusters where the ICM is approximately in hydrostatic equilibrium with the underlying dark matter potential. In this case, only small scale turbulent vortices are expected which exhibit smaller angular momenta. For an isotropic distribution of vortex orientations, line-of-sight integration and beam convolution average the resulting kinetic SZ effect out to zero. Thus, these turbulent motions can only contribute in second order to the thermal SZ effect.

It would be useful to know the peculiar velocity of the galaxy cluster in order to remove the degeneracy of the SZ cavity depth with respect to the different bubble compositions and the kinetic SZ effect. In the case of a general morphology of a galaxy cluster, in particular for non-axis-symmetric objects, it is impossible to unambiguously deproject the cluster in order to derive the peculiar velocity given only a single frequency SZ observation and an X-ray image (Zaroubi et al. 1998, 2001). For multi-frequency SZ observations of the entire cluster, Aghanim et al. (2003) theoretically discuss possibilities in order to break parameter degeneracies between the Compton parameter, the electron temperature and the cluster peculiar velocity for an appropriate choice of observing frequencies.
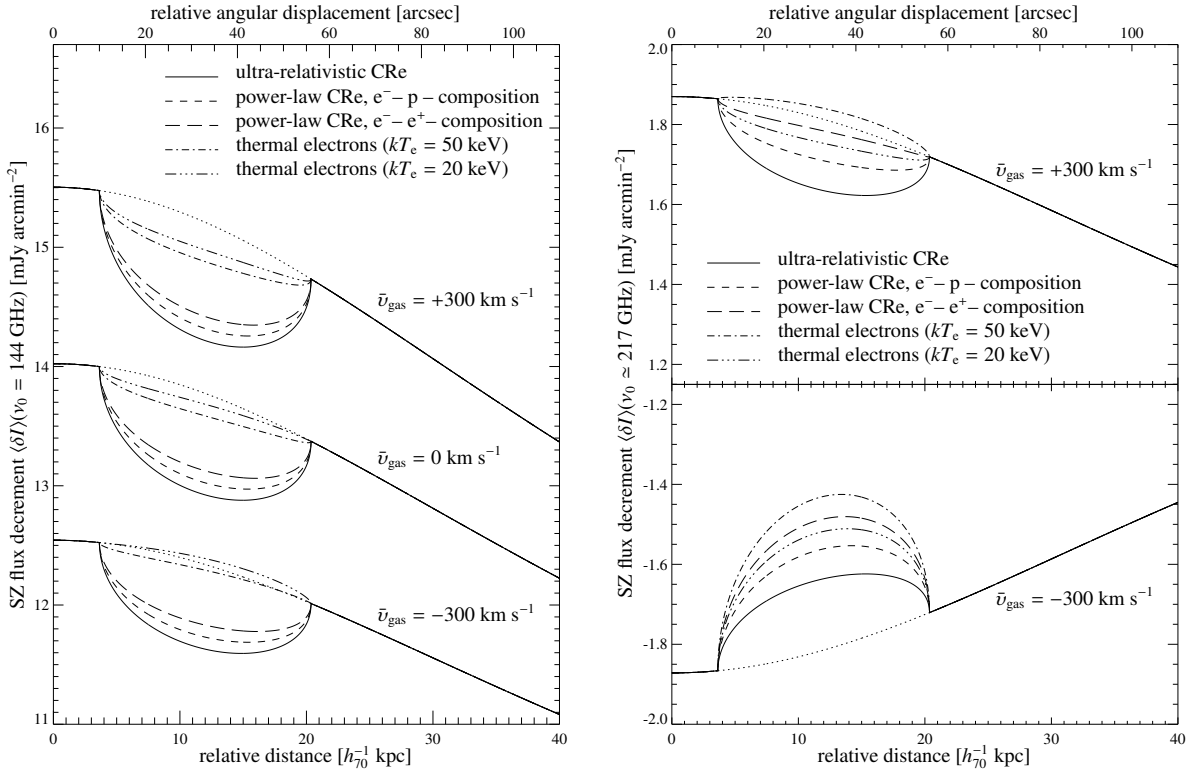
Figure 8.4.: Unconvolved SZ flux decrement along an impact parameter through the center of the southern bubble of Perseus. The *left panel* shows the SZ flux decrement at the *ALMA* frequency band centered on $\nu_0 = 144$ GHz while the *right panel* assumes a central fiducial frequency of $\nu_0 \simeq 217$ GHz. Compared are five different scenarios of the composition of the plasma bubbles to the undisturbed SZ profile (dotted thin line), respectively. The three (two) set of lines correspond to three (two) differently assumed average bulk velocities along the line-of-sight, $\bar{v}_{gas}$, of the thermal gas of Perseus.

Considering possible gaseous substructure along the line-of-sight towards the radio plasma bubble and a possibly non-spherical bubble geometry, it might be impossible to discriminate between morphologically similar bubble compositions (scenarios 4 and 5) in the case of a single frequency *ALMA* or *GBT* observation.

8.7.2. Perseus plasma bubbles at different frequencies

The left panel of Fig. 8.4 compares three set of lines corresponding to different average line-of-sight streaming velocities at the *ALMA* frequency band which samples the extremum of the thermal SZ flux decrement ($\nu_0 = 144$ GHz). The effect of an overall decrease in the SZ flux decrement for the approaching cluster ($\bar{v}_{gas} = -300$ km s^{-1}) can be clearly seen. The amplitude of the kinetic SZ effect depends on the dimensionless average velocity of the thermal gas, which amounts in our case to $\bar{\beta}_{gas} = \bar{v}_{gas}/c \simeq 10^{-3}$. On the other hand, the amplitude of the thermal SZ effect depends on the inverse normalized thermal beta-parameter, $\beta_{th}^{-1} = kT_e/(m_e c^2) \simeq 10^{-2}$, where we inserted the average temperature of the Perseus cluster. At the extremum of the thermal SZ flux decrement, the kinetic SZ flux amounts to an approximately 10% correction to the thermal SZ effect for the choice of our fiducial cluster velocity. However, this small effect is responsible for the qualitative difference of the observable SZ cavities resulting from plasma bubbles: assuming a receding cluster and a dynamically dominant thermal proton and electron distribution (scenarios 4 and 5), we still obtain a detectable depth of the SZ cavity which almost disappears for an approaching cluster.
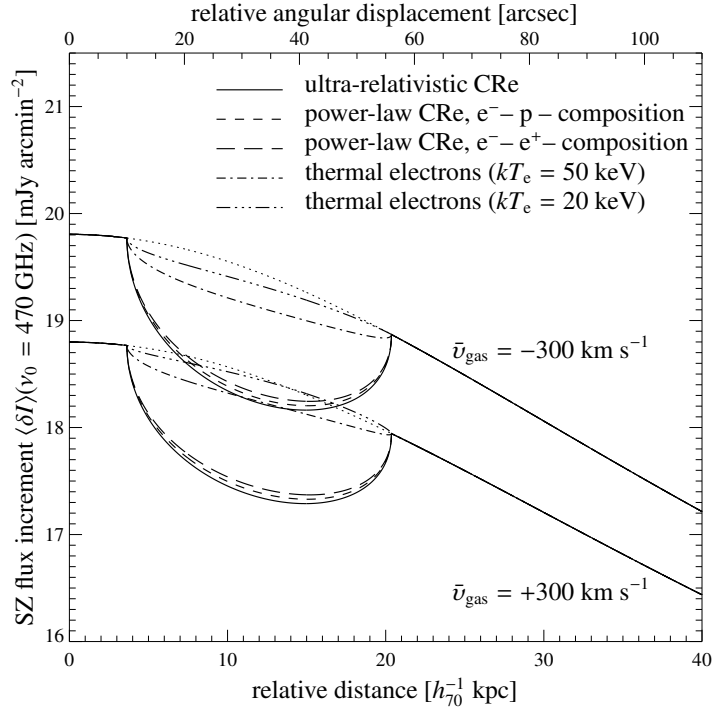
Figure 8.5.: Unconvolved SZ flux increment along an impact parameter through the center of the southern bubble of Perseus at the frequency band centered on $\nu_0 \simeq 470$ GHz. Compared are five different scenarios of the composition of the plasma bubbles to the undisturbed SZ profile (dotted thin line), respectively. The two set of lines correspond to two differently assumed average bulk velocities along the line-of-sight, $\bar{\upsilon}_{gas}$, of the thermal gas of Perseus.

The right panel of Fig. 8.4 shows the unconvolved SZ flux decrement assuming a central frequency of $\nu_0 = 217.34$ GHz and bandwidth of $\Delta\nu = 40$ GHz. Allowing for finite frequency response of the instrument's receivers, this fiducial frequency corresponds to a vanishing frequency band-averaged thermal SZ flux decrement. Thus, the kinetic SZ effect represents the main effect at this frequency showing a positive SZ flux decrement for a receding cluster, i.e. we would detect a reduced flux of CMB photons in that direction. At this frequency range, a relativistic electron population always causes a positive relativistic SZ flux decrement owing to the higher crossover frequency $\nu_c \gtrsim 217$ GHz and irrespective of the cluster's velocity. This effect causes an enhanced SZ flux contrast of the bubble for an approaching cluster compared to a receding one, depending on the specific composition of the plasma bubble.

The interchange of SZ flux decrements for different bubble compositions is remarkable compared to the case of $\nu_0 = 144$ GHz. The largest impact of the bubble's SZ cavity is provided by the trans-relativistic thermal electron population of 50 keV owing to its comparably large frequency band-averaged SZ flux decrement. The SZ flux decrements of the other bubble compositions are smaller because the crossover frequency of the thermal electron population of $kT_e = 20$ keV lies closer to the non-relativistic crossover frequency while the amplitudes of the spectral distortions of the relativistic electron populations are smaller (cf. Fig. 8.3). Relativistic corrections to the thermal SZ flux resulting from the thermal electrons with temperatures of $kT_e \simeq 3 - 7$ keV are negligible: the resulting profiles of the SZ flux decrement are similar in morphology to the kinetic SZ flux decrement and would correspond at this frequency to an additional kinetic SZ effect of only ~ 10 km s^{-1}.

Owing to the proximity of the Perseus cluster to the Galactic plane, SZ observations at even higher frequencies might be challenging due to the Galactic dust emission which represents the major Galactic foreground at these frequencies (see e.g. Schlegel et al. 1998, Finkbeiner et al. 1999, 2000, Schäfer et al. 2004). In an exemplary manner, we also show the expected SZ cavity around a fiducial frequency which samples the maximum of the SZ

flux increment.[4] For a cluster with a temperature of 5 keV, the normal thermal relativistic corrections disappear at $\nu_0 = 470$ GHz when taking into account the detector's finite frequency response of $\Delta\nu = 40$ GHz. Secondly, at this frequency the kinetic SZ effect has only a small additional contribution (Aghanim et al. 2003). Hence, one could expect that the SZ signal from the bubble could be even more prominent. This is investigated in Fig. 8.5 which shows the unconvolved SZ flux increment along an impact parameter through the center of the southern bubble of Perseus at $\nu_0 = 470$ GHz. The different bubble compositions qualitatively show the same behavior as for the SZ decrement at the frequency band around $\nu_0 = 144$ GHz. However, the SZ flux contrast of the bubble is much higher as well as the degeneracy owing to the kinetic SZ effect is reduced. Thus, for clusters not being outshone by the Galactic dust emission, observations at this frequency range seem to be most promising in order to infer the bubble composition.

8.8. Observing strategy

The previous results imply the following observing strategy for the *ALMA* compact core configuration or the *GBT*. A short duration observation (a few hours) of the inner rim of the southern X-ray cavity within the Perseus cool-core region should either yield a 5σ detection of an SZ cavity or not. The case of a significant detection either proves the existence of a dynamically dominant CRp population, magnetic fields, or an ultra-relativistic CRe population within the radio plasma bubble while the contrary excludes this hypothesis on the 5σ level.

Such a non-detection of the bubble would require a longer integration time in order to detect the SZ flux decrement of the plasma bubble at the desired significance level. A detection of a very shallow SZ cavity indicates a dynamically dominant hot thermal electron population within radio plasma bubbles. The underlying physical scenario is degenerate for an observed intermediate depth of the SZ cavity (such as an SZ flux level in between our scenarios 3 and 4). Possibilities include trans-relativistic thermal electron distributions or soft CRe power-law distributions exhibiting a spectral index of approximately $\alpha = 3$ as well as a small lower cutoff p_1 implying a mean momentum of $\langle p \rangle \sim 1$. Follow-up multi-frequency SZ observations in combination with X-ray spectroscopy could disentangle the different scenarios and possibly estimate the temperature or spectral characteristics of the dynamically dominant electron population (Shimon & Rephaeli 2002, Enßlin & Hansen 2004). The detection of such an SZ flux would enable one to draw conclusions concerning the particular jet scenario being responsible for the inflation of the plasma bubble.

The case of a deep SZ cavity with an associated detection of dynamically dominant CRps, magnetic fields, or ultra-relativistic CRes leads to an immediate question about the composition of radio ghosts. Thus, an additional SZ observation of the ghost cavity in Perseus could yield answers about the potential entrainment of ICM into the plasma bubble during its buoyant rise in the cluster atmosphere. If a large fraction of entrained gas in the bubble provides significant pressure support, it must have experienced Coulomb heating through CRes in order not to be detected in X-rays. This would result in a reduced SZ flux contrast of the ghost cavity and leads to a faint or undetectable SZ flux decrement of the ghost cavity.

8.9. Conclusion and outlook

This chapter provides a theoretical framework for studying the SZ decrement of radio plasma bubbles within clusters of galaxies. X-ray observations are proportional to the square of the thermal electron density and probe the core region of the cluster. On the other hand, the SZ effect is proportional to the thermal electron pressure enabling the detection of plasma bubbles further outwards of the respective clusters. Assuming spherically symmetric plasma bubbles, we simulate an *ALMA* and a *GBT* observation of the cool core regions of the Perseus cluster and Abell 2052. In this context, we investigate physically different scenarios of the composition of the plasma bubbles: as long as the bubble is dynamically dominated by relativistic electrons, protons, or magnetic fields, there exists a realistic chance to detect plasma bubbles in the SZ flux decrement. Non-detection of radio bubbles with the SZ effect at the position of X-ray cavities hints towards a dynamically dominant hot thermal electron population within radio plasma bubbles. Detection of a non-thermal pressure support should be possible within a few hours observation with ALMA or GBT in the case of Perseus and a few tens of hours in the case of Abell 2052.

---

[4]This might find application for a galaxy cluster with an X-ray cavity at high Galactic latitude (e.g., Abell 2052) or in the case of Perseus, once the Galactic dust emission is properly removed.

Pursuing high-sensitivity multi-frequency SZ observations, it will be challenging but not impossible to infer the detailed nature of the different possible populations of the bubble. For realistic observations, the frequency dependence of the relativistic SZ signal is contaminated by the presence of the kinetic SZ signal. It would be optimal to have a frequency channel centered on the crossover frequency of the thermal SZ effect in order to infer the energy spectrum of the dynamically dominant population and to measure the temperature or spectral characteristics of the electron population.

The results of this chapter were worked out in collaboration with T.A. Enßlin and C.L. Sarazin. A paper entitled "Unveiling the composition of radio plasma bubbles in galaxy clusters with the Sunyaev-Zel'dovich effect" *has been published in the journal* Astronomy & Astrophysics (Pfrommer, Enßlin & Sarazin, 2005, A&A, 430, 799).

9. A description of cosmic ray gas for cosmological applications

Abstract

Galactic non-equilibrium processes like shock waves and turbulence have generated magnetic fields and cosmic rays (CRs) in the interstellar medium. Cosmic rays play a decisive role within our Galaxy: their pressure, along with that of the thermal gas, balances gravity, they trace past energetic events such as supernovae, and they reveal the underlying structure of the baryonic matter distribution through their interactions. To study the impact of CRs, we develop an approximative framework to treat dynamical and radiative effects of CRs in cosmological simulations. The guiding principle is a balance between capturing as many physical properties of CR populations as possible while simultaneously requiring as little extra computational resources as possible. The CR spectrum is approximated by a single, constant spectral index power-law, with spatially and temporal varying normalization and low-energy cut-off. Particle number and energy conservation principles are used to derive evolution equations for the basic variables due to adiabatic and non-adiabatic processes. Such are compression, rarefaction, CR injection via both shocks of supernova remnants and structure formation shock waves, in-situ re-acceleration of CRs, CR spatial diffusion, CR energy losses due to Coulomb interactions, Bremsstrahlung, and hadronic interactions with the background gas, including the associated γ-ray and radio emission due to subsequent pion decay. Furthermore, we explain how the formalism can be included into smoothed-particle-hydrodynamics simulations.

9.1. Introduction

9.1.1. Motivation

The interstellar medium (ISM) of galaxies is very complex and its energy budget is composed of thermal and non-thermal components. The non-thermal components are magnetic fields and cosmic rays which are known to contribute roughly as much energy and pressure each as the thermal gas contributes to the ISM, at least in our own Galaxy. Numerical simulations and semi-analytical models of galaxy and large-scale structure formation neglected the effects of these non-thermal components so far for simplicity despite their dynamical importance.

Although there have been some attempts to equip SPH galaxy formation codes with magnetic field descriptions on the MHD level (Dolag et al. 1999), a fully dynamical treatment of the CR component was not yet attempted due to the very complex CR physics involved. There has been some effort to furnish grid based MHD codes with a diffusive CR component in order to study isolated effects like Parker instabilities (Kuwabara et al. 2004, Hanasz & Lesch 2003). However, these codes are not suited for galaxy formation simulations in a cosmological setting due to the missing adaptive resolution needed and the many extra components like dark matter, stellar populations, etc. Although there have been numerical implementations of discretized CR energy spectra on top of grid based cosmological simulations (Miniati 2001), these implementations neglect the hydrodynamical pressure of such a CR component. Additionally, the amount of computer resources required for these in terms of memory and CPU-time is substantial. This renders such code to be unattractive for the purpose of galaxy formation and inhibits the inclusion of CRs into expensive simulation runs in cases where it is not clear ab initio if CRs are crucial or not.

An accurate description of CRs would follow the evolution of their spectral energy distribution as a function of time and space in addition to the computation of their dynamical, non-linear feedback to hydrodynamics. In order to allow the inclusion of CRs and their effects into numerical simulations and semi-analytic descriptions of galaxy formation, we develop a simplified description of the CR dynamics and physics which should be a compromise between two opposite requirements, namely: (i) as many physical properties and peculiarities of CR populations as possible should be captured, and (ii) as little extra computational resources as possible should be used. The emphasis

is given to the dynamical impact of CRs on hydrodynamics, and not on an accurate spectral representation of the CRs. The guiding principles are energy and particle number conservations, and adiabatic invariants. Non-adiabatic processes will be mapped onto modifications of these principles.

9.1.2. Approximations and assumptions

1. Only the dominant CR proton population is modeled, assuming that the presence of α-particles and heavier ions would not change the dynamical picture. In contrast to heavier ions, α-particles carry a significant fraction of the total CR energy. Nevertheless, the assumption is a reasonable approximation, since the energy density of α-particles can be absorbed into the proton spectrum. As a coarse approximation, a GeV energy α-particle can be regarded as an ensemble of four individual nucleons traveling together due to the relatively weak MeV nuclear binding energies compared to the kinetic energy of relativistic protons. For hadronic interactions the fact that the four nucleons are bound is of minor importance. Since Coulomb cooling is proportional to the square of the nucleus' charge, each of the four nucleons of the α-particle is experiencing a loss of kinetic energy which is identical to the loss that a free CR proton with exactly the same specific energy would feel.

2. The dynamically relevant physical quantities are the kinetic energy density $\varepsilon_{\rm CR}$ and the average energy $T_{\rm CR} = \varepsilon_{\rm CR}/n_{\rm CR}$ of the CR population. For an assumed power-law spectrum with steep spectral index α at high CR momenta, these two quantities are completely determined by specifying the power-law normalization constant C and the CR low-momentum cutoff q. No high-momentum cutoff of the spectrum is considered, since for a sufficiently steep spectrum ($\alpha > 2$), the high-energy range is dynamically unimportant. The dynamics is dominated by particles with momenta closest to $m_{\rm p} c$ (the particles at the lower cutoff, or around $m_{\rm p} c$, whichever is larger).

3. A momentum power-law CR spectrum with spectral index α is assumed. This is not only consistent with the observation of Galactic CRs ($\alpha \approx 2.75$) but also predicted by typical CR acceleration and diffusion models, which usually give momentum power-law spectra (see Schlickeiser 2002, for a review).

4. The CR spectral index α is assumed to be the same everywhere. This suppresses several typical CR effects like spectral steepening due to transport effects, or spectral flattening due to fresh particle injection. However, these effects are not believed to be essential for for the global dynamics of the ISM to first order, justifying our simplification. However, some effects can still be roughly captured by our description.[1]

9.1.3. Captured Physics

The framework is set up to include a number of essential physical processes of a CR gas like particle acceleration, diffusion, and particle interactions. This should allow to study the impact of a variety of physical processes on galaxies, clusters of galaxies, and the large scale intergalactic medium, e.g.:

1. hydrodynamical effects of CRs

2. CR injection by diffusive shock acceleration

3. in-situ re-acceleration by plasma waves

4. non-local feedback from CR injection due to CR diffusion

5. CR modified shock structures

6. heating of cold gas by CRs

7. CR driven galactic winds

8. Parker instabilities of spiral galaxy disks

---

[1]Using momentum conservation, the formalisms to be presented in this chapter can be extended to account for a variable spectral index.

9. morphology of gamma ray emission

10. morphology of radio emission due to secondary electrons

9.1.4. Structure

The basic formalism is introduced in Sect. 9.2, in which the approximative description of the CR gas is introduced and its adiabatic evolution described. Non-adiabatic processes are discussed in Sect. 9.3: CR injection via shocks of supernova remnants (Sect. 9.3.1), and of structure formation shock waves (Sect. 9.3.2); CR spatial diffusion (Sect. 9.3.3); in-situ re-acceleration of CRs (Sect. 9.3.4); CR energy losses due to Coulomb interactions (Sect. 9.3.5), Bremsstrahlung (Sect. 9.3.6), and hadronic interactions with the background gas (Sect. 9.3.7), including the associated γ-radiation from the π^0-decays (Sect. 9.3.8) and the radio emission of the electrons and positrons resulting from $\pi^\pm$-decays (Sect. 9.3.9). Sect. 9.4 describes how the formalism can be included into a simulation code based on Smoothed-Particle-Hydrodynamics (SPH). Conclusions and outlook are given in Sect. 9.5.

9.2. Formalism

In this section, we develop the description of a CR population in a volume element, which is comoving with the background fluid. This Lagrangian perspective allows a strongly simplified description, since the advective transport processes are fully characterized by the description of the effect of adiabatic volume changes. We will introduce convenient adiabatic invariant variables, which therefore would be constant in time if non-adiabatic processes were neglected. Certainly, non-adiabatic processes have to be included, and we develop the formulae how the adiabatic invariant variables change accordingly. The chosen formalism is well suited to be implemented in numerical simulations. In Sect. 9.4, we explain how a SPH code has to be modified to include our CR description.

Since we only consider CR protons, which are at least in our Galaxy the dominant CR species, it is convenient to introduce the dimensionless momentum $p = P_p/(m_p c)$. The differential particle momentum spectrum per volume element is assumed to be a single power-law above the minimum momentum q:

$$f(p) = \frac{\mathrm{d}N}{\mathrm{d}p\,\mathrm{d}V} = C\,p^{-\alpha}\,\theta(p-q). \tag{9.1}$$

$\theta(x)$ denotes the Heaviside step function. Note, that we use an effective one-dimensional distribution function $f(p) \equiv 4\pi p^2 f^{(3)}(p)$. The differential CR spectrum can vary spatially and temporally (although for brevity we suppress this in our notation) through the spatial dependence of the normalization $C = C(\boldsymbol{x}, t)$ and the cutoff $q = q(\boldsymbol{x}, t)$. α is assumed to be constant in space and time.

Adiabatic compression or expansion leaves the phase-space density of the CR population invariant, leading to a momentum shift according to $p \to p' = (\rho/\rho_0)^{1/3} p$ for a change in density from ρ_0 to ρ. Since this is fully reversible, it is useful to introduce the invariant cutoff and normalization q_0 and C_0 which describe the CR population via Eqn. (9.1) if the ISM is adiabatically compressed or expanded relative to the reference density ρ_0. The actual parameter are then given by

$$q(\rho) = (\rho/\rho_0)^{\frac{1}{3}}\,q_0 \quad \text{and} \quad C(\rho) = (\rho/\rho_0)^{\frac{\alpha+2}{3}}\,C_0. \tag{9.2}$$

These variables are a suitable choice to be used in a Lagrangian description of the ISM.

The CR number density is

$$n_{\mathrm{CR}} = \int_0^\infty \mathrm{d}p\,f(p) = \frac{C\,q^{1-\alpha}}{\alpha-1} = \frac{C_0\,q_0^{1-\alpha}}{\alpha-1}\,\frac{\rho}{\rho_0}, \tag{9.3}$$

provided $\alpha > 1$. The kinetic energy density of the CR population is

$$\varepsilon_{\mathrm{CR}} = \int_0^\infty \mathrm{d}p\,f(p)\,T_p(p) = \frac{C\,m_p\,c^2}{\alpha-1}\left[\frac{1}{2}\,\mathcal{B}_{\frac{1}{1+q^2}}\left(\frac{\alpha-2}{2},\frac{3-\alpha}{2}\right) + q^{1-\alpha}\left(\sqrt{1+q^2}-1\right)\right], \tag{9.4}$$

where $T_p(p) = (\sqrt{1+p^2}-1)\,m_p\,c^2$ is the kinetic energy of a proton with momentum p, $\mathcal{B}_x(a,b)$ denotes the incomplete Beta-function, and $\alpha > 2$ is assumed. The average CR kinetic energy $T_{\mathrm{CR}} = \varepsilon_{\mathrm{CR}}/n_{\mathrm{CR}}$ is therefore

$$T_{\mathrm{CR}} = \left[\frac{q^{\alpha-1}}{2}\,\mathcal{B}_{\frac{1}{1+q^2}}\left(\frac{\alpha-2}{2},\frac{3-\alpha}{2}\right) + \sqrt{1+q^2}-1\right]m_p\,c^2. \tag{9.5}$$
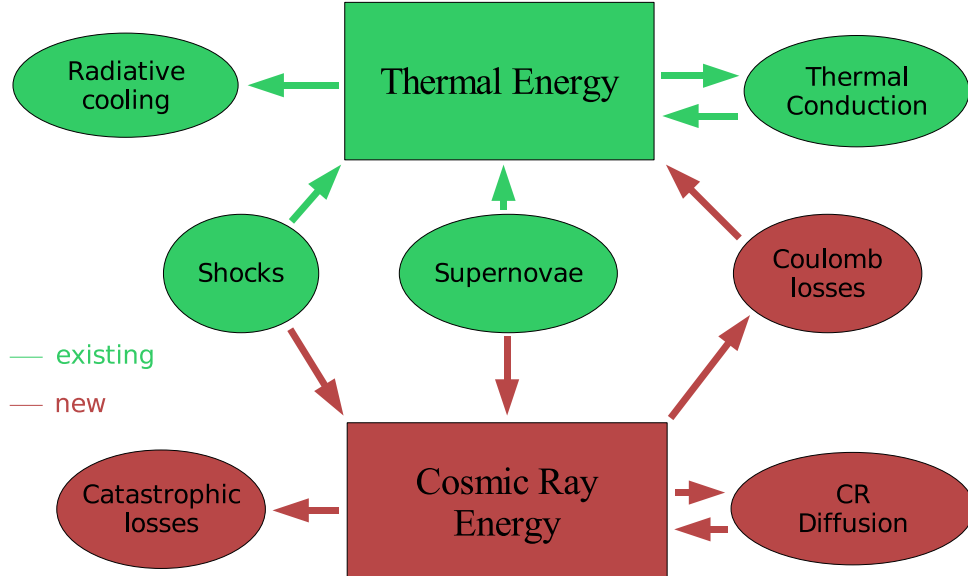
119

Figure 9.1.: Schematic view of the interplay of thermal and non-adiabatic CR processes that govern the hydrodynamics. The processes on the left-hand side are cooling processes that simultaneously shed light on the respective component. In the case of CRs, the relevant observables are radio synchrotron and inverse Compton radiation by secondary electrons and pion decay induced γ-ray emission.

The CR pressure is

$$P_{\mathrm{CR}} = \frac{m_{\mathrm{p}} c^2}{3} \int_0^\infty \mathrm{d}p \, f(p) \beta \, p = \frac{C \, m_{\mathrm{p}} c^2}{6} \, \mathcal{B}_{\frac{1}{1+q^2}}\left(\frac{\alpha-2}{2}, \frac{3-\alpha}{2}\right), \tag{9.6}$$

where $\beta := v/c = p/\sqrt{1+p^2}$ is the dimensionless velocity of the CR particle. Note, that for $2 < \alpha < 3$ the kinetic energy density and pressure of the CR populations are well defined for the limit $q \to 0$, although the total CR number density diverges.

The adiabatic exponent of the CR population is defined by

$$\gamma_{\mathrm{CR}} \equiv \left.\frac{\mathrm{d} \log P_{\mathrm{CR}}}{\mathrm{d} \log \rho}\right|_S, \tag{9.7}$$

while the derivative has to be taken at constant entropy S. Using Eqns. (9.2) and (9.6), we obtain for the CR adiabatic exponent

$$\gamma_{\mathrm{CR}} = \frac{\rho}{P_{\mathrm{CR}}} \left(\frac{\partial P_{\mathrm{CR}}}{\partial C} \frac{\partial C}{\partial \rho} + \frac{\partial P_{\mathrm{CR}}}{\partial q} \frac{\partial q}{\partial \rho}\right) = \frac{\alpha+2}{3} - \frac{2}{3} q^{2-\alpha} \beta(q) \left[\mathcal{B}_{\frac{1}{1+q^2}}\left(\frac{\alpha-2}{2}, \frac{3-\alpha}{2}\right)\right]^{-1}. \tag{9.8}$$

Note that in contrast to the usual adiabatic exponent, the CR adiabatic exponent is time dependent due to its dependence on the lower cutoff of the CR population, q. Considering a mixture of thermal and CR gas, it is appropriate to define an effective adiabatic index by

$$\gamma_{\mathrm{eff}} \equiv \left.\frac{\mathrm{d} \log(P_{\mathrm{th}} + P_{\mathrm{CR}})}{\mathrm{d} \log \rho}\right|_S = \frac{\gamma_{\mathrm{th}} P_{\mathrm{th}} + \gamma_{\mathrm{CR}} P_{\mathrm{CR}}}{P_{\mathrm{th}} + P_{\mathrm{CR}}}. \tag{9.9}$$

9.3. Non-adiabatic processes

The spectrum of a CR population within a volume is shaped by various physical processes, such as particle injection and escape, continuous and catastrophic energy losses, and re-acceleration. Although all these processes leave

their characteristic signatures in the CR spectrum, we have to describe their effects in terms of our two dynamical variables C and q (or C_0 and q_0). In order to resemble the key features of the real CR dynamics using our simplified description, we have to make the proper choice how to modify our variables by the different processes. The guiding lines are the energy and particle number conservation.

Imagine a non-adiabatic process leading to a change dn_{CR} in the number density and $d\varepsilon_{CR}$ in the energy density of the particles during an infinitesimal time interval dt. This would imply changes in (C, q) which are given by

$$\begin{pmatrix} dC \\ dq \end{pmatrix} = \begin{pmatrix} \partial C/\partial n_{CR} & \partial C/\partial \varepsilon_{CR} \\ \partial q/\partial n_{CR} & \partial q/\partial \varepsilon_{CR} \end{pmatrix} \begin{pmatrix} dn_{CR} \\ d\varepsilon_{CR} \end{pmatrix}. \tag{9.10}$$

Using the definitions in Eqns. (9.3) and (9.4) this can be evaluated to

$$dC = C \frac{d\varepsilon_{CR} - T_p(q)\, dn_{CR}}{\varepsilon_{CR} - T_p(q)\, n_{CR}} \tag{9.11}$$

$$dq = \frac{q}{\alpha - 1} \frac{d\varepsilon_{CR} - T_{CR}\, dn_{CR}}{\varepsilon_{CR} - T_p(q)\, n_{CR}}. \tag{9.12}$$

These relations are reasonable which can also be demonstrated by the following thought experiments: if a process increases ε_{CR} and n_{CR} simultaneously by the same factor $1 + \delta$, so that $d\varepsilon_{CR}/\varepsilon_{CR} = dn_{CR}/n_{CR} = \delta$, one gets only a change in the normalization ($dC = \delta C$), but not in the cutoff ($dq = 0$), as it should be. If one adds an infinitesimal amount of particles dn_{CR} with exactly the kinetic energy of the cutoff $T_p(q)$, so that $d\varepsilon_{CR} = T_p(q)\, dn_{CR}$, the normalization is unchanged ($dC = 0$), but the cutoff is lowered ($dq = -q\, dn_{CR}/((\alpha - 1)\, n_{CR}) \Rightarrow n_{CR} \propto q^{1-\alpha}$), again as it should be.

The adiabatically invariant variables change according to

$$dC_0 = \left(\frac{\rho}{\rho_0}\right)^{-\frac{\alpha+2}{3}} dC = C_0 \frac{d\varepsilon_{CR} - T_p(q)\, dn_{CR}}{\varepsilon_{CR} - T_p(q)\, n_{CR}}, \tag{9.13}$$

$$dq_0 = \left(\frac{\rho}{\rho_0}\right)^{-\frac{1}{3}} dq = \frac{q_0}{\alpha - 1} \frac{d\varepsilon_{CR} - T_{CR}\, dn_{CR}}{\varepsilon_{CR} - T_p(q)\, n_{CR}}, \tag{9.14}$$

where we used for convenience a notation which is mixed in the variant and invariant variables. Ways to numerically implement the evolutions of C_0 and q_0 are discussed in Appendix 9.4.4.

9.3.1. CR injection by supernovae

Shock waves in supernova remnants are believed to be the most dominant CR injection mechanism in the galactic context. A significant fraction $\zeta_{SN} \sim 0.1 - 0.3$ of the kinetic energy of a supernova may end up in the CR population. Therefore we set $(d\varepsilon_{CR}/dt)_{SN} = \zeta_{SN}\, d\varepsilon_{SN}/dt$ and $(d\varepsilon_{th}/dt)_{SN} = (1 - \zeta_{SN})\, d\varepsilon_{SN}/dt$, where $d\varepsilon_{SN}/dt$ is the SN energy release rate per volume. The increase in CR number density is given by $(dn_{CR}/dt)_{SN} = (d\varepsilon_{CR}/dt)_{SN}/T_{CR}^{inj}$, where

$$T_{CR}^{inj} = m_p\, c^2 \left[\frac{q_{inj}^{\alpha_{inj}-1}}{2}\, \mathcal{B}_{\frac{1}{1+q^2}}\left(\frac{\alpha-2}{2}, \frac{3-\alpha}{2} \right) + \sqrt{1 + q_{inj}^2} - 1 \right] \tag{9.15}$$

is the average kinetic energy of an injection power-law spectrum with spectral index α_{inj} and lower momentum cutoff q_{inj}. A plausible value for the injection spectral index is $\alpha_{inj} = 2.4$. The low-momentum cutoff can be set to $q_{inj} \sim \sqrt{kT/(m_p\, c^2)}$ since the power-law spectrum resulting from shock acceleration reaches down to the thermal population with temperature kT. However, in numerical practice it may be more economical to use some higher value for q_{inj} since in many circumstances Coulomb losses will rapidly remove the lower energy part of the CR spectrum so that the energy of these CRs is transfered to the thermal gas shortly after injection. A slight re-calibration of ζ_{SN} can take this into account, so that a numerical code does not have to follow the appearance of a temporarily existing, low energy, super-thermal CR population. A criteria to find an adequate q_{inj} is given by the requirement that the Coulomb-loss timescale $\tau_C(q_{inj}) = |T_p(q_{inj})/(dT_p(q_{inj})/dt)_C|$ (see Eqn. (9.48)) of the particles near the injection cutoff should be on the order of the simulation time-step.

9.3.2. CR shock acceleration

In this section, we focus on CR acceleration processes at gas accretion and galaxy merger shock waves in the framework of *diffusive shock acceleration* and modify the description of Miniati (2001). The shock surface separates two regions: the *upstream regime* defines the region in front of the shock which is causally unconnected for super sonic shock waves whereas the *downstream regime* defines the wake of the shock wave. The shock front itself is the region in which the mean plasma velocity changes rapidly on small scales given by plasma physical processes. Seen from the rest frame of the shock, particles are impinging on the shock surface at a rate per unit shock surface $\rho_2 v_2 = \rho_1 v_1$. Here v_1 and v_2 indicate the plasma velocities (relative to the shock's rest frame) in the upstream and downstream regime of the shock, respectively. The mass densities in the respective shock regime are denoted by ρ_1 and ρ_2.

We assume that after passing though the shock front most of the gas thermalizes to a Maxwell-Boltzmann distribution with characteristic post-shock temperature T_2:

$$f_{\text{th2}}(p) = 4\pi n_{\text{th}} \left(\frac{m_{\text{p}} c^2}{2\pi \, kT_2} \right)^{3/2} p^2 \exp\left(-\frac{m_{\text{p}} c^2 \, p^2}{2 \, kT_2} \right), \qquad (9.16)$$

where the number density of particles of the thermal distribution in the downstream regime, $n_{\text{th}} = n_2$, as well as T_2 can be inferred by means of the mass, momentum, and energy conservation laws at the shock surface for a gas composed of CRs and thermal constituents. For cosmological applications, we have to consider the primordial composition of the cosmological fluid, i.e. we replace the proton mass m_{p} by the mean particle mass $\bar{\mu}$:

$$m_{\text{p}} \to \bar{\mu} = \frac{4 m_{\text{p}}}{3 X_{\text{H}} + 1 + X_{\text{ion}}}, \qquad (9.17)$$

where the hydrogen mass-fraction of the baryonic matter is denoted by $X_{\text{H}} = 0.76$ and the ionization grade is given by X_{ion}.

Chapter 10 describes the formalism for instantaneously and self-consistently inferring the shock strength and all other quantities in the downstream regime of the shock within the framework of SPH simulations. Supposing that a fraction of these particles experiences stochastic diffusive shock acceleration by diffusing back and forth over the shock front, the test particle theory of diffusive shock acceleration predicts a resulting CR power-law distribution in momentum space. Within our model, this CR injection process can be treated instantaneously. For a particle in the downstream region of the shock to return upstream it is necessary to meet two requirements: the particle's effective velocity component parallel to the shock normal has to be larger than the velocity of the shock wave and its energy has to be large enough to escape the "trapping" process by Alfvén waves being generated in the downstream turbulence (Malkov & Völk 1995, Malkov & Völk 1998). Thus, only particles of the high-energy tail of the distribution are able to return to the upstream shock regime in order to become accelerated. The complicated detailed physical processes of the specific underlying acceleration mechanism are conveniently compressed into a few parameters (Jones & Kang 1993, Berezhko et al. 1994, Kang & Jones 1995), one of which defines the momentum threshold for the particles of the thermal distribution to be accelerated,

$$q_{\text{inj}} = x_{\text{inj}} p_{\text{th}} = x_{\text{inj}} \sqrt{\frac{2 \, kT_2}{m_{\text{p}} c^2}}. \qquad (9.18)$$

Since Coulomb losses efficiently modify the low energy part of the injected CR spectrum, we propose to follow the recipe presented at the end of Sect. 9.3.1, i.e. increasing the low energy spectral break without changing the normalization of the CR spectrum.

In the linear regime of CR acceleration, the thermal distribution joins in a smooth manner into the resulting CR power-law distribution at q_{inj} so that x_{inj} represents the only parameter in our diffusive shock acceleration model,

$$f_{\text{CR,lin}}(p) = X_{\text{ion}} f_{\text{th}}(q_{\text{inj}}) \left(\frac{p}{q_{\text{inj}}} \right)^{-\alpha_{\text{inj}}} \theta(p - q_{\text{inj}}). \qquad (9.19)$$

Fixing the normalization of the injected CR spectrum by such a continuity condition automatically determines C_{inj} which depends on the second adiabatic invariant. The slope of the injected CR spectrum is given by

$$\alpha_{\text{inj}} = \frac{r + 2}{r - 1}, \quad \text{where} \quad r = \frac{\rho_2}{\rho_1} = \frac{v_1}{v_2} \qquad (9.20)$$

denotes the shock compression ratio (Bell 1978a,b, Drury 1983a). In the linear regime, the number density of injected CR particles is given by

$$\Delta n_{\text{CR,lin}} = \int_0^\infty \mathrm{d}p \, f_{\text{CR,lin}}(p) = X_{\text{ion}} f_{\text{th}}(q_{\text{inj}}) \frac{q_{\text{inj}}}{\alpha_{\text{inj}} - 1}. \tag{9.21}$$

This enables us to infer the particle injection efficiency which is a measure of the fraction of downstream thermal gas particles which experience diffusive shock acceleration,

$$\eta_{\text{CR,lin}} \equiv \frac{\Delta n_{\text{CR,lin}}}{n_{\text{th}}} = X_{\text{ion}} \frac{4}{\sqrt{\pi}} \frac{x_{\text{inj}}^3}{\alpha_{\text{inj}} - 1} \, e^{-x_{\text{inj}}^2}. \tag{9.22}$$

The particle injection efficiency is independent of the downstream post-shock temperature T_2. These considerations allows one to infer the dynamically relevant injected CR energy density in the linear regime:

$$\Delta \varepsilon_{\text{CR,lin}} = \eta_{\text{CR,lin}} T_{\text{CR}}(\alpha_{\text{inj}}, q_{\text{inj}}) \, n_{\text{th}}(T_2). \tag{9.23}$$

In our description, the CR energy injection efficiency in the linear regime is defined to be the energy density ratio of freshly injected CRs to the total dissipated energy density in the downstream regime,

$$\zeta_{\text{lin}} = \frac{\Delta \varepsilon_{\text{CR,lin}}}{\Delta \varepsilon_{\text{diss}}}, \quad \text{where} \quad \Delta \varepsilon_{\text{diss}} = \varepsilon_{\text{th2}} - \varepsilon_{\text{th1}} r^\gamma. \tag{9.24}$$

The dissipated energy density in the downstream regime, $\Delta \varepsilon_{\text{diss}}$, is given by the difference of the thermal energy densities in the pre- and post-shock regime while correcting for the contribution of the adiabatic part of the energy increase due to the compression of the gas over the shock.

In order not to violate energy conservation as well as conditions of the linear theory of diffusive shock acceleration, ζ_{lin} has to obey a boundary condition which ensures that the dynamical pressure exerted by CRs is smaller than the ram pressure of the flow $\rho_1 v_1^2$ yielding

$$\frac{P_{\text{CR}}}{\rho_1 v_1^2} = \frac{(\alpha - 1) \, c^2 \, \eta_{\text{CR,lin}}}{6 \, v_1 v_2} q_{\text{inj}}^{\alpha-1} \mathcal{B}_{\frac{1}{1+q_{\text{inj}}^2}} \left(\frac{\alpha - 2}{2}, \frac{3 - \alpha}{2} \right) < 1, \tag{9.25}$$

where $\alpha = \alpha_{\text{inj}}$. For practical purposes, which will be encountered for instance in cosmological SPH simulations, this boundary condition can be strongly simplified. Thus, we propose the following modification of the CR energy injection efficiency in order to account for the saturation effect at high values of the Mach number:

$$\zeta_{\text{inj}} = \left[1 - \exp\left(-\frac{\zeta_{\text{lin}}}{\zeta_{\text{max}}} \right) \right] \zeta_{\text{max}}. \tag{9.26}$$

Numerical studies of shock acceleration suggest a value of $\zeta_{\text{max}} \simeq 0.5$ for the limiting case of the CR energy injection efficiency (Ryu et al. 2003). These considerations allows one to infer the injected CR energy density in terms of the energy injection efficiency of diffusive shock acceleration processes,

$$\Delta \varepsilon_{\text{CR,inj}} = \zeta_{\text{inj}} \Delta \varepsilon_{\text{diss}}. \tag{9.27}$$

The average kinetic energy of $T_{\text{CR}}(\alpha_{\text{inj}}, q_{\text{inj}})$ of an injection power-law spectrum with CR spectral index α_{inj} is given by Eqn. (9.15), however with the lower CR momentum cutoff of Eqn. (9.18). In combination with the slope α_{inj}, the value of x_{inj} regulates the amount of kinetic energy which is transferred to the CRs. Theoretical studies of shock acceleration at galactic supernova remnants suggest a range of $x_{\text{inj}} \simeq 3.3$ to 3.6 implying an particle injection efficiency of $\eta_{\text{CR,lin}} \simeq 10^{-4}$ to 10^{-3} (Drury et al. 1989, Jones & Kang 1993, Berezhko et al. 1994, Kang & Jones 1995, Malkov & Völk 1995).

Fig. 9.2 shows the CR energy injection efficiency ζ_{inj} as a function of spectral index α_{inj}. It can be clearly seen, that our simplified model for the diffusive shock acceleration fails in the limit of weak shocks and over-predicts the injection efficiency. Especially in this regime, Coulomb losses have to be taken into account which remove the low-energetic part of the injected CR spectrum efficiently on a short timescale (cf. Sect. 9.3.5). This gives rise to an effective CR energy efficiency ζ_{Coulomb} which is obtained by keeping the normalization of the CR spectrum while
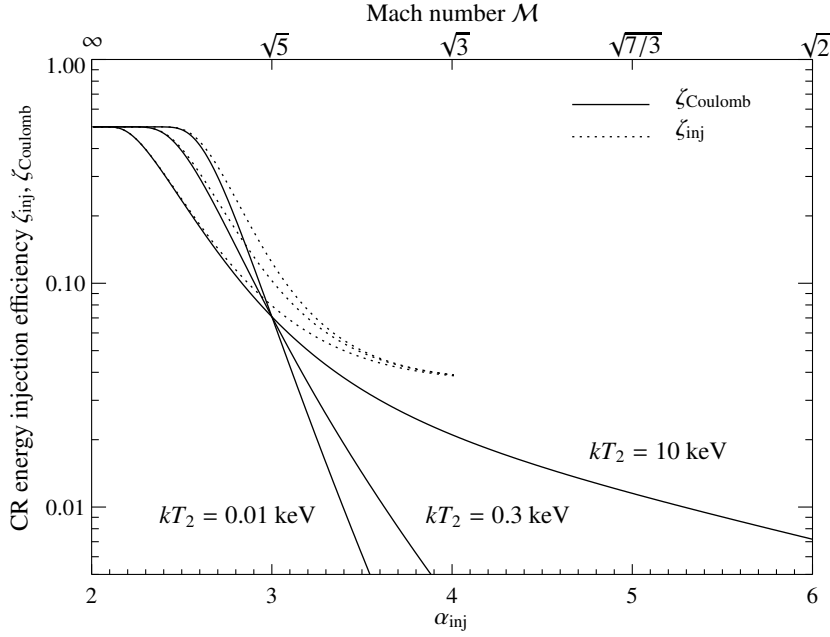
Figure 9.2.: CR energy injection efficiency for the diffusive shock acceleration process. Shown is the CR energy injection efficiency ζ_{inj} (dotted) for the three post-shock temperatures $kT_2/\text{keV} = 0.01, 0.3$, and 10. An effective CR energy efficiency $\zeta_{Coulomb}$ (solid) is obtained by considering Coulomb losses which remove the low-energetic part of the injected CR spectrum on a short timescale. We adopted the following values for our model parameters, $x_{inj} = 3.5$, $\zeta_{max} = 0.5$, and $q_{Coulomb} = 0.03$.

simultaneously increasing the cutoff: $q_{inj} \rightarrow q_{Coulomb}$. Thus, in the linear regime the effectively injected CR energy density is given by

$$\Delta\varepsilon_{CR,lin,Coulomb} = \Delta n_{CR,lin} T_{CR}(\alpha_{inj}, q_{Coulomb}) \left(\frac{q_{Coulomb}}{q_{inj}}\right)^{1-\alpha_{inj}}. \tag{9.28}$$

The effective CR energy efficiency $\zeta_{Coulomb}$ in the linear regime is obtained by analogy to the previous considerations,

$$\zeta_{lin,Coulomb} = \frac{\Delta\varepsilon_{CR,lin,Coulomb}}{\Delta\varepsilon_{diss}}. \tag{9.29}$$

Following our suggestion for saturation effects of the shock acceleration given in Eqn. (9.26), we can obtain the effectively injected CR energy density in the non-linear regime $\Delta\varepsilon_{CR,inj,Coulomb}$. Assuming a dominant thermal gas component, the spectral index α_{inj} can be translated into the Mach number of the shock, $\mathcal{M}_1$, depending on the adiabatic index of the thermal gas γ,

$$\mathcal{M}_1 = \sqrt{\frac{2(2 + \alpha_{inj})}{1 + 2\alpha_{inj} - 3\gamma}}. \tag{9.30}$$

For a pure thermal gas, the spectral index $\alpha_{inj} = 2$ formally corresponds to an infinite Mach number.

9.3.3. CR diffusion

The ubiquitous cosmic magnetic fields prevent charged relativistic particles to travel macroscopic distances with their intrinsic velocity close to the speed of light. Instead, the particles gyrate around, and travel slowly along magnetic field lines. Occasionally, they get scattered on magnetic irregularities. On macroscopic scales, the transport can often be described as a diffusion process if the gyro-radius can be regarded to be small. The diffusion is highly anisotropic with respect to the direction of the local magnetic field, characterized by a parallel $\kappa_\parallel$ and a perpendicular $\kappa_\perp$ diffusion coefficient. Both are usually functions of location and particle momentum.

Microscopically, the scattering of the CR on magnetic irregularities of MHD waves slows down the parallel transport, but allows the perpendicular transport since it de-places the gyro-center of the CRs. Therefore, both microscopic diffusion coefficients depend on the scattering frequency ν_{scatt}, but with inverse proportionalities: $\kappa_\parallel \propto \nu_{\text{scatt}}^{-1}$ and $\kappa_\perp \propto \nu_{\text{scatt}}$. Particles are best scattered by MHD waves with a wavelength comparable to the CR's gyro-radii, which itself depends on the particle momentum. The various wavelength bands are differently strongly populated. Therefore, the scattering frequency is usually a function of the particle momentum. The exact functionality depends on the small-scale plasma turbulence spectrum, on scales comparable to the CR gyro-radii.

In this picture (e.g. see Bieber & Matthaeus 1997), the diffusion coefficients can be written as

$$\kappa_\parallel = \frac{\kappa_{\text{Bohm}}}{\varepsilon} \tag{9.31}$$

$$\kappa_\perp = \frac{\varepsilon}{1 + \varepsilon^2}\, \kappa_{\text{Bohm}} \,. \tag{9.32}$$

Here, $\varepsilon \ll 1$ is the ratio of scattering frequency ν_{scatt} to the gyro-frequency $\Omega = v/r_g$, and $\kappa_{\text{Bohm}} = v\, r_g/3 = v\, p\, m_p\, c^2/(3\, Z\, e\, B)$ is the Bohm diffusion coefficient. In most circumstances, $\kappa_\perp$ will be many orders of magnitude smaller than $\kappa_\parallel$. Thus, from a microscopic point of view CR cross field diffusion seems to be nearly impossible.

Macroscopically, the cross-field particle transport is much faster than the microscopic diffusion coefficient suggests. The reason for this is that any small displacement from the initial field line, which a CR achieved by a perpendicular microscopic diffusion step, can strongly (often exponentially) be amplified if the CR travels along its new field line (Rechester & Rosenbluth 1978, Duffy et al. 1995). This is caused by diverging magnetic field lines due to a random walk in turbulent environment. This effect should always be present to some level even if a large-scale mean field dominates the general magnetic field orientation. The resulting effective diffusion coefficient $\bar{\kappa}_\perp$ is difficult to estimate from first principles (see the discussion in Enßlin 2003), but its dependence on the particle momentum is the same as that of the parallel diffusion coefficient, due to the dominant role the parallel diffusion plays in the effective cross field transport. We therefore assume

$$\bar{\kappa}_\perp(p) = \delta_\perp\, \kappa_\parallel(p) \tag{9.33}$$

with typically $\delta_\perp \sim 10^{-4} - 10^{-2}$ (Giacalone & Jokipii 1999, Enßlin 2003), but see Narayan & Medvedev (2001) for arguments of a larger $\delta_\perp \sim 10^{-1}$. In order to be flexible about the underlying MHD turbulence which fixes the momentum dependency of $\kappa_\parallel$ we assume

$$\bar{\kappa}_\parallel(p) = \kappa_\parallel(p) = \kappa_0\, \beta\, p^{d_p}\, \gamma^{d_\gamma} = \kappa_0\, p^{d_p+1}\, \gamma^{d_\gamma-1} \,. \tag{9.34}$$

The velocity factor β expresses the reduction of diffusion speed for non-relativistic particles. For a power-law turbulence spectrum $E(k)\, dk \propto k^{-\alpha_{\text{turb}}}\, dk$ one obtains $d_p = 2 - \alpha_{\text{turb}}$ and $d_\gamma = 0$, e.g. $d_p = \frac{1}{3}$ for a Kolmogorov-type spectrum. We have included the parameter d_γ in order to allow for low-energy deviations from a pure momentum power-law dependence. Such deviations can e.g. be caused by modifications of the turbulence spectrum due to MHD-wave-damping by the low-energy bulk of the CR population with small gyro-radii.

The equation describing the evolution of the CR spectrum $f(x, p, t)$ due to diffusion is

$$\left(\frac{\partial f}{\partial t}\right)_{\text{diff}} = \frac{\partial}{\partial x_i} \kappa_{ij} \frac{\partial f}{\partial x_j} \,, \tag{9.35}$$

where the diffusion tensor

$$\kappa_{ij}(p) = \kappa_\parallel(p)\, [b_i\, b_j + \delta_\perp\, (\delta_{ij} - b_i\, b_j)] = \tilde{\kappa}_{ij}\, p^{d_p+1}\, \gamma^{d_\gamma-1} \,. \tag{9.36}$$

is anisotropic with respect to the local main magnetic field direction $b(x) = B(x)/B(x)$. Since we are interested in a simplified description, we have to translate Eqn. (9.35) into changes of CR number and energy density. Integrating Eqn. (9.35) over p leads to an equation governing the change in CR number density due to diffusion:

$$\left(\frac{\partial n_{\text{CR}}}{\partial t}\right)_{\text{diff}} = \frac{\partial}{\partial x_i} \tilde{\kappa}_{ij} \frac{\partial}{\partial x_j} \left\{ \frac{C}{\alpha - 2 - d_p} \left[q^{-\alpha+2+d_p} \left(1 + q^2\right)^{-\frac{1-d_\gamma}{2}} \right. \right.$$
$$\left. \left. - \frac{1 - d_\gamma}{2}\, \mathcal{B}_{\frac{1}{1+q^2}} \left(\frac{\alpha - 1 - d_p - d_\gamma}{2}, \frac{4 + d_p - \alpha}{2} \right) \right] \right\} \,. \tag{9.37}$$

This can only lead to reasonable results if the condition $\alpha > 1 + d_p + d_\gamma$ is fulfilled. For a Kolmogorov-turbulence diffusion coefficient ($d_p = \frac{1}{3}$, $d_\gamma = 0$), this translates into $\alpha > 1.33$.

One could assume that the transported energy is simply $(d\varepsilon_{CR})_{diff} = T_{CR} \, (dn_{CR})_{diff}$. However, this ansatz would ignore that the more energetic particles diffuse faster implying that the effective CR energy diffusion is more rapid than the CR number diffusion. In order to model this, we multiply Eqn. (9.35) by $T_p(p)$ and integrate over p. This leads to

$$
\begin{aligned}
\left(\frac{\partial \varepsilon_{CR}}{\partial t}\right)_{diff} &= \frac{\partial}{\partial x_i} \tilde{\kappa}_{ij} \frac{\partial}{\partial x_j} \left\{ \frac{C \, m_p \, c^2}{\alpha - 2 - d_p} \left[q^{-\alpha+2+d_p} \left(\left(1 + q^2\right)^{\frac{d_\gamma}{2}} - \left(1 + q^2\right)^{\frac{d_\gamma-1}{2}} \right) \right.\right. \\
&+ \frac{1 - d_\gamma}{2} \, \mathcal{B}_{\frac{1}{1+q^2}} \left(\frac{\alpha - 1 - d_p - d_\gamma}{2}, \frac{4 + d_p - \alpha}{2} \right) \\
&+ \left.\left. \frac{d_\gamma}{2} \, \mathcal{B}_{\frac{1}{1+q^2}} \left(\frac{\alpha - 2 - d_p - d_\gamma}{2}, \frac{4 + d_p - \alpha}{2} \right) \right]\right\}.
\end{aligned}
\tag{9.38}
$$

This equation can only lead to reasonable results if the condition $\alpha > 2 + d_p + d_\gamma$ is fulfilled. For a Kolmogorov-turbulence diffusion coefficient ($d_p = \frac{1}{3}$, $d_\gamma = 0$), this translates into $\alpha > 2.33$.

9.3.4. CR in-situ re-acceleration

The diffusive propagation of CRs implies that CR particles scatter resonantly on plasma waves with wavelength comparable to their gyro-radii. Since these waves are propagating, the CRs exchange not only momentum, but also energy with the waves, leading to a re-acceleration of an existing cosmic ray population. Since the CR-number is not changed by this process, we can state:

$$
\left(\frac{\partial n_{CR}}{\partial t}\right)_{re-acc} = 0
\tag{9.39}
$$

The change in the CR energy can be derived from the according Fokker-Planck equation for the 3-dimensional momentum distribution function $f^{(3)}(p) = f(p)/(4\pi p^2)$ of an isotropic CR distribution:

$$
\left(\frac{\partial f^{(3)}(p)}{\partial t}\right)_{re-acc} = \frac{1}{p^2} \frac{\partial}{\partial p} \left(p^2 \, D_p \frac{\partial f^{(3)}}{\partial p} \right),
\tag{9.40}
$$

where D_p is the (pitch-angle averaged) momentum-space diffusion coefficient. D_p is a function of p, which we parameterize by

$$
D_p = D_0 \, p^{1-a_p} \, \gamma^{1-a_\gamma}.
\tag{9.41}
$$

Taking the appropriate moments of Eqn. (9.40) leads to evolution equation for the CR number density, Eqn. (9.39), and for the CR energy density,

$$
\left(\frac{\partial \varepsilon_{CR}}{\partial t}\right)_{re-acc} = C \, D_0 \, m_p c^2 (2 + \alpha) \left[\frac{1}{2} \mathcal{B}_{\frac{1}{1+q^2}} \left(\frac{\alpha + a_p + a_\gamma - 2}{2}, \frac{2 - \alpha - a_p}{2} \right) + \left(\sqrt{1 + q^2} - 1 \right) q^{\alpha - a_p} \left(1 + q^2\right)^{(1-a_\gamma)/2} \right],
\tag{9.42}
$$

which is valid for $\alpha > 2 - a_p - a_\gamma$.

The parameterization of the momentum diffusion coefficient is chosen to be similar to the one of the spatial diffusion coefficient because of a their related physical background: both are due to scattering on the same plasma waves. Quasi-linear calculations of the Fokker-Planck transport coefficient of charged particles interacting with plasma waves (see Schlickeiser 2002) demonstrate that both, the spatial- and the momentum-diffusion coefficient depend mainly on the pitch-angle diffusion coefficient $D_{\mu\mu} = D_{\mu\mu}(p, \mu)$, where $\mu = \cos\theta$ is the cosine of the pitch-angle θ:

$$
D_p = \frac{p^2 V_A^2}{v^2} \int_{-1}^{1} d\mu \, D_{\mu\mu}(p, \mu)
\tag{9.43}
$$

$$
\kappa_\| = \frac{v^2}{8} \int_{-1}^{1} d\mu \frac{(1 - \mu^2)^2}{D_{\mu\mu}(p, \mu)}
\tag{9.44}
$$

Here, V_A is the phase-velocity of the scattering plasma waves which are usually assumed to be Alfvén waves[2] with $V_A = B/\sqrt{4\pi\rho}$. In the relevant inertia ranges of the MHD-turbulence spectra, it is expected that the amplitude but not the composition of waves change with wavelength and therefore the pitch-angle diffusion coefficient should be separable in p and μ, e.g. $D_{\mu\mu}(p,\mu) = D_1(p)\,D_2(\mu)$. This allows to relate the two diffusion coefficients via:

$$D_p\,\kappa_{\parallel} = p^2\,V_A^2 X_2\,, \tag{9.45}$$

where X_2 is a constant of order unity, and is formally given by

$$X_2 = \frac{1}{8}\left(\int_{-1}^{1}\mathrm{d}\mu\,D_2(\mu)\right)\left(\int_{-1}^{1}\mathrm{d}\mu\,\frac{(1-\mu^2)^2}{D_2(\mu)}\right). \tag{9.46}$$

Therefore, in the framework of quasi-linear approximation, the parameters describing in-situ re-acceleration and diffusion are related via

$$a_p = d_p\,, \quad a_\gamma = d_\gamma\,, \quad \text{and} \quad D_0 = V_A^2 X_2/\kappa_0\,, \tag{9.47}$$

e.g. for a Kolmogorov-like spectrum of Alfvén waves $a_p = d_p = \frac{1}{3}$, $a_\gamma = d_\gamma = 0$, and $X_2 \sim O(1)$.

9.3.5. Coulomb losses

The energy loss of a proton by Coulomb losses in a plasma is given by Gould (1972):

$$-\left(\frac{\mathrm{d}T_p(p)}{\mathrm{d}t}\right)_C = \frac{4\,\pi\,e^4\,n_e}{m_e\,\beta\,c}\left[\ln\left(\frac{2m_e c^2\beta p}{\hbar\omega_{pl}}\right) - \frac{\beta^2}{2}\right] \tag{9.48}$$

Here, $\omega_{pl} = \sqrt{4\pi e^2 n_e/m_e}$ is the plasma frequency, and n_e is the number density of free electrons. We note, that in a neutral gas the Coulomb losses can approximatively be estimated with the same formulae, if n_e is taken to be the total electron number (free plus bound), although atomic charge shielding effects should lower the Coulomb losses somehow.

In order to obtain the Coulomb energy losses of the CR population, one has to integrate Eqn. (9.48) over the spectrum $f(p)$. This integration can certainly be performed numerically. For fast and efficient applications, an approximative analytical expression might be more practical. We derive such an expression by replacing the term $\beta\,p$ in the Coulomb logarithm with its mean value for the given spectrum, which can be written as $\langle\beta\,p\rangle = 3\,P_{CR}/(m_p\,c^2\,n_{CR})$.[3] The Coulomb energy losses are then

$$-\left(\frac{\mathrm{d}\varepsilon_{CR}}{\mathrm{d}t}\right)_C \approx \frac{2\pi C e^4 n_e}{m_e\,c}\left[\ln\left(\frac{2m_e c^2\,\langle\beta\,p\rangle}{\hbar\,\omega_{pl}}\right)\mathcal{B}_{\frac{1}{1+q^2}}\left(\frac{\alpha-1}{2}, -\frac{\alpha}{2}\right) - \frac{1}{2}\,\mathcal{B}_{\frac{1}{1+q^2}}\left(\frac{\alpha-1}{2}, -\frac{\alpha-2}{2}\right)\right] \tag{9.49}$$

Since Coulomb losses only affect the lower energy part of the spectrum and therefore should leave the normalization unaffected we propose to set $(\mathrm{d}n_{CR}/\mathrm{d}t)_C = (\mathrm{d}\varepsilon_{CR}/\mathrm{d}t)_C/T_p(q)$. This mimics the effect of Coulomb losses on a spectrum quiet well, since Coulomb losses remove the lowest energy particles most efficiently from the spectrum and moves them into the thermal pool. Since also their energy is thermalized, $(\mathrm{d}\varepsilon_{th}/\mathrm{d}t)_C = -(\mathrm{d}\varepsilon_{CR}/\mathrm{d}t)_C$ and $(\mathrm{d}n_p/\mathrm{d}t)_C = -(\mathrm{d}n_{CR}/\mathrm{d}t)_C$. The second equation (proton number conservation) can be neglected for convenience due to the smallness of the effect.

9.3.6. Bremsstrahlung losses

Bremsstrahlung energy losses of protons are usually negligible, since they are suppressed by a factor $m_e^2/m_p^2 \approx 3\cdot 10^{-7}$ compared to the usually also small electron bremsstrahlung losses. Therefore, we do not included bremsstrahlung energy losses of protons in our description.

---

[2]Also the stronger damped fast magneto-sonic waves are discussed as efficient accelerators due to their higher phase velocity (e.g. Eilek 1979, Cassano & Brunetti 2005).

[3]This leads to a slight overestimate of the energy losses. A slight underestimate results by setting $\langle\beta\,p\rangle \to q^2/\sqrt{1+q^2}$ in Eqn. 9.49. As long these two terms lead to similar loss rates our approximately treatment is a good description. Otherwise the integration has to be performed numerically.

9.3.7. Catastrophic losses

Another important process is the inelastic reaction of CR nuclei with atoms and molecules of interstellar and intergalactic matter. The CR protons interact hadronically with the ambient thermal gas and produce mainly neutral and charged pions, provided their momentum exceeds the kinematic threshold $q_{thr} m_p c^2 = 0.78$ GeV for the reaction. The neutral pions decay after a mean lifetime of 9×10^{-17} s into γ-rays while the charged pions decay into secondary electrons (and neutrinos):

$$
\begin{aligned}
\pi^\pm &\rightarrow \mu^\pm + \nu_\mu/\bar{\nu}_\mu \rightarrow e^\pm + \nu_e/\bar{\nu}_e + \nu_\mu + \bar{\nu}_\mu \\
\pi^0 &\rightarrow 2\gamma \, .
\end{aligned}
$$

Using hadronic interactions, only the CR population above the kinematic threshold q_{thr} is visible through its decay products in γ-ray and synchrotron emission. Because of baryon number conservation in strong and electro-weak interactions, we always end up with pions and two protons in this CR-proton hadronic interaction (the possibly produced neutron will decay after a mean lifetime of 886 s into a second proton). Thus, the CR number density is conserved, implying $dn_{CR}/dt = 0$.

To obtain a description of CR catastrophic energy losses, we start from the pion source function which describes the pion production rate of a single relativistic proton of total energy $E_p = \gamma m_p c^2$,

$$
s_\pi(E_\pi, E_p) \equiv \frac{dN}{dE_\pi dE_p dV dt} = c n_N \xi \bar{\sigma}_{pp} \delta(E_\pi - \langle E_\pi \rangle) \, \theta[p_p(E_p) - p_{thr}], \tag{9.50}
$$

where $\bar{\sigma}_{pp} \simeq 32$ mbarn is the total pion cross section on average and $n_N = n_e/(1 - \frac{1}{2} X_{He})$ denotes the target nucleon density in the ICM while assuming primordial element composition with $X_{He} = 0.24$, which holds approximately. Note, that this differential pion source function is an approximation with respect to the pion energy. Because we only use the integrated source function, this treatment is well justified. In Dermer's model (Dermer 1986a,b), which is motivated by accelerator experiments, the pion multiplicity is independent of energy, $\xi \simeq$ constant, yielding the mean pion energy,

$$
\langle E_\pi \rangle (E_p) = K_p \frac{T_p(p)}{\xi} = K_p \frac{E_p - m_p c^2}{\xi}, \tag{9.51}
$$

where $K_p \simeq 1/2$ denotes the inelasticity of the reaction in the limiting regime (Mannheim & Schlickeiser 1994).[4] Integrating the pion energy weighted source function over all pion energies E_π yields the energy loss of a single CR proton owing to pion production,

$$
-\left(\frac{dE_p}{dt}\right)_\pi = \int_0^{E_{\pi_{max}}} dE_\pi E_\pi \, s(E_\pi, E_p) = c n_N \xi \, \bar{\sigma}_{pp} K_p \, (E_p - m_p c^2) \, \theta(p_p - q_{thr}). \tag{9.52}
$$

Thus, the total energy loss of CRs is independent on the detailed mechanisms how the energy has been imparted on pions during hadronic interactions. The change in energy density of CRs because of catastrophic losses is given by

$$
-\left(\frac{d\varepsilon_{CR}}{dt}\right)_{cata} = \int_0^\infty dp \, f(p) \left(\frac{dE_p}{dt}\right)_\pi = c n_N \, \bar{\sigma}_{pp} K_p \, \varepsilon_{CR}[\max(q, q_{thr})], \tag{9.53}
$$

where ε_{CR} is given by Eqn. (9.4) in which the lower spectral break q has to be replace by $\max(q, q_{thr})$.

9.3.8. Gamma ray emission

An analytic formula describing the omnidirectional (i.e. integrated over 4π solid angle) differential γ-ray source function resulting from pion-decay of a power-law CR population is given in Pfrommer & Enßlin (2004a):

$$
s_\gamma(E_\gamma) \, dE_\gamma \, dV \simeq \frac{2^4 C}{3\alpha} \frac{\sigma_{pp} n_N}{m_p c} \left(\frac{m_p}{2 m_{\pi^0}}\right)^\alpha \left[\left(\frac{2E_\gamma}{m_{\pi^0} c^2}\right)^\delta + \left(\frac{2E_\gamma}{m_{\pi^0} c^2}\right)^{-\delta}\right]^{-\alpha/\delta} dE_\gamma \, dV. \tag{9.54}
$$

---

[4]On average, a leading nucleon and a pion jet leave the interaction site in direction of the incident protons diametrically and carrying the high longitudinal momenta owing to Lorentz contraction of the interacting nuclei in the center of mass system and Heisenberg's uncertainty relation (Nachtmann 1990).

The formalism also includes the detailed physical processes at the threshold of pion production like the velocity distribution of CRs, momentum dependent inelastic CR-proton cross section, and kaon decay channels. The shape parameter δ and the effective cross section σ_{pp} depend on the spectral index of the γ-ray spectrum α according to

$$\delta \quad \simeq \quad 0.14\,\alpha^{-1.6} + 0.44 \qquad \text{and} \tag{9.55}$$

$$\sigma_{pp} \quad \simeq \quad 32 \cdot \left(0.96 + e^{4.4 - 2.4\,\alpha}\right) \text{ mbarn.} \tag{9.56}$$

There is a detailed discussion in Pfrommer & Enßlin (2004a) how the γ-ray spectral index α_γ relates to the spectral index of the parent CR population α. In Dermer's model, the pion multiplicity is independent of energy yielding the relation $\alpha_\gamma = \alpha$ (Dermer 1986a,b).

The derivation of the pion-decay induced γ-ray source function implicitly assumed the kinematic threshold q_{thr} to be above the lower break of the CR spectrum q. This assumption is satisfied in the case of our Galaxy where a flattening of the CR spectrum occurs below the kinematic energy threshold $E_{thr} = 1.22$ GeV (Simpson 1983). If the inequality $q < q_{thr}$ is violated in the simulation for sufficiently long timescales, the resulting γ-ray emission maps have to be treated with caution: increasing the lower break q of the CR spectrum implies a lower resulting pion bump in the differential γ-ray source function around $m_{\pi^0}c^2/2 \simeq 67.5$ MeV.

Provided the CR population has a power-law spectrum, the integrated γ-ray source density λ_γ for pion decay induced γ-rays can be obtained by integrating the γ-ray source function $s_\gamma(E_\gamma)$ in Eqn. (9.54) over an energy interval yielding

$$\lambda_\gamma \quad = \quad \lambda_\gamma(E_1, E_2) = \int_{E_1}^{E_2} dE_\gamma\, s_\gamma(E_\gamma) = \frac{4\,C}{3\,\alpha\delta}\,\frac{m_{\pi^0}c\,\sigma_{pp}n_N}{m_p} \left(\frac{m_p}{2m_{\pi^0}}\right)^\alpha \left[\mathcal{B}_x\left(\frac{\alpha+1}{2\,\delta}, \frac{\alpha-1}{2\,\delta}\right)\right]_{x_1}^{x_2}, \tag{9.57}$$

$$x_i \quad = \quad \left[1 + \left(\frac{m_{\pi^0}c^2}{2\,E_i}\right)^{2\,\delta}\right]^{-1} \quad \text{for } i \in \{1, 2\}. \tag{9.58}$$

The γ-ray number flux $\mathcal{F}_\gamma$ is derived by means of volume integration over the emission region and correct accounting for the growth of the area of the emission sphere on which the photons are distributed:

$$\mathcal{F}_\gamma(E_1, E_2) = \frac{1+z}{4\pi\,D^2} \int dV\, \lambda_\gamma[(1+z)E_1, (1+z)E_2]. \tag{9.59}$$

Here D denotes the luminosity distance and the additional factors of $1 + z$ account for the cosmological redshift of the photons.

9.3.9. Hadronically induced synchrotron emission

This sections describes the hadronically induced radio synchrotron emission while employing the steady-state approximation for the cosmic ray electron (CRe) spectrum. This is only justified if the dynamical and diffusive timescales are long compared to the synchrotron timescale. Moreover, this section neglects possible re-acceleration processes of CRes like continuous in-situ acceleration via resonant pitch angle scattering by turbulent Alfvén waves as originally proposed by Jaffe (1977) as well as CRe injection by other processes.

Following for instance Dolag & Enßlin (2000) and Pfrommer & Enßlin (2004a), the steady-state CRe spectrum is governed by injection of secondaries and cooling processes so that it can be described by the continuity equation

$$\frac{\partial}{\partial E_e}\left(\dot{E}_e(E_e)f_e(E_e)\right) = s_e(E_e)\,. \tag{9.60}$$

For $\dot{E}_e(p) < 0$ this equation is solved by

$$f_e(E_e) = \frac{1}{|\dot{E}_e(E_e)|} \int_{E_e}^\infty dE'_e\, s_e(E'_e)\,. \tag{9.61}$$

For the energy range of interest, the cooling of the radio emitting CRes is dominated by synchrotron and inverse Compton losses:

$$-\dot{E}_e(E_e) = \frac{4\,\sigma_T\,c}{3\,m_e^2\,c^4}\left[\varepsilon_B + \varepsilon_{ph}\right] E_e^2\,, \tag{9.62}$$

where σ_T is the Thomson cross section, $\varepsilon_B = B^2/(8\pi)$ is the local magnetic field energy density, and $\varepsilon_{ph} = \varepsilon_{CMB} + \varepsilon_{stars}$ is the energy density of the cosmic microwave background (CMB) and starlight photon field. $\varepsilon_{CMB} = B_{CMB}^2/(8\pi)$ can be expressed by an equivalent field strength $B_{CMB} = 3.24\,(1+z)^2\,\mu G$. ε_{stars} has to be guessed, calculated from information of the star distribution, or ignored.

Assuming that the parent CRp population is represented by a power-law (9.1), the CRe population above a GeV is therefore described by a power-law spectrum

$$f_e(E_e) = \frac{C_e}{GeV}\left(\frac{E_e}{GeV}\right)^{-\alpha_e}, \tag{9.63}$$

$$\text{and} \quad C_e = \frac{16^{2-\alpha_e}}{\alpha_e - 2}\frac{\sigma_{pp}\, m_e^2\, c^4}{\sigma_T\, GeV}\frac{n_N C}{\varepsilon_B + \varepsilon_{ph}}\left(\frac{m_p c^2}{GeV}\right)^{\alpha-1}, \tag{9.64}$$

where the effective CR-proton cross section σ_{pp} is given by Eqn. (9.56).

The synchrotron emissivity j_ν at frequency ν and per steradian of such a CRe population (9.63), which is located in an isotropic distribution of magnetic fields (Eqn. (6.36) in Rybicki & Lightman 1979), is obtained after averaging over an isotropic distribution of electron pitch angles yielding

$$j_\nu = A_{E_{syn}}(\alpha_e)\, C_e \left[\frac{\varepsilon_B}{\varepsilon_{B_c}}\right]^{(\alpha_\nu+1)/2} \propto \varepsilon_{CRe}\, B^{\alpha_\nu+1}\, \nu^{-\alpha_\nu}, \tag{9.65}$$

$$B_c = \sqrt{8\pi\varepsilon_{B_c}} = \frac{2\pi m_e^3 c^5 \nu}{3\,e\,GeV^2} \simeq 31\left(\frac{\nu}{GHz}\right)\mu G, \tag{9.66}$$

$$A_{E_{syn}} = \frac{\sqrt{3\pi}}{32\pi}\frac{B_c\, e^3}{m_e c^2}\frac{\alpha_e + \frac{7}{3}}{\alpha_e + 1}\frac{\Gamma\left(\frac{3\alpha_e - 1}{12}\right)\Gamma\left(\frac{3\alpha_e + 7}{12}\right)\Gamma\left(\frac{\alpha_e + 5}{4}\right)}{\Gamma\left(\frac{\alpha_e + 7}{4}\right)}, \tag{9.67}$$

where $\Gamma(a)$ denotes the Γ-function (Abramowitz & Stegun 1965), $\alpha_\nu = (\alpha_e - 1)/2 = \alpha/2$, and B_c denotes a (frequency dependent) characteristic magnetic field strength which implies a characteristic magnetic energy density ε_{B_c}. Line-of-sight integration of the radio emissivity j_ν yields the surface brightness of the radio emission S_ν.

9.4. Smoothed particle hydrodynamics

In this section, we describe how the dynamical effects of a CR population can be included into smoothed particle hydrodynamics (SPH).

9.4.1. Lagrangian fluid dynamics

The Lagrange density of a magneto-hydrodynamical gas-CR medium is

$$\mathcal{L}(\boldsymbol{r}, \dot{\boldsymbol{r}}) = \frac{1}{2}\rho\,\dot{\boldsymbol{r}}^2 - \varepsilon_{th}(\rho, A) - \varepsilon_{CR}(\rho, C_0, q_0) - \varepsilon_B, \tag{9.68}$$

where $\varepsilon_{th} = \rho A_0\,(\rho/\rho_0)^{\gamma-1}/(\gamma-1)$ is the thermal energy density of a gas with adiabatic index γ and an entropy described by the adiabatic invariant A. Any adiabatic invariant $X \in \{A_0, C_0, q_0\}$ is simply advected with an adiabatic flow:

$$\frac{dX}{dt} = \left(\frac{dX}{dt}\right)_{non-adiabatic}, \tag{9.69}$$

where the right-hand side allows for non-adiabatic changes discussed in Sect. 9.3. The density evolves according to

$$d\ln\rho/dt = -\nabla\cdot\dot{\boldsymbol{r}}, \tag{9.70}$$

and the magnetic field according to the MHD-induction law:

$$\frac{\partial\boldsymbol{B}}{\partial t} = \nabla\times(\dot{\boldsymbol{r}}\times\boldsymbol{B} - \eta\,\nabla\times\boldsymbol{B}) \tag{9.71}$$

9.4.2. SPH formulation

In smoothed particle hydrodynamics (SPH), the fluid is represented by an ensemble of particles, which carry the mass, energy, and various properties of the fluid elements. Macroscopic properties of the medium such as the density at position r_i of the i-th particle are calculated according to

$$\rho_i = \sum_j m_j \, W(|r_i - r_j|, h_i) \, , \tag{9.72}$$

where m_j is the mass of the j-th fluid element and $W(r, h)$ is the SPH smoothing kernel. The SPH particle positions r_i are the dynamical variables of the simulation. However, in the approach of Springel & Hernquist (2002), which we extend in this work to an additional CR population and to allow for a general equation of state of the gas, also the smoothing-kernel lengths h_i are dynamical variables of a Lagrangian function.

We introduce the CR spectrum of the i-th SPH particle

$$m_i \, \hat{f}_i(p) = m_i \, \frac{\mathrm{d}N_{\mathrm{CR}}}{\mathrm{d}p \, \mathrm{d}m} = \frac{m_i}{\rho(r_i)} \, \frac{\mathrm{d}N_{\mathrm{CR}}}{\mathrm{d}p \, \mathrm{d}V} = \frac{m_i}{\rho(r_i)} \, f_i(p) \tag{9.73}$$

with the help of the CR number per momentum and unit gas mass $\hat{f}_i(p)$. Our power-law template spectra are then described by

$$\hat{f}_i(p) = \hat{C}_i \, p^{-\alpha} \, \theta(p - q_i), \tag{9.74}$$

where $\hat{C}_i = C(r_i)/\rho(r_i)$ denotes the CR normalization constant of the i-th SPH particle. Similarly, we introduce the CR energy, CR density, and thermal energy per unit gas mass with $\hat{\varepsilon}_{\mathrm{CR}} = \varepsilon_{\mathrm{CR}}/\rho$, $\hat{n}_{\mathrm{CR}} = n_{\mathrm{CR}}/\rho$, and $\hat{\varepsilon}_{\mathrm{th}} = \varepsilon_{\mathrm{th}}/\rho$, respectively. The equations, defining these quantities and their changes due to adiabatic and non-adiabatic processes in terms of $\hat{C}$ and q, can be obtained from the corresponding formulae in the article by replacing C with $\hat{C}$. For instance, Eqn. (9.4) yields

$$\hat{\varepsilon}_{\mathrm{CR},i} = \int_0^\infty \mathrm{d}p \, \hat{f}_i(p) \, T_{\mathrm{p}}(p) = \frac{\hat{C}_i \, m_{\mathrm{p}} \, c^2}{\alpha - 1} \left[\frac{1}{2} \, \mathcal{B}_{\frac{1}{1+q_i^2}} \left(\frac{\alpha - 2}{2}, \frac{3 - \alpha}{2} \right) + q_i^{1-\alpha} \left(\sqrt{1 + q_i^2} - 1 \right) \right] , \tag{9.75}$$

and so on.

An elegant way of deriving the equations of motions for a SPH simulation uses the Lagrange formalism. The SPH discretized Lagrangian is

$$\mathcal{L}(q, \dot{q}) = \sum_i \frac{m_i}{2} \, \dot{r}_i^2 - \sum_i m_i \, \hat{\varepsilon}_i + \sum_i \lambda_i \, \phi_i \, , \tag{9.76}$$

where $\hat{\varepsilon}_i = \hat{\varepsilon}_{\mathrm{th}} + \hat{\varepsilon}_{\mathrm{CR}}$ is the total energy per mass of the i-th SPH particle, and $q = (\{r_i\}, \{h_i\}, \{\lambda_i\})$, which is not to be confused with the CR spectral cutoff q, denotes all degrees of freedom of the system, namely the components of the SPH particle positions r_i and the smoothing lengths h_i and their velocities. The λ_is are Lagrange multipliers introduced by Springel & Hernquist (2002) in order to incorporate the choice of the smoothing length h_i into the Lagrangian via the function

$$\phi_i(q) = \frac{4\,\pi}{3} \, h_i^3 \, \rho_i - M_{\mathrm{SPH}} \, , \tag{9.77}$$

where M_{SPH} is the required mass within the smoothing kernel.

Here, we have ignored the description of magnetic fields within the SPH-Lagrangian. We will treat magnetic field evolution separately from this Lagrangian formalism, and add their forces ad-hoc to the momentum equations of the SPH particles. This is along the lines of Dolag et al. (1999), and seems to work well in typical cosmological settings. However, we note that the dynamical influence of magnetic fields could also be included into the SPH Lagrange-function as Price & Monaghan (2004a,b) demonstrate.

If one derives the SPH-equation of motion from a Lagrangian, one obtains a dynamical system which obeys energy and entropy conservation. Non-adiabatic processes, like shock waves, radiative energy losses and energy exchange of the thermal and relativistic fluids, thermal conduction, and CR diffusion have to be added into these equations. The way such process should be implemented in case of CR populations should become clear from this work.

9.4.3. Equations of motion

The equations of motions (of the adiabatic, non-magnetic part) of the SPH description follow from the Hamilton principle, namely

$$\frac{\mathrm{d}}{\mathrm{d}t}\frac{\partial \mathcal{L}}{\partial \boldsymbol{q}} - \frac{\partial \mathcal{L}}{\partial \dot{\boldsymbol{q}}} = 0. \tag{9.78}$$

The equation determining the smoothing length of the i-th particle follows from the variation of the action with respect to the Lagrange-multiplier λ_i. The corresponding part of the Euler-Lagrange equations yields

$$\phi_i = 0, \tag{9.79}$$

which for the special form chosen in Eqn. (9.77) leads to an implicit formula for h_i that has to be solved numerically in practice.

Variation with respect to h_i leads to an equation for λ_i:

$$\lambda_i = \frac{\partial \hat{\varepsilon}_i}{\partial h_i}\left[\frac{\partial \phi_i}{\partial h_i}\right]^{-1} = \frac{\partial \hat{\varepsilon}_i}{\partial \rho_i}\frac{\partial \rho_i}{\partial h_i}\left[\frac{\partial \phi_i}{\partial h_i}\right]^{-1}. \tag{9.80}$$

Using now Eqn. (9.77), one gets

$$\lambda_i = \frac{3\,m_i}{4\,\pi\,h_i^3}\frac{\partial \hat{\varepsilon}_i}{\partial \rho_i}\,g_i, \quad\text{with}\quad g_i \equiv \left[1 + \frac{h_i}{3\rho_i}\frac{\partial \rho_i}{\partial h_i}\right]^{-1}. \tag{9.81}$$

Furthermore, the thermodynamical pressure is defined as

$$P = -\left(\frac{\partial E}{\partial V}\right)_S, \tag{9.82}$$

where $S = S_i$ denotes the entropy of a SPH particle volume element of size $V = V_i = \rho_i/m_i$ and internal energy $E = m_i\,\hat{\varepsilon}_i$. This pressure definition can be used to express the derivative of the SPH particle energy with respect to the local density in terms of the total (thermal plus CR) thermodynamical pressure:

$$\frac{\partial \hat{\varepsilon}_i}{\partial \rho_i} = \frac{P_i}{\rho_i^2} = \frac{P_{th,i} + P_{\mathrm{CR},i}}{\rho_i^2} \tag{9.83}$$

One might argue that this derivation should only be correct for thermodynamic systems, and therefore not necessarily for CR populations which do not exhibit a Boltzmann distribution function. However, the concept of entropy, and the concept of adiabatic processes, which do not change phase space density and therefore leave entropy constant, is well defined for an arbitrary distribution function. Therefore, Eqn. (9.83) is a generally valid result, which can also be confirmed by an explicit calculation.[5]

Thus, the Lagrange-formalism for a variable SPH smoothing length introduced by Springel & Hernquist (2002) for a polytropic equation of state can easily be generalized to a general equation of state by replacing the thermal gas pressure by the total pressure of all fluid components. A calculation along the lines of Springel & Hernquist (2002) shows that the SPH-particle equations of motion read

$$\frac{\mathrm{d}\boldsymbol{v}_i}{\mathrm{d}t} = -\sum_j m_j\left[g_i\frac{P_i}{\rho_i^2}\nabla_i\,W_{ij}(h_i) + g_j\frac{P_j}{\rho_j^2}\nabla_i\,W_{ij}(h_j)\right], \tag{9.84}$$

with $\boldsymbol{v}_i = \dot{\boldsymbol{r}}_i$, $P_i = P_{th,i} + P_{\mathrm{CR},i}$ the thermal plus CR pressure, and $W_{ij}(h_i) = W(|\boldsymbol{r}_i - \boldsymbol{r}_j|, h_i)$.

---

[5]The internal energy per SPH particle of an ideal (thermal and/or relativistic) gas can be written as $m_i\,\hat{\varepsilon}_i = m_i\,\sum_a \int \mathrm{d}p\,\hat{f}_{a,i}(p)\,T_a(p)$, where a
is the index over the particle species (electrons, protons, etc.) with momentum-space distribution functions $\hat{f}_{a,i}(p)$, and $T_a(p)$ the relativistic correct kinetic energy of the particles (Eqn. (9.5)). A straightforward calculation of $\partial \hat{\varepsilon}_i/\partial \rho_i$, which uses the first equality in Eqn. (9.6), leads then to Eqn. (9.83).

9.4.4. Numerically updating the CR spectrum

Update the adiabatic invariant variables $\hat{C}_0$ and q_0 is most conveniently done via Eqn. (9.13) and (9.14). However, if the relative changes during a numerical time-step are large, e.g. due to rapid CR production at a location without a substantial initial CR population, these equations would have to be integrated on a refined time-grid, or solved with an implicit integration scheme. Both methods would be very time-consuming. Therefore, we propose another updating scheme: from the initial variables $\hat{C}_0(t_0)$ and $q_0(t_0)$ at time t_0, the corresponding momentary particle number $\hat{n}_{CR}$ and energy density $\hat{\varepsilon}_{CR}$, and average particle energy T_{CR} are calculated according to Eqns. (9.2) to (9.5). Then $\hat{n}_{CR}$, $\hat{\varepsilon}_{CR}$, and T_{CR} are updated according to the non-adiabatic CR energy and number losses or gains during that time-step. And finally, these updated values have to be translated back into updated values of $\hat{C}_0(t_1)$ and $q_0(t_1)$. This is easiest by first inverting Eqn. (9.5) in order to calculate q, and then to use Eqns. (9.2) and (9.3) to get the updated $\hat{C}_0(t_1)$ and $q_0(t_1)$. The inversion of Eqn. (9.5) has to be done numerically for $T_{CR} \sim m_p c^2$, e.g. using pre-calculated numerical tables. However, for the asymptotic regimes we propose the following accurate inversion formulae based on a Taylor expansion:

$$q(\tau) = \begin{cases} q_a + \dfrac{q_a^{4-\alpha}}{(3-\alpha)\,\mathcal{B}}, & \tau = T_{CR}/(m_p\,c^2) \ll 1 \\[2ex] \dfrac{\alpha-2}{\alpha-1}\,(\tau+1), & \tau = T_{CR}/(m_p\,c^2) \gg 1 \end{cases}, \tag{9.85}$$

$$\text{with} \quad q_a = \left(\frac{2\,\tau}{\mathcal{B}}\right)^{\frac{1}{\alpha-1}}, \text{ and } \mathcal{B} = \mathcal{B}\left(\frac{\alpha-2}{2}, \frac{3-\alpha}{2}\right) \tag{9.86}$$

9.5. Conclusion and outlook

We have shown how various adiabatic and non-adiabatic processes can be described for a simplified CR spectrum, consisting of a power-law with fixed spectral index, but varying normalization and low-energy cutoff. The CR spectral index has to be chosen in advance to resemble a typical spectral index for the system under consideration. We also explained how the CR gas can be self-consistently included into a SPH simulation code, e.g. by keeping energy and particle number conserved up to numerical accuracy, by keeping CR entropy exactly conserved in adiabatic processes, and by taking into account the dynamical forces from CR pressure gradients.

This work is aiming to set an initial framework for follow up work on the impact of CR populations on galaxy and large-scale structure formation. It is accompanied by two papers describing the implementation and testing of (i) the CR formalism as described here into the GADGET simulation code (Jubelgas et al. 2005), and (ii) an SPH shock capturing method allowing to follow CR injection at structure formation shock waves (see Chapter 10 or Pfrommer et al. (2005)). Further applications are in preparation.

The results of this chapter were worked out in a collaboration that was led by T.A. Enßlin, and completed by myself, V. Springel, and M. Jubelgas. A paper entitled "A description of cosmic ray gas for cosmological applications" *will be submitted to the journal* Monthly Notices of the Royal Astronomical Society.

10. Structure formation shocks in cosmological SPH simulations

Abstract

We develop a formalism for the identification and accurate estimation of the strength of structure formation shocks *during* cosmological smoothed particle hydrodynamics (SPH) simulations. Shocks not only play a decisive role for the thermalization of gas in virializing structures but also for the acceleration of relativistic cosmic rays (CRs) through diffusive shock acceleration. Our formalism is applicable both to ordinary non-relativistic thermal gas, and to plasmas composed of CRs and thermal gas. To this end, we derive an analytical solution to the one-dimensional Riemann shock tube problem for a composite plasma of CRs and thermal gas. We apply our methods to study the properties of structure formation shocks in high-resolution hydrodynamic simulations of the ΛCDM model. We find that most of the energy is dissipated in weak internal shocks with Mach numbers $\mathcal{M} \sim 2$ which are predominantly central flow shocks or merger shock waves traversing halo centers. Collapsed cosmological structures are surrounded by external shocks with much higher Mach numbers up to $\mathcal{M} \sim 1000$, but they play only a minor role in the energy balance of thermalization. This is because of the higher pre-shock gas densities within non-linear structures, and the significant increase of the mean shock speed as the characteristic halo mass grows with cosmic time. We show that after the epoch of cosmic reionization the Mach number distribution is significantly modified by an efficient suppression of strong external shock waves due to the associated increase of the sound speed of the diffuse gas. Invoking a model for CR acceleration in shock waves, we find that the average strength of shock waves responsible for CR energy injection is higher than for shocks that dominate the thermalization of the gas. This implies that the dynamical importance of shock-injected CRs is comparatively large in the low-density halo infall regions, but is less important for the weaker flow shocks occurring in central high-density regions of halos. When combined with radiative dissipation and star formation, our formalism can also be used to study CR injection by supernova shocks, or to construct models for shock-induced star formation in the interstellar medium.

10.1. Introduction

10.1.1. Structure formation shock waves

Cosmological shock waves form abundantly in the course of structure formation, both due to infalling pristine cosmic plasma which accretes onto filaments, sheets and halos, as well as due to supersonic flows associated with merging substructures (Quilis et al. 1998, Miniati et al. 2000, Ryu et al. 2003, Gabici & Blasi 2003, Pavlidou & Fields 2005). Additionally, shock waves occur due to non-gravitational physics in the interstellar and intracluster media, e.g. as a result of supernova explosions. Structure formation shock waves propagate through the cosmic tenuous plasma, which is compressed at the transition layer of the shock while a part of the kinetic energy of the incoming plasma is dissipated into internal energy of the post-shock gas. Because of the large collisional mean free path, the energy transfer proceeds through collective electromagnetic viscosity which is provided by ubiquitous magnetic irregularities (Wentzel 1974, Kennel et al. 1985).

Cosmologically, shocks are important in several respects: (1) shock waves dissipate gravitational energy associated with hierarchical clustering into thermal energy of the gas contained in dark matter halos, thus supplying the intra-halo medium with entropy and thermal pressure support. Radiative cooling is then required to compress the gas further to densities that will allow star formation. (2) Shocks also occur around moderately overdense filaments, which leads to a heating of the intragalactic medium. Sheets and filaments are predicted to host a warm-hot intergalactic medium with temperatures in the range $10^5 \, \text{K} < T < 10^7 \, \text{K}$ whose evolution is primarily driven by shock heating from gravitational perturbations breaking on mildly nonlinear, non-equilibrium structures (Hellsten et al. 1998, Cen & Ostriker 1999, Davé et al. 2001, Furlanetto & Loeb 2004, Kang et al. 2005). Thus, the

shock-dissipated energy traces the large scale structure and contains information about its dynamical history. (3) Besides thermalization, collisionless shocks are also able to accelerate ions of the high-energy tail of the Maxwellian through diffusive shock acceleration (DSA) (for reviews see Drury 1983b, Blandford & Eichler 1987, Malkov & Drury 2001). These energetic ions are reflected at magnetic irregularities through magnetic resonances between the gyro-motion and waves in the magnetized plasma and are able to gain energy in moving back and forth through the shock front. This acceleration process typically yields a cosmic ray (CR) population with a power-law distribution of the particle momenta. Nonlinear studies of DSA have shown that a considerable part of the kinetic energy flux passing through shocks can be channeled into nonthermal populations, up to about one-half of the initial kinetic energy of the shock (Berezhko et al. 1995, Ellison et al. 1996, Malkov 1998, 1999, Kang et al. 2002). Note that CRs have sufficient momentum not to resonate with the electromagnetic turbulence in the shock front itself. They hence experience the shock as a discontinuity, i.e. the CR population is adiabatically compressed by the shock (e.g., Drury 1983b).

Indeed, CR electrons have been observed in the intra-cluster medium (ICM) of galaxy clusters through their diffuse synchrotron emission (Kim et al. 1989, Giovannini et al. 1993, Deiss et al. 1997). In addition to these extended radio halos which show a similar morphology compared to the thermal X-ray emission, there have been extended radio relics observed in the cluster periphery (e.g., Röttgering et al. 1997) which might well coincide with merger shock waves as proposed by Enßlin et al. (1998). Some clusters have also been reported to exhibit an excess of hard X-ray emission compared to the expected thermal bremsstrahlung of the hot ICM, most probably produced by inverse Compton up-scattering of cosmic microwave background photons by relativistic electrons (Fusco-Femiano et al. 1999, Sanders et al. 2005). It has been proposed that a fraction of the diffuse cosmological γ-ray background radiation originates from the same processes (Loeb & Waxman 2000, Miniati 2002, Reimer et al. 2003, Berrington & Dermer 2003, Kuo et al. 2005).

To date, there are two different scenarios explaining these non-thermal emission processes: (1) reacceleration processes of 'mildly' relativistic electrons ($\gamma \simeq 100 - 300$) being injected over cosmological timescales into the ICM by sources like radio galaxies, supernova remnants, merger shocks, or galactic winds, which all can provide an efficient supply of highly-energetic CR electrons. Owing to their long lifetimes of a few times 10^9 years these 'mildly' relativistic electrons can accumulate within the ICM (Sarazin 2002), until they experience continuous in-situ acceleration either via shock acceleration or resonant pitch angle scattering on turbulent Alfvén waves (Jaffe 1977, Schlickeiser et al. 1987, Brunetti et al. 2001, Ohno et al. 2002, Brunetti et al. 2004a). (2) In the ICM, the CR protons have lifetimes of the order of the Hubble time (Völk et al. 1996), which is long enough to diffuse away from the production site and to maintain a space-filling distribution over the cluster volume. These CR protons can interact hadronically with the thermal ambient gas producing secondary electrons, neutrinos, and γ-rays in inelastic collisions throughout the cluster volume, generating radio halos through synchrotron emission (Dennison 1980, Vestrand 1982, Blasi & Colafrancesco 1999, Dolag & Enßlin 2000, Pfrommer & Enßlin 2003, 2004a,b). Cosmological simulations support the possibility of a hadronic origin of cluster radio halos (Miniati et al. 2001).

10.1.2. Hydrodynamical simulations

Hydrodynamical solvers of cosmological codes are generally classified into two main categories: (1) Lagrangian methods like smoothed particle hydrodynamics (SPH) which discretize the mass of the fluid, and (2) Eulerian codes, which discretize the fluid volume. SPH methods were first proposed by Gingold & Monaghan (1977) and Lucy (1977) and approximate continuous fluid quantities by means of kernel interpolation over a set of tracer particles. Over the years, the SPH techniques has been steadily improved for cosmological applications (Evrard 1988, Hernquist & Katz 1989, Navarro & White 1993, Springel & Hernquist 2002), where it benefits from an unmatched ease of including self-gravity.

In contrast, Eulerian methods discretize space and represent continuous fields on a mesh. Originally, Eulerian codes employed a mesh which is fixed in space (Cen & Ostriker 1993, Yepes et al. 1995) or adaptively moving (Pen 1998), while more recently, adaptive mesh refinement (AMR) algorithms have been developed for cosmological applications (Berger & Colella 1989, Bryan & Norman 1997, Norman & Bryan 1999, Kravtsov et al. 2002), which can adapt to regions of interest in a flexible way.

Grid-based techniques offer superior capabilities for capturing hydrodynamical shocks. In some algorithms, this can be done even without the aid of artificial viscosity, thanks to the use of Riemann solvers at the cell-level, so that a very low residual numerical viscosity is achieved. However, codes employing static meshes still lack the resolution and flexibility necessary to tackle structure formation problems in a hierarchically clustering universe,

which is characterized by a very large dynamic range and a hierarchy of substructure at all stages of the evolution. For example, techniques based on a fixed mesh are seriously limited when one tries to study the formation of individual galaxies in a cosmological volume, simply because the internal galactic structure such as disk and bulge components can then in general not be sufficiently well resolved. A new generation of AMR codes which begin to be applied in cosmology (Abel et al. 2002, Kravtsov et al. 2002, Refregier & Teyssier 2002) may in principle resolve this problem. However, a number of grid-based problems remain even here, for example the dynamics is not Galilean-invariant, and there can be spurious advection and mixing errors, especially for large bulk velocities across the mesh.

These problems can be avoided in SPH, which thanks to its Lagrangian nature and its accurate treatment of self-gravity is particularly well suited for structure formation problems. SPH adaptively and automatically increases the resolution in dense regions such as galactic halos or centers of galaxy clusters, which are the regions of primary interest in cosmology. One drawback of SPH is the dependence on the artificial viscosity which has to deliver the necessary entropy injection in shocks. While the parameterization of the artificial viscosity can be motivated in analogy with the Riemann problem (Monaghan 1997), the shocks themselves are broadened over the SPH smoothing scale and not resolved as discontinuities, but post-shock quantities are calculated very accurately. However, to date it has not been possible to identify and measure the shock strengths instantaneously with an SPH simulation.

Being interested in dynamical implications of CRs on structure formation and galaxy evolution, one faces not only the problem of the interplay of gravity and hydrodynamics of a plasma composed of CRs and thermal particles but in addition radiative processes such as cooling and supernova feedback. To date, AMR codes have not yet matured to the point that they can address all these requirements throughout a cosmological volume, although there are recent efforts along these lines (e.g. Kang & Jones 2005, Jones & Kang 2005). It would therefore be ideal if SPH codes for structure formation could acquire the ability to detect shocks reliably *during* simulations. Previous work on shock detection in SPH simulations (Keshet et al. 2003) was restricted to a posteriori analysis of two subsequent simulation time-slices, which can then be used to approximately detect a certain range of shocks as entropy jumps.

10.1.3. Motivation and structure

This chapter seeks to close this gap in order to allow studies of the following questions: (1) the cosmic evolution of shock strengths provides rich information about the thermal history of the baryonic component of the Universe: where and when is the gas heated to its present temperatures, and which shocks are mainly responsible for it? Does the missing baryonic component in the present-day universe reside in a warm-hot intergalactic medium? (2) CRs are accelerated at structure formation shocks through diffusive shock acceleration: what are the cosmological implications of such a CR component? (3) Shock waves are modified by nonlinear back-reaction of the accelerated CRs and their spatial diffusion into the pre-shock regime: Does this change the cosmic thermal history or give rise to other effects? (4) Simulating realistic CR profiles within galaxy clusters can provide detailed predictions for the expected radio synchrotron and γ-ray emission. What are the observational signatures of this radiation that is predicted to be observed with the upcoming new generation of γ-ray instruments (imaging atmospheric Čerenkov telescopes and the GLAST satellite) and radio telescopes (LOFAR and extended VLA)?

The purpose of this chapter is to study the properties of structure formation shock waves in self-consistent cosmological simulations, allowing us to explore their role for the thermalization of the pristine plasma, as well as for the acceleration of relativistic CRs through DSA. In particular, we develop a framework for quantifying the importance of CRs during cosmological structure formation, including an accounting of the effects of adiabatic compressions and rarefactions of CR populations, as well as of numerous non-adiabatic processes. Besides CR injection by structure formation shocks, the latter include CR shock injection of supernova remnants, in-situ re-acceleration of CRs, spatial diffusion of CRs, CR energy losses due to Coulomb interactions, Bremsstrahlung, and hadronic interactions with the background gas, and the associated γ-ray and radio emission due to subsequent pion decay. A full description of these CR processes and their formulation for cosmological applications is described in Chapter 9, while the numerical implementation within the SPH formalism is given by Jubelgas et al. (2005). In this work we provide a crucial input for this modeling: a formalism for identifying and accurately estimating the strength of structure formation shocks on-the-fly during cosmological SPH simulations.

The chapter is structured as follows: the basic cosmic ray variables are introduced in Sect. 10.2. The formalism for identifying and measuring the Mach number of shock waves instantaneously within an SPH simulation is described in Sect. 10.3 for a purely thermal gas as well as for a composite plasma of CRs and thermal gas. The numerical implementation of the algorithm is discussed in Sect. 10.4. In Sect. 10.5, we compare shock tube simulations to

analytic solutions of the Riemann problem which are presented in Appendices B.1 and B.2. Finally, in Sect. 10.6, we perform cosmological non-radiative simulations to study CR energy injection at shocks, and the influence of reionization on the Mach number distribution. A summary in Sect. 10.7 concludes the chapter.

10.2. Basic cosmic ray variables

Since we only consider CR protons[1], which are at least in our Galaxy the dominant CR species, it is convenient to introduce the dimensionless momentum $p = P_p/(m_p c_{light})$. CR electrons with $\gamma < 100$ experience efficient Coulomb losses such that their energy density is significantly diminished compared to the CR energy density (Sarazin 2002). The differential particle momentum spectrum per volume element is assumed to be a single power-law above the minimum momentum q:

$$f(p) = \frac{dN}{dp\,dV} = C\,p^{-\alpha}\,\theta(p - q). \tag{10.1}$$

$\theta(x)$ denotes the Heaviside step function. Note that we use an effective one-dimensional distribution function $f(p) \equiv 4\pi p^2 f^{(3)}(p)$. The differential CR spectrum can vary spatially and temporally (although for brevity we suppress this in our notation) through the spatial dependence of the normalization $C = C(\mathbf{r}, t)$ and the cutoff $q = q(\mathbf{r}, t)$.

Adiabatic compression or expansion leaves the phase-space density of the CR population unchanged, leading to a momentum shift according to $p \to p' = (\rho/\rho_0)^{1/3}\,p$ for a change in density from ρ_0 to ρ. Since this is fully reversible, it is useful to introduce the invariant cutoff and normalization q_0 and C_0 which describe the CR population via Eqn. (10.1) if the inter-stellar medium (ISM) or ICM is adiabatically compressed or expanded to the reference density ρ_0. The actual parameters are then given by

$$q(\rho) = (\rho/\rho_0)^{\frac{1}{3}}\,q_0 \quad \text{and} \quad C(\rho) = (\rho/\rho_0)^{\frac{\alpha+2}{3}}\,C_0. \tag{10.2}$$

These adiabatically invariant variables are a suitable choice to be used in a Lagrangian description of the CR population.

The CR number density is

$$n_{CR} = \int_0^\infty dp\,f(p) = \frac{C\,q^{1-\alpha}}{\alpha - 1}, \tag{10.3}$$

provided, that $\alpha > 1$. The kinetic energy density of the CR population is

$$\varepsilon_{CR} = \int_0^\infty dp\,f(p)\,T_p(p) = \frac{C\,m_p c_{light}^2}{\alpha - 1} \left[\frac{1}{2}\,\mathcal{B}_{\frac{1}{1+q^2}}\left(\frac{\alpha - 2}{2}, \frac{3 - \alpha}{2}\right) + q^{1-\alpha}\left(\sqrt{1 + q^2} - 1\right) \right], \tag{10.4}$$

where $T_p(p) = (\sqrt{1 + p^2} - 1)\,m_p c_{light}^2$ is the kinetic energy of a proton with momentum p, and $\mathcal{B}_x(a, b)$ denotes the incomplete Beta-function where $\alpha > 2$ is assumed. The CR pressure is

$$P_{CR} = \frac{m_p c_{light}^2}{3} \int_0^\infty dp\,f(p)\,\beta\,p = \frac{C\,m_p c_{light}^2}{6}\,\mathcal{B}_{\frac{1}{1+q^2}}\left(\frac{\alpha - 2}{2}, \frac{3 - \alpha}{2}\right), \tag{10.5}$$

where $\beta \equiv v/c_{light} = p/\sqrt{1 + p^2}$ is the dimensionless velocity of the CR particle. The CR population can hydro-dynamically be described by an isotropic pressure component as long as the CRs are coupled to the thermal gas by small scale chaotic magnetic fields. Note that for $2 < \alpha < 3$ the kinetic energy density and pressure of the CR populations are well defined for the limit $q \to 0$, although the total CR number density diverges.

The adiabatic exponent of the CR population is defined by

$$\gamma_{CR} \equiv \left. \frac{d\log P_{CR}}{d\log \rho} \right|_S, \tag{10.6}$$

---

[1] α-particles carry a significant fraction of the total CR energy. Nevertheless, the assumption of considering only CR protons is a reasonable approximation, since the energy density of α-particles can be absorbed into the proton spectrum. A GeV energy α-particle can be approximated as an ensemble of four individual nucleons traveling together due to the relatively weak MeV nuclear binding energies compared to the kinetic energy of relativistic protons.

while the derivative has to be taken at constant entropy S. Using Eqns. (10.2) and (10.5), we obtain for the CR adiabatic exponent

$$\gamma_{\text{CR}} = \frac{\rho}{P_{\text{CR}}} \left(\frac{\partial P_{\text{CR}}}{\partial C} \frac{\partial C}{\partial \rho} + \frac{\partial P_{\text{CR}}}{\partial q} \frac{\partial q}{\partial \rho} \right) = \frac{\alpha + 2}{3} - \frac{2}{3} q^{2-\alpha} \beta(q) \left[\mathcal{B}_{\frac{1}{1+q^2}} \left(\frac{\alpha - 2}{2}, \frac{3 - \alpha}{2} \right) \right]^{-1}. \tag{10.7}$$

Note that in contrast to the usual adiabatic exponent, the CR adiabatic exponent is time dependent due to its dependence on the lower cutoff of the CR population, q. Considering a composite of thermal and CR gas, it is appropriate to define an effective adiabatic index by

$$\gamma_{\text{eff}} \equiv \left. \frac{\text{d} \log(P_{\text{th}} + P_{\text{CR}})}{\text{d} \log \rho} \right|_S = \frac{\gamma_{\text{th}} P_{\text{th}} + \gamma_{\text{CR}} P_{\text{CR}}}{P_{\text{th}} + P_{\text{CR}}}. \tag{10.8}$$

10.3. Mach numbers within the SPH formalism

The shock surface separates two regions: The *upstream regime* (pre-shock regime) defines the region in front of the shock whereas the *downstream regime* (post-shock regime) defines the wake of the shock wave. The shock front itself is the region in which the mean plasma velocity changes rapidly on small scales given by plasma physical processes. All calculations in this section are done in the rest frame of the shock which we assume to be non-relativistic. This assumption is justified in the case of cosmological structure formation shock waves for which typical shock velocities are of the order of 10^3 km s^{-1}.

Particles are impinging on the shock surface at a rate per unit shock surface, j, while conserving their mass:

$$\rho_1 v_1 = \rho_2 v_2 = j. \tag{10.9}$$

Here v_1 and v_2 indicate the plasma velocities (relative to the shock's rest frame) in the upstream and downstream regime of the shock, respectively. The mass densities in the respective shock regime are denoted by ρ_1 and ρ_2. Momentum conservation implies

$$P_1 + \rho_1 v_1^2 = P_2 + \rho_2 v_2^2, \tag{10.10}$$

where P_i denotes the pressure in the respective regime $i \in \{1, 2\}$. The energy conservation law at the shock surface reads

$$(\varepsilon_1 + P_1)\rho_1^{-1} + \frac{v_1^2}{2} = (\varepsilon_2 + P_2)\rho_2^{-1} + \frac{v_2^2}{2}. \tag{10.11}$$

ε_i denotes the internal energy density in the regime $i \in \{1, 2\}$. Combining solely these three equations without using any additional information about the equation of state, we arrive at the following system of two equations:

$$j^2 = \rho_1^2 \mathcal{M}_1^2 c_1^2 = \frac{(P_2 - P_1)\rho_1 \rho_2}{\rho_2 - \rho_1} \tag{10.12}$$

$$\frac{\rho_2}{\rho_1} = \frac{2\varepsilon_2 + P_1 + P_2}{2\varepsilon_1 + P_1 + P_2}. \tag{10.13}$$

Here we introduced the Mach number in the upstream regime, $\mathcal{M}_1 = v_1/c_1$, which is the plasma velocity in units of the local sound speed $c_1 = \sqrt{\gamma P_1/\rho_1}$.[2]

10.3.1. Polytropic gas

Non-radiative polytropic gas in the regime $i \in \{1, 2\}$ is characterized by its particular equation of state,

$$\varepsilon_i = \frac{1}{\gamma - 1} P_i \quad \text{or equivalently} \quad P_i = P_0 \left(\frac{\rho_i}{\rho_0} \right)^\gamma, \tag{10.14}$$

---

[2]Note, that the symbol c (sometimes with subscript) denotes the sound velocity.

where γ denotes the adiabatic index. This allows us to derive the well-known Rankine-Hugoniot conditions which relate quantities from the upstream to the downstream regime solely as a function of $\mathcal{M}_1$:

$$\frac{\rho_2}{\rho_1} = \frac{(\gamma + 1)\mathcal{M}_1^2}{(\gamma - 1)\mathcal{M}_1^2 + 2}, \tag{10.15}$$

$$\frac{P_2}{P_1} = \frac{2\gamma\mathcal{M}_1^2 - (\gamma - 1)}{\gamma + 1}, \tag{10.16}$$

$$\frac{T_2}{T_1} = \frac{\left[2\gamma\mathcal{M}_1^2 - (\gamma - 1)\right]\left[(\gamma - 1)\mathcal{M}_1^2 + 2\right]}{(\gamma + 1)^2 \mathcal{M}_1^2}. \tag{10.17}$$

In cosmological simulations using a Lagrangian description of hydrodynamics such as SPH, it is infeasible to identify the rest frame of each shock and thus $\mathcal{M}_1$ unambiguously, especially in the presence of multiple oblique structure formation shocks. As an approximative solution, we rather propose the following procedure, which takes advantage of the entropy-conserving formulation of SPH (Springel & Hernquist 2002). For one particle, the instantaneous injection rate of the entropic function due to shocks is computed, i.e. $\mathrm{d}A/\mathrm{d}t$, where A denotes the entropic function $A(s)$ defined by

$$P = A(s)\rho^\gamma, \tag{10.18}$$

and s gives the specific entropy. Suppose further that the shock is broadened to a scale of order the SPH smoothing length $f_h h$, where $f_h \sim 2$ denotes a factor which has to be calibrated against shock-tubes. We can roughly estimate the time it takes the particle to pass through the broadened shock front as $\Delta t = f_h h / v$, where one may approximate v with the pre-shock velocity v_1. Assuming that the present particle temperature is a good approximation for the pre-shock temperature, we can also replace v_1 with $\mathcal{M}_1 c_1$.

Based on these assumptions and using $\Delta A_1 \simeq \Delta t \, \mathrm{d}A_1/\mathrm{d}t$, one can estimate the jump of the entropic function the particle will receive while passing through the shock:

$$\frac{A_2}{A_1} = \frac{A_1 + \Delta A_1}{A_1} = 1 + \frac{f_h h}{\mathcal{M}_1 c_1 A_1}\frac{\mathrm{d}A_1}{\mathrm{d}t}, \tag{10.19}$$

$$\frac{A_2}{A_1} = \frac{P_2}{P_1}\left(\frac{\rho_1}{\rho_2}\right)^\gamma = f_A(\mathcal{M}_1), \tag{10.20}$$

where

$$f_A(\mathcal{M}_1) \equiv \frac{2\gamma\mathcal{M}_1^2 - (\gamma - 1)}{\gamma + 1}\left[\frac{(\gamma - 1)\mathcal{M}_1^2 + 2}{(\gamma + 1)\mathcal{M}_1^2}\right]^\gamma, \tag{10.21}$$

using Eqns. (10.15) and (10.16). Combining Eqns. (10.19) and (10.20), we arrive at the final equation which is a function of Mach number only:

$$\left[f_A(\mathcal{M}_1) - 1\right]\mathcal{M}_1 = \frac{f_h h}{c_1 A_1}\frac{\mathrm{d}A_1}{\mathrm{d}t}. \tag{10.22}$$

The right hand side can be estimated individually for each particle, and the left side depends only on $\mathcal{M}_1$. Determining the root of the equation hence allows one to estimate a Mach number for each particle.

10.3.2. Composite of cosmic rays and thermal gas

In the presence of a gas composed of cosmic rays and thermal components, Eqns. (10.9) to (10.13) are still applicable if one identifies the energy density ε_i and the pressure P_i with the sum of the individual components in the regime $i \in \{1, 2\}$,

$$\varepsilon_i = \varepsilon_{\mathrm{CR}i} + \varepsilon_{\mathrm{th}i}, \tag{10.23}$$

$$P_i = P_{\mathrm{CR}i} + P_{\mathrm{th}i}. \tag{10.24}$$

The sound speed of such a composite gas is $c_i = \sqrt{\gamma_{\mathrm{eff},i} P_i / \rho_i}$, where $\gamma_{\mathrm{eff},i}$ is given by Eqn. (10.8). Note that in contrast to the single-component fluid, for the general case there is no equivalent to the equation of state (Eqn. (10.14))

in terms of the total energy density ε_i, because of the additivity of both pressure and energy density. For later convenience, we introduce the shock compression ratio x_s and the thermal pressure ratio y_s,

$$x_s = \frac{\rho_2}{\rho_1} \quad \text{and} \quad y_s = \frac{P_{th2}}{P_{th1}}. \tag{10.25}$$

While taking the equation of state (Eqn. (10.14)) for the thermal gas component, we assume adiabatic compression of the CRs at the shock[3],

$$P_{CR2} = P_{CR1} x_s^{\gamma_{CR}} \quad \text{and} \quad \varepsilon_{CR2} = \varepsilon_{CR1} x_s^{\gamma_{CR}}. \tag{10.26}$$

Here we assume a constant CR spectral index over the shock which holds only approximately owing to the weak dependence of the CR lower momentum cutoff q on the density (Eqn. (10.2)).

For the composite of thermal and CR gas, it is convenient to define the effective entropic function A_{eff} and its time derivative,

$$A_{eff} = (P_{th} + P_{CR})\rho^{-\gamma_{eff}}, \tag{10.27}$$

$$\frac{dA_{eff}}{dt} = \frac{dA_{th}}{dt}\rho^{\gamma_{th}-\gamma_{eff}}. \tag{10.28}$$

The expression for the time derivative of the effective adiabatic function uses the approximation of adiabatic compression of the CRs at the shock. Using the same assumptions like in the non-radiative case, we estimate the jump of the entropic function for the particle on passing through the shock made of composite gas:

$$\frac{A_{eff,2}}{A_{eff,1}} = \frac{\left(P_{CR2} + P_{th2}\right)\rho_2^{-\gamma_{eff,2}}}{\left(P_{CR1} + P_{th1}\right)\rho_1^{-\gamma_{eff,1}}} = 1 + \frac{f_h h}{\mathcal{M}_1 c_1 A_{eff,1}} \frac{dA_{eff,1}}{dt}. \tag{10.29}$$

Combining Eqns. (10.12), (10.13), (10.26), and (10.29), we arrive at the following system of equations,

$$f_1(x_s, y_s) = x_s[P_2(x_s, y_s) - P_1]\left[P_2(x_s, y_s)(x_s\rho_1)^{-\gamma_{eff,2}(x_s,y_s)} - P_1\rho_1^{-\gamma_{eff,1}}\right]^2$$

$$- P_1^2(x_s - 1)\rho_1^{1-2\gamma_{eff,1}}\left(\frac{f_h h}{A_{eff,1}}\frac{dA_{eff,1}}{dt}\right)^2 = 0, \tag{10.30}$$

$$f_2(x_s, y_s) = 2\varepsilon_2(x_s, y_s) + P_1 + P_2(x_s, y_s) - x_s\left[2\varepsilon_1 + P_1 + P_2(x_s, y_s)\right] = 0. \tag{10.31}$$

The effective adiabatic index in the post-shock regime is given by

$$\gamma_{eff,2}(x_s, y_s) = \frac{\gamma_{CR}P_{CR2}(x_s) + \gamma_{th}y_s P_{th1}}{P_2(x_s, y_s)}. \tag{10.32}$$

Given all the quantities in the pre-shock regime, we can solve for the roots x_s and y_s of this system of two non-linear equations. This system of equations turns out to be nearly degenerate for plausible values of pre-shock quantities such that it might be convenient to apply the following coordinate transformation:

$$(x_s, y_s) \rightarrow (x_s, z_s) \quad \text{with} \quad z_s = \frac{y_s - x_s}{4}. \tag{10.33}$$

The Mach number $\mathcal{M}_1$ and the jump of internal specific energies can then be obtained by

$$\mathcal{M}_1 = \sqrt{\frac{(P_2 - P_1)x_s}{\rho_1 c_1^2(x_s - 1)}} \quad \text{and} \tag{10.34}$$

$$\frac{u_2}{u_1} = \frac{y_s}{x_s} \quad \text{where} \quad u = \frac{P_{th}}{(\gamma_{th} - 1)\rho}. \tag{10.35}$$

---

[3]Due to their much larger gyroradii and high velocities, CR protons should not participate in the plasma processes of collisionless shock waves.

10.4. Numerical implementation

10.4.1. Polytropic gas

Applying the algorithm of inferring the shock strength within the SPH formalism in a straightforward manner will lead to systematically underestimated values of the Mach number for SPH particles which are located *within the SPH broadened shock surface*: the proposed algorithm of Sect. 10.3 assumes that the present particle quantities such as entropy, sound velocity, and smoothing length are good representations of the hydrodynamical state in the pre-shock regime, which is not longer the case for particles within the SPH broadened shock surface. To overcome this problem, we define a decay time interval $\Delta t_{\mathrm{dec}} = \min[f_h h/(\mathcal{M}_1 c), \Delta t_{\mathrm{max}}]$, during which the Mach number is set to the maximum value that is estimated during the transition from the pre-shock regime to the shock surface. At this maximum, the corresponding particle quantities are good approximations of the hydrodynamical values in the pre-shock regime. We thus have a finite temporal resolution for detecting shocks, which is of order the transit time through the broadened shock front. Note that Δt_{max} is just introduced as a safeguard against too long decay times for very weak shocks.

Secondly, there is no universal value f_h which measures the SPH shock broadening accurately irrespective of the Mach number of the shock, especially in the regime of strong shocks. We therefore use the original algorithm (with $f_h = 2$) only for estimated Mach numbers with $\mathcal{M}_{\mathrm{est}} < 3$, while for stronger shocks, we apply an empirically determined formula (calibrated against shock-tubes) which corrects for the additional broadening of strong shocks and smoothly joins into the weak shock regime:

$$\mathcal{M}_{\mathrm{cal}} = \left(a\mathcal{M}_{\mathrm{est}}^b + c\exp^{-\mathcal{M}_{\mathrm{est}}/3}\right)\mathcal{M}_{\mathrm{est}}, \tag{10.36}$$

where $a = 0.09$, $b = 1.34$, and $c = 1.66$. These numbers may depend on the viscosity scheme of the SPH implementation.

10.4.2. Composite of cosmic rays and thermal gas

Our formalism of inferring the jump conditions for a composite of cosmic rays and thermal gas yields the density jump, $x_s = \rho_2/\rho_1$, and the thermal pressure jump at the shock, $y_s = P_{\mathrm{th2}}/P_{\mathrm{th1}}$ (Sect. 10.3.2). As described in the previous section (Sect. 10.4.1), the values for the estimated jump conditions are systematically underestimated in the regime of strong shocks ($\mathcal{M}_1 \gtrsim 5$) implying an additional broadening of the shock surface. Thus, we proceed the same way as above: using the value of the density jump x_s, we derive the Mach number of the shock through Eqn. (10.34) and recalibrate it for strong shocks. In addition, we use the decay time Δt_{dec} as before in the thermal case to obtain reliable Mach number estimates. The post-shock density is then obtained by multiplying the stored pre-shock density with the density jump x_s.

In the case of a thermal pressure jump at the shock y_s, we decided not to derive another empirical formula but rather exploit CR physics at non-relativistic shocks. Since the CR population is adiabatically compressed at the shock in the limit of strong shocks, the total pressure jump is nearly solely determined by the jump to the thermal pressure in the post-shock regime, i.e. we can safely neglect the contribution of CRs to the pressure jump. This assumption is justified as long as the CR pressure is not dominated by sub-relativistic CRs of low energy which is on the other hand a very short lived population owing to Coulomb interactions in the ICM. Thus, the thermal post-shock pressure for $\mathcal{M}_1 \gtrsim 5$ is estimated as

$$P_{\mathrm{th2}} \simeq \frac{2\gamma_{\mathrm{th}}\mathcal{M}_1^2 - (\gamma_{\mathrm{th}} - 1)}{\gamma_{\mathrm{th}} + 1} P_1, \tag{10.37}$$

where $\mathcal{M}_1$ is obtained by Eqn. (10.36), and P_1 denotes the stored total pre-shock pressure.

10.5. Shock tubes

To assess the reliability of our formalism and the validity of our numerical implementation, we perform a sequence of shock-tube simulations with Mach numbers ranging from $\mathcal{M} = 1.4$ up to $\mathcal{M} = 100$. We use a three-dimensional problem setup which is more demanding and more realistic than carrying out the computation in one dimension.
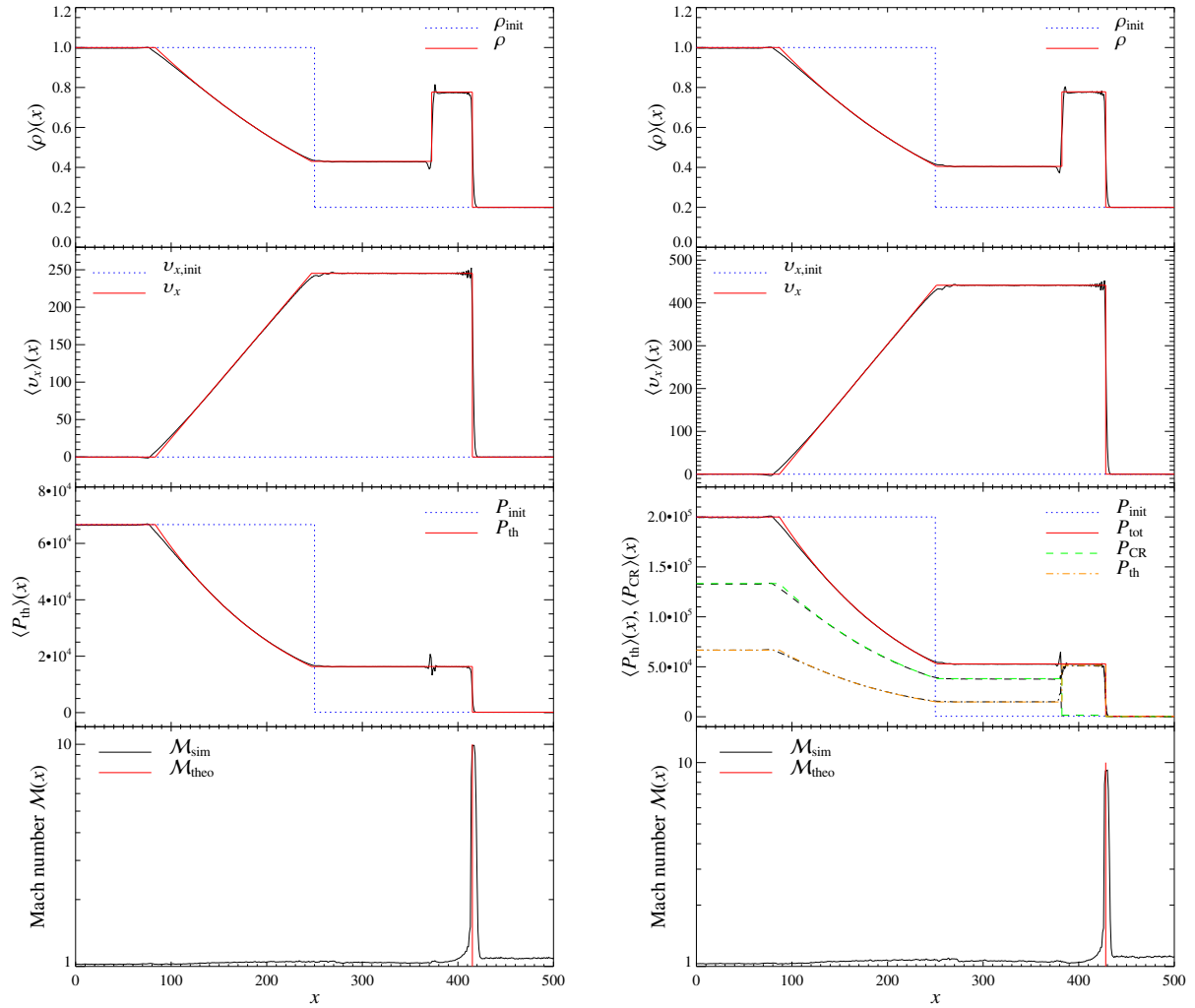
Figure 10.1.: Shock-tube test carried out in a periodic three-dimensional box which is longer in *x*-direction than in the other two dimensions where a shock with the Mach number $\mathcal{M} = 10$ develops. The numerical result of the volume averaged hydrodynamical quantities $\langle\rho(x)\rangle$, $\langle P(x)\rangle$, $\langle v_x(x)\rangle$, and $\langle\mathcal{M}(x)\rangle$ within bins with a spacing equal to the interparticle separation of the denser medium is shown in black and compared with the analytic result in color. *Left panels:* Shock-tubes are filled with pure thermal gas ($\gamma = 5/3$). *Right panels:* Shock-tubes are filled with a composite of cosmic rays and thermal gas. Initially, the relative CR pressure is $X_{\mathrm{CR}} = P_{\mathrm{CR}}/P_{\mathrm{th}} = 2$ in the left half-space ($x < 250$), while we assume pressure equilibrium between CRs and thermal gas for $x > 250$.
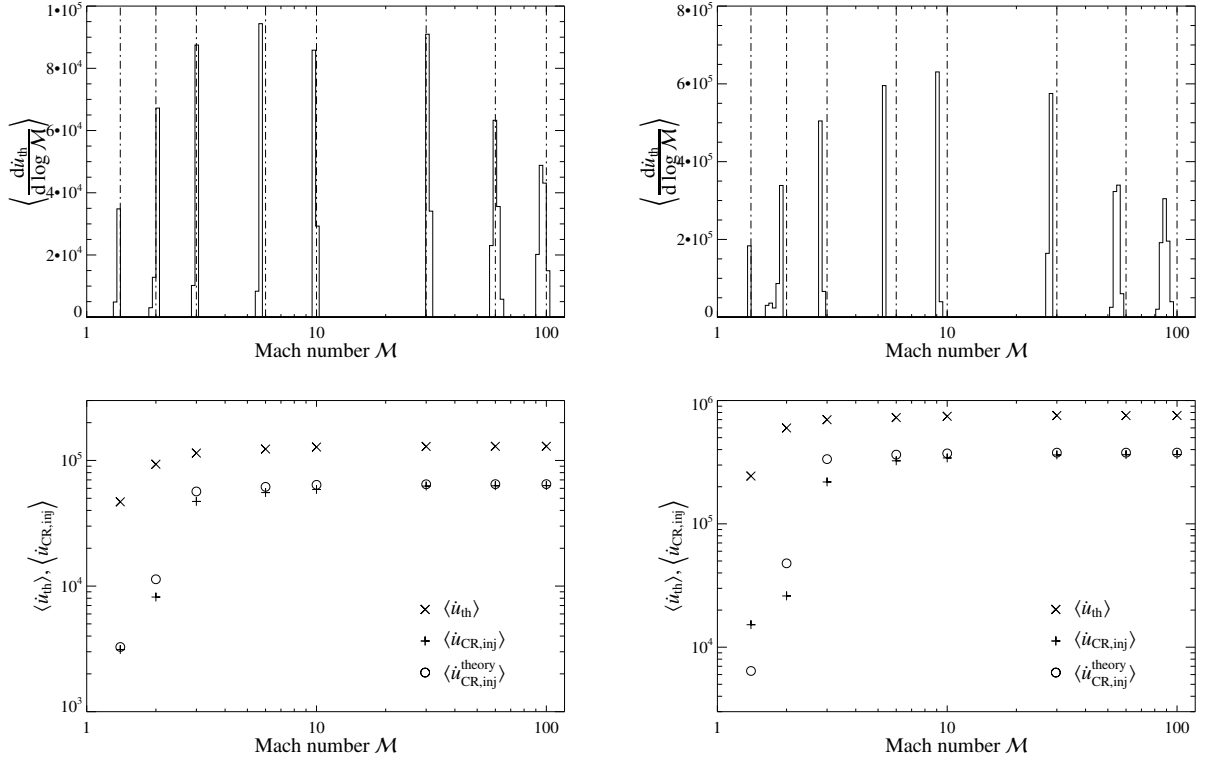
Figure 10.2.: Mach number distributions weighted by the change of dissipated energy per time interval, $\langle \mathrm{d}\dot{u}_{\mathrm{th}}/(\mathrm{d}\log\mathcal{M})\rangle$ for our eight three-dimensional shock-tubes. *Left panels:* Shock-tubes are filled with pure thermal gas ($\gamma = 5/3$). *Right panels:* Shock-tubes are filled with a composite of cosmic rays and thermal gas. Initially, the relative CR pressure is $X_{\mathrm{CR}} = P_{\mathrm{CR}}/P_{\mathrm{th}} = 2$ in the left half-space, while we assume pressure equilibrium between CRs and thermal gas. *Bottom panels:* Shown are the change of dissipated energy per time interval, $\langle \dot{u}_{\mathrm{th}}\rangle$ (shown with ×), the shock-injected CR energy $\langle \dot{u}_{\mathrm{CR,inj}}\rangle$ (+), and the theoretically expected injected CR energy $\langle \dot{u}_{\mathrm{CR,inj}}^{\mathrm{theory}}\rangle$ (○) which is calculated following Chapter 9.

Here and in the following, we drop the subscript '1' of the pre-shock Mach number for convenience. By comparing with known analytic solutions, we are able to demonstrate the validity of our implemented formalism.

There exists an analytic solution of the Riemann shock-tube problem in the case of a fluid described by a polytropic equation of state, $\varepsilon = P/(\gamma - 1)$ (cf. Appendix B.1). Unfortunately, a composite of thermal gas and CRs does not obey this relation. Thus, we derive an analytic solution to the Riemann shock-tube problem for the composite of CRs and thermal gas in Appendix B.2. This analytic solution assumes the CR adiabatic index (Eqn. (10.6)) to be constant over the shock-tube and neglects CR diffusion such that the problem remains analytically treatable.

10.5.1. Polytropic thermal gas

We consider eight standard shock-tube tests (Sod 1978) which provide a validation of both the code's solution to hydrodynamic problems and our Mach number formalism. We consider first an ideal gas with $\gamma = 5/3$, initially at rest. The left half-space ($x < 250$) is filled with gas at unit density, $\rho_2 = 1$, and $P_2 = (\gamma - 1) \, 10^5$, while $x > 250$ is filled with low density gas $\rho_1 = 0.2$ at low pressure. The exact value of the low pressure gas has been chosen such that the resulting solutions yield the Mach numbers $\mathcal{M} = \{1.4, 2, 3, 6, 10, 30, 60, 100\}$ (cf. Appendix B.1). We set up the initial conditions in 3D using an irregular glass-like distribution of particles of equal mass in hydrostatic equilibrium. They are contained in a periodic box which is longer in x-direction than in the other two dimensions, y and z.

In the left panel of Figure 10.1, we show the result for the case of the Mach number $\mathcal{M} = 10$ obtained with the GADGET-2 code (Springel 2005, Springel et al. 2001) at time $t = 0.5$. Shown are the volume averaged hydrodynamical quantities $\langle \rho(x) \rangle$, $\langle P(x) \rangle$, $\langle v_x(x) \rangle$, and $\langle \mathcal{M}(x) \rangle$ within bins with a spacing equal to the interparticle separation of the denser medium and represented by solid black lines. One can clearly distinguish five regions of gas with different hydrodynamical states. These regions are separated by the head and the tail of the leftwards propagating rarefaction wave, and the rightwards propagating contact discontinuity and the shock wave. The overall agreement with the analytic solution is good, while the discontinuities are resolved within $2 - 3$ SPH smoothing lengths. Despite the shock broadening, the post-shock quantities are calculated very accurately. Our formalism is clearly able to detect the shock and precisely measure its strength, i.e. the Mach number $\mathcal{M}$. The pressure quantity drawn is not the hydrodynamically acting pressure of the SPH dynamics but $P = (\gamma - 1)\rho u$, a product of two fields that are calculated each using SPH interpolation. Thus, the observed characteristic pressure blip at the contact discontinuity has no real analogue neither in the averaged x-component of the velocity $\langle v_x(x) \rangle$ nor in the averaged Mach number $\langle \mathcal{M}(x) \rangle$. The x-component of the velocity $\langle v_x(x) \rangle$ shows tiny post-shock oscillations which might be damped with higher values of the artificial viscosity on the expense of a broader shock surface. The leftwards propagating rarefaction wave seems to exhibit a slightly faster signal velocity compared to the sound velocity. This might be attributed to the SPH averaging process which obtains additional information on the SPH smoothing scale.

In the left panel of Figure 10.2, we show the Mach number distributions weighted by the change of dissipated energy per time interval, $\langle \mathrm{d}\dot{u}_{\mathrm{th}}/(\mathrm{d}\log\mathcal{M}) \rangle$ for our eight shock-tubes. The sharp peaks of these distributions around their expected values $\log\mathcal{M}$ are apparent. This demonstrates the reliability of our formalism to precisely measure shock strengths instantaneously during SPH simulations. The bottom panel shows their integral, i.e. the change of dissipated energy per time interval, $\langle \dot{u}_{\mathrm{th}} \rangle$. The rising dissipated energy with growing Mach number reflects the larger amount of available kinetic energy for dissipation.

We additionally calculate the shock-injected CR energy using our formalism of diffusive shock acceleration described in Chapter 9. However, the injected CR energy $\langle \dot{u}_{\mathrm{CR,inj}} \rangle$ was only monitored and not dynamically tracked. For comparison, we also show the theoretically expected injected CR energy $\langle \dot{u}_{\mathrm{CR,inj}}^{\mathrm{theory}} \rangle = \zeta_{\mathrm{inj}} \langle \dot{u}_{\mathrm{th}} \rangle$, where ζ_{inj} is the energy efficiency due to diffusive shock acceleration (cf. Chapter 9 for details). The good comparison of the simulated and theoretically expected shock-injected CR energy demonstrates that our formalism is reliably able to describe the on-the-fly acceleration of CRs during the simulation.

10.5.2. Composite of cosmic rays and thermal gas

Again, we consider eight shock-tube simulations containing a composite of cosmic rays and thermal gas, providing a useful validation of our CR implementation in solving basic hydrodynamic problems as well as our Mach number formalism in the presence of CRs. In these simulations, we neither inject shock-accelerated CRs nor consider CR diffusion: these processes would lead to CR modified shock structures and shall be the subject of a companion

paper.

To characterize this composite fluid, we define the relative CR pressure $X_{CR} = P_{CR}/P_{th}$. Our composite gas is initially at rest, while the left half-space ($x < 250$) is filled with gas at unit density, $\rho_2 = 1$, $X_{CR2} = 2$, and $P_{th2} = (\gamma - 1) \, 10^5$, while $x > 250$ is filled with low density gas $\rho_1 = 0.2$, $X_{CR1} = 1$, at low pressure. The exact value of the low pressure gas has again been chosen such that the resulting solutions yield the Mach numbers $\mathcal{M} = \{1.4, 2, 3, 6, 10, 30, 60, 100\}$ (cf. Appendix B.2). Otherwise, we use the same initial setup as in Sect. 10.5.1. This CR load represents a rather extreme case and can be taken as the limiting case for our Mach number formalism in the presence of CRs. Cosmologically, it may find application in galaxy mergers where the outer regions might be composed of an adiabatically expanded composite gas containing a high CR component.

In the right panel of Figure 10.1, we show the result for the case of the Mach number $\mathcal{M} = 10$ obtained with GADGET-2 at time $t = 0.3$. The agreement with the analytic solution is good, while the discontinuities are resolved within $2 - 3$ SPH smoothing lengths. Despite the shock broadening, the post-shock quantities are calculated very accurately. In the case of composite gas, our formalism is clearly able to detect the shock and measure its strength with a Mach number accuracy better than 10%. Although the total pressure remains constant across the contact discontinuity, the partial pressure of CRs and thermal gas interestingly are changing. This behavior reflects the adiabatic compression of the CR pressure component across the shock wave. A posteriori, this justifies our procedure of inferring the thermal pressure jump at the shock for a composite of CRs and thermal gas in Eqn. (10.37).

In the right panel of Figure 10.2, we show the Mach number distributions weighted by the change of dissipated energy per time interval, $\langle \mathrm{d}\dot{u}_{th}/(\mathrm{d}\log\mathcal{M})\rangle$ for our eight shock-tubes. While our formalism is able to measure the shock strength with a Mach number accuracy better than 10%, the distributions are sharply peaked. This demonstrates the reliability of our formalism to measure shock strengths for the composite gas instantaneously during SPH simulations.

The bottom panel shows the change of dissipated energy per time interval, $\langle \dot{u}_{th}\rangle$ together with the shock-injected CR energy $\langle \dot{u}_{CR,inj}\rangle$. Concerning the amount of injected CR energy, we neglected cooling processes such as Coulomb interactions with thermal particles: this would effectively result in a density dependent recalibration of the maximum CR energy efficiency ζ_{max} of the otherwise arbitrary absolute value of our fiducial density. In the case of high Mach numbers, there is a good agreement between the simulated and theoretically expected shock-injected CR energy while there are discrepancies at low Mach numbers: our formalism estimates volume averaged Mach numbers with an accuracy better than 10%; this uncertainty translates to estimates of the density jump x_s and the thermal pressure jump y_s with a scatter among different SPH particles. In the regime of weak shocks, the CR energy efficiency due to diffusive shock acceleration ζ_{inj} is extremely sensitive to these two quantities, leading to larger uncertainties for the shock-injected CR energy in the case of a high CR load. However, the overall trend for the shock-injected CR energy can still be matched in such an extreme physical environment.

10.6. Non-radiative cosmological simulations

10.6.1. Simulation setup

As a first application of our formalism, we are here interested in studying the spatial distribution of cosmological structure formation shocks in combination with Mach number statistics. We focus on the "concordance" cosmological cold dark matter model with a cosmological constant (ΛCDM). The cosmological parameters of our model are: $\Omega_m = \Omega_{dm} + \Omega_b = 0.3$, $\Omega_b = 0.04$, $\Omega_\Lambda = 0.7$, $h = 0.7$, $n = 1$, and $\sigma_8 = 0.9$. Here, Ω_m denotes the total matter density in units of the critical density for geometrical closure, $\rho_{crit} = 3H_0^2/(8\pi G)$. Ω_b and Ω_Λ denote the densities of baryons and the cosmological constant at the present day. The Hubble constant at the present day is parameterized as $H_0 = 100\, h\, \mathrm{km\ s^{-1} Mpc^{-1}}$, while n denotes the spectral index of the primordial power-spectrum, and σ_8 is the *rms* linear mass fluctuation within a sphere of radius $8\, h^{-1}\mathrm{Mpc}$ extrapolated to $z = 0$. This model yields a reasonable fit to current cosmological constraints and provides a good framework for investigating cosmological shocks.

Our simulations were carried out with an updated and extended version of the massively parallel TreeSPH code GADGET-2 (Springel 2005, Springel et al. 2001) including now self-consistent cosmic ray physics (Enßlin et al. 2005, Jubelgas et al. 2005). Our reference simulation employed 2×256^3 particles which were simulated within a periodic box of comoving size $100\, h^{-1}\mathrm{Mpc}$, so the dark matter particles had masses of $4.3 \times 10^9\, h^{-1}\, M_\odot$ and the SPH particles $6.6 \times 10^8\, h^{-1}\, M_\odot$. The SPH densities were computed from 32 neighbors which leads to our minimum gas resolution of approximately $2 \times 10^{10}\, h^{-1}\, M_\odot$. The gravitational force softening was of a spline form (e.g., Hernquist

& Katz 1989) with a plummer equivalent softening length of $13\,h^{-1}$Mpc comoving. In order to test our numerical resolution, we additionally simulated the same cosmological model with 2×128^3 particles, with a softening length twice that of the reference simulation.

Initial conditions were laid down by perturbing a homogeneous particle distribution with a realization of a Gaussian random field with the ΛCDM linear power spectrum. The displacement field in Fourier space was constructed using the Zel'dovich approximation, with the amplitude of each random phase mode drawn from a Rayleigh distribution. For the initial redshift we chose $1 + z_{\text{init}} = 50$ which translates to an initial temperature of the gas of $T_{\text{init}} = 57$ K. This reflects the fact that the baryons are thermally coupled to the CMB photons via Compton interactions with the residual free electrons after the universe became transparent until it eventually decoupled at $1 + z_{\text{dec}} \simeq 100(\Omega_{\text{b}}h^2/0.0125)^{2/5}$. In all our simulations, we stored the full particle data at 100 output times, equally spaced in $\log(1 + z)$ between $z = 40$ and $z = 0$.

In order to investigate the effects of reionization on the Mach number statistics, we additionally perform two similar simulations which contain a simple reionization model where we impose a minimum gas temperature of $T = 10^4$ K at a redshift of $z = 10$ to all SPH particles. We decided to adopt this simplified model to study its effect on the Mach number statistics rather than a more complicated reionization history. A more realistic scenario might be to add energy only to gas within halos above a certain density in combination with energy input from QSO activity, and to describe the merging of the reionization fronts and their evolution into the lower density regions (e.g., Ciardi et al. 2003).

The simulation reported here follow only non-radiative gas physics. We neglected several physical processes, such as radiative cooling, galaxy/star formation, and feedback from galaxies and stars including cosmic ray pressure. Our primary focus are shocks that are mostly outside the cluster core regions. Thus, the conclusions drawn in this work should not be significantly weakened by the exclusion of these additional radiative processes.

10.6.2. Visualization of the Mach number

In the SPH formalism, continuous fields $A(\boldsymbol{x})$ such as the hydrodynamical quantities are represented by the values A_i at discrete particle positions $\boldsymbol{r}_i = (x_i, y_i, z_i)$ with a local spatial resolution given by the SPH smoothing length h_i. To visualize a scalar quantity in two dimensions we employ the mass conserving *scatter* approach for the projection, where the particle's smoothing kernel is distributed onto cells of a Cartesian grid which is characterized by its physical mesh size g. The line-of-sight integration of any quantity $A(\boldsymbol{x})$ at the pixel at position $\boldsymbol{r} = (x, y, z)$ is determined as the average of integration of all lines of sight passing through the pixel,

$$\langle a(\boldsymbol{x}_\perp)\rangle_{\text{los}} = g^{-2} \sum_i h_i^{-3} \left[\int_{x-g/2}^{x+g/2} \mathrm{d}x_i \int_{y-g/2}^{y+g/2} \mathrm{d}y_i \int_{-h_i}^{h_i} \mathrm{d}z_i \, \mathcal{K}\left(\frac{r}{h_i}\right) A_i \right], \tag{10.38}$$

with $r = \sqrt{(x_i - x)^2 + (y_i - y)^2 + z_i^2}$, and where the summation is extended over all particles in the desired slice of projection. The function $\mathcal{K}$ is the dimensionless spherically symmetric cubic spline kernel suggested by Monaghan & Lattanzio (1985).

The left-hand side of Fig. 10.3 shows the time evolution of the density contrast δ averaged over the line-of-sight with a comoving projection length $L_{\text{proj}} = 10\,h^{-1}$ Mpc:

$$\left\langle 1 + \delta_{\text{gas}}(\boldsymbol{x}_\perp) \right\rangle_{\text{los}} = \frac{\langle \Sigma(\boldsymbol{x}_\perp)\rangle_{\text{los}}}{L_{\text{proj}}\, \rho_{\text{crit}}\, \Omega_{\text{b}}}, \tag{10.39}$$

where Σ denotes the surface mass density. The fine-spun cosmic web at high redshift evolves into a much more pronounced, knotty and filamentary structure at late times, as a result of the hierarchical structure formation process driven by gravity.

The right-hand side of Fig. 10.3 shows the time evolution of the density weighted temperature averaged over the line-of-sight. Again, the growth of galaxy clusters visible as large bright regions with temperatures around 10^7K is clearly visible. Through dissipation, the shock waves convert part of the gravitational energy associated with cosmological structure formation into internal energy of the gas, apart from the additional contribution due to adiabatic compression caused by the material infalling at later times which itself is compressed at these shock waves. The large black regions show voids which cool down during cosmic evolution due to two effects: while the universe expands, non-relativistic gas is adiabatically expanded and cools according to $T \propto V^{1-\gamma} \propto a^{-2}$ for $\gamma = 5/3$
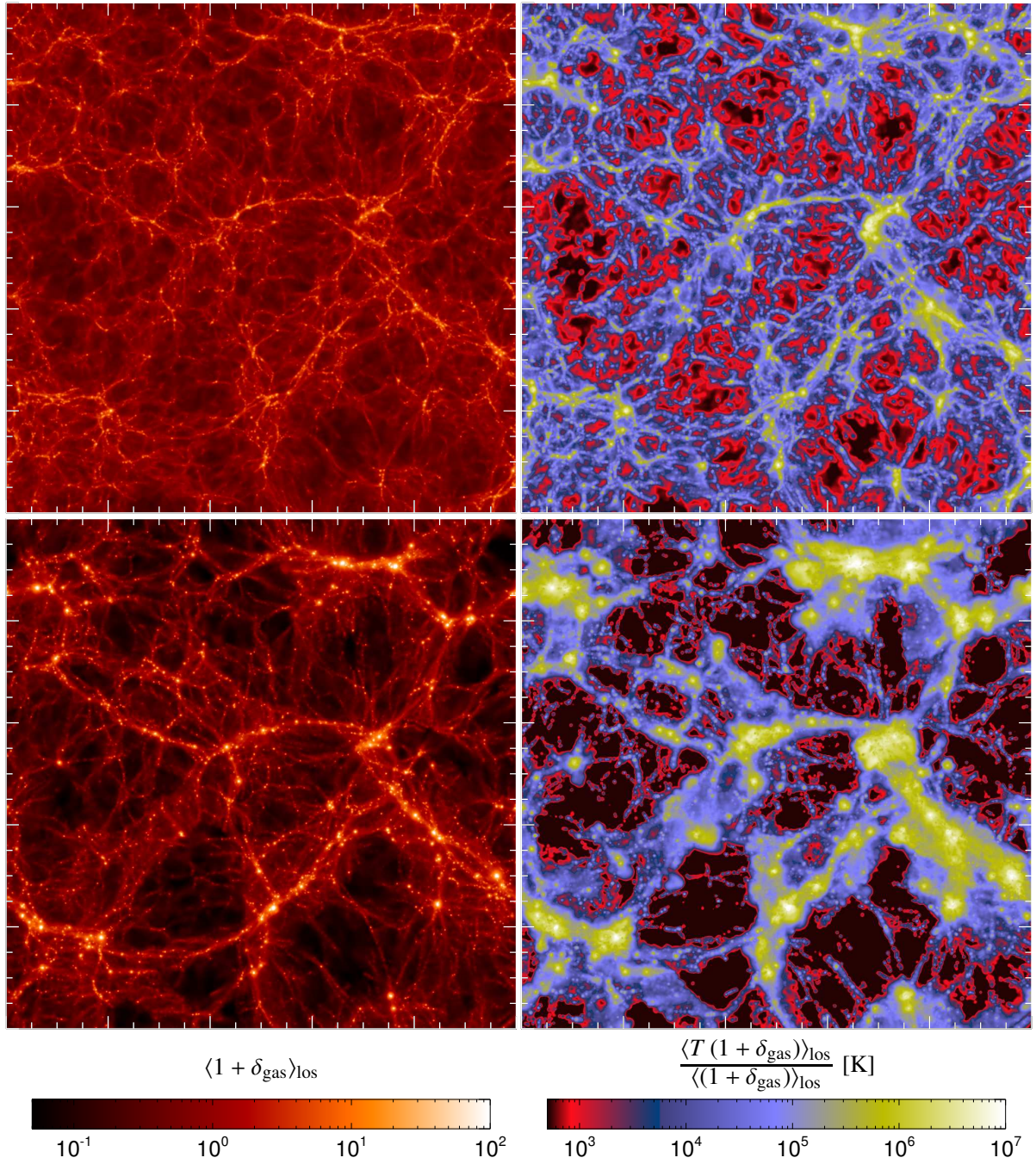
$$\langle 1 + \delta_{\text{gas}} \rangle_{\text{los}}$$

$$\frac{\langle T\,(1 + \delta_{\text{gas}}) \rangle_{\text{los}}}{\langle (1 + \delta_{\text{gas}}) \rangle_{\text{los}}}\ [\text{K}]$$
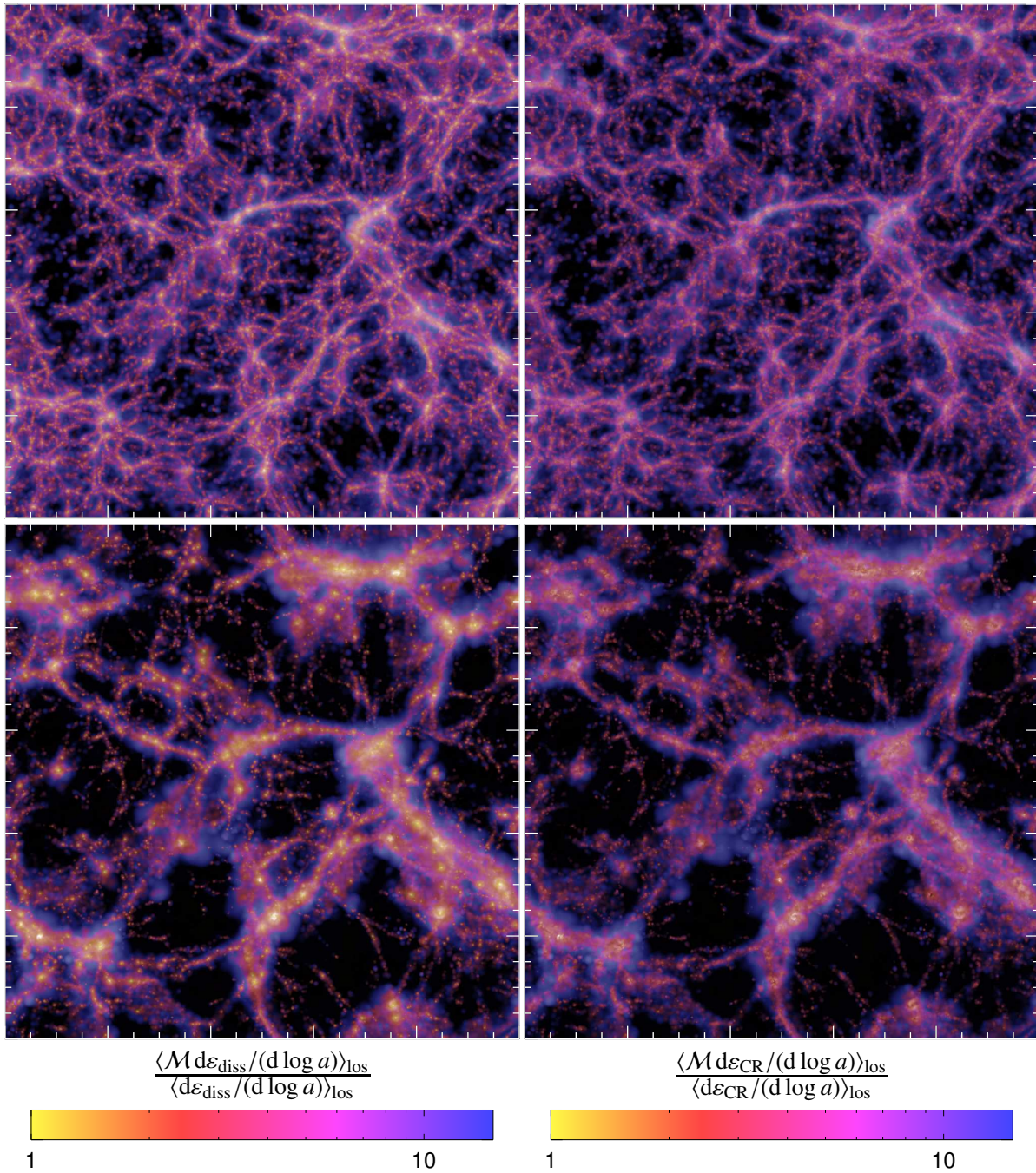
Figure 10.3.: Visualization of a non-radiative cosmological simulation at redshift $z = 2$ (*top panels*) and $z = 0$ (*bottom panels*). Shown are the overdensity of the gas (*left-hand side*) and the density weighed gas temperature (*right-hand side*). These pictures have a comoving side length of $100\ h^{-1}$ Mpc while the projection length along the line-of-sight amounts to $10\ h^{-1}$ Mpc.

148

Figure 10.4.: Mach number visualization of a non-radiative cosmological simulation at redshift $z = 2$ (*top panels*) and $z = 0$ (*bottom panels*). The color hue of the maps on the left-hand side encodes the spatial Mach number distribution weighted by the rate of energy dissipation at the shocks, normalized to the simulation volume. The maps on the right-hand side show instead the Mach number distribution weighted by the rate of CR energy injection above $q = 0.8$, the threshold of hadronic interactions. The brightness of each pixel is determined by the respective weights, i.e. by the energy production density. These pictures have a comoving length of $100 \, h^{-1}$ Mpc on a side. Most of the energy is dissipated in weak shocks which are situated in the internal regions of groups or clusters, while collapsed cosmological structures are surrounded by strong external shocks (shown in blue).

when shock heating is still absent. Secondly, matter is flowing towards filaments during structure formation, hence the voids get depleted, providing an additional adiabatic expansion of the remaining material.

Figure 10.4 shows a visualization of the responsible structure formation shocks and their corresponding strengths. The color scaling represents the spatial Mach number distribution weighted by the rate of energy dissipation at the shocks, and normalized to the simulation volume (left-hand side). The Mach number distribution weighted by the rate of CR energy injection is shown in the right hand side, again normalized to the simulation volume. The brightness of these pixels scales with the respective weights, i.e. by the rates of energy dissipation or injection, respectively. The spatial Mach number distribution impressively reflects the nonlinear structures and voids of the density and temperature maps of Fig. 10.3. It is apparent that most of the energy is dissipated in weak shocks which are situated in the internal regions of groups or clusters while collapsed cosmological structures are surrounded by external strong shocks (shown in blue). These external shocks are often referred to as 'first shocks', because here the compressed gas has been processed for the first time in its cosmic history through shock waves.

Following Ryu et al. (2003), we classify structure formation shocks into two broad populations which are labeled as *internal* and *external* shocks, depending on whether or not the associated pre-shock gas was previously shocked. Rather than using a thermodynamical criterion such as the temperature, we prefer a criterion such as the overdensity δ in order not to confuse the shock definition once we will follow radiatively cooling gas in galaxies (in practice, we use the criterion of a critical pre-shock overdensity $\delta > 10$ for the classification of an internal shock). *External* shocks surround filaments, sheets, and halos while *internal* shocks are located within the regions bound by external shocks and are created by flow motions accompanying hierarchical structure formation. For more detailed studies, internal shocks can be further divided into three types of shock waves: (1) accretion shocks caused by infall from sheets to filaments or halos and from filaments to halos, (2) merger shocks resulting from merging halos, and (3) supersonic chaotic flow shocks inside nonlinear structures which are produced in the course of hierarchical clustering.

In contrast to the present time, the comoving surface area of external shock waves surpasses that of internal shocks at high redshift, due to the small fraction of mass bound in large halos and the simultaneous existence of an all pervading fine-spun cosmic web with large surface area. Also, there the thermal gas has a low sound velocity $c = \sqrt{\gamma P/\rho} = \sqrt{\gamma(\gamma - 1)u}$ owing to the low temperature, so once the diffuse gas breaks on mildly nonlinear structures, strong shock waves develop that are characterized by high Mach numbers $\mathcal{M} = v_\mathrm{s}/c$. Nevertheless, the energy dissipation rate in internal shocks is always higher compared to external shocks because the mean shock speed and pre-shock gas densities are significantly larger for internal shocks.

We use the same color and brightness scale for the Mach number distribution weighted by the injected CR energy rate normalized to the simulation volume (right-hand side of Fig. 10.4). We emphasize two important points which have fundamental implications for the CR population in galaxy clusters: (1) there is an absence of weak shocks (shown in yellow) when the Mach number distribution is weighted by the injected CR energy. This reflects the Mach number dependent energy injection efficiency: the CR injection is saturated for strong shocks which leads to similar spatial distribution of both weightings, by dissipated energy as well as by injected CR energy. In contrast, most of the dissipated energy is thermalized in weak shocks and only small parts are used for the acceleration of relativistic particles (compare Fig. 10.5). (2) The mechanism of energy dissipation at shocks is very density dependent, implying a tight correlation of weak internal shocks and the amount of dissipated energy. This can be seen by the strongly peaked brightness distribution of the dissipated energy rate towards the cluster centers. For the CR-weighted case, this correlation is counteracted by the CR energy injection efficiency leading to a smoother brightness distribution of the CR energy injection. This has the important implication that the ratio of CR injected energy to dissipated thermal energy is increasing as the density declines. Relative to the thermal non-relativistic energy density, the CR energy density is dynamically more important at the outer cluster regions and dynamically less important at the cluster centers.

10.6.3. Mach number statistics

10.6.3.1. Influence of reionization

To quantify previous considerations, we compute the differential Mach number distribution weighted by the dissipated energy normalized to the simulation volume $\mathrm{d}^2\varepsilon_\mathrm{diss}(a, \mathcal{M})/(\mathrm{d}\log a\, \mathrm{d}\log \mathcal{M})$ at different redshifts. The top left panel of Fig. 10.6 shows this Mach number distribution for our reference simulation with reionization (showing a resolution of 2×256^3), while the top right panel shows this distribution for the simulation without reioniza-

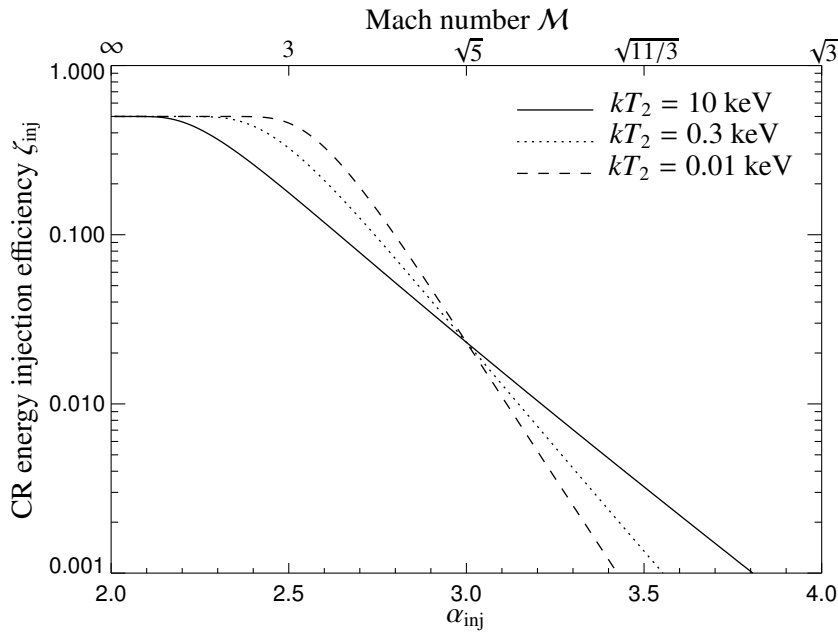**Figure 10.5.:** CR energy injection efficiency for the diffusive shock acceleration process. Shown is the CR energy injection efficiency $\zeta_{\mathrm{inj}} = \varepsilon_{\mathrm{CR}}/\varepsilon_{\mathrm{diss}}$ for the three post-shock temperatures $kT_2/\mathrm{keV} = 0.01, 0.3$, and 10. We inject only CRs above the kinematic threshold $q_{\mathrm{threshold}} = 0.83$ of the hadronic CRp-p interaction which are able to produce pions that successively decay into secondary electrons, neutrinos, and γ-rays. We choose equipartition between injected CR energy and dissipated thermal non-relativistic energy as saturation value of the CR energy injection efficiency, i.e. $\zeta_{\mathrm{max}} = 0.5$ (Ryu et al. 2003).

tion. The lower left panel shows both distributions integrated over the scale factor, $\mathrm{d}\varepsilon_{\mathrm{diss}}(\mathcal{M})/(\mathrm{d}\log\mathcal{M})$, in addition to the Mach number distribution weighted by the injected CR energy normalized to the simulation volume, $\mathrm{d}\varepsilon_{\mathrm{CR}}(\mathcal{M})/(\mathrm{d}\log\mathcal{M})$ (see Sect. 10.6.3.2). Internal shocks are shown with dotted lines and external shocks with dashed lines. The lower right panel shows the evolution of the dissipated energy due to shock waves with scale factor, $\mathrm{d}\varepsilon_{\mathrm{diss}}(a)/(\mathrm{d}\log a)$, for the models with and without reionization.

Several important points are apparent: (1) The median of the Mach number distribution weighted by the dissipated energy decreases as cosmic time evolves, i.e. the average shock becomes weaker at later times. (2) There is an increasing amount of energy dissipated at shock waves as the universe evolves because the mean shock speed is significantly growing when the characteristic mass becomes larger with time. This trend starts to level off at redshift $z \simeq 1$ although the median Mach number in shocks continuous to decrease. (3) Reionization influences the Mach number distribution predominantly at early times (however after reionization took place) and suppresses strong external shock waves efficiently. The reason is that reionization of the thermal gas increases its sound speed $c = \sqrt{\gamma n k T/\rho}$ dramatically, so that weaker shocks are produced for the same shock velocities. (4) The time integrated Mach number distribution weighted by the dissipated energy peaks at Mach numbers $1 \lesssim \mathcal{M} \lesssim 3$. The main contribution in terms of energy dissipation originates from internal shocks because of enhanced pre-shock densities and mean shock speeds. (5) External shocks dominate the Mach number distribution at early times while internal shocks take over at $z \simeq 9$ (depending somewhat on the resolution of the simulation). Their amount of dissipated energy surpasses that in external shocks by over an order of magnitude at the present time. Internal shocks play a more important role than external shocks in dissipating energy associated with structure formation.

The total shock-dissipated energy in our simulation box amounts to $E_{\mathrm{diss}} = 2.27 \times 10^{64}$ erg. This translates to a mean energy deposition per particle of $E_{\mathrm{diss}}\,\mu/(\rho_{\mathrm{cr}}\Omega_{\mathrm{b}}V) = 0.63$ keV, where $\mu = 4m_{\mathrm{p}}/(3 + 5X_{\mathrm{H}})$ is the mean particle weight assuming full ionization and $X_{\mathrm{H}} = 0.76$ is the primordial hydrogen mass fraction. Our results agree well with those of Ryu et al. (2003) in the case of internal shocks while our external shocks tend to be weaker. This can be attributed to our differing definition of internal/external shocks as we prefer a density criterion and use the critical pre-shock overdensity $\delta > 10$ for the classification of an internal shock.
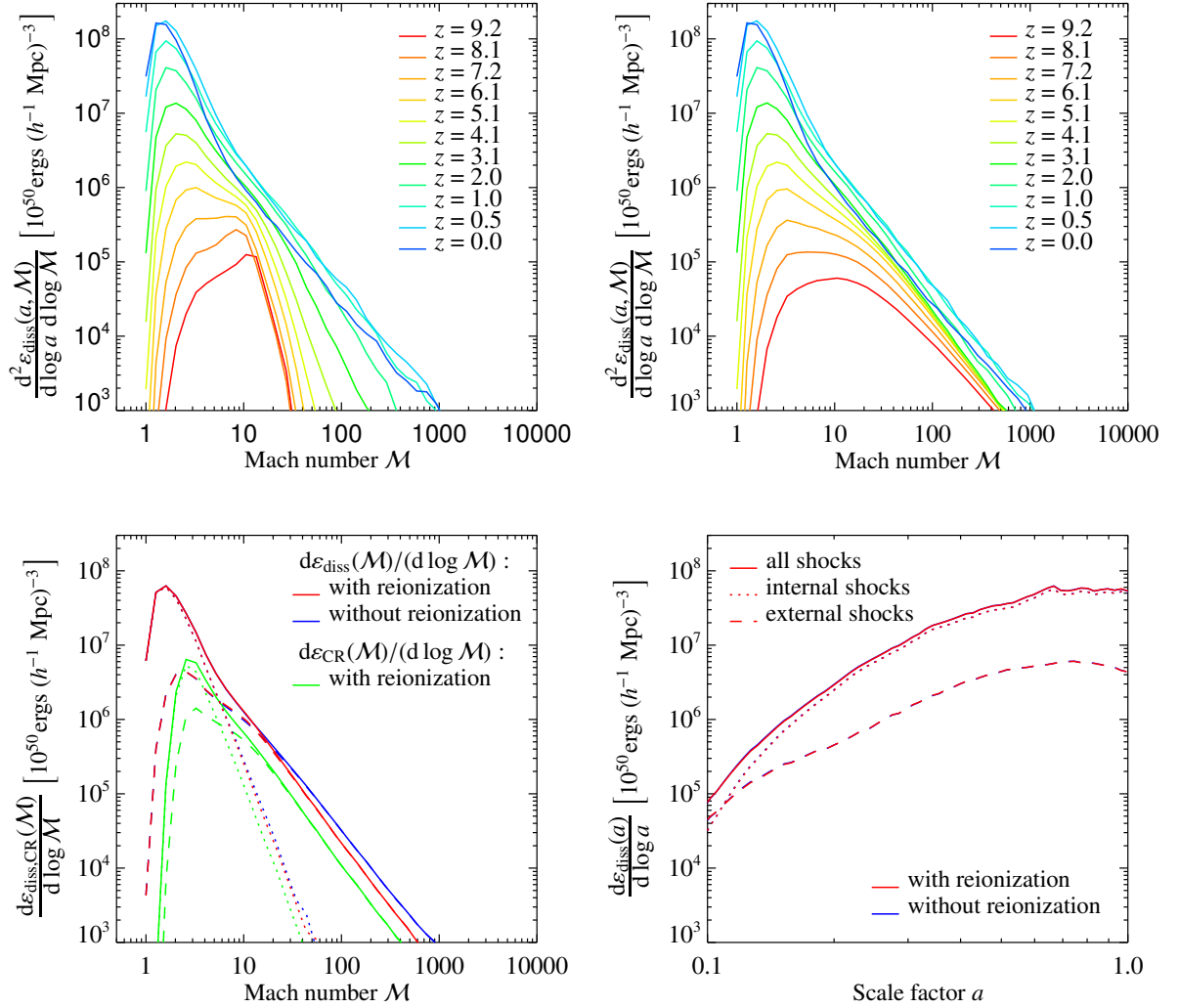
Figure 10.6.: Influence of reionization on the Mach number statistics of non-radiative cosmological simulations. The *top left panel* shows the differential Mach number distribution $\mathrm{d}^2\varepsilon_{\mathrm{diss}}(a, \mathcal{M})/(\mathrm{d}\log a\, \mathrm{d}\log \mathcal{M})$ for our reference simulation with reionization while the *top right panel* shows this distribution for the simulation without reionization. The *lower left panel* shows both distributions integrated over the scale factor, $\mathrm{d}\varepsilon_{\mathrm{diss}}(\mathcal{M})/(\mathrm{d}\log \mathcal{M})$ in addition to the Mach number distribution weighted by the injected CR energy rate normalized to the simulation volume, $\mathrm{d}\varepsilon_{\mathrm{CR}}(\mathcal{M})/(\mathrm{d}\log \mathcal{M})$ (green). Internal shocks are shown with dotted lines and external shocks with dashed lines. The *lower right panel* shows the evolution of the dissipated energy due to shock waves with scale factor, $\mathrm{d}\varepsilon_{\mathrm{diss}}(a)/(\mathrm{d}\log a)$. The models with and without reionization lie on top of each other.
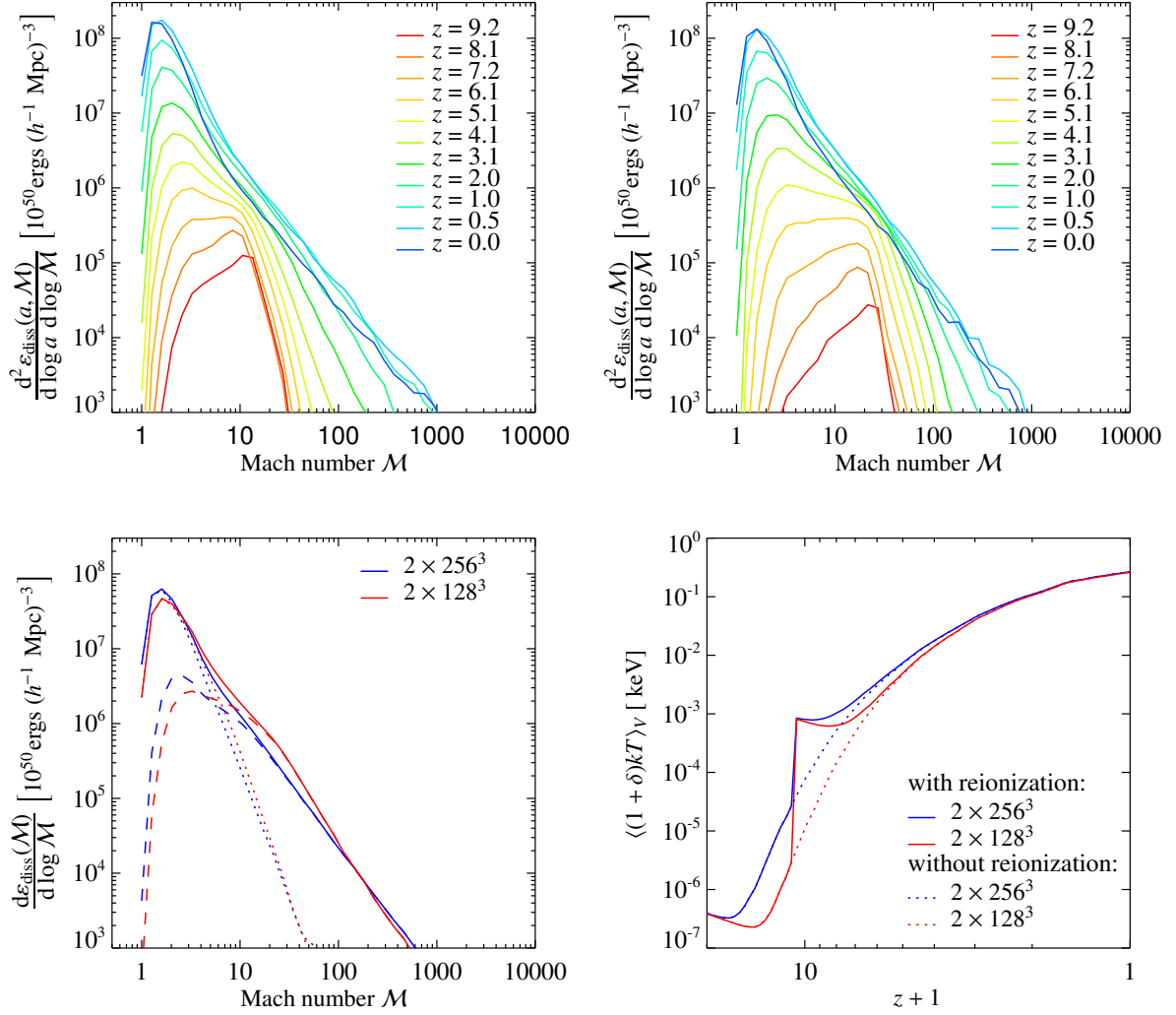
Figure 10.7.: Resolution study: Mach number statistics for non-radiative cosmological simulations with a reionization epoch at $z = 10$. The *top left panel* shows the differential Mach number distribution $d^2\varepsilon_{diss}(a, \mathcal{M})/(d \log a\, d \log \mathcal{M})$ for our reference simulation with a resolution of 2×256^3 while the *top right panel* shows this distribution for the simulation with a resolution of 2×128^3. The *lower left panel* shows both distributions integrated over the scale factor, $d\varepsilon_{diss}(\mathcal{M})/(d \log \mathcal{M})$. Internal shocks are shown with dotted lines and external shocks with dashed lines. The *lower right panel* shows the evolution of the density-weighted temperature with redshift. Shown are different resolutions in our models with and without reionization.

10.6.3.2. Cosmic ray acceleration

In our non-radiative cosmological simulations we additionally calculate the expected shock-injected CR energy using our formalism of diffusive shock acceleration described in Enßlin et al. (2005). This formalism follows a model based on plasma physics for the leakage of thermal ions into the CR population. However, in the present analysis, the injected CR energy $du_{CR,inj}/(d \log a)$ was only monitored and not dynamically tracked. In our model, the CR population is described by single power-law distribution which is uniquely determined by the dimensionless momentum cutoff q, the normalization C, and the spectral index α. Considering shock injected CRs only, the spectral index is determined by $\alpha = (x_s + 2)/(x_s - 1)$, where x_s denotes the density jump at the shock.

Our simplified model for the diffusive shock acceleration fails in the limit of weak shocks and over-predicts the injection efficiency. Especially in this regime, Coulomb losses have to be taken into account which remove the low-energetic part of the injected CR spectrum efficiently on a short timescale giving rise to an effective CR energy efficiency. Thus, the instantaneous injected CR energy $du_{CR,inj}/(d \log a)$ depends on the simulation timestep and the resolution. To provide a resolution independent statement about the injected CR energy, we decided to rethermalize the injected CR energy below the cutoff $q_{threshold} = 0.83$. This cutoff has the desired property, that it coincides with the kinematic threshold of the hadronic CR p-p interaction to produce pions which decay into secondary electrons (and neutrinos) and γ-rays:

$$\pi^{\pm} \quad \rightarrow \quad \mu^{\pm} + \nu_{\mu}/\bar{\nu}_{\mu} \rightarrow e^{\pm} + \nu_e/\bar{\nu}_e + \nu_{\mu} + \bar{\nu}_{\mu}$$
$$\pi^{0} \quad \rightarrow \quad 2\gamma \,.$$

Only CR p above this kinematic threshold are therefore visible through their decay products in both the γ-ray and radio bands via radiative processes, making them directly observationally detectable.

The lower left panel of Fig. 10.6 shows the Mach number distribution weighted by the injected CR energy rate and normalized to the simulation volume, $d\varepsilon_{CR}(\mathcal{M})/(d \log \mathcal{M})$ (solid green). The effect of the CR injection efficiency $\zeta_{inj} = \varepsilon_{CR}/\varepsilon_{diss}$ can easily be seen: while the CR injection is saturated for strong shocks to $\zeta_{max} = 0.5$, in weak shocks most of the dissipated energy is thermalized and only small parts are used for the acceleration of relativistic particles. Effectively, this shifts the maximum and the mean value of the Mach number distribution weighted by the shock-dissipated energy towards higher values in the case of the distribution weighted by the injected CR energy. This effect is even stronger when considering only CRs with a lower cutoff $q = 10, 30$ which are responsible for radio halos observed at frequencies above 100 MHz, assuming typical magnetic field strengths of $B = 10, 1 \, \mu G$, respectively. This follows from the mono-energetic approximation of the hadronic electron production and synchrotron formula,

$$\nu_s = \frac{3eB}{2\pi m_e c} \gamma_e^2, \quad \text{where} \quad \gamma_e \simeq \frac{q}{16} \frac{m_p}{m_e} \tag{10.40}$$

and e denotes the elementary charge.

As the regime of strong shocks is dominated by external shocks where the CR injection is saturated, CRs are dynamically more important in dilute regions and dynamically less important at the cluster centers compared to the thermal non-relativistic gas. As weak shocks are mainly internal shocks we have to distinguish between their different appearance: strong internal shocks are most probably accretion shocks produced by infalling gas from sheets or filaments towards clusters, or peripherical merger shocks which steepen as they propagate outwards in the shallow cluster potential, highlighting the importance of CR injection in the outer cluster regions relative to thermally dissipated gas at shocks. In contrast, CR injection is dynamically less important in the case of flow shocks at the cluster centers or merging shock waves traversing the cluster center. From these considerations we again draw the important conclusion that the ratio of CR injected energy to dissipated thermal energy at shocks is an increasing function of decreasing density. Such a CR distribution is required within galaxy clusters to explain the diffuse radio synchrotron emission of galaxy clusters (so-called radio halos) within the hadronic model of secondary electrons. For that, we assume a stationary CR electron spectrum which balances hadronic injection of secondaries and synchrotron and inverse Compton cooling processes (Brunetti 2002, Pfrommer & Enßlin 2004a,b). However, to make more precise statements about the origin of cluster radio halos, more work is needed which studies the effect of the CR dynamics including CR diffusion and other CR injection processes such as supernovae driven galactic winds.

10.6.3.3. Resolution study

To study numerical convergence we perform two additional simulations with a resolution of 2×128^3, respectively, for our models with and without reionization. Figure 10.7 shows this resolution study for non-radiative cosmological simulations with a reionization epoch at $z = 10$. The lower right panel of Fig. 10.7 shows the evolution of the density-weighted temperature with redshift, $\langle (1 + \delta)T \rangle_V (z)$. Shown are different resolutions in our models with and without reionization. The two differently resolved simulations (2×256^3 and 2×128^3) have converged well at redshifts $z \lesssim 4$. In our reference simulation, the adiabatic decay of the mean temperature is halted at slightly higher redshift: because of the better mass resolution of this simulation, nonlinear structures of smaller mass can be resolved earlier while converting part of their gravitational binding energy into internal energy through structure formation shock waves. In the simulation with reionization, the temperature increases discontinuously at $z = 10$, declines again with the adiabatic expansion, until shock heating takes over at $z \sim 7 - 8$ (depending on the resolution of the simulation). At $z = 0$, all simulations yield a mean density-weighted temperature of $\simeq 0.3$ keV. Comparing this density-weighted energy to the shock-deposited mean energy per particle of $E_{\mathrm{diss}} \simeq 0.63$ keV, we obtain the mean adiabatic compression factor of the cosmic plasma, $\{kT/[(\gamma - 1)E_{\mathrm{diss}}]\}^{1/(\gamma-1)} \simeq 0.6$. After the plasma has been shock-heated, relaxation processes in the course of virialization let the plasma expand adiabatically on average. Secondly, mildly non-linear structures characterized by a shallow gravitational potential are partly effected by the Hubble flow which forces them to adiabatically expand.

The top left panel shows the differential Mach number distribution $\mathrm{d}^2\varepsilon_{\mathrm{diss}}(a, \mathcal{M})/(\mathrm{d}\log a\,\mathrm{d}\log\mathcal{M})$ for our reference simulation with a resolution of 2×256^3 while the top right panel shows this distribution for the simulation with a resolution of 2×128^3. The lower left panel shows both distributions integrated over the scale factor, $\mathrm{d}\varepsilon_{\mathrm{diss}}(\mathcal{M})/(\mathrm{d}\log\mathcal{M})$. Internal shocks are shown with dotted lines and external shocks with dashed lines. One immediately realizes that the question if the first shocks are fully converged among simulations of different resolution is not well posed because nonlinear structures of smaller mass can be resolved collapsing earlier in higher resolution simulations. Accordingly, the differential Mach number distribution is not well converged at redshifts $z \gtrsim 6$ while the distribution is well converged for $z \lesssim 3$. Since most of the energy is dissipated at late times, where our differential Mach number distribution is well converged, the integrated distribution $\mathrm{d}\varepsilon_{\mathrm{diss}}(\mathcal{M})/(\mathrm{d}\log\mathcal{M})$ shows only marginal differences among the differently resolved simulations. In particular, our statements about CR injection at structure formation shocks are robust with respect to resolution issues.

10.7. Summary and conclusions

We provide a formalism for identifying and estimating the strength of structure formation shocks in cosmological SPH simulations on-the-fly, both for non-relativistic thermal gas as well as for a plasma composed of a mixture of cosmic rays (CRs) and thermal gas. In addition, we derive an analytical solution to the one-dimensional Riemann shock tube problem for the composite plasma of CRs and thermal gas (Appendix B.2). In the case of non-relativistic thermal gas, shock-tube simulations within a periodic three-dimensional box that is longer in x-direction than in the other two dimensions show that our formalism is able to unambiguously detect and accurately measure the Mach numbers of shocks, while in the case of plasma composed of cosmic rays (CRs) and thermal gas, the Mach numbers of shocks are estimated with an accuracy better than 10%. In both cases, we find a very good agreement of the averaged simulated hydrodynamical quantities (such as density, pressure, and velocity) and the analytical solutions. Using our formalism for diffusive shock acceleration, we additionally calculate and monitor the shock-injected CR energy, but without dynamically tracking this CR energy component; the latter will be studied in forthcoming work. The good agreement between the simulated and theoretically expected shock-injected CR energy demonstrates that our formalism is reliably able to accelerate CRs instantaneously during the simulation.

Subsequently, we identified and studied structure formation shock waves using cosmological N-body/ hydrodynamical SPH simulations for a concordance ΛCDM universe in a periodic cubic box of comoving size $100\,h^{-1}$Mpc. We performed simulations with and without a reionization epoch at $z = 10$ in order to investigate the effects of reionization on the Mach number distribution. Our sets of simulations follow only non-radiative gas physics where we neglected additional physical processes, such as radiative cooling, star formation, and feedback from galaxies and stars including cosmic ray pressure. Since we are mainly interested in shock waves situated mostly outside the cluster core regions, the conclusions drawn in this chapter should not be significantly weakened by the exclusion of those radiative processes. Furthermore, these simplifications align our work with the mesh-based simulations of

Ryu et al. (2003) and enable a direct comparison and verification of our results. We classify cosmological shock waves as internal and external shocks, depending on whether or not the associated pre-shock gas was previously shocked (cf. Ryu et al. 2003). Rather than using a thermodynamical criterion such as the temperature, we prefer a density criterion such as the overdensity δ in order not to confuse the shock definition once we will follow radiatively cooling gas in galaxies. External shocks surround filaments, sheets, and halos where the pristine adiabatically cooling gas is shocked for the first time. Internal shocks on the other hand are located within the regions bound by external shocks and are created by flow motions accompanying hierarchical structure formation. Their population includes accretion shocks produced by infalling material along the filaments into clusters, merger shocks resulting from infalling halos, and flow shocks inside nonlinear structures which are excited by supersonic motions of subclumps.

The Mach number distribution weighted by the dissipated energy shows in detail that most of the energy is dissipated in weak shocks which are situated in the internal regions of groups or clusters while collapsed cosmological structures are surrounded by external strong shocks which have a minor impact on the energy balance. The evolution of the Mach number distribution shows that the average shock strength becomes weaker at later times while there is an increasing amount of energy dissipated at shock waves as cosmic time evolves because the mean shock speed increases together with the characteristic mass of halos forming during cosmic structure formation. For the same reason, internal shocks play a more important role than external shocks in dissipating energy associated with structure formation, especially at small redshift. The energy input through reionization processes influences the Mach number distribution primarily during a period following the reionization era and suppresses strong external shock waves efficiently because of the significant increase of the sound speed of the inter-galactic medium.

Weighting the Mach number distribution by the injected CR energy shows the potential dynamical implications of CR populations in galaxy clusters and halos: the maximum and the mean value of the Mach number distribution, weighted by the shock-dissipated energy, is effectively shifted towards higher values of the Mach number when the distribution is weighted by the injected CR energy. In other words, the average shock wave responsible for CR energy injection is stronger compared to the average shock which thermalizes the plasma. The fundamental reason for this lies in the theory of diffusive shock acceleration at collisionless shock waves and can be phenomenologically described by a CR injection efficiency: while the CR injection is saturated to an almost equipartition value between injected CR energy and dissipated thermal energy for strong shocks, in weak shocks most of the dissipated energy is thermalized and only small parts are used for the acceleration of relativistic particles. Relative to the thermal non-relativistic energy density, the shock-injected CR energy density is dynamically more important at the outer dilute cluster regions and less important at the cluster centers since weak shock waves predominantly occur in high-density regions. This has the crucial consequence that the ratio of CR injected energy to dissipated thermal energy is an increasing function as the density declines. Such a CR distribution within galaxy cluster is required to explain the diffuse radio synchrotron emission of galaxy clusters (so-called radio halos) within the hadronic model of secondary electrons. In order to draw thorough conclusions about the origin of cluster radio halos, more work is needed which studies the effect of the CR dynamics comprising of CR injection and cooling processes as well as CR diffusion mechanisms.

We note that our new formalism for shock-detection in SPH simulations should have a range of interesting applications in simulations of galaxy formation. For example, when combined with radiative dissipation and star formation, our method can be used to study CR injection by supernova shocks, or to construct models for shock-induced star formation in the interstellar medium (e.g. Barnes 2004). It should also be useful to improve the accuracy of predictions for the production of γ-rays by intergalactic shocks (e.g. Keshet et al. 2003).

The results of this chapter were worked out in collaboration with V. Springel, T.A. Enßlin, and M. Jubelgas. A paper entitled "Structure formation shocks in cosmological SPH simulations with relativistic particle populations" *will be submitted to the journal* Monthly Notices of the Royal Astronomical Society.

11. Conclusions and theoretical prospects

In each of the proceeding chapters, I gave a discussion and conclusions of the main results found in the corresponding sections. Here, I will reiterate the most important findings and conclusions while putting them into a cosmological context and pointing out the future perspective.

In this thesis, I studied non-equilibrium processes such as cosmic rays (CRs) and magnetic fields in clusters of galaxies. The influence of these non-thermal components on structure formation and galaxy evolution has been neglected so far despite their importance. Although the standard model of concordance cosmology began its triumphant success supported by various observations and numerical simulations, a few observational discrepancies with the standard model on galactic scales challenge this successful picture. Some of the inconsistencies may be circumvented by additionally considering the certainly existent non-thermal components. The advent of multi-faced γ-ray astronomy with the third generation of Čerenkov telescopes and the future satellite mission GLAST (*Gamma-ray Large Area Space Telescope*) as well as new development in radio astronomy with the extended VLA (*Very Large Array*) and the future LOFAR (*LOw Frequency ARray*) project call for advances in theoretical and numerical astrophysics of non-thermal phenomena.

This thesis is organized into two main parts: the first major part is dedicated to an analytical study of CR protons in clusters of galaxies and their hadronic interactions with the ambient thermal plasma using multi-frequency observational results. This detailed study is followed by a theoretical proposal for an observation aiming at unveiling the still unknown dynamically dominant CR component of radio plasma bubbles. In the second part, a description of CR gas for cosmological applications especially suited for hydrodynamical simulations is presented. In the course, I focus on developing a formalism of instantaneously identifying and estimating the strength of structure formation shocks during cosmological simulations to accelerate CRs through diffusive shock acceleration.

The first main part starts with Chapter 5, where I provide a theoretical framework for analytically modeling multi-frequency signatures resulting from hadronic CR proton interactions with protons of the ambient thermal plasma. These interactions produce charged and neutral pions which successively decay into γ-rays and relativistic electrons or positrons. The γ-ray source function resulting from decaying neutral pions is presented for two analytical models that describe this hadronic reaction: the simpler *fireball model* assumes a state of hot quark-gluon plasma in thermal equilibrium after the hadronic interaction that subsequently ablates pions with energy dependent multiplicities. Motivated by accelerator experiments, *Dermer* proposed a model that is able to make detailed predictions for the pion decay induced γ-ray spectrum while including more realistic effects near the pion production threshold. Using the newly developed γ-ray source function, I derive an analytic relation between the γ-ray and bolometric X-ray fluxes: this relation can find application in compiling a suitable sample of galaxy clusters which are promising candidates for future detection of diffuse γ-rays. The stationary spectrum of hadronically originating secondary electrons is presented furthermore. It allows the calculation of accompanying synchrotron and inverse Compton emission and yields thus additional and complementary information about the non-thermal energetic content of clusters. Unlike hadronically induced γ-ray emission, these non-thermal emission processes of secondary CR electrons provide however a biased tracer of the underlying CR proton population due to the presence of possibly different CR electron populations and the degeneracy of the synchrotron emissivity with magnetic energy density.

In Chapter 6, I apply this theoretical framework to clusters of galaxies in order to investigate the question of the dynamical influence of CRs on the intra-cluster medium (ICM). Using the analytic relation between γ-ray and bolometric X-ray fluxes, I identify a sample of observationally promising cluster candidates (including cooling core clusters) for constraining the CR proton population. The spatial distribution of CRs within the ICM is assumed to follow three different scenarios: in the isobaric model, the CR energy density is assumed to be proportional to the thermal energy density of the ICM, i.e. $X_{CR} = \varepsilon_{CR}/\varepsilon_{th}$. In the scenario of adiabatic compression of CRs during the formation of the cooling core, this proportionality is imposed prior to the transition. A third model assumes a single central point source injecting the CRs whose final distribution is governed by diffusion. Comparing to EGRET (*Energetic Gamma Ray Experiment Telescope*) upper limits on the γ-ray emission, I am able to constrain the CR

proton population in the central regions of nearby galaxy clusters to $X_{\mathrm{CRp}} < 20\%$. This demonstrates that CRs are not dynamically dominating the central cluster regions although the presence of CRs may thermodynamically stabilize the cooling core. Additionally, I examine the CR proton population within the giant elliptical galaxy M 87 using the TeV γ-ray detection of the HEGRA (*High Energy Gamma Ray Astronomy*) collaboration. Both the expected radial γ-ray profile and the required amount of CRs support this hadronic scenario.

Furthermore, I study the hypothesis that the diffuse radio synchrotron emission of galaxy clusters is produced by hadronically originating relativistic electrons. Excellent agreement between the observed and theoretical radio brightness profiles is obtained for the radio mini halo in Perseus. Since the CR proton and magnetic energy densities necessary to reproduce the observed radio flux are very plausible, I propose synchrotron emission from secondary electrons as an attractive explanation of the radio mini-halos found in cooling core clusters. To explain the giant radio halo of Coma with the hadronic model of secondary electrons, the CR proton-to-thermal energy density profile has to increase radially up to a moderate CR energy density of $X_{\mathrm{CR}} \sim 10\%$ while assuming plausible parameters for the magnetic field and CRs. This model can be tested with future sensitive γ-ray observations of the accompanying π^0-decays. Understanding the underlying formation mechanism of radio halos would open up a complementary observational window for studies of the dynamical evolution and the interplay of different astrophysical processes in galaxy clusters.

The trilogy of hadronic CR interaction is completed with Chapter 7 where I estimate magnetic field strengths and CR energy densities of radio emitting galaxy clusters by minimizing the non-thermal energy density contained in CR electrons, protons, and magnetic fields. The *classical* minimum energy estimate can be constructed independently of the origin of the radio synchrotron emitting CR electrons yielding thus an absolute minimum of the non-thermal energy density. Provided the observed synchrotron emission is generated by a CR electron population originating from hadronic CR proton interactions, I introduce the *hadronic* minimum energy criterion which is a non-parametric approach yielding an absolute minimum energy state and provides a solid foundation to scrutinize the hadronic model on the basis of radio synchrotron emission alone. For both approaches, I derive the theoretically expected tolerance regions for the inferred minimum energy densities. Application to the radio halo of the Coma cluster and the radio mini-halo of the Perseus cluster yields equipartition between cosmic rays and magnetic fields within the expected tolerance regions. In the hadronic scenario, the inferred central magnetic field strength ranges from 2.4 μG (Coma) to 8.8 μG (Perseus), while the optimal CRp energy density is constrained to 2% ± 1% of the thermal energy density (Perseus). Using the non-parametric minimum energy approach, I discuss the possibility of a hadronic origin of the Coma radio halo while current observations favor such a scenario for the Perseus radio mini-halo. Combining future expected detections of radio synchrotron, hard X-ray inverse Compton, and hadronically induced γ-ray emission should allow an estimate of volume averaged cluster magnetic fields and provide information about their dynamical state.

The previously presented methods for investigating the CR population are predominantly sensitive to the central cluster regions due the present high plasma densities and magnetic field strengths. The *Chandra* X-ray Observatory is finding a large number of cavities in these central cooling core regions of the X-ray emitting intra-cluster medium which often coincide with the lobes of the central radio galaxy. Usually, it is assumed that these cavities are partly or completely inflated by CR gas of unknown composition (electron/proton or electron/positron gas). In Chapter 8, I propose high-resolution Sunyaev-Zel'dovich (SZ) observations to infer the still unknown dynamically dominant component of the radio plasma bubbles. To this end, I calculate the thermal and relativistic SZ emission of different compositions of these plasma bubbles while simultaneously allowing for the cluster's kinetic SZ effect. As examples, I present simulations of an ALMA (*Atacama Large Millimeter Array*) observation and of a GBT (*Green Bank Telescope*) observation of the cores of the Perseus cluster and Abell 2052. I predict a 5σ detection of the southern radio bubble of Perseus in a few hours with the GBT and ALMA while assuming a relativistic electron population within the bubble. In Abell 2052, a similar detection would require a few tens of hours with either telescope, the longer exposures mainly being the result of the higher redshift and the lower central temperature of this cluster. Future high-sensitivity multi-frequency SZ observations will be able to infer the energy spectrum of the dynamically dominant electron population in order to measure its temperature or spectral characteristics. This knowledge can yield indirect indications for an underlying radio jet model.

In the second major part of my thesis, I address the problem of constructing an accurate and self-consistent numerical model for the description of CRs that aims at studying the dynamical influence of CRs on structure formation and galaxy evolution. Galactic non-equilibrium processes like shock waves and turbulence have generated magnetic fields and CRs in the interstellar medium. These CRs play a decisive role within our Galaxy: their pressure, along with that of the thermal gas, balances gravity, they trace past energetic events such as supernovae, and they reveal

the underlying structure of the baryonic matter distribution through their interactions. In collaboration with Torsten Enßlin, I develop in Chapter 9 an approximative framework to treat dynamical and radiative effects of CRs in cosmological simulations. The guiding principle is a balance between capturing as many physical properties of CR populations as possible while simultaneously requiring as little extra computational resources as possible. The CR spectrum is approximated by a single, constant spectral index power-law, with spatially and temporal varying normalization and low-energy cutoff. Particle number and energy conservation principles are used to derive evolution equations for the basic variables due to adiabatic and non-adiabatic processes. Such are compression, rarefaction, CR injection via both shocks of supernova remnants and structure formation shock waves, in-situ reacceleration of CRs, CR spatial diffusion, CR energy losses due to Coulomb interactions, Bremsstrahlung, and hadronic interactions with the background gas, including the associated γ-ray and radio emission due to subsequent pion decay. Furthermore, we explain how the formalism can be included into smoothed-particle-hydrodynamics simulations.

Finally, in Chapter 10, I develop a formalism for the identification and accurate estimation of the strength of structure formation shocks *during* cosmological smoothed particle hydrodynamics simulations. Shocks not only play a decisive role for the thermalization of gas in virializing structures but also for the acceleration of CRs through diffusive shock acceleration. The formalism is applicable both to ordinary non-relativistic thermal gas, and to plasmas composed of CRs and thermal gas. To this end, I derive an analytical solution to the one-dimensional Riemann shock tube problem for a composite plasma of CRs and thermal gas. I apply these methods to study the properties of structure formation shocks in high-resolution hydrodynamic simulations of the ΛCDM model. I find that most of the energy is dissipated in weak internal shocks which are predominantly central flow shocks or merger shock waves traversing halo centers. Collapsed cosmological structures are surrounded by external shocks with much higher Mach number, but they play only a minor role in the energy balance of thermalization. I show that after the epoch of cosmic reionization, the Mach number distribution is significantly modified by an efficient suppression of strong external shock waves due to the associated increase of the sound speed of the diffuse gas. Invoking a model for CR acceleration in shock waves, I find that the average strength of shock waves responsible for CR energy injection is higher than for shocks that dominate the thermalization of the gas. This implies that the dynamical importance of the shock-injected CR energy density is largest in the low-density halo infall regions, but is dynamically less important for the weaker shocks occurring in central high-density regions of halos.

The developed numerical methods open up new possibilities to investigate the cosmological role of CR protons while potentially providing the footing for answering some cosmological problems. At the centers of non-merging galaxy clusters, the relaxation process is instable and would theoretically lead to catastrophic cooling of cluster cooling cores which is absent in X-ray observations. The interplay of active galactic nuclei with the ambient plasma in connection with CRs may play a significant role in the solution to this so-called *cluster cooling flow problem* because CRs provide a temperature floor which thermodynamically stabilizes the cooling system. Strong galactic winds might be driven by CR protons through Parker instabilities of spiral disks leading to the chemical enrichment of the intergalactic medium. This mechanism might solve the *enrichment problem* of high iron abundances of the intra-cluster medium. Hydrodynamical simulations of the CR component allow realistic predictions of radio synchrotron, inverse Compton, and γ-ray emission. This is indispensable for the interpretation of future observations in these wavelength regimes.

In our Galaxy, the energy density of the CR component is in equipartition with the thermal and the magnetic energy density. Tracing this CR population self-consistently may solve problems of the standard cosmological model on galactic scales. To reconcile the amount of halo substructure in numerical simulations and observations, star formation has to be efficiently suppressed in low mass substructure within hydrodynamical simulations. The slow cooling CR component is able to prevent these system from forming stars by blowing up the galactic gas disk which is an elegant solution to this *substructure problem*. Using the formalism of instantaneously identifying and accurately estimating the strength of shock waves, one can also address the problem of diffusive shock acceleration at supernova remnants and simulate the resulting radiative processes. Cross-correlating the simulated maps with those obtained from multi-frequency observations can yield important insight into plasma physical processes at supernova shocks. Thus, successful studies of non-equilibrium processes in structure formation and galaxy evolution might provide the opportunity of interesting future discoveries and resolve some cosmological problems. This would be an important step towards a coherent understanding of cosmology.

A. Deprojection of X-ray surface brightness profiles represented by double-β profiles

Owing to the enhanced electron density in the central region the X-ray surface brightness profile $S_X(r_\perp)$ in cooling flow cluster can be represented by double β models,

$$S_X(r_\perp) = \sum_{i=1}^{2} S_i \left[1 + \left(\frac{r_\perp}{r_{c_i}} \right)^2 \right]^{-3\beta_i + 1/2}, \tag{A.1}$$

where the X-ray surface brightness profile is a line of sight projection of the squared electron density and the cooling function relative to the squared electron density $\tilde{\Lambda}_X(T_e)$,

$$S_X(r_\perp) = \int_{-\infty}^{\infty} dz\, n_e^2 \left(\sqrt{r_\perp^2 + z^2} \right) \tilde{\Lambda}_X \left[T_e \left(\sqrt{r_\perp^2 + z^2} \right) \right] \tag{A.2}$$

$$= 2 \int_{r_\perp}^{\infty} dr\, \frac{r\, n_e^2(r)\, \tilde{\Lambda}_X[T_e(r)]}{\sqrt{r^2 - r_\perp^2}}. \tag{A.3}$$

Thus the electron density $n_e(r)$ can be derived from $S_X(r_\perp)$ by inverting the Abel equation

$$n_e^2(r)\, \tilde{\Lambda}_X[T_e(r)] = -\frac{1}{\pi r} \frac{d}{dr} \int_r^{\infty} dy\, \frac{y\, S_X(y)}{\sqrt{y^2 - r^2}} \tag{A.4}$$

$$= -\frac{1}{\pi} \int_r^{\infty} dy\, \frac{S_X'(y)}{\sqrt{y^2 - r^2}}, \tag{A.5}$$

where the prime denotes the derivative. For the second equation we used that $n_e(r)$ is bounded for $r \to \infty$. Using Eq. (A.1) this equation can be solved analytically yielding

$$n_e^2(r) = \frac{1}{\tilde{\Lambda}_X[T_e(r)]} \sum_{i=1}^{2} \frac{S_i}{2\pi r_{c_i}} \frac{6\beta_i - 1}{\left(1 + r^2/r_{c_i}^2 \right)^{3\beta_i}} \mathcal{B} \left(\frac{1}{2}, 3\beta_i \right), \tag{A.6}$$

where $\mathcal{B}(a, b)$ denotes the beta-function (Abramowitz & Stegun 1965). Provided the central density $n_e(0)$ is known and assuming furthermore the special case of equality of the two β parameter, $\beta_1 = \beta_2$, we arrive at the following compact formula for the electron density profile $n_e(r)$

$$n_e(r) = \left[\frac{\tilde{\Lambda}_X[T_e(0)]}{\tilde{\Lambda}_X[T_e(r)]} \times \sum_{i=1}^{2} n_i^2 \left(1 + \frac{r^2}{r_{c_i}^2} \right)^{-3\beta} \right]^{1/2}, \tag{A.7}$$

$$n_i = n_e(0) \left(\sum_{j=1}^{2} \frac{S_j\, r_{c_i}}{S_i\, r_{c_j}} \right)^{-1/2}. \tag{A.8}$$

Generalizing to n-fold β-profiles can be obtained by means of induction.

B. Riemann shock tube problem

B.1. Shock tube with thermal gas

The Riemann shock-tube calculation of Sod (1978) has become a generally accepted test of numerical hydrodynamical codes. As a baseline for later extension, we present in the section the quasi-analytical solution for the Riemann problem in the standard case of a polytropic gas. Then, in Appendix B.2 we derive the quasi-analytic solution in the case of a gas composed of CRs and thermal gas, where the effective adiabatic index depends on the different equations of state and changes across the shock-tube.

In the following, we summarize the key considerations which lead to the solution of the Riemann problem, for completeness (see e.g. Courant & Friedrichs 1948, Toro 1997, Rasio & Shapiro 1991, for a compact representation). For the initial state, we assume a state with higher pressure in the left half-space without loss of generality. At any time $t > 0$, this leads to the development of five regions of gas with different hydrodynamical states which are numbered in ascending order from the right. These regions are separated by the head and the tail of the leftwards propagating rarefaction wave, and the rightwards propagating contact discontinuity and the shock wave. Mass, momentum and energy conservation laws are represented by the generalized Rankine-Hugoniot conditions for a given coordinate system:

$$
\begin{aligned}
v_d[\rho] &= [\rho v], \\
v_d[\rho v] &= [\rho v^2 + P], \\
v_d\left[\rho\frac{v^2}{2} + \varepsilon\right] &= \left[\left(\rho\frac{v^2}{2} + \varepsilon + P\right)v\right].
\end{aligned}
\tag{B.1}
$$

Here v_d denotes the speed of the discontinuity under consideration with respect to our coordinate system and we introduced the abbreviation $[F] = F_i - F_j$ for the jump of some quantity F across the discontinuity. Within the leftwards propagating rarefaction wave, the generalized Riemann invariants yield an isentropic change of state, $ds = 0$, and conserve the quantity Γ^+:

$$
\Gamma^+ = v + \int_0^\rho \frac{c(\rho')}{\rho'}\,d\rho' = v + \frac{2\,c(\rho)}{\gamma - 1} = \text{const.}
\tag{B.2}
$$

For the last step, we assumed a polytropic equation of state $P = A\rho^\gamma$. Appropriately combining these equations, the solution can be expressed as follows:

$$
\rho(x, t) =
\begin{cases}
\rho_5, & x \le -c_5 t, \\
\rho_5\left[-\mu^2\frac{x}{c_5 t} + (1 - \mu^2)\right]^{2/(\gamma-1)}, & -c_5 t < x \le -v_t t, \\
\rho_3, & -v_t t < x \le v_2 t, \\
\rho_2, & v_2 t < x \le v_s t, \\
\rho_1, & x > v_s t,
\end{cases}
\tag{B.3}
$$

$$
P(x, t) =
\begin{cases}
P_5, & x \le -c_5 t, \\
P_5\left[-\mu^2\frac{x}{c_5 t} + (1 - \mu^2)\right]^{2\gamma/(\gamma-1)}, & -c_5 t < x \le -v_t t, \\
P_2 = P_3, & -v_t t < x \le v_s t, \\
P_1, & x > v_s t,
\end{cases}
\tag{B.4}
$$

$$
v(x, t) =
\begin{cases}
0, & x \le -c_5 t, \\
(1 - \mu^2)\left(\frac{x}{t} + c_5\right), & -c_5 t < x \le -v_t t, \\
v_2 = v_3, & -v_t t < x \le v_s t, \\
0, & x > v_s t.
\end{cases}
\tag{B.5}
$$

Here $\mu^2 = (\gamma - 1)/(\gamma + 1)$, $c_1 = \sqrt{\gamma P_1/\rho_1}$, and $c_5 = \sqrt{\gamma P_5/\rho_5}$ are the speeds of sound, v_t is the speed of propagation of the rarefaction wave's tail, and v_s is the shock speed. The post-shock pressure is obtained by solving (numerically) the non-linear equation, which is derived from the Rankine-Hugoniot conditions over the shock while ensuring the conservation of the two Riemann invariants of Eqn. (B.2):

$$\left(\frac{P_2}{P_1} - 1\right) \sqrt{\frac{1 - \mu^2}{\gamma \left(P_2/P_1 + \mu^2\right)}} - \frac{2}{(\gamma - 1)} \frac{c_5}{c_1} \left[1 - \left(\frac{P_2}{P_5}\right)^{(\gamma-1)/(2\gamma)}\right] = 0. \tag{B.6}$$

The density on the left of the contact discontinuity is $\rho_3 = \rho_5 (P_2/P_5)^{1/\gamma}$, since the gas is adiabatically connected to the left. The post-shock density ρ_2 is also derived from the Rankine-Hugoniot conditions,

$$\rho_2 = \rho_1 \left(\frac{P_2 + \mu^2 P_1}{P_1 + \mu^2 P_2}\right). \tag{B.7}$$

The post-shock gas velocity v_2 is obtained from the rarefaction wave equation, $x/t = v - c$, and usage of the Riemann invariant Γ^+:

$$v_2 = v_3 = \frac{2c_5}{(\gamma - 1)} \left[1 - \left(\frac{P_2}{P_5}\right)^{(\gamma-1)/(2\gamma)}\right], \tag{B.8}$$

and from Eqn. (B.5) we derive the speed of propagation of the rarefaction wave's tail $v_t = c_5 - v_2/(1 - \mu^2)$. Finally, mass conservation across the shock yields

$$v_s = \frac{v_2}{1 - \rho_1/\rho_2}. \tag{B.9}$$

B.2. Shock tube for a composite of cosmic rays and thermal gas

B.2.1. Derivation

In contrast to the previous case, the composite of CRs and thermal gas does not obey a polytropic equation of state. In this section, we present an analytical derivation of the Riemann shock-tube problem for the composite of polytropic gas and a component that is adiabatically compressed at the shock such as relativistic gas or a homogeneous magnetic field which is parallel to the shock front. For the analytical derivation, we adopt the following two approximations: (i) We assume the CR adiabatic index (Eqn. (10.6)) to be constant over the shock-tube, and (ii) we neglect CR diffusion. The first assumption is justified as long as the CR pressure is not dominated by trans-relativistic CRs of low energy while the second assumption is a strong simplification with respect to simulating realistic shocks including CRs (Kang & Jones 2005). However, including CR diffusion complicates the problem significantly such that it is not any more analytically tractable.

For the initial state, we again assume a state with higher pressure in the left half-space. At any time $t > 0$, five regions of gas with different hydrodynamical states coexist, and are numbered in ascending order from the right. We use the notation $P_i = P_{CR,i} + P_{th,i}$ and $\varepsilon_i = \varepsilon_{CR,i} + \varepsilon_{th,i}$ for the composite quantities in region i. The full solution of the initial value problem consists of determining 12 unknown quantities in the regions (2) and (3): ρ_2, v_2, P_{CR2}, P_{th2}, ε_{CR2}, ε_{th2}, and ρ_3, v_3, P_{CR3}, P_{th3}, ε_{CR3}, ε_{th3}. The thermal gas obeys a polytropic equation of state, i.e. $\varepsilon_{th,i} = P_{th,i}/(\gamma_{th} - 1)$ for $i \in \{2, 3\}$ and the regions (2) and (3) are separated by a contact discontinuity, implying vanishing mass flux through it and thus, $v_2 = v_3$ and $P_2 = P_3$. This reduces the dimensionality of our problem to 8 unknowns. In our approximation, the CRs are adiabatically expanded over the rarefaction wave and adiabatically compressed at the shock while obeying a polytropic equation of state:

$$
\begin{aligned}
P_{CR3} &= P_{CR5} \left(\frac{\rho_3}{\rho_5}\right)^{\gamma_{CR}}, & \varepsilon_{CR3} &= \varepsilon_{CR5} \left(\frac{\rho_3}{\rho_5}\right)^{\gamma_{CR}}, \\
P_{CR2} &= P_{CR1} \left(\frac{\rho_2}{\rho_1}\right)^{\gamma_{CR}}, & \varepsilon_{CR2} &= \varepsilon_{CR1} \left(\frac{\rho_2}{\rho_1}\right)^{\gamma_{CR}},
\end{aligned}
\tag{B.10}
$$

which further reduces the dimensionality by 4 unknowns. Moreover, the thermal gas is also adiabatically expanded over the rarefaction wave yielding $P_{th3} = P_{th5}(\rho_3/\rho_5)^{\gamma_{th}}$. Hence, we need 3 more linearly independent equations for the solution: 2 are obtained by considering the Rankine-Hugoniot conditions (Eqn. (B.1)) in a stationary system of

reference with $v_\mathrm{d} = v_\mathrm{s}$. The last equation is given by the Riemann invariant Γ^+, where the effective speed of sound is given by $c = \sqrt{\gamma_\mathrm{eff} P/\rho}$:

$$\Gamma^+ = v + \int_0^\rho \frac{c(\rho')}{\rho'} \mathrm{d}\rho' = v + I(\rho) = \mathrm{const.} \quad \mathrm{with} \quad I(\rho) = \int_0^\rho \sqrt{\tilde{A}_\mathrm{CR} x^{\gamma_\mathrm{CR}-3} + \tilde{A}_\mathrm{th} x^{\gamma_\mathrm{th}-3}} \mathrm{d}x. \tag{B.11}$$

Here, we use the abbreviations $\tilde{A}_i = \gamma_i A_i$ where $i \in \{\mathrm{th}, \mathrm{CR}\}$ and $A_i = P_i \rho^{-\gamma_i}$ denotes the invariant adiabatic function over the rarefaction wave. Introducing the difference of the adiabatic indices of the two populations, $\Delta\gamma = \gamma_\mathrm{th} - \gamma_\mathrm{CR}$, the solution to the integral $I(\rho)$ is given by

$$I(\rho) = \frac{\sqrt{\tilde{A}_\mathrm{CR}}}{\Delta\gamma} \left(\frac{\tilde{A}_\mathrm{CR}}{\tilde{A}_\mathrm{th}} \right)^{(\gamma_\mathrm{CR}-1)/(2\Delta\gamma)} \mathcal{B}_{x(\rho)} \left(\frac{\gamma_\mathrm{CR}-1}{2\Delta\gamma}, \frac{1-\gamma_\mathrm{th}}{2\Delta\gamma} \right) \quad \mathrm{with} \quad x(\rho) = \frac{\tilde{A}_\mathrm{th} \rho^{\gamma_\mathrm{th}}}{\tilde{A}_\mathrm{CR} \rho^{\gamma_\mathrm{CR}} + \tilde{A}_\mathrm{th} \rho^{\gamma_\mathrm{th}}}. \tag{B.12}$$

Although the second argument of the incomplete Beta-function is always negative, $I(\rho)$ is well defined as long as we consider a non-zero CR pressure which is characterized by $\tilde{A}_\mathrm{CR} > 0$, and γ_CR sufficiently far from γ_th, i.e. $\Delta\gamma > 0$. For $\tilde{A}_\mathrm{CR} = 0$, the integral can be solved in closed form, yielding $I(\rho) = 2c(\rho)/(\gamma_\mathrm{th} - 1)$.

B.2.2. Solution of the Riemann problem

The densities leftwards and rightwards of the contact discontinuity, ρ_3 and ρ_2, are obtained by solving (numerically) the following non-linear system of equations. It is derived from matching the possible post-shock states (pressure and density) with the possible post-rarefaction wave states while simultaneously ensuring the conservation laws over the rarefaction wave and the shock:

$$\begin{aligned} f_1(x_\mathrm{s}, x_\mathrm{r}) &\equiv [P_2(x_\mathrm{r}) - P_1](x_\mathrm{s} - 1) - \rho_1 x_\mathrm{s} [I(\rho_5) - I(x_\mathrm{r}\rho_5)]^2 &= 0, \\ f_2(x_\mathrm{s}, x_\mathrm{r}) &\equiv [P_2(x_\mathrm{r}) + P_1](x_\mathrm{s} - 1) + 2[x_\mathrm{s}\varepsilon_1 - \varepsilon_2(x_\mathrm{s}, x_\mathrm{r})] &= 0. \end{aligned} \tag{B.13}$$

Here we introduced the shock compression ratio $x_\mathrm{s} \equiv \rho_2/\rho_1$ and the rarefaction ratio $x_\mathrm{r} \equiv \rho_3/\rho_5$. Furthermore, the implicit dependences on x_s and x_r can explicitly be expressed as follows,

$$P_2(x_\mathrm{r}) = P_3(x_\mathrm{r}) = P_\mathrm{CR5} x_\mathrm{r}^{\gamma_\mathrm{CR}} + P_\mathrm{th5} x_\mathrm{r}^{\gamma_\mathrm{th}}, \tag{B.14}$$

$$P_\mathrm{CR2}(x_\mathrm{s}) = P_\mathrm{CR1} x_\mathrm{s}^{\gamma_\mathrm{CR}}, \tag{B.15}$$

$$\varepsilon_2(x_\mathrm{s}, x_\mathrm{r}) = \varepsilon_\mathrm{CR1} x_\mathrm{s}^{\gamma_\mathrm{CR}} + \frac{1}{\gamma_\mathrm{th} - 1}[P_2(x_\mathrm{r}) - P_\mathrm{CR2}(x_\mathrm{s})]. \tag{B.16}$$

The roots of the non-linear system of equations (Eqn. (B.13)) immediately yield the post-shock pressure of the fluid via Eqn. (B.14). The post-shock velocity $v_2 = v_3$ and the shock speed v_s are then obtained from the Rankine-Hugoniot relations,

$$v_2 = \sqrt{[P_2(x_\mathrm{r}) - P_1] \frac{\rho_2 - \rho_1}{\rho_2 \rho_1}}, \tag{B.17}$$

$$v_\mathrm{s} = \frac{\rho_2 v_2}{\rho_2 - \rho_1}. \tag{B.18}$$

Using the previous results, we can construct the solution to the generalized Riemann problem for CRs and thermal

gas as follows:

$$
\rho(x,t) \;=\;
\begin{cases}
\rho_5, & x \le -c_5 t, \\
\rho(x,t), & -c_5 t < x \le -v_t t, \\
\rho_3, & -v_t t < x \le v_2 t, \\
\rho_2, & v_2 t < x \le v_s t, \\
\rho_1, & x > v_s t,
\end{cases}
\tag{B.19}
$$

$$
P(x,t) \;=\;
\begin{cases}
P_5, & x \le -c_5 t, \\
A_{\mathrm{CR}}\,\rho(x,t)^{\gamma_{\mathrm{CR}}} + A_{\mathrm{th}}\,\rho(x,t)^{\gamma_{\mathrm{th}}}, & -c_5 t < x \le -v_t t, \\
P_2 = P_3, & -v_t t < x \le v_s t, \\
P_1, & x > v_s t,
\end{cases}
\tag{B.20}
$$

$$
v(x,t) \;=\;
\begin{cases}
0, & x \le -c_5 t, \\
\dfrac{x}{t} + \sqrt{\tilde{A}_{\mathrm{CR}}\,\rho(x,t)^{\gamma_{\mathrm{CR}}-1} + \tilde{A}_{\mathrm{th}}\,\rho(x,t)^{\gamma_{\mathrm{th}}-1}}, & -c_5 t < x \le -v_t t, \\
v_2 = v_3, & -v_t t < x \le v_s t, \\
0, & x > v_s t.
\end{cases}
\tag{B.21}
$$

Here $c_5 = \sqrt{\gamma_{\mathrm{eff}5} P_5 / \rho_5}$ is the effective speed of sound, v_t is the speed of propagation of the rarefaction wave's tail, and v_s is the shock speed. Matching the rarefaction wave equation to the density of the post-contact discontinuity yields v_t:

$$
v_t = I(\rho_3) - I(\rho_5) + \sqrt{\tilde{A}_{\mathrm{CR}}\,\rho_3^{\gamma_{\mathrm{CR}}-1} + \tilde{A}_{\mathrm{th}}\,\rho_3^{\gamma_{\mathrm{th}}-1}}.
\tag{B.22}
$$

The density within the rarefaction regime is obtained by solving (numerically) the non-linear equation for a given (x,t), which is derived from the rarefaction wave equation,

$$
I[\rho(x,t)] - I(\rho_5) + \frac{x}{t} + \sqrt{\tilde{A}_{\mathrm{CR}}\,\rho(x,t)^{\gamma_{\mathrm{CR}}-1} + \tilde{A}_{\mathrm{th}}\,\rho(x,t)^{\gamma_{\mathrm{th}}-1}} = 0.
\tag{B.23}
$$

C. Supplementary tables

C.1. Parameters of profiles for the sample of nearby galaxy clusters

Parameters of electron density profiles $n_e(r)$ of our cluster sample are given in Table C.1 where the clusters are ordered according to their property of containing a cooling flow (upper part) or not (lower part). Note that the parameters are subject to different formulae (C.1) and (C.2),

$$n_e(r) = \sum_{i=1}^{2} n_i \left(1 + \frac{r^2}{r_{c_i}^2} \right)^{-3\beta/2}, \tag{C.1}$$

$$n_e(r) = \left[\frac{\tilde{\Lambda}[T_e(0)]}{\tilde{\Lambda}[T_e(r)]} \times \sum_{i=1}^{2} n_i^2 \left(1 + \frac{r^2}{r_{c_i}^2} \right)^{-3\beta} \right]^{1/2}. \tag{C.2}$$

Equation (C.2) follows from deprojection of X-ray surface brightness profiles which are represented by double β models. The derivation of this deprojection is given in Appendix A. For simplicity and consistency with the X-ray surface brightness profiles given in Mohr et al. (1999) we ignored the weak dependency on $T_e(r)$ in Eq. (C.2).

In order to model the temperature profiles $T_e(r)$ for our cooling flow cluster sample we applied the universal temperature profile for relaxed clusters proposed by Allen et al. (2001) to data taken from the literature,

$$T_e(r) = T_0 + (T_1 - T_0) \left[1 + \left(\frac{r}{r_{temp}} \right)^{-\eta} \right]^{-1}. \tag{C.3}$$

This equation matches the temperature profile well up to radii of $\sim 0.3\, r_{vir}$, which is sufficient for our purposes since we are especially interested in the core region of clusters. The parameters of the temperature profile for particular cluster are given in Table C.2.

C.2. Limits on cosmic ray protons in nearby galaxy clusters

Table C.3 shows constraints for X_{CRp} using the isobaric model and the adiabatic CRp model as explained in Sect. 6.3.3. For clusters like Perseus, Virgo, Ophiuchus, and Coma we can obtain quite tight constraints on the population of CRp. Because in the adiabatic model the CRp scaling parameter X_{CRp} is a function of radius, the value $X_{CRp}^{adiabatic}$ refers to the unprimed quantity in Eq. (6.8) which reflects the outer core region of the cluster.

Table C.4 shows upper limits on the CRp density parameter $\tilde{n}_{CRp,0}$, the CRp number parameter $\tilde{N}_{CRp}$, and the averaged CRp luminosity L_{CRp} of the central active galaxy as explained in Sect. 6.3.4. This shows that within this conceptually simple model we are able to put constraints on L_{CRp}. The limits which are strongest in the case of M87 in the Virgo cluster represent conservative bounds since we choose the active CRp diffusion scenario resulting in spectral steepening of the CRp population.

C.3. Prediction of the diffuse γ-ray emission in nearby galaxy clusters

Following the formalism described in Sect. 6.3.2 and comparing the resulting γ-ray flux $\mathcal{F}_\gamma(E > E_{thr})$ to expected flux sensitivities of Čerenkov telescopes $\mathcal{F}_{\gamma,exp}(E > E_{thr})$, we obtain possible upper limits on the CRp scaling parameter X_{CRp} for an integrated volume out to a radial distance of $3\, h_{70}^{-1}$ Mpc. Table C.5 shows constraints for X_{CRp} using the isobaric and the adiabatic model of CRp described in Sect. 6.2. By comparing these limits to

those obtained by analyzing synchrotron emission in the Perseus and Coma cluster (see Table 6.1) and assuming a substantial contribution of hadronically originating CRe to these radio halos there is a realistic chance to detect extragalactic pion decay induced γ-ray emission in clusters like Perseus, Virgo, Ophiuchus, and Coma.

C.4. Plasma bubbles in galaxy clusters: profiles of the Perseus cluster and Abell 2052

The following Table C.6 gives supplementary information on the profiles of the Perseus cluster and Abell 2052 for our investigation concerning the study of the composition of plasma bubbles in galaxy clusters with the SZ effect in Chapter 8.

As an analytically feasible toy model, we assume spherical geometry of the plasma bubble and adopt the general n-fold β-profile for the electron pressure of the ICM which might find application for cool-core clusters:

$$P_{\mathrm{e}}(r) = n_{\mathrm{e}}(r)kT_{\mathrm{e}}(r) = \sum_{i=1}^{N} P_i \left[1 + \left(\frac{r}{r_{y,i}} \right)^2 \right]^{-3\beta_{y,i}/2} . \tag{C.4}$$

The amplitude of the kinetic SZ effect is proportional to the line-of-sight integrated electron density for which we also assume a general n-fold β-profile:

$$n_{\mathrm{e}}(r) = \sum_{i=1}^{N} n_i \left[1 + \left(\frac{r}{r_{w,i}} \right)^2 \right]^{-3\beta_{w,i}/2} . \tag{C.5}$$

The bubble parameters r_{c} and r_{b} correspond to the distance from the cluster center to the bubble center and the bubble radius, respectively, and have been measured from the X-ray maps. The azimuthal angle to the bubble center ϕ is measured from the axis defined by positive values of the relative right ascension while η_{s} denotes the angle of the normal vector of the mushroom-shaped southern bubble in A 2052 which we model as a half-sphere.

Table C.1.: Parameters of electron density profiles $n_e(r)$ of our cluster sample (central densities n_i are subject to different formulae (C.1) and (C.2)). The cluster are ordered according to their property of being a cooling flow cluster (upper part) or a non-cooling flow cluster (lower part).

Cluster	z	n_1 [$h_{70}^{1/2}$ cm^{-3}]	r_{c_1} [h_{70}^{-1} kpc]	β_1	n_2 [$h_{70}^{1/2}$ cm^{-3}]	r_{c_2} [h_{70}^{-1} kpc]	β_2	Equation	References
A85	0.0551	3.08×10^{-2}	45	0.662	3.87×10^{-3}	226	0.662	(C.2)	(a), (b)
A426 (Perseus)	0.0179	4.6×10^{-2}	57	1.2	4.79×10^{-3}	200	0.58	(C.1)	(c), (d)
A2199	0.0302	3.37×10^{-2}	29	0.663	7.17×10^{-3}	116	0.663	(C.2)	(a), (b)
A3526 (Centaurus)	0.0114	8.05×10^{-2}	8.6	0.569	3.65×10^{-3}	99	0.569	(C.2)	(a), (d)
Ophiuchus	0.0280	1.71×10^{-2}	56	0.705	7.47×10^{-3}	190	0.705	(C.2)	(a), (e)
Triangulum Australis	0.0510	7.31×10^{-3}	151	0.816	2.63×10^{-3}	444	0.816	(C.2)	(a), (f)
Virgo	0.0036	1.5×10^{-1}	1.6	0.42	1.3×10^{-2}	20	0.47	(C.2)	(g), (h)
A1656 (Coma)	0.0231	3.4×10^{-3}	294	0.75				(C.1)	(i), (d)
A2256	0.0581	3.57×10^{-3}	347	0.828				(C.1)	(a), (d)
A2319	0.0557	7.35×10^{-3}	152	0.536				(C.1)	(a), (d)
A3571	0.0391	9.37×10^{-3}	124	0.61				(C.1)	(a), (d)

(a) Mohr et al. (1999), (b) Oegerle & Hill (2001), (c) Churazov et al. (2003), (d) Struble & Rood (1999), (e) Lahav et al. (1989), (f) McHardy et al. (1981), (g) Matsushita et al. (2002), (h) Ebeling et al. (1998), (i) Briel et al. (1992)

Table C.2.: Parameters of temperature profiles $T_e(r)$ of our cluster sample. The estimated γ-ray flux $\mathcal{F}_{\gamma,\text{est}}$ (> 100 MeV) was calculated using the $\mathcal{F}_\gamma$–F_X scaling relation (Eq. (5.27)) with $\alpha_p = 2.3$ and bolometric X-ray fluxes from David et al. (1993). Note that $\mathcal{F}_\gamma$ scales linearly with X_{CRp} which was set to $X_{CRp} = 0.01\, X_{0.01}$ in this table. The range for $\mathcal{F}_{\gamma,\text{est}}$ reflects the temperature spread in cooling flow clusters between the central temperature T_0 and the peripheral temperature T_1.

Cluster	Experiment	kT_0 [keV]	kT_1 [keV]	r_{temp} [h_{70}^{-1} kpc]	η	$\mathcal{F}_{\gamma,\text{est}}$ (> 100 MeV) [$X_{0.01}\ 10^{-10}$ cm^{-2} s^{-1}]	References
A85	BeppoSAX MECS	5.5	9.0	312	2	1.8 ... 2.3	(a), (b)
A426 (Perseus)	XMM-Newton MOS	3.0	7.0	94	3	19.1 ...29.2	(c)
A2199	Chandra ACIS	1.6	4.3	21.5	1.8	1.3 ... 2.2	(d), (e)
A3526 (Centaurus)	ASCA GIS	2.2	4.0	22	3	2.2 ... 2.9	(f)
Ophiuchus	ASCA GIS	12.8				22.0	(f)
Triangulum Australis	ASCA GIS	10.3				4.8	(f)
Virgo	XMM-Newton PN/MOS	1.0	3.0	13.5	1	3.2 ... 5.6	(g)
A1656 (Coma)	XMM-Newton MOS	8.3				13.1	(h)
A2256	Chandra ACIS	6.7				2.3	(i)
A2319	ASCA GIS	9.7				5.4	(f)
A3571	ASCA GIS	7.2				4.5	(f)

(a) Irwin & Bregman (2000), (b) Lima Neto et al. (2001), (c) Churazov et al. (2003), (d) Voigt et al. (2002), (e) Johnstone et al. (2002), (f) White (2000), (g) Matsushita et al. (2002), (h) Arnaud et al. (2001), (i) Sun et al. (2002)

Table C.3.: Upper limits on the CRp scaling parameter X_{CRp} by comparing the integrated flux above 100 MeV to EGRET upper limits assuming a γ-ray spectral index in Dermer's model $\alpha_\gamma = \alpha_p$. The spatial distribution of CRp is given by the isobaric and the adiabatic model of CRp, respectively (see Sects. 6.2.1 and 6.2.2).

Cluster	$\mathcal{F}_\gamma$ (> 100 MeV) [10^{-8} cm^{-2} s^{-1}]	$X_{CRp}^{isobaric}$				$X_{CRp}^{adiabatic}$			
		$\alpha_p = 2.1$	$\alpha_p = 2.3$	$\alpha_p = 2.5$	$\alpha_p = 2.7$	$\alpha_p = 2.1$	$\alpha_p = 2.3$	$\alpha_p = 2.5$	$\alpha_p = 2.7$
A85 ……………	< 6.32	3.53	1.97	2.09	3.11	2.58	1.41	1.48	2.16
A426 (Perseus) …..	< 3.72	0.14	0.08	0.08	0.13	0.12	0.06	0.07	0.10
A2199 ………….	< 9.27	6.14	3.42	3.64	5.42	5.74	3.18	3.38	5.00
A3526 (Centaurus)	< 5.31	1.54	0.86	0.91	1.36	1.45	0.80	0.85	1.26
Ophiuchus ………..	< 5.00	0.30	0.17	0.18	0.26				
Triangulum Australis	< 8.13	1.93	1.07	1.14	1.70				
Virgo ……………	< 2.18	0.18	0.10	0.11	0.16	0.16	0.09	0.09	0.14
A1656 (Coma) ……	< 3.81	0.45	0.25	0.27	0.40				
A2256 ………….	< 4.28	3.15	1.75	1.87	2.78				
A2319 ………….	< 3.79	0.86	0.48	0.51	0.76				
A3571 ………….	< 6.34	1.85	1.03	1.09	1.63				

Table C.4.: Cooling flow clusters: Upper limits on the CRp density parameter $\tilde{n}_{\mathrm{CRp},0}$ and average CRp luminosity L_{CRp} of the central active galaxy by comparing the integrated flux above 100 MeV to EGRET upper limits assuming a γ-ray spectral index in Dermer's model $\alpha_\gamma = \alpha_{\mathrm{p}}$. The spatial distribution of CRp is calculated according to the diffusion model of CRp away from a central AGN assuming $\alpha_{\mathrm{p}} = \alpha_{\mathrm{inj}} + \alpha_{\mathrm{diff}}$, where $\alpha_{\mathrm{diff}} = 1/3$. **Non-cooling flow clusters:** Upper limits on the CRp number parameter $\tilde{N}_{\mathrm{CRp}}$ and average CRp luminosity L_{CRp} without any diffusion induced spectral steepening, i.e. $\alpha_{\mathrm{p}} = \alpha_{\mathrm{inj}}$. Note that L_{CRp} scales in the case of cooling flow clusters with the diffusion coefficient κ_0 while it only depends on the CRp injection time t_{inj} for non-cooling flow clusters (see Sect. 6.2.3).

CF Cluster	$\tilde{n}_{\mathrm{CRp},0}\ [h_{70}^{1/2}\ \mathrm{cm}^{-3}]$				$L_{\mathrm{CRp}}\ \left[h_{70}^{-1/2}\ \mathrm{erg\ s}^{-1}\left(\frac{\kappa_0}{10^{29}\,\mathrm{cm}^2\,\mathrm{s}^{-1}}\right)\right]$			
	$\alpha_{\mathrm{p}} = 2.4$	$\alpha_{\mathrm{p}} = 2.5$	$\alpha_{\mathrm{p}} = 2.7$	$\alpha_{\mathrm{p}} = 2.9$	$\alpha_{\mathrm{p}} = 2.4$	$\alpha_{\mathrm{p}} = 2.5$	$\alpha_{\mathrm{p}} = 2.7$	$\alpha_{\mathrm{p}} = 2.9$
A85 ……………	6.0×10^{-5}	7.2×10^{-5}	9.9×10^{-5}	1.3×10^{-4}	5.5×10^{45}	2.7×10^{45}	1.9×10^{45}	2.0×10^{45}
A426 (Perseus) ….	2.4×10^{-6}	2.9×10^{-6}	3.9×10^{-6}	5.2×10^{-6}	2.2×10^{44}	1.1×10^{44}	7.4×10^{43}	8.1×10^{43}
A2199 …………	3.2×10^{-5}	3.8×10^{-5}	5.3×10^{-5}	7.0×10^{-5}	3.0×10^{45}	1.4×10^{45}	9.9×10^{44}	1.1×10^{45}
A3526 (Centaurus)	4.3×10^{-6}	5.1×10^{-6}	7.1×10^{-6}	9.4×10^{-6}	3.9×10^{44}	1.9×10^{44}	1.3×10^{44}	1.5×10^{44}
Ophiuchus ………	1.5×10^{-5}	1.8×10^{-5}	2.5×10^{-5}	3.3×10^{-5}	1.4×10^{45}	6.6×10^{44}	4.6×10^{44}	5.1×10^{44}
Triangulum Australis	1.4×10^{-4}	1.7×10^{-4}	2.3×10^{-4}	3.1×10^{-4}	1.3×10^{46}	6.2×10^{45}	4.3×10^{45}	4.8×10^{45}
Virgo ……………	2.5×10^{-7}	3.1×10^{-7}	4.2×10^{-7}	5.6×10^{-7}	2.4×10^{43}	1.1×10^{43}	7.9×10^{42}	8.7×10^{42}

NCF Cluster	$\tilde{N}_{\mathrm{CRp}}\ [h_{70}^{1/2}]$				$L_{\mathrm{CRp}}\ \left[h_{70}^{3/2}\ \mathrm{erg\ s}^{-1}\left(\frac{t_{\mathrm{inj}}}{3\,\mathrm{Gyr}}\right)^{-1}\right]$			
	$\alpha_{\mathrm{p}} = 2.1$	$\alpha_{\mathrm{p}} = 2.3$	$\alpha_{\mathrm{p}} = 2.5$	$\alpha_{\mathrm{p}} = 2.7$	$\alpha_{\mathrm{p}} = 2.1$	$\alpha_{\mathrm{p}} = 2.3$	$\alpha_{\mathrm{p}} = 2.5$	$\alpha_{\mathrm{p}} = 2.7$
A1656 (Coma) ……	1.6×10^{64}	2.5×10^{64}	3.7×10^{64}	5.1×10^{64}	2.7×10^{45}	1.5×10^{45}	1.6×10^{45}	2.4×10^{45}
A2256 ……………	1.1×10^{65}	1.8×10^{65}	2.6×10^{65}	3.6×10^{65}	1.9×10^{46}	1.1×10^{46}	1.1×10^{46}	1.7×10^{46}
A2319 …………	4.5×10^{64}	7.0×10^{64}	1.0×10^{65}	1.4×10^{65}	7.5×10^{45}	4.2×10^{45}	4.4×10^{45}	6.6×10^{45}
A3571 …………	2.8×10^{64}	4.4×10^{64}	6.5×10^{64}	9.0×10^{64}	4.7×10^{45}	2.6×10^{45}	2.8×10^{45}	4.2×10^{45}

Table C.5.: Expected limits on the CRp scaling parameter $X_{\rm CRp}$ by comparing the integrated pion decay induced γ-ray flux above 100 GeV to sensitivity limits of Čerenkov telescopes of $\mathcal{F}_{\gamma,\exp}(E > E_{\rm thr}) = 10^{-12}\,\gamma\,{\rm cm}^{-2}\,{\rm s}^{-1}\,(E_{\rm thr}/100\,{\rm GeV})^{1-\alpha_\gamma}$ assuming a γ-ray spectral index in Dermer's model $\alpha_\gamma = \alpha_{\rm p}$. Note that limits on $X_{\rm CRp}$ roughly $\lesssim 0.01$ for $\alpha_{\rm p} = 2.3$ in the isobaric model provide good chances to detect γ-rays in these particular clusters with new generation Čerenkov telescopes.

Cluster	$X_{\rm CRp}^{\rm isobaric}$				$X_{\rm CRp}^{\rm radiabatic}$			
	$\alpha_{\rm p} = 2.1$	$\alpha_{\rm p} = 2.3$	$\alpha_{\rm p} = 2.5$	$\alpha_{\rm p} = 2.7$	$\alpha_{\rm p} = 2.1$	$\alpha_{\rm p} = 2.3$	$\alpha_{\rm p} = 2.5$	$\alpha_{\rm p} = 2.7$
A85	3.7×10^{-2}	6.5×10^{-2}	2.2×10^{-1}	1.0	2.7×10^{-2}	4.7×10^{-2}	1.5×10^{-1}	7.1×10^{-1}
A426 (Perseus)	2.5×10^{-3}	4.5×10^{-3}	1.5×10^{-2}	7.0×10^{-2}	2.1×10^{-3}	3.6×10^{-3}	1.2×10^{-2}	5.5×10^{-2}
A2199	4.4×10^{-2}	7.7×10^{-2}	2.6×10^{-1}	1.2	4.1×10^{-2}	7.2×10^{-2}	2.4×10^{-1}	1.1
A3526 (Centaurus)	1.9×10^{-2}	3.4×10^{-2}	1.1×10^{-1}	5.3×10^{-1}	1.8×10^{-2}	3.2×10^{-2}	1.1×10^{-1}	5.0×10^{-1}
Ophiuchus	4.0×10^{-3}	7.0×10^{-3}	2.3×10^{-2}	1.1×10^{-1}				
Triangulum Australis	1.6×10^{-2}	2.8×10^{-2}	9.3×10^{-2}	4.4×10^{-1}				
Virgo	4.1×10^{-3}	7.3×10^{-3}	2.4×10^{-2}	1.1×10^{-1}	3.8×10^{-3}	6.7×10^{-3}	2.2×10^{-2}	1.0×10^{-1}
A1656 (Coma)	7.9×10^{-3}	1.4×10^{-2}	4.6×10^{-2}	2.2×10^{-1}				
A2256	4.9×10^{-2}	8.6×10^{-2}	2.9×10^{-1}	1.4				
A2319	1.5×10^{-2}	2.6×10^{-2}	8.9×10^{-2}	4.2×10^{-1}				
A3571	1.9×10^{-2}	3.4×10^{-2}	1.1×10^{-1}	5.3×10^{-1}				

Table C.6.: Profiles of the Perseus cluster and Abell 2052: Parameters of the deprojected electron pressure profiles which obey an *n*-fold β-profile defined by Eqn. (C.4), the deprojected electron density profiles (Eqn. C.5), and the individual parameters of the northern and southern plasma bubbles within the cool core regions of the Perseus cluster and Abell 2052, respectively. The parameters r_c and r_b correspond to the distance from the cluster center to the bubble center and the bubble radius, respectively. The azimuthal angle to the bubble center ϕ is measured from the axis defined by positive values of the relative right ascension while η_s denotes the angle of the normal vector of the mushroom-shaped southern bubble in A 2052 which we model as a half-sphere. In Perseus, 1″ corresponds to 0.36 h_{70}^{-1} kpc and in A 2052, 1″ corresponds to 0.69 h_{70}^{-1} kpc.

Cluster pressure profile:

Cluster	P_1 $[h_{70}^{1/2}$ keV cm$^{-3}]$	P_2 $[h_{70}^{1/2}$ keV cm$^{-3}]$	P_3 $[h_{70}^{1/2}$ keV cm$^{-3}]$	$r_{y,1}$ $[h_{70}^{-1}$ kpc]	$r_{y,2}$ $[h_{70}^{-1}$ kpc]	$r_{y,3}$ $[h_{70}^{-1}$ kpc]	$\beta_{y,1}$	$\beta_{y,2}$	$\beta_{y,3}$
A 426 (Perseus)	0.118	0.036		47	178		0.94	0.55	
A 2052	1.034	−0.723	−0.258	22.6	28.4	237	0.658	0.746	128

Cluster density profile:

Cluster	n_1 $[h_{70}^{1/2}$ cm$^{-3}]$	n_2 $[h_{70}^{1/2}$ cm$^{-3}]$	$r_{w,1}$ $[h_{70}^{-1}$ kpc]	$r_{w,2}$ $[h_{70}^{-1}$ kpc]	$\beta_{w,1}$	$\beta_{w,2}$
A 426 (Perseus)	4.60×10^{-2}	4.8×10^{-3}	57	200	1.2	0.58
A 2052	3.75×10^{-2}	2.9×10^{-3}	29	197	0.84	0.80

Southern bubble:

Cluster	$r_{c,s}$	$r_{b,s}$	ϕ_s	η_s
A 426 (Perseus)	33″	23″	−50°	
A 2052	4.4″	16.4″	−128°	77°

Northern bubble:

Cluster	$r_{c,n}$	$r_{b,n}$	ϕ_n
A 426 (Perseus)	17″	17″	90°
A 2052	13″	11″	90°

Bibliography

Abel T., Bryan G. L., Norman M. L., 2002, Science, 295, 93

Abell G. O., 1958, ApJS, 3, 211

Abell G. O., Corwin H. G., Olowin R. P., 1989, ApJS, 70, 1

Abramowitz M., Stegun I. A., 1965, Handbook of mathematical functions. Dover, New York

Aghanim N., Hansen S. H., Pastor S., Semikoz D. V., 2003, Journal of Cosmology and Astro-Particle Physics, 5, 7

Aharonian F., Akhperjanian A., Beilicke M., Bernlöhr K., Börst H.-G., Bojahr H., Bolz O., Coarasa T., Contreras J. L., Cortina J., Denninghoff S., Fonseca M. V., et al. 2003, A&A, 403, L1

Aharonian F. A., Akhperjanian A. G., Aye K.-M., Bazer-Bachi A. R., Beilicke M., Benbow W., Berge D., Berghaus P., Bernlöhr K., Bolz O., Boisson C., Borgmeier C., et al. 2004, Nature, 432, 75

Albrecht A., Steinhardt P. J., 1982, Physical Review Letters, 48, 1220

Allen S. W., Schmidt R. W., Fabian A. C., 2001, MNRAS, 328, L37

Allen S. W., Schmidt R. W., Fabian A. C., 2002, MNRAS, 334, L11

Arnaud M., Aghanim N., Gastaud R., Neumann D. M., Lumb D., Briel U., Altieri B., Ghizzardi S., Mittaz J., Sasseen T. P., Vestrand W. T., 2001, A&A, 365, L67

Baade W., Zwicky F., 1934, Proceedings of the National Academy of Science, 20, 259

Badhwar G. D., Golden R. L., Stephens S. A., 1977, Phys. Rev. D, 15, 820

Bahcall N. A., McKay T. A., Annis J., Kim R. S. J., Dong F., Hansen S., Goto T., Gunn J. E., Miller C., Nichol R. C., Postman M., Schneider D., Schroeder J., Voges W., Brinkmann J., Fukugita M., 2003, ApJS, 148, 243

Bai J. M., Lee M. G., 2001, ApJ, 549, L173

Baltz E. A., Briot C., Salati P., Taillet R., Silk J., 2000, Phys. Rev. D, 61, 23514

Banday A. J., Gorski K. M., Bennett C. L., Hinshaw G., Kogut A., Lineweaver C., Smoot G. F., Tenorio L., 1997, ApJ, 475, 393

Bardeen J. M., Bond J. R., Kaiser N., Szalay A. S., 1986, ApJ, 304, 15

Barnes J., Hut P., 1986, Nature, 324, 446

Barnes J. E., 2004, MNRAS, 350, 798

Bartelmann M., Schneider P., 2001, Phys. Rep., 340, 291

Beck R., 2001, Space Science Reviews, 99, 243

Beck R., Brandenburg A., Moss D., Shukurov A., Sokoloff D., 1996, ARA&A, 34, 155

Bell A. R., 1978a, MNRAS, 182, 147

Bell A. R., 1978b, MNRAS, 182, 443

Benson A. J., Bower R. G., Frenk C. S., Lacey C. G., Baugh C. M., Cole S., 2003, ApJ, 599, 38

Benson A. J., Frenk C. S., Lacey C. G., Baugh C. M., Cole S., 2002, MNRAS, 333, 177

Berezhko E., Ksenofontov L., Yelshin V., 1995, Nuclear Physics B Proceedings Supplements, 39, A171

Berezhko E. G., Yelshin V. K., Ksenofontov L. T., 1994, Astroparticle Physics, 2, 215

Berezinsky V. S., Blasi P., Ptuskin V. S., 1997, ApJ, 487, 529

Berger M. J., Colella P., 1989, J. Comput. Phys., 82, 64

Berrington R. C., Dermer C. D., 2003, ApJ, 594, 709

Bertschinger E., 1985, ApJS, 58, 39

Beuermann K., Kanbach G., Berkhuijsen E. M., 1985, A&A, 153, 17

Bicknell G. V., Begelman M. C., 1996, ApJ, 467, 597

Bieber J. W., Matthaeus W. H., 1997, ApJ, 485, 655

Biermann P. L., Strittmatter P. A., 1987, ApJ, 322, 643

Birkinshaw M., 1999, Phys. Rep., 310, 97

Blandford R., Eichler D., 1987, Phys. Rep., 154, 1

Blandford R. D., Ostriker J. P., 1978, ApJ, 221, L29

Blanton E. L., Sarazin C. L., McNamara B. R., 2003, ApJ, 585, 227

Blanton E. L., Sarazin C. L., McNamara B. R., Wise M. W., 2001, ApJ, 558, L15

Blasi P., 1999, ApJ, 525, 603

Blasi P., 2000, ApJ, 532, L9

Blasi P., Colafrancesco S., 1999, Astroparticle Physics, 12, 169

Blasi P., Olinto A. V., Stebbins A., 2000, ApJ, 535, L71

Böhringer H., Voges W., Fabian A. C., Edge A. C., Neumann D. M., 1993, MNRAS, 264, L25

Bond J. R., Cole S., Efstathiou G., Kaiser N., 1991, ApJ, 379, 440

Brüggen M., Kaiser C. R., 2001, MNRAS, 325, 676

Brüggen M., Kaiser C. R., Churazov E., Enßlin T. A., 2002, MNRAS, 331, 545

Briel U. G., Henry J. P., Böhringer H., 1992, A&A, 259, L31

Brown R., Emerson D., Baars J., L. D., et al. 2000, ALMA Project Book, Ch. 2

Brunetti G., 2002, in Bowyer S., Hwang C.-Y., eds, Matter and Energy in Clusters of Galaxies Vol. 301 of ASP Conf. Ser.. Astron. Soc. Pac., San Francisco, p. 349

Brunetti G., Blasi P., Cassano R., Gabici S., 2004a, MNRAS, 350, 1174

Brunetti G., Blasi P., Cassano R., Gabici S., 2004b, MNRAS, 350, 1174

Brunetti G., Feretti L., Giovannini G., Setti G., 1999, in Diffuse Thermal and Relativistic Plasma in Galaxy Clusters Particle Reacceleration in the Coma Cluster and the Radio, EUV and Hard X-Ray Emissions. p. 263

Brunetti G., Setti G., Comastri A., 1997, A&A, 325, 898

Brunetti G., Setti G., Feretti L., Giovannini G., 2001, MNRAS, 320, 365

Bryan G. L., Norman M. L., 1997, in ASP Conf. Ser. 123: Computational Astrophysics; 12th Kingston Meeting on Theoretical Astrophysics p. 363

Buote D. A., 2001, ApJ, 553, L15

Burbidge G. R., 1956, ApJ, 124, 416

Burns J. O., 1990, AJ, 99, 14

Butler B., Brown B., Blitz L., Welch J., Carlstrom J., Woody D., Churchwell E., 1999, ALMA Memo Series No. 243

Carilli C. L., Perley R. A., Harris D. E., 1994, MNRAS, 270, 173

Carilli C. L., Taylor G. B., 2002, ARA&A, 40, 319

Carroll S. M., Press W. H., Turner E. L., 1992, ARA&A, 30, 499

Cassano R., Brunetti G., 2005, MNRAS, 357, 1313

Cavaliere A., Fusco-Femiano R., 1976, A&A, 49, 137

Celotti A., Kuncic Z., Rees M. J., Wardle J. F. C., 1998, MNRAS, 293, 288

Cen R., 2005, ApJ, 620, 191

Cen R., Ostriker J. P., 1993, ApJ, 417, 404

Cen R., Ostriker J. P., 1999, ApJ, 514, 1

Chandran B. D. G., 2004, ApJ, 616, 169

Chandran B. D. G., Maron J. L., 2004, ApJ, 602, 170

Chandrasekhar S., 1942, Principles of stellar dynamics

Cho J., Lazarian A., Honein A., Knaepen B., Kassinos S., Moin P., 2003, ApJ, 589, L77

Churazov E., Brüggen M., Kaiser C. R., Böhringer H., Forman W., 2001, ApJ, 554, 261

Churazov E., Forman W., Jones C., Böhringer H., 2000, A&A, 356, 788

Churazov E., Forman W., Jones C., Böhringer H., 2003, ApJ, 590, 225

Ciardi B., Stoehr F., White S. D. M., 2003, MNRAS, 343, 1101

Clarke T. E., Kronberg P. P., Böhringer H., 2001, ApJ, 547, L111

Colafrancesco S., Blasi P., 1998, Astroparticle Physics, 9, 227

Colafrancesco S., Marchegiani P., Palladino E., 2003, A&A, 397, 27

Couchman H. M. P., 1991, ApJ, 368, L23

Courant R., Friedrichs K. O., 1948, Supersonic flow and shock waves. Pure and Applied Mathematics, New York: Interscience, 1948

Dalton G. B., Maddox S. J., Sutherland W. J., Efstathiou G., 1997, MNRAS, 289, 263

Daum A., Hermann G., Hess M., Hofmann W., Lampeitl H., Pühlhofer G., Aharonian F., Akhperjanian A. G., Barrio J. A., Beglarian A. S., Bernlöhr K., Beteta J. J. G., et al. 1997, Astroparticle Physics, 8, 1

Davé R., Cen R., Ostriker J. P., Bryan G. L., Hernquist L., Katz N., Weinberg D. H., Norman M. L., O'Shea B., 2001, ApJ, 552, 473

David L. P., Forman W., Jones C., 1991, ApJ, 380, 39

David L. P., Jones C., Forman W., 1995, ApJ, 445, 578

David L. P., Slyz A., Jones C., Forman W., Vrtilek S. D., Arnaud K. A., 1993, ApJ, 412, 479

Davis M., Efstathiou G., Frenk C. S., White S. D. M., 1985, ApJ, 292, 371

Davis M., Peebles P. J. E., 1983, ApJ, 267, 465

De Young D. S., 2003, MNRAS, 343, 719

Dehnen W., 2000, ApJ, 536, L39

Deiss B. M., Reich W., Lesch H., Wielebinski R., 1997, A&A, 321, 55

Dennis T. J., Chandran B. D. G., 2005, ApJ, 622, 205

Dennison B., 1980, ApJ, 239, L93

Dermer C. D., 1986a, ApJ, 307, 47

Dermer C. D., 1986b, A&A, 157, 223

Dermer C. D., Sturner S. J., Schlickeiser R., 1997, ApJS, 109, 103

d'Inverno R., 1992, Introducing Einstein's Relativity. Clarendon, Oxford

Dolag K., Bartelmann M., Lesch H., 1999, A&A, 348, 351

Dolag K., Enßlin T. A., 2000, A&A, 362, 151

Dolag K., Schindler S., Govoni F., Feretti L., 2001, A&A, 378, 777

Dolgov A. D., Hansen S. H., Pastor S., Semikoz D. V., 2001, ApJ, 554, 74

Drury L., 1983a, Space Science Reviews, 36, 57

Drury L. O., 1983b, Reports of Progress in Physics, 46, 973

Drury L. O., Markiewicz W. J., Völk H. J., 1989, A&A, 225, 179

Duffy P., Kirk J. G., Gallant Y. A., Dendy R. O., 1995, A&A, 302, L21

Ebeling H., Edge A. C., Bohringer H., Allen S. W., Crawford C. S., Fabian A. C., Voges W., Huchra J. P., 1998, MNRAS, 301, 881

Efstathiou G., Davis M., White S. D. M., Frenk C. S., 1985, ApJS, 57, 241

Eilek J. A., 1979, ApJ, 230, 373

Einstein A., 1915, Sitzungsberichte der Preußischen Akademie der Wissenschaften, 1, 831

Eke V. R., Cole S., Frenk C. S., 1996, MNRAS, 282, 263

Ellison D. C., Baring M. G., Jones F. C., 1996, ApJ, 473, 1029

Elsässer D., Mannheim K., 2005, Physical Review Letters, 94, 171302

Enßlin T. A., 1999, in Böhringer H., Feretti L., Schuecker P., eds, Diffuse Thermal and Relativistic Plasma in Galaxy Clusters Vol. 271 of MPE Report, Radio ghosts. p. 275

178

Enßlin T. A., 2002, A&A, 396, L17

Enßlin T. A., 2003, A&A, 399, 409

Enßlin T. A., Biermann P. L., 1998, A&A, 330, 90

Enßlin T. A., Biermann P. L., Klein U., Kohle S., 1998, A&A, 332, 395

Enßlin T. A., Biermann P. L., Kronberg P. P., Wu X.-P., 1997, ApJ, 477, 560

Enßlin T. A., Brüggen M., 2002, MNRAS, 331, 1011

Enßlin T. A., Gopal-Krishna 2001, A&A, 366, 26

Enßlin T. A., Hansen S. H., 2004, astro-ph/0401337

Enßlin T. A., Heinz S., 2002, A&A, 384, L27

Enßlin T. A., Kaiser C. R., 2000, A&A, 360, 417

Enßlin T. A., Lieu R., Biermann P. L., 1999, A&A, 344, 409

Enßlin T. A., Pfrommer C., Springel V., Jubelgas M., 2005, MNRAS, submitted

Enßlin T. A., Röttgering H., 2002, A&A, 396, 83

Enßlin T. A., Vogt C., 2003, A&A, 401, 835

Ensslin T. A., Vogt C., 2005, astro-ph/0505517

Enßlin T. A., Wang Y., Nath B. B., Biermann P. L., 1998, A&A, 333, L47

Evrard A. E., 1988, MNRAS, 235, 911

Evrard A. E., 1989, ApJ, 341, L71

Evrard A. E., 2004, in Clusters of Galaxies: Probes of Cosmological Structure and Galaxy Evolution Galaxy Clusters as Probes of Cosmology and Astrophysics. p. 1

Fabian A. C., 2001, in Neumann D. M., ed., XXIth Moriond Astrophysics Meeting on 'Galaxy Clusters and the High Redshift Universe Observed in X-rays'

Fabian A. C., Sanders J. S., Ettori S., Taylor G. B., Allen S. W., Crawford C. S., Iwasawa K., Johnstone R. M., Ogle P. M., 2000, MNRAS, 318, L65

Felten J. E., Morrison P., 1966, ApJ, 146, 686

Feretti L., 1999, in IAU Symp. 199: 'The Universe at Low Radio Frequencies'

Fermi E., 1949, Physical Review, 75, 1169

Fermi E., 1950, Prog. Theor. Phys., 5, 570

Fillmore J. A., Goldreich P., 1984, ApJ, 281, 1

Finkbeiner D. P., Davis M., Schlegel D. J., 1999, ApJ, 524, 867

Finkbeiner D. P., Davis M., Schlegel D. J., 2000, ApJ, 544, 81

Finoguenov A., Jones C., 2001, ApJ, 547, L107

Forman W., Kellogg E., Gursky H., Tananbaum H., Giacconi R., 1972, ApJ, 178, 309

Freedman W. L., Madore B. F., Gibson B. K., Ferrarese L., Kelson D. D., Sakai S., Mould J. R., Kennicutt R. C., Ford H. C., Graham J. A., Huchra J. P., Hughes S. M. G., Illingworth G. D., Macri L. M., Stetson P. B., 2001, ApJ, 553, 47

Furlanetto S. R., Loeb A., 2004, ApJ, 611, 642

Fusco-Femiano R., dal Fiume D., Feretti L., Giovannini G., Grandi P., Matt G., Molendi S., Santangelo A., 1999, ApJ, 513, L21

Fusco-Femiano R., Orlandini M., Brunetti G., Feretti L., Giovannini G., Grandi P., Setti G., 2004, ApJ, 602, L73

Gabici S., Blasi P., 2003, ApJ, 583, 695

Giacalone J., Jokipii J. R., 1999, ApJ, 520, 204

Gingold R. A., Monaghan J. J., 1977, MNRAS, 181, 375

Giovannini G., Feretti L., Venturi T., Kim K. T., Kronberg P. P., 1993, ApJ, 406, 399

Giovannini G., Tordi M., Feretti L., 1999, New Astronomy, 4, 141

Gitti M., Brunetti G., Setti G., 2002, A&A, 386, 456

Gnedin O. Y., 2003, ApJ, 582, 141

Goldstein M. L., Roberts D. A., Matthaeus W. H., 1995, ARA&A, 33, 283

Gould R. J., 1972, Physica, 58, 379

Govoni F., Enßlin T. A., Feretti L., Giovannini G., 2001, A&A, 369, 441

Greisen K., 1966, Physical Review Letters, 16, 748

Gull S. F., Northover J. E., 1973, Nature, 244, 80

Gunn J. E., Gott J. R. I., 1972, ApJ, 176, 1

Gursky H., Kellogg E., Murray S., Leong C., Tananbaum H., Giacconi R., 1971, ApJ, 167, L81

Guth A. H., 1981, Phys. Rev. D, 23, 347

Hanasz M., Lesch H., 2003, A&A, 412, 331

Hansen S. H., Pastor S., Semikoz D. V., 2002, ApJ, 573, L69

Harris D. E., Kapahi V. K., Ekers R. D., 1980, A&AS, 39, 215

Heckman T. M., Armus L., Miley G. K., 1990, ApJS, 74, 833

Heinz S., Choi Y., Reynolds C. S., Begelman M. C., 2002, ApJ, 569, L79

Hellsten U., Gnedin N. Y., Miralda-Escudé J., 1998, ApJ, 509, 56

Hernquist L., Katz N., 1989, ApJS, 70, 419

Herschel F. W., 1785, Phil. Trans., 75, 213

Hess V. F., 1912, Phys. Z., 13, 1084

Hillas A. M., 1984, ARA&A, 22, 425

Hirotani K., Iguchi S., Kimura M., Wajima K., 1998, in Abstracts of the 19th Texas Symposium on Relativistic Astrophysics and Cosmology, held in Paris, France, Dec. 14-18, 1998. Eds.: J. Paul, T. Montmerle, and E. Aubourg (CEA Saclay).

Hockney R. W., Eastwood J. W., 1981, Computer Simulation Using Particles. Computer Simulation Using Particles, New York: McGraw-Hill, 1981

Hoeft M., Brüggen M., 2004, ApJ, 617, 896

Huang Z., Sarazin C. L., 1998, ApJ, 496, 728

Hudson M. J., 2004, private communication

Hudson M. J., Lucey J. R., Smith R. J., Steel J., 1997, MNRAS, 291, 488

Hudson M. J., Smith R. J., Lucey J. R., Branchini E., 2004, MNRAS, 352, 61

Hwang C., 1997, Science, 278, 1917

Irwin J. A., Bregman J. N., 2000, ApJ, 538, 543

Itoh N., Nozawa S., 2004, A&A, 417, 827

Iyudin A. F., Böhringer H., Dogiel V., Morfill G., 2004, A&A, 413, 817

Jackson J. D., 1975, Classical electrodynamics. 92/12/31, New York: Wiley, 1975, 2nd ed.

Jaffe W. J., 1977, ApJ, 212, 1

Jain B., Mo H. J., White S. D. M., 1995, MNRAS, 276, L25

Jain B., Seljak U., White S., 2000, ApJ, 530, 547

Jenkins A., Frenk C. S., White S. D. M., Colberg J. M., Cole S., Evrard A. E., Couchman H. M. P., Yoshida N., 2001, MNRAS, 321, 372

Jing Y. P., 2000, ApJ, 535, 30

Johnstone R. M., Allen S. W., Fabian A. C., Sanders J. S., 2002, MNRAS, 336, 299

Jones C., Forman W., 1984, ApJ, 276, 38

Jones T. W., Kang H., 1993, ApJ, 402, 560

Jones T. W., Kang H., 2005, arXiv:astro-ph/0506212

Jubelgas M., Springel V., Dolag K., 2004, MNRAS, 351, 423

Jubelgas M., Springel V., Enßlin T. A., Pfrommer C., 2005, MNRAS, in preparation

Jungman G., Kamionkowski M., Griest K., 1996, Phys. Rep., 267, 195

Kang H., Jones T. W., 1995, ApJ, 447, 944

Kang H., Jones T. W., 2005, ApJ, 620, 44

Kang H., Jones T. W., Gieseler U. D. J., 2002, ApJ, 579, 337

Kang H., Ryu D., Cen R., Song D., 2005, ApJ, 620, 21

Kang H., Ryu D., Jones T. W., 1996, ApJ, 456, 422

Kennel C. F., Edmiston J. P., Hada T., 1985, Washington DC American Geophysical Union Geophysical Monograph Series, 34, 1

Kerscher M., Schmalzing J., Retzlaff J., Borgani S., Buchert T., Gottlober S., Muller V., Plionis M., Wagner H., 1997, MNRAS, 284, 73

Keshet U., Waxman E., Loeb A., Springel V., Hernquist L., 2003, ApJ, 585, 128

Kim K. ., Kronberg P. P., Giovannini G., Venturi T., 1989, Nature, 341, 720

King I. R., 1962, AJ, 67, 471

King I. R., 1966, AJ, 71, 64

Klypin A. A., Shandarin S. F., 1983, MNRAS, 204, 891

Kravtsov A. V., Klypin A., Hoffman Y., 2002, ApJ, 571, 563

Kravtsov A. V., Klypin A. A., Khokhlov A. M., 1997, ApJS, 111, 73

Kravtsov A. V., Yepes G., 2000, MNRAS, 318, 227

Krimsky G. F., 1977, Sov. Phys. Dokl., 23, 327

Kuehr H., Witzel A., Pauliny-Toth I. I. K., Nauber U., 1981, A&AS, 45, 367

Kuo P., Bowyer S., Hwang C., 2005, ApJ, 618, 675

Kuo P., Hwang C., Ip W., 2003, ApJ, 594, 732

Kuo P., Hwang C., Ip W., 2004, ApJ, 604, 108

Kuwabara T., Nakamura K., Ko C. M., 2004, ApJ, 607, 828

Lahav O., Fabian A. C., Edge A. C., Putney A., 1989, MNRAS, 238, 881

Landau L. D., Lifshitz E. M., 1975, The classical theory of fields. Oxford: Pergamon Press, 1975

Lecar M., 1975, in IAU Symp. 69: Dynamics of the Solar Systems Dynamical Friction in the Coma Cluster. p. 161

Lemoine M., Sigl G., 2001, LNP Vol. 576: Physics and Astrophysics of Ultra-High-Energy Cosmic Rays, 576

Liang H., Dogiel V. A., Birkinshaw M., 2002, MNRAS, 337, 567

Liang H., Hunstead R. W., Birkinshaw M., Andreani P., 2000, ApJ, 544, 686

Lieu R., Mittaz J. P. D., Bowyer S., Breen J. O., Lockman F. J., Murphy E. M., Hwang C. ., 1996, Science, 274, 1335

Lima Neto G. B., Pislar V., Bagchi J., 2001, A&A, 368, 440

Loeb A., Waxman E., 2000, Nature, 405, 156

Lucy L. B., 1977, AJ, 82, 1013

Lynden-Bell D., 1967, MNRAS, 136, 101

Mac Low M., Ferrara A., 1999, ApJ, 513, 142

Malkov M. A., 1998, Phys. Rev. E, 58, 4911

Malkov M. A., 1999, ApJ, 511, L53

Malkov M. A., Drury L., 2001, Reports of Progress in Physics, 64, 429

Malkov M. A., Völk H. J., 1998, Advances in Space Research, 21, 551

Malkov M. A., Völk H. J., 1995, A&A, 300, 605

Malyshkin L., 2001, ApJ, 554, 561

Mannheim K., Schlickeiser R., 1994, A&A, 286, 983

Markevitch M., Gonzalez A. H., Clowe D., Vikhlinin A., Forman W., Jones C., Murray S., Tucker W., 2004, ApJ, 606, 819

Mason B. S., 2004, private communication

Matsushita K., Belsole E., Finoguenov A., Böhringer H., 2002, A&A, 386, 77

Mazzotta P., Kaastra J. S., Paerels F. B., Ferrigno C., Colafrancesco S., Mewe R., Forman W. R., 2002, ApJ, 567, L37

McHardy I. M., Lawrence A., Pye J. P., Pounds K. A., 1981, MNRAS, 197, 893

McNamara B. R., Wise M., Nulsen P. E. J., David L. P., Sarazin C. L., Bautz M., Markevitch M., Vikhlinin A., Forman W. R., Jones C., Harris D. E., 2000, ApJ, 534, L135

McNamara B. R., Wise M. W., Nulsen P. E. J., David L. P., Carilli C. L., Sarazin C. L., O'Dea C. P., Houck J., Donahue M., Baum S., Voit M., O'Connell R. W., Koekemoer A., 2001, ApJ, 562, L149

Mecke K. R., Buchert T., Wagner H., 1994, A&A, 288, 697

Messier C., 1784, Connaissance des Temps. (Paris)

Meyer J., Drury L. O., Ellison D. C., 1997, ApJ, 487, 182

Miniati F., 2001, Computer Physics Communications, 141, 17

Miniati F., 2002, MNRAS, 337, 199

Miniati F., Jones T. W., Kang H., Ryu D., 2001, ApJ, 562, 233

Miniati F., Ryu D., Kang H., Jones T. W., 2001, ApJ, 559, 59

Miniati F., Ryu D., Kang H., Jones T. W., Cen R., Ostriker J. P., 2000, ApJ, 542, 608

Misner C. W., Thorne K. S., Wheeler J. A., 1973, Gravitation. San Francisco: W.H. Freeman and Co., 1973

Mohr J. J., Mathiesen B., Evrard A. E., 1999, ApJ, 517, 627

Monaghan J. J., 1997, Journal of Computational Physics, 136, 298

Monaghan J. J., Lattanzio J. C., 1985, A&A, 149, 135

Moskalenko I. V., Strong A. W., 1998, ApJ, 493, 694

Nachtmann O., 1990, Elementary particle physics: Concepts and phenomena. Springer

Narayan R., Medvedev M. V., 2001, ApJ, 562, L129

Nath B. B., Biermann P. L., 1994, MNRAS, 267, 447

Navarro J. F., Frenk C. S., White S. D. M., 1997, ApJ, 490, 493

Navarro J. F., White S. D. M., 1993, MNRAS, 265, 271

Neilsen E. H., Tsvetanov Z. I., 2000, ApJ, 536, 255

Nipoti C., Binney J., 2004, MNRAS, 349, 1509

Norman M. L., Bryan G. L., 1999, in ASSL Vol. 240: Numerical Astrophysics p. 19

Novikov D., Schmalzing J., Mukhanov V. F., 2000, A&A, 364, 17

Oegerle W. R., Hill J. M., 2001, AJ, 122, 2858

Ohno H., Takizawa M., Shibata S., 2002, ApJ, 577, 658

Ostriker J. P., Tremaine S. D., 1975, ApJ, 202, L113

Pacholczyk A. G., 1970, Radio astrophysics. Nonthermal processes in galactic and extragalactic sources. Series of Books in Astronomy and Astrophysics, San Francisco: Freeman, 1970

Parker E. N., 1969, Space Sci. Rev., 9, 651

Pavlidou V., Fields B. D., 2005, arXiv:astro-ph/0504485

Peacock J. A., Dodds S. J., 1996, MNRAS, 280, L19

Pedlar A., Ghataure H. S., Davies R. D., Harrison B. A., Perley R., Crane P. C., Unger S. W., 1990, MNRAS, 246, 477

Pen U., 1998, ApJS, 115, 19

Peterson J. R., Kahn S. M., Paerels F. B. S., Kaastra J. S., Tamura T., Bleeker J. A. M., Ferrigno C., Jernigan J. G., 2003, ApJ, 590, 207

Peterson J. R., Paerels F. B. S., Kaastra J. S., Arnaud M., Reiprich T. H., Fabian A. C., Mushotzky R. F., Jernigan J. G., Sakelliou I., 2001, A&A, 365, L104

Petrosian V. ., 2001, ApJ, 557, 560

Pfrommer C., Enßlin T. A., 2003, A&A, 407, L73

Pfrommer C., Enßlin T. A., 2004a, A&A, 413, 17

Pfrommer C., Enßlin T. A., 2004b, MNRAS, 352, 76

Pfrommer C., Enßlin T. A., Sarazin C. L., 2005, A&A, 430, 799

Pfrommer C., Springel V., Enßlin T. A., Jubelgas M., 2005, MNRAS, submitted

Pietz J., Kerp J., Kalberla P. M. W., Burton W. B., Hartmann D., Mebold U., 1998, A&A, 332, 55

Pohl M., 1993, A&A, 270, 91

Press W. H., Schechter P., 1974, ApJ, 187, 425

Price D. J., Monaghan J. J., 2004a, MNRAS, 348, 123

Price D. J., Monaghan J. J., 2004b, MNRAS, 348, 139

Quilis V., Bower R. G., Balogh M. L., 2001, MNRAS, 328, 1091

Quilis V., Ibanez J. M. A., Saez D., 1998, ApJ, 502, 518

Rachen J. P., Stanev T., Biermann P. L., 1993, A&A, 273, 377

Ramaty R., Kozlovsky B., Lingenfelter R. E., Reeves H., 1997, ApJ, 488, 730

Rasio F. A., Shapiro S. L., 1991, ApJ, 377, 559

Ratra B., Peebles P. J. E., 1988, Phys. Rev. D, 37, 3406

Rechester A., Rosenbluth M., 1978, Phys. Rev. Lett., 40, 38

Rees M. J., 1967, MNRAS, 137, 429

Refregier A., Teyssier R., 2002, Phys. Rev. D, 66, 043002

Reimer O., Pohl M., Sreekumar P., Mattox J. R., 2003, ApJ, 588, 155

Renzini A., 1997, ApJ, 488, 35

Rephaeli Y., 1995a, ARA&A, 33, 541

Rephaeli Y., 1995b, ApJ, 445, 33

Rephaeli Y., Gruber D., 2003, ApJ, 595, 137

Rephaeli Y., Ulmer M., Gruber D., 1994, ApJ, 429, 554

Roettiger K., Burns J. O., Stone J. M., 1999, ApJ, 518, 603

Rossetti M., Molendi S., 2004, A&A, 414, L41

Röttgering H. J. A., Wieringa M. H., Hunstead R. W., Ekers R. D., 1997, MNRAS, 290, 577

Rottmann H., Mack K.-H., Klein U., Wielebinski R., 1996, A&A, 309, L19

Ruszkowski M., Begelman M. C., 2002, ApJ, 581, 223

Rybicki G. B., Lightman A. P., 1979, Radiative processes in astrophysics. New York, Wiley-Interscience, 1979.

Ryu D., Kang H., Hallman E., Jones T. W., 2003, ApJ, 593, 599

Sanders J. S., Fabian A. C., Dunn R. J. H., 2005, MNRAS, 360, 133

Sarazin C. L., 1988, X-ray emission from clusters of galaxies. Cambridge Astrophysics Series, Cambridge: Cambridge University Press, 1988

Sarazin C. L., 1999, ApJ, 520, 529

Sarazin C. L., 2002, in Feretti L., Gioia I., G. G., eds, ASSL Vol. 272: Merging Processes in Galaxy Clusters, The Physics of Cluster Mergers, Kluwer Academic Publishers, Dordrecht, p. 1

Sazonov S. Y., Sunyaev R. A., 2000, A&A, 354, L53

Schödel R., Ott T., Genzel R., Hofmann R., Lehnert M., Eckart A., Mouawad N., Alexander T., Reid M. J., Lenzen R., Hartung M., Lacombe F., et al. 2002, Nature, 419, 694

Schäfer B. M., Pfrommer C., Bartelmann M., Springel V., Hernquist L., 2004, astro-ph/0407089

Schäfer B. M., Pfrommer C., Hell R., Bartelmann M., 2004, astro-ph/0407090

Schechter P., 1976, ApJ, 203, 297

Schindler S., Castillo-Morales A., De Filippis E., Schwope A., Wambsganss J., 2001, A&A, 376, L27

Schlegel D. J., Finkbeiner D. P., Davis M., 1998, ApJ, 500, 525

Schlickeiser R., 2002, Cosmic ray astrophysics. Springer.

Schlickeiser R., Sievers A., Thiemann H., 1987, A&A, 182, 21

Schmalzing J., Gottlöber S., Klypin A. A., Kravtsov A. V., 1999, MNRAS, 309, 1007

Schuecker P., Finoguenov A., Miniati F., Böhringer H., Briel U. G., 2004, A&A, 426, 387

Shapiro M. M., 1999, in ASP Conf. Ser. 171: LiBeB Cosmic Rays, and Related X- and Gamma-Rays How Cosmic Rays Get Started. p. 138

Sheth R. K., Tormen G., 1999, MNRAS, 308, 119

Shimon M., Rephaeli Y., 2002, ApJ, 575, 12

Sijbring L. G., 1993, PhD thesis, Groningen University

Sikora M., Madejski G., 2000, ApJ, 534, 109

Simpson J. A., 1983, Annual Review of Nuclear and Particle Science, 33, 323

Skilling J., 1975, MNRAS, 172, 557

Snowden S. L., Egger R., Freyberg M. J., McCammon D., Plucinsky P. P., Sanders W. T., Schmitt J. H. M. M., Truemper J., Voges W., 1997, ApJ, 485, 125

Sod G. A., 1978, Journal of Computational Physics, 27, 1

Soker N., 2003, MNRAS, 342, 463

Spergel D. N., Verde L., Peiris H. V., Komatsu E., Nolta M. R., Bennett C. L., Halpern M., Hinshaw G., Jarosik N., Kogut A., Limon M., Meyer S. S., Page L., Tucker G. S., Weiland J. L., Wollack E., Wright E. L., 2003, ApJS, 148, 175

Spitzer L. J., Harm R., 1958, ApJ, 127, 544

Springel V., 2005, astro-ph/0505010

Springel V., Hernquist L., 2002, MNRAS, 333, 649

Springel V., Yoshida N., White S. D. M., 2001, New Astronomy, 6, 79

Stecker F. W., 1970, Ap&SS, 6, 377

Stecker F. W., 1971, Cosmic gamma rays. Baltimore: Mono Book Corp.

Stephens S. A., Badhwar G. D., 1981, Ap&SS, 76, 213

Stoehr F., White S. D. M., Springel V., Tormen G., Yoshida N., 2003, MNRAS, 345, 1313

Strong A. W., Moskalenko I. V., Reimer O., 2000, ApJ, 537, 763

Strong A. W., Moskalenko I. V., Reimer O., 2004, ApJ, 613, 956

Struble M. F., Rood H. J., 1999, ApJS, 125, 35

Sun M., Murray S. S., Markevitch M., Vikhlinin A., 2002, ApJ, 565, 867

Sunyaev R. A., Zeldovich I. B., 1980, ARA&A, 18, 537

Sunyaev R. A., Zel'dovich Y. B., 1972, Comments Astrophys. Space Phys., 4, 173

Takizawa M., Naito T., 2000, ApJ, 535, 586

Taylor G. B., Perley R. A., 1993, ApJ, 416, 554

The L. S., White S. D. M., 1986, AJ, 92, 1248

Thierbach M., Klein U., Wielebinski R., 2003, A&A, 397, 53

Tornatore L., Borgani S., Springel V., Matteucci F., Menci N., Murante G., 2003, MNRAS, 342, 1025

Toro E. F., 1997, Riemann Solvers and Numerical Methods for Fluid Dynamics. Springer

Tribble P. C., 1993, MNRAS, 263, 31

Valinia A., Marshall F. E., 1998, ApJ, 505, 134

Valtaoja E., 1984, A&A, 135, 141

Venturi T., Giovannini G., Feretti L., 1990, AJ, 99, 1381

Vestrand W. T., 1982, AJ, 87, 1266

Vogt C., Enßlin T. A., 2003, A&A, 412, 373

Vogt C., Enßlin T. A., 2005, A&A, 434, 67

Voigt L. M., Schmidt R. W., Fabian A. C., Allen S. W., Johnstone R. M., 2002, MNRAS, 335, L7

Voit G. M., 2005, Reviews of Modern Physics, 77, 207

Voit G. M., Bryan G. L., Balogh M. L., Bower R. G., 2002, ApJ, 576, 601

Völk H. J., Aharonian F. A., Breitschwerdt D., 1996, Space Sci. Rev., 75, 279

Waxman E., 2000, Nuclear Physics B Proceedings Supplements, 87, 345

Wentzel D. G., 1974, ARA&A, 12, 71

Wetterich C., 1988, Nuclear Physics B, 302, 645

Wetterich C., 1995, A&A, 301, 321

White D. A., 2000, MNRAS, 312, 663

White M., 2001, A&A, 367, 27

White S. D. M., 1976, MNRAS, 174, 19

White S. D. M., Efstathiou G., Frenk C. S., 1993, MNRAS, 262, 1023

White S. D. M., Frenk C. S., 1991, ApJ, 379, 52

White S. D. M., Frenk C. S., Davis M., 1983, ApJ, 274, L1

White S. D. M., Navarro J. F., Evrard A. E., Frenk C. S., 1993, Nature, 366, 429

White S. D. M., Rees M. J., 1978, MNRAS, 183, 341

Wiebel-Sooth B., Biermann P. L., 1998, Landolt-Boernstein Numerical Data and Functional Relationships. Vol. New Series Vol. VI 3C, Springer

Wright E. L., 1979, ApJ, 232, 348

Wu K. K. S., Fabian A. C., Nulsen P. E. J., 2000, MNRAS, 318, 889

Xu G., 1995, ApJS, 98, 355

Yepes G., Kates R., Khokhlov A., Klypin A., 1995, in Clustering in the Universe p. 209

Yoshida N., Springel V., White S. D. M., Tormen G., 2000, ApJ, 544, L87

Young A. J., Wilson A. S., Mundell C. G., 2002, ApJ, 579, 560

Zaroubi S., Squires G., de Gasperis G., Evrard A. E., Hoffman Y., Silk J., 2001, ApJ, 561, 600

Zaroubi S., Squires G., Hoffman Y., Silk J., 1998, ApJ, 500, L87

Zatsepin G. T., Kuzmin V. A., 1966, Sov. Phys. JETP Lett., 4, 78

Zwicky F., 1937, ApJ, 86, 217

Acknowledgements

Publications

Refereed Publications:

1. **C. Pfrommer**, T.A. Enßlin:
   Probing the cosmic ray population of the giant elliptical galaxy M 87 with observed TeV gamma-rays,
   2003, *A&A*, 407, L73

2. **C. Pfrommer**, T.A. Enßlin:
   Constraining the population of cosmic ray protons in cooling flow clusters with gamma-ray and radio observations: Are radio mini-halos of hadronic origin?
   2004, *A&A*, 413, 17

3. **C. Pfrommer**, T.A. Enßlin:
   Estimating galaxy cluster magnetic fields by the classical and hadronic minimum energy criterion,
   2004, *MNRAS*, 352, 76

4. **C. Pfrommer**, T.A. Enßlin, C. Sarazin:
   Unveiling the composition of radio plasma bubbles in galaxy clusters with the Sunyaev-Zel'dovich effect,
   2005, *A&A*, 430, 799

5. T. Hamana, M. Bartelmann, N. Yoshida, **C. Pfrommer**:
   Statistical distribution of gravitational-lensing excursion angles: Winding ways to us from the deep universe,
   2005, *MNRAS*, 356, 829

6. B.M. Schäfer, **C. Pfrommer**, S. Zaroubi:
   Redshift estimation of clusters by wavelet decomposition of their Sunyaev-Zel'dovich morphology,
   2005, *MNRAS*, 362, 1418

Submitted publications:

7. **C. Pfrommer**, V. Springel, T.A. Enßlin, M. Jubelgas:
   Structure formation shocks in cosmological SPH simulations with relativistic particle populations,
   2005, *MNRAS*, submitted

8. T.A. Enßlin, **C. Pfrommer**, V. Springel, M. Jubelgas:
   Cosmic ray physics in calculations of cosmological structure formation,
   2005, *MNRAS*, submitted

9. B.M. Schäfer, **C. Pfrommer**, M. Bartelmann, V. Springel, L. Hernquist:
   Detecting Sunyaev-Zel'dovich clusters with Planck: I. Construction of all-sky thermal and kinetic SZ-maps,
   2005, *MNRAS*, submitted, [astro-ph/0407089]

10. B.M. Schäfer, **C. Pfrommer**, R. Hell, M. Bartelmann:
    Detecting Sunyaev-Zel'dovich clusters with Planck: II. Foreground components and optimised filtering schemes,
    2005, *MNRAS*, submitted, [astro-ph/0407090]

Conference Proceedings

11. T.A. Enßlin, C. Vogt, **C. Pfrommer**:
Magnetic fields and cosmic rays in cooling flows,
2003 in *The Riddle of Cooling Flows in Galaxies and Clusters of Galaxies*, eds. T.H. Reiprich, J.C. Kempner,
N. Soker, [astro-ph/0310028]
Published electronically at http://www.astro.virginia.edu/coolflow/

12. **C. Pfrommer**, T.A. Enßlin:
The quest for cosmic ray protons in clusters of galaxies,
2004, JKAS, 37, 455 in *Cosmic Rays and Magnetic Fields in Large Scale Structure*, eds. D. Ryu, H. Kang

13. T.A. Enßlin, C. Vogt, **C. Pfrommer**:
Magnetic fields in clusters of galaxies,
2004, in *The Magnetized Plasma in Galaxy Evolution*, Proceedings of a Conference held at Krakow, Poland,
[astro-ph/0501338]

Curriculum Vitae

Personal data

Name:	Christoph Pfrommer
Adress:	Max-Planck-Institut für Astrophysik,
	Karl-Schwarzschild-Straße 1,
	85741 Garching, Germany
e-mail:	pfrommer@mpa-garching.mpg.de
Birth:	October 22, 1975, Ulm, Germany
Nationality:	German citizenship

Education

1982 to 1986	**Grundschule** (elementary school), Neu-Ulm/Pfuhl, Germany
1986 to 1995	Bertha-von-Suttner Gymnasium, Neu-Ulm, Germany
May, 1995	**Abitur** (final examination of secondary education),
	Bertha-von-Suttner Gymnasium, Neu-Ulm, Germany,
	one-year project: "Basics and axiomatics of non-Euclidean geometries"
1995 to 1996	**Solo Bassoonist** in Military Music Band (completed military service),
	Gebirgsmusikkorps 1, Garmisch-Partenkirchen, Germany

Academic record

1996 to 2002	**Study of Physics** at Friedrich Schiller Universität, Jena, Germany
Sep. 1998	**Vordiplom in Physics** (diploma comparable to B.S.)
	Friedrich Schiller Universität, Jena, Germany
1999 to 2000	**Special Graduate Student** in Physics,
	Harvard University Graduate School of Arts and Science,
	Cambridge, Massachusetts, USA
2000 to 2002	**Diploma thesis** at Max-Planck Institut für Astrophysik, Garching, Germany:
	"Cosmological weak lensing of the cosmic microwave background by large scale structures",
	Supervisors: Prof. Dr. S.D.M. White, Prof. Dr. R. Meinel, Prof. Dr. M.Bartelmann
Jul. 2002	**Diplom in Physics**, (diploma comparable to M.S.),
	Friedrich Schiller Universität, Jena, Germany
2002 to 2005	**PhD student** at Max-Planck-Institut für Astrophysik, Garching, Germany,
	participation in the "*European Research Training Network –*
	The Physics of the Intergalactic Medium"
Jul. 2004	**Participation in the Heraeus Summer School**,
	"Physics with Cosmic Accelerators", Bad Honnef, Germany

Fellowships

1996 to 2002	**Scholarship** by *Evangelisches Studienwerk Villigst*
1999 to 2000	**Stipend** by *Evangelisches Studienwerk Villigst* in support of the studies at Harvard University